UTS UNIVERSITY OF TECHNOLOGY SYDNEY

Development of a Smart Gas Metal Arc Welding System Using Acoustic Sensing

by Mitchell Cullen

Thesis submitted in fulfilment of the requirements for the degree of

Doctor of Philosophy

under the supervision of Associate Professor JC Ji and Dr Guoqiang Zhang

University of Technology Sydney
Faculty of Engineering and IT
May 2023

CERTIFICATE OF ORIGINAL AUTHORSHIP

I, Mitchell Cullen, declare that this thesis is submitted in fulfilment of the requirements for the award of Doctor of Philosophy, in the School of Mechanical and Mechatronic Engineering at the University of Technology Sydney.

This thesis is wholly my own work unless otherwise referenced or acknowledged. In addition, I certify that all information sources and literature used are indicated in the thesis.

This document has not been submitted for qualifications at any other academic institution.

This research is supported by the Australian Government Research Training Program.

Signature: Production Note:
Signature removed prior to publication.

Date: 18/01/2024

TABLE OF CONTENTS

LIST OF FIGURES

LIST OF TABLES

List of Equations

ABSTRACT

Gas Metal Arc Welding (GMAW) is a widely utilized welding process that involves the formation of an electric arc between a consumable wire electrode and a metal workpiece, protected from contaminants by a shielding gas. While GMAW is a reliable, fast, and effective welding method, controlling it can be challenging, especially in automated processes where skilled operators are absent. Skilled welders traditionally rely on audible and visual cues to control the arc, ensuring proper penetration and minimizing the occurrence of defects.

Automated robotic welding processes currently lack an adequate quality control system that can replicate the abilities of experienced welders. This deficiency leads to expensive quality control checks after production, increased labour time for reworks, and extended downtime while rectifying issues. However, the implementation of an effective real-time quality control system enables the immediate detection of defects during production, allowing prompt resolution and avoiding costly post-production checks.

This research aims to replicate the abilities of manual welders by utilizing acoustic signals to monitor the droplet transfer process. Signal processing and machine learning techniques are employed to analyse the acoustic signals and monitor the formation of the weld bead. By monitoring the droplet transfer process, it becomes possible to assess the physical properties of the weld bead as it forms, thereby detecting defects like porosity and burn-through. Additionally, a digital twin of the weld bead formation was created to provide real-time visualization of penetration depth and cross-sectional profile growth. This new system is able to accurately detect the droplet transfer mode, defects, and plot the penetration profile with 96%, 90%, and 90% accuracy respectively.

The acoustic monitoring system developed in this study offers simplicity, easy installation, and non-intrusiveness, making it an ideal plug-and-play solution for modern automated industrial GMAW welding applications. Its implementation minimizes costs and downtime associated with troubleshooting, non-destructive testing, and on-site reworks.

ACKNOWLEDGEMENTS

To start off with I would like to say a huge thank you to my supervisor, Prof. JC Ji for all of his support and mentorship over the past few years. You've taught me so much and made my time here incredibly enjoyable. Thanks for everything you've done for me!

I'd also like to say thanks to my previous supervisor, Prof. Xiaojun Qiu. Thank you so much for giving me the opportunity to undertake this project. I'd also like to thank my co-supervisor Dr Guoqiang Zhang for his guidance throughout my candidature as well as Dr. Sipei Zhao for all of his technical advice.

I would also like to extend a massive thanks to Ben Poole and the guys at Scott Automation & Robotics for all their support and helping me out when I needed it the most. You guys stuck your neck out for me and saved this research by lending me your equipment and workshop space during the pandemic when I thought this project was doomed. There's no way I could have finished this without you!

Finally, and most importantly, I'd like to say thanks to both my parents, Cathy and Craig Cullen, and my amazing partner Michelle Chan. Thank you for all you love and support, especially enduring through my endless rants. Honestly I don't know how you put up with my antics at the best of times, let alone the past few years. I know I've driven you all mad, especially this past year, but thanks for always having my back no matter what. You all mean the world to me!

Publication List

Current Publications

At this stage 1 journal paper and 3 conference papers have been produced based on the contents of this thesis.

Journal Articles:

- *Classification of transfer modes in gas metal arc welding using acoustic signal analysis* –This paper outlines the contents of chapter 4 in which a new GMAW transfer mode detection and classification system by analysing the acoustic signal is presented. This system was developed using a custom feature selection and optimisation algorithm that extracted features from the sound signal and classified the droplet transfer process using an SVM classifier. This system was able to accurately detect and classify the transfer modes with up to 96% accuracy.

Conference Papers:

- *Acoustic Based Classification of Transfer Modes in Gas Metal Arc Welding* – This paper is also based on the contents of chapter 4. This conference paper expands on the results presented in the previously mentioned journal article.
- *Real time acoustic based burn through detection in gas metal arc welding* – This paper outlines the contents of chapter 5. In this paper, a new real time GMAW burn through detection system is presented. This system uses the previously developed transfer mode detection algorithm to monitor the welding process in real time. An algorithm was developed to monitor the fluctuations in the transfer modes to predict when the welding arc has started burning through the base material. This system was able to accurately detect burn through locations with approximately 90% accuracy.
- *Acoustic based GMAW penetration depth identification using droplet transfer monitoring* – This paper outlines the contents of chapter 6. In this paper, a penetration estimation method for GMAW by monitoring the droplet transfer process is presented. By using a combination of several input parameters, alongside information regarding the droplet transfer mode extracted from the sound signal, an estimation of the weld bead's root penetration depth can be calculated.

Future Publications

In addition to the currently published journal article and conference papers, an additional 2 journal papers are currently being prepared based on the contents of this thesis.

Journal Articles:

- This paper will combine the contents of chapters 5 and 6 of this thesis which cover both real time defect detection and penetration depth estimation in Gas Metal Arc Welding (GMAW). This paper will demonstrate that by monitoring the fluctuations in the droplet transfer process,

it is possible to detect porosity and burn through while estimating the penetration depth of the weld pool in real time.

- *A real time GMAW profile plotting algorithm and digital twin* – This paper will be based on the contents of chapter 7 concerning weld bead growth and penetration profile mapping in GMAW. In this paper, a new method of modelling the profile of both the weld bead and the penetration profile in real time will be introduced. This is done by using an analytical model built upon the geometric distribution of the weld pool while monitoring the droplet transfer process to estimate the heat input.

CHAPTER 1 - Introduction

1.1. Gas Metal Arc Welding

Gas Metal Arc Welding (GMAW) is a process that utilizes a high-powered electric arc to melt and fuse a metal workpiece with a wire electrode. To protect both the workpiece and the electrode and facilitate arc generation, a shielding gas is employed to prevent contamination from the surrounding air .[1]

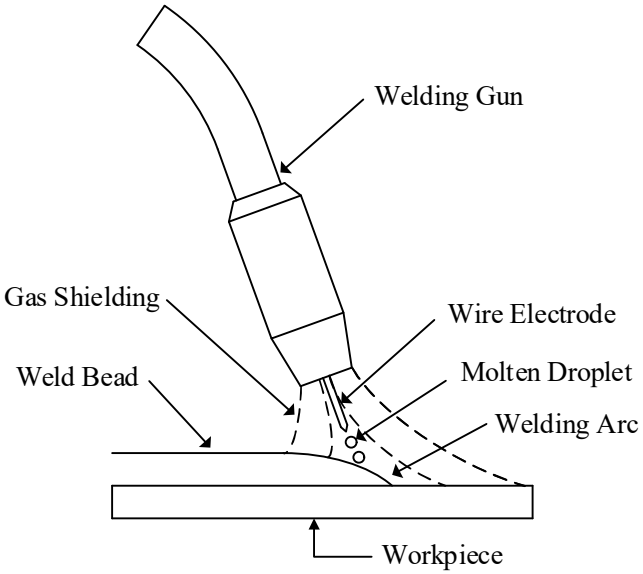

Figure 1.1 - The GMAW Welding Process

As industries increasingly adopt automation, researchers have endeavoured to enhance the GMAW process. However, automated applications still lack the robustness and flexibility exhibited by manual welding processes executed by skilled and trained welders [2].

Skilled welders possess the ability to detect and correct faults during the GMAW process, as well as adjust welding settings based on audio and visual feedback cues. Research has demonstrated the usefulness of audio signals generated during welding for welders to determine the appropriateness of welding settings for a specific application [1]. Numerous researchers have investigated these audio signals over the years, striving to comprehend their mechanics and leverage them to enhance quality control in the GMAW process, akin to a trained welder. However, substantial research remains necessary to improve the automated GMAW process to the level achieved by expert welders.

1.2. Problem Statement

Process monitoring and quality control pose significant challenges in robotic GMAW applications. Currently, there is no comprehensive GMAW monitoring system available on the market, leading to costly quality control checks after production, increased labour time for reworks, and extended downtime while rectifying issues. The objective of this research is to develop a comprehensive GMAW monitoring system based on acoustic signals by monitoring the droplet transfer process. This monitoring enables the assessment of physical properties during weld bead formation, facilitating the detection of defects such as porosity and burn through. Furthermore, a real-time digital twin of the weld bead formation will be constructed, providing visualization of penetration depth and cross-sectional profile growth.

1.3. Objectives

This thesis encompasses three major objectives, which are as follows:

1. The first objective is to create a comprehensive system capable of monitoring the GMAW welding process. This model should accurately detect and classify the transfer mode in use and identify any mode changes that occur during the weld. By achieving this, a robust classification system can be established, minimizing errors in the GMAW process and verifying the appropriate transfer mode.
2. The second objective is to develop a fault detection system that identifies issues during the welding process. This system aims to detect major faults such as porosity, lack of penetration, and burn-through, providing information about the type, location, and severity of the fault. By detecting these faults, the system can alert the user to inspect the weld and assess its suitability or initiate a new welding process. Additionally, the system should enable real-time troubleshooting and immediate cessation.
3. The final major objective of this thesis is to develop a real-time algorithm for weld bead penetration and plotting using the transfer mode detection system. This penetration system will utilize dynamic information from the transfer mode detection system, along with several other welding parameters, to plot the shape and penetration depth of the weld bead as it grows. A digital twin of the system will be developed in real-time to help the operator confirm that the weld bead profile is forming as intended.

1.4. Contributions

1.4.1. Transfer Mode Detection

The first major contribution of this thesis is the development of an acoustic-based GMAW transfer mode detection system. Transfer modes play a significant role in determining the characteristics of a weld and how the process is performed. However, there has been limited research on automatically classifying these signals, and most existing literature focuses on observations of a single transfer mode. This research explores an unexplored area and offers several potential benefits.

One of the main benefits of a transfer mode detection algorithm is its ability to reduce costs in medium to large-scale welding applications. Currently, weld beads are often oversized to account for potential fusion issues and ensure structural integrity. With an accurate model that detects and classifies transfer modes, the weld seam can be verified, allowing for a smaller factor of safety in the design of weldments. This results in material savings and reduces welding and quality monitoring time, leading to overall cost reduction and improved quality control.

1.4.2. Fault Detection

The second major contribution of this thesis is the development of a real-time defect detection system based on transfer mode monitoring. Many types of faults can occur during the welding process and detecting them is crucial for ensuring the structural integrity of the weld. While previous studies have investigated methods to detect specific faults, there is still a lack of a widely adopted method for automatically detecting multiple faults across different transfer modes [3-7]. Developing such a system offers several benefits.

One of the main benefits of a fault detection algorithm is its ability to reliably detect major flaws in GMAW welds that may not be visible to the naked eye. Detecting these faults before failure occurs saves time and costs associated with manufacturing new parts to replace failed ones. Additionally, the algorithm can identify faults missed in automated GMAW applications, reducing inspection time.

1.4.3. Weld Bead Plotting

The final major contribution of this thesis is the development of a real-time weld bead plotting algorithm and digital twin system. The shape and penetration profile of a weld bead are crucial for determining its structural integrity. Currently, methods in the literature either rely on computationally expensive post-weld CFD analysis or calculate average estimates of the weld bead profile. A real-time plotting algorithm offers significant benefits.

Having a plotting algorithm that works in real time allows operators to identify issues with the weld bead's penetration profile remotely. They can modify input parameters during the weld to ensure the weld penetration profile meets the requirements.

1.5. Thesis Overview

To elaborate on the aforementioned contributions, this thesis will be structured as follows:

1. An extensive literature review will be presented, providing a comprehensive understanding of the GMAW process. This review will delve into the underlying principles that drive the welding process, as well as provide a brief overview of the current literature on GMAW process automation.
2. Following the literature review, the design of the experimental test rig used to develop the systems mentioned in the contributions above will be detailed. This section will cover the design and technical specifications of both the test rig and the data collection system.

3. The first significant contribution of this thesis, the acoustic-based GMAW transfer mode detection system, will be presented. This section will discuss the methodologies and techniques employed to develop the transfer mode detection system, accompanied by validated experimental results.
4. The second major contribution, a real-time GMAW defect detection system, will be presented in two chapters. This section will primarily focus on the detection of two common welding defects: porosity and burn-through, along with a penetration depth estimation system. The methodologies used and the experiments conducted to validate the proposed models will be thoroughly discussed.
5. The final contribution, real-time GMAW penetration and weld bead profile plotting, will be presented. This section will encompass the mathematical model introduced to simulate the growth of the weld bead and penetration profile in real time. Additionally, a comparison of the results with experimentally obtained data will be provided.
6. The concluding section will summarize the key findings and conclusions of this thesis. Furthermore, it will outline potential future research directions to further enhance the existing knowledge and address any remaining gaps in the field.

By following this structured layout, this thesis aims to provide a comprehensive understanding of the GMAW process, present innovative contributions in transfer mode detection, defect detection, and weld bead profiling, and propose avenues for future research.

CHAPTER 2 – GMAW LITERATURE REVIEW

In this chapter, a detailed overview of the gas metal arc welding process and its characteristics will be presented. Following this an overview of current welding automation methods will be presented covering transfer mode detection, defect detection, process control, penetration measurement and weld bead plotting.

2.1. GMAW Parameters

As stated in **CHAPTER 1**, GMAW is a welding process that consists of a consumable wire electrode which is superheated and fused with a base material by passing a high current through the wire. This entire process is shielded with a protective gas to protect the final weld bead from unwanted contaminants.

This welding process can be broken down into three main stages as shown in **Figure 2.1**. These three stages are the input stage, where initial parameters are set at the beginning of the welding process, the welding stage where the welding process is performed and is further affected by intermediate variables, and the finished stage in which the final output variables are produced.

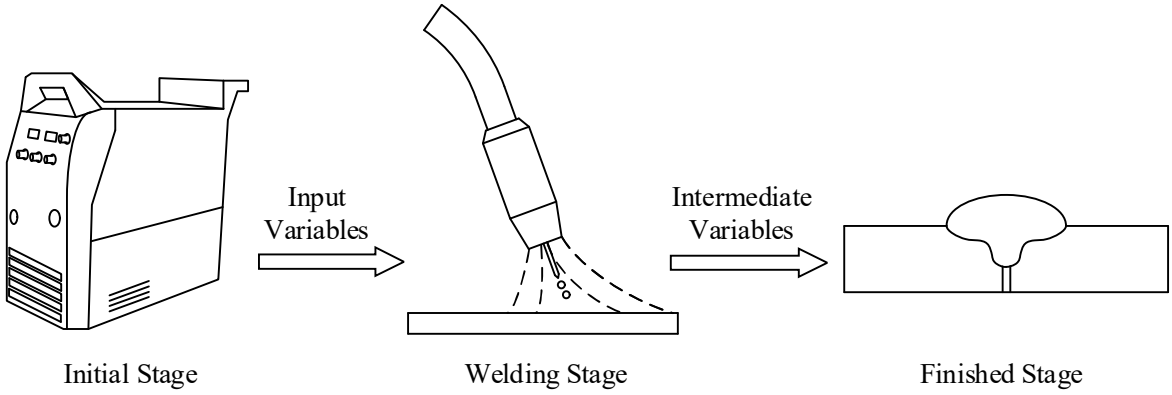

Figure 2.1 - GMAW process decomposition

These variables that drive and are generated by the welding process can be seen in **Table 2.1**.

Table 2.1 - Welding process parameters

Input Variable	Intermediate Variables	Output Variables
Supply Voltage	Current	Weld bead geometry
Wire feed speed	Stick out	Depth penetration
Contact Tip to Workpiece Distance (CTWD)	Arc length	Mechanical properties
Travel speed	Arc pressure	Microstructure
Torch angle	Arc Shape	
Work angle	Heat Transfer	
Torch motion pattern	Cooling Rate	

Gas composition	Melting rate
Gas flow rate	Mass transfer
Electrode diameter	Transfer mode
Electrode material	Weld pool dimensions
Workpiece material	
Joint geometry	

2.1.1. Input Variables

In GMAW, several initial variables are set to drive the welding process. These parameters are outlined as follows:

Voltage: In GMAW, the welding supply voltage is set at a constant value. This value affects the length of the welding arc, in turn affecting both the final weld bead's height and width.

Wire feed speed: Wire feed speed is the speed in which the consumable wire electrode is fed from the welding power source into the welding arc. In combination with the welding voltage, the wire feed speed is one of the main factors in determining the welding current that is passed through the wire electrode.

CTWD: Contact Tip to Workpiece Distance (CTWD) as described is the distance from the electrode tip to the workpiece that is being welded. This distance can be seen in **Figure 2.5** which shows the CTWD in context of the welding arc and its derived variables stick out length and arc length.

Travel speed: Travel speed is the speed in which the welding torch is moved in the welding direction. Slower travel speeds result in more heat and material being deposited into the weld, with less heat and material being deposited as the travel speed increases.

Torch angle: The torch angle is the angle in which the welding torch makes with the workpiece in the welding direction. In standard operating conditions, the torch angle is normally set to be up to +/- 15 degrees, with a positive angle being known as "push" technique and a negative angle being known as "pull" technique. Typically, when using push technique, the weld pool is pushed forward by the welding arc resulting in a wider, flatter weld bead, whereas a pull angle will lead to a narrower, taller weld bead. These angles can be seen in **Figure 2.2**.

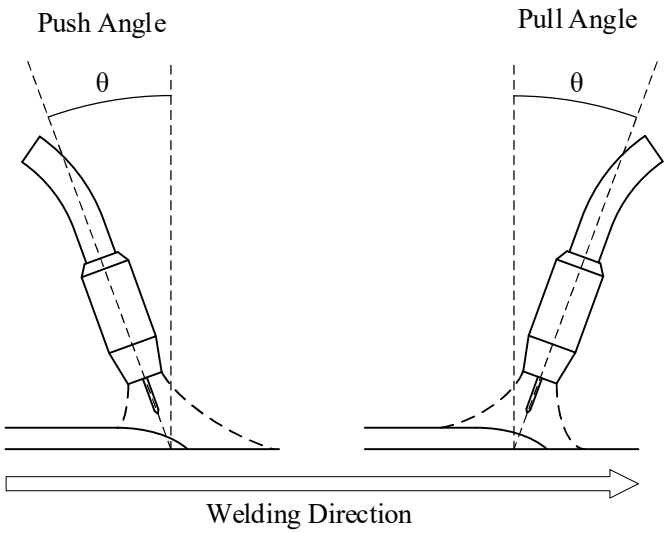

Figure 2.2 - Torch Angle

Work angle: The work angle is the angle the welding torch makes with the workpiece perpendicular to the welding direction. This can be seen in **Figure 2.3**.

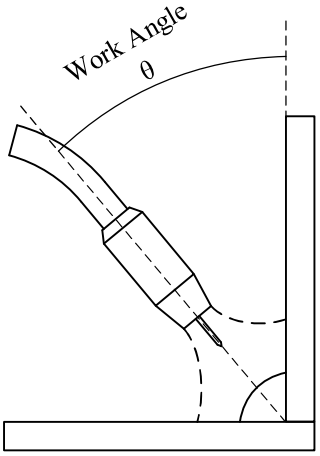

Figure 2.3 - Work Angle

Torch motion: Torch motion describes the motion in which the welding torch moves along the weld path. In GMAW the two main methods of torch motion are steady motion, which as the name implies, moves the welding torch forward at a constant speed, and weaving motion, which weaves the welding torch back and forward in the welding direction to "push or pull" the weld pool.

Gas Composition: Depending on the application, a variety of shielding gasses can be used in the GMAW process. In Metal Inert Gas (MIG) welding, an argon, or primarily argon based mixture is used as an inert gas to protect the weld pool from unwanted external contaminants. Similarly in Metal Active Gas (MAG) welding, CO_2 or a CO_2 based mixture is used. This gas composition plays a large part in changing the resistance of the welding arc, surface tension of the welding droplet and general heat distribution of the welding process.

Gas flow: Gas flow rate is the rate in which the shielding gas flows out of the welding torch to surround the wire electrode. Higher flow rates result in better coverage of the weld pool, however if the flow rate is too high, turbulence can occur resulting in atmospheric gasses mixing into the weld pool leading to the possibility of welding defects occurring. If the flow rate is set too low, the weld pool will be subject to inadequate shielding gas coverage, also leading to atmospheric gasses mixing into the weld pool.

Electrode diameter: In GMAW, the diameter of the wire electrode is selected based on the desired application. Typically, electrode diameters range between, 0.7 to 2.4 mm. As electrode diameters increase, so too does the current required to heat and melt the wire. Similarly, larger electrode diameters allow for faster material deposition rates, greater heat inputs, and deeper penetration profiles.

Electrode material: Similar to gas composition, several differ electrode material compositions can be used. Typically, the electrode type is selected based on the materials being welded, with most modern wire types including a deoxidising component. As the electrode wire melts and mixes with the weld pool to form the final weld bead, the material composition is crucial to the final mechanical strength of the joint.

Workpiece material: The base workpiece material also plays a large role in the GMAW process. The material properties of the metal being melted greatly affect the generation of the welding arc, the formation of the weld pool, and the mechanical properties and appearance of the final weld bead.

Joint Geometry: In GMAW there are 5 main types of joint geometry; butt joints, lap joints, tee joints, corner joints, and edge joints. These joint geometries can be seen in **Figure 2.4**.

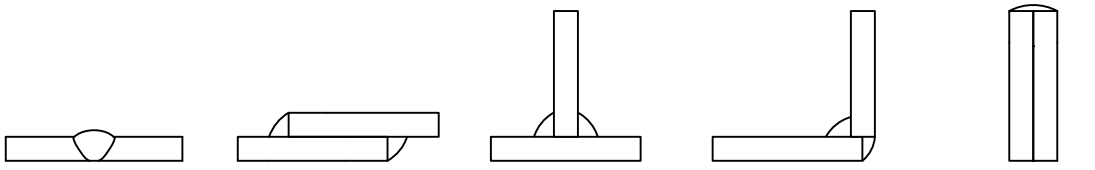

Figure 2.4 - Standard GMAW Joint Geometries

2.1.2. Intermediate Variables

Driven by the welding input variables, intermediate variables describe the physical welding process. These variables, while not being directly controllable, are influenced depending on multiple different factors. The standard intermediate welding variables are described below.

Welding current: The welding current is responsible for heating and melting both the wire electrode and the base material. In standard constant voltage GMAW, the welding current is influenced by the resistance of the electrode wire, the resistance over the arc length, shielding gas composition, wire feed rate and welding voltage.

Stick out: Stick out length is the distance in which the wire electrode protrudes from the contact tip. Stick out length is affected primarily by the wire feed speed.

Arc length: Similar to stick out length, arc length is the distance from the end of the wire electrode to the molten weld pool. This is affected by a combination of welding voltage, wire feed speed, and welding gas composition. CTWD, stick out, and arc length can all be seen in **Figure 2.5**.

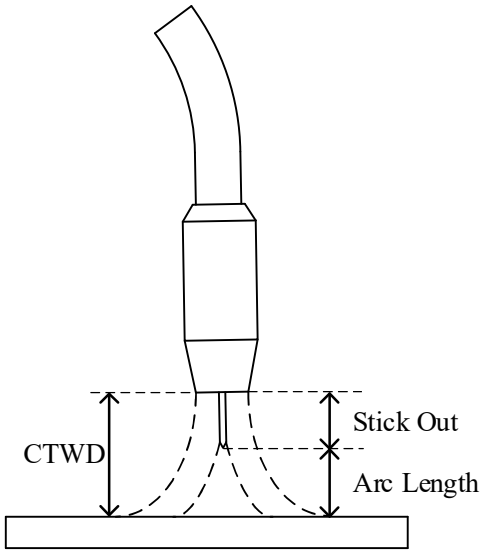

Figure 2.5 - CTWD, Stick out & Arc length comparison

Arc pressure: Arc pressure is the total pressure of the arc plasma and is critical in affecting the distribution of the welding current.

Arc shape: Arc shape describes the shape and distribution of the welding arc plasma. This shape is heavily affected by the electrical conductivity of the welding gas, gas flow rate, and welding voltage. Similar to the arc pressure, the arc shape is also critical in determining the distribution of the current and heat distribution.

Heat transfer: Heat is transferred in GMAW primarily along the welding arc. The heat transferred into the base material is influenced by almost all input parameters, particularly from the welding voltage, gas composition and wire feed speed.

Cooling rate: The cooling rate describes the rate in which the molten weld pool cools and forms the weld bead. This is influenced by the both the heat transfer and the travel speed.

Melting rate: The melting rate is the rate in which the wire electrode is melted and transferred into the weld pool. It is mainly affected by the voltage, gas composition and wire feed speed.

Mass transfer: Similar to melting rate, the mass transfer rate is the rate in which the filler wire is transferred into the weld pool. This rate is influenced by both with wire feed speed and the electrode diameter.

Transfer mode: Transfer modes describe the process in which the electrode wire melts and transfers the molten material into the weld pool. Transfer modes are a critical process which heavily influence the stability of the welding arc. Similar to heat transfer, transfer modes are influenced by a combination of all of the input parameters. These transfer modes will be further discussed in **Section 2.2**.

Weld pool dimensions: The weld pool dimensions describe the length, width and depth of the molten weld pool. This is influenced by a combination of both the heat transfer and metal deposition.

2.1.3. Output Variables

Affected by the intermediate variables of the GMAW process, the output variables describe the final produced weld bead and its properties. These output variables are described as follows:

Weld bead geometry: The geometry of the weld bead describes the height, width and curvature of the solidified weld bead that sits above the base material.

Depth penetration: The depth penetration profile describes the shape and depth of the area in which the molten weld pool has penetrated and mixed the filler and base materials together beneath the surface of the welded joint.

Mechanical properties: The mechanical properties include its tensile strength, hardness and impact toughness of the produced weld. This also includes the uniformity of the welded joint.

Microstructure: The microstructure of the joint includes the grain size, pattern, and chemical composition of the formed weld bead. This microstructure is critical in determining the mechanical properties of the weld bead.

2.2. Transfer modes

In GMAW the molten droplets are transferred from the end of the electrode wire into the molten weld pool along the electric welding arc. This process can occur in a number of different ways depending on factors such as the droplet size, growth time and detachment frequency [8]. The way in which these droplets form and transfer is known as a "transfer mode". Transfer modes are a critical factor in the final quality of the weld by affecting the weld bead penetration, heat transfer and material deposition rate of the welding process. These transfer modes are influenced by a number of different input and intermediate parameters including the welding current, voltage, CTWD, electrode material, welding gas composition, wire feed speed, welding speed and material composition.

2.2.1. Transfer Mode Classification

Over the years the definition and classification of GMAW transfer modes has changed several times. The original classification system was first introduced in 1986 as the international institute of welding (IIW) classification by Lancaster [9], which shows the relationship between the transfer modes as the welding current increases, changing from the short circuit transfer modes to globular and spray transfers. This model also shows the presence of the theoretical transition current between the globular and spray transfer modes. The relationship between this transition current and the droplet size was investigated by [10], where the transition between globular and spray transfer mode was found to be a more gradual process than originally outlined in the IIW classification. This model was further improved upon over the years by a number of different researchers [11, 12] with the current model in use today purposed by Scotti [8]. The current model that is in use can be seen in **Figures 2.6 - 2.7** which shows the relationship between the welding current and voltage as well as the fundamental transfer

modes. These GMAW transfer modes can be broken down into 3 main classes; Natural, Controlled and Interchangeable transfer modes.

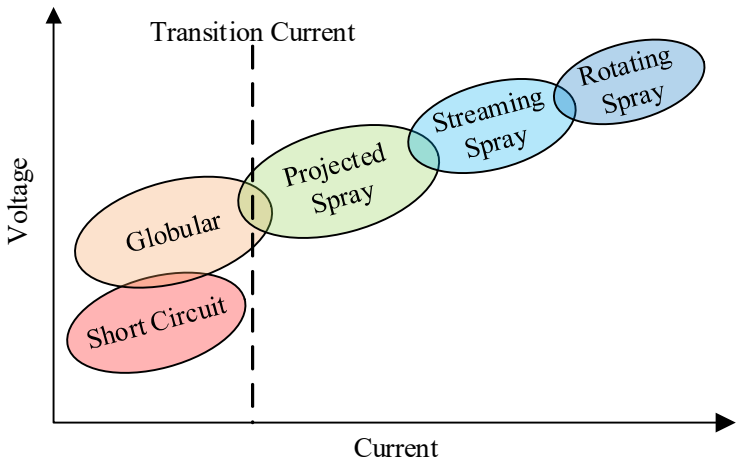

Figure 2.6 - Fundamental transfer modes

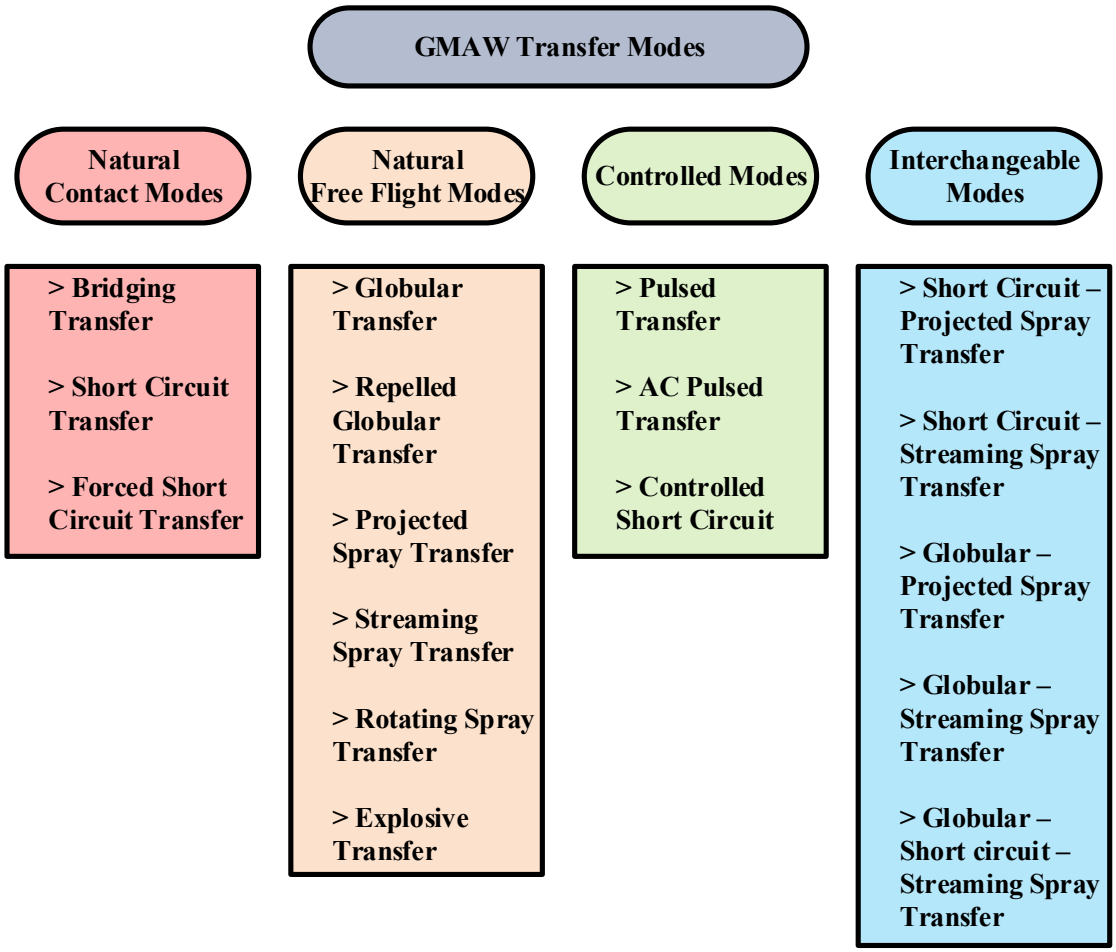

Figure 2.7 - GMAW Transfer Mode Groups

Natural transfer modes consist of stable transfer modes that occur under normal circumstances without any external control methods produced by the welding machine. This group consists of three main subgroups; short circuit transfer, globular transfer and spray transfer.

2.2.1.1. Short Circuit Transfer

In short circuit transfer the molten droplet at the end of the electrode increases in size until such a point that it makes contact with the molten weld pool. At this point a short circuit is formed between the electrode and the weld pool causing an increase in current while transferring material across to the weld pool. In this stage necking occurs around the molten bridge leading to a combination of surface tension and pinch effect forces which detach the droplet from the electrode. Short circuit transfer generally occurs at low welding currents which do not have enough energy to melt the droplet and detach it in time before it hits the weld pool [8]. Short circuit transfer is generally used in applications that require low heat inputs and are susceptible to warping such as sheet metal and pipe welding applications. The drawback of using this method however is the excess spatter generation, fume generation, lack of fusion, lower gap bridgability and arc instability [13].

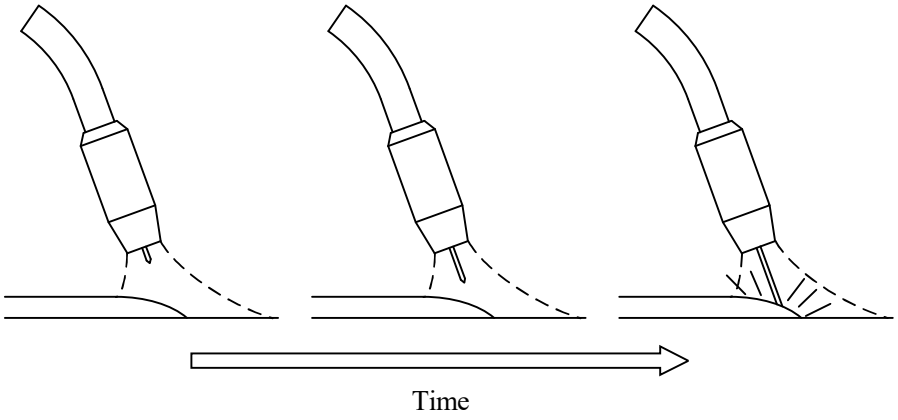

Figure 2.8 - Short Circuit Transfer

2.2.1.2. Globular Transfer mode

In globular transfer the molten droplet exceeds the diameter of the electrode wire, detaching before making contact with the weld pool. The droplet grows in size while attached to the end of the electrode due to the surface tension holding the droplet together and eventually detaches once the gravitational and aerodynamic forces eventually overcome this surface tension force. On top of this, the pinch effect can also play a role in droplet detachment due to the size difference between the wire electrode and the molten droplet. In this transfer mode the droplets can reach sizes of up to 1.5 to 3 times the diameter of the welding electrode and have a relatively low transfer frequency. This frequency can be as low as 1-10 droplets per second which is generally much lower than all the other transfer modes. This transfer mode generally occurs at low to moderate currents and moderate to high voltages due to extended arc length which allows it to avoid short circuiting [8]. Unlike other transfer modes, globular transfer has a very limited amount of applications due to a number of shortcomings. As globular transfer is heavily

reliant on gravitational forces, it is not very suitable for welding in any sort of angled or overhead positions. In addition, as the droplet is not accelerated towards the weld pool, it can lead to insufficient heating and a shallow, broad weld bead. As well as this, due to the size and nature of the droplet transfer it has a tendency to create excess spatter and weld instability. Considering these factors, globular transfer is only suited to welding thin materials at a low current range [13].

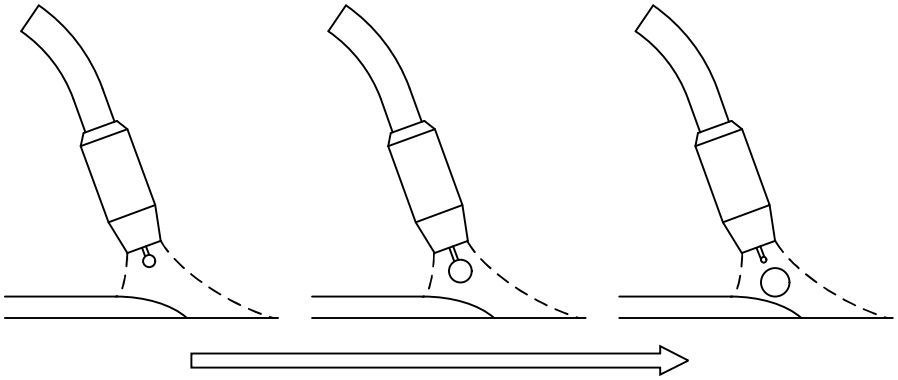

Figure 2.9 - Globular Transfer Mode

2.2.1.3. Spray Transfer Mode

Spray transfer or projected spray transfer occurs when the molten droplet detaches from the electrode while having a diameter that is smaller than the welding electrode. These droplets are transferred to the weld pool at an increasingly high frequency as the welding current increases. The droplet detachment is caused by a strong pinch effect due to the tip of the wire electrode becoming pointed due to the large electromagnetic force from the high current. This transfer mode occurs when the welding current exceeds the transition current and maintains a high voltage. Due to the rapid transfer of droplets in this mode, there is very little current oscillation compared to the other modes resulting in a much more stable current across the welding arc [8]. Spray transfer mode is generally used in applications that require a large heat input or require a high deposition rate. Spray transfer is normally used to weld very thick plate materials together due to the high heat input needed to successfully penetrate the materials. However, similar to globular transfer, spray transfer also struggles to weld in vertical and overhead positions due to the large size of its weld pool. Despite this drawback spray transfer is a preferred method of GMAW in a large variety of applications due to its high arc stability and low spatter generation [13].

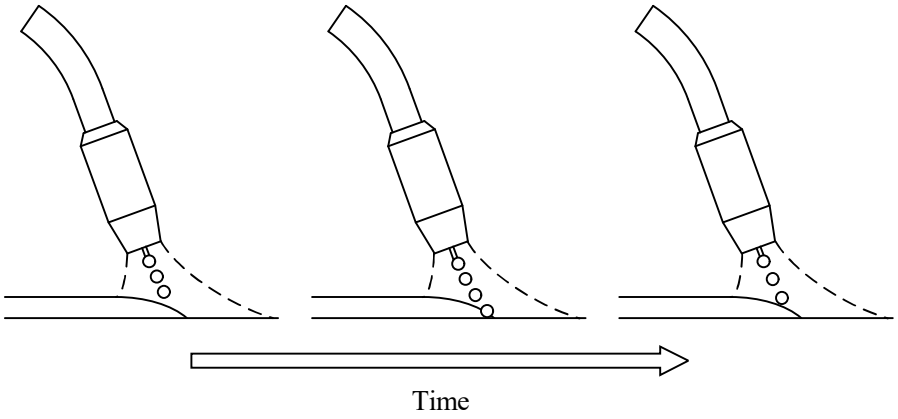

Figure 2.10 - Spray Transfer Mode

2.2.2. Controlled Transfer Modes

Due to the nature and limitations of a majority of the natural transfer modes, special controlled transfer modes have been developed by researchers as a means of overcoming these shortcomings. Controlled transfer modes such as the pulsed transfer mode and short arc controlled transfer modes that are detailed below.

2.2.2.1. Pulsed Transfer

Pulsed Transfer mode is a controlled transfer mode that involves ramping up the welding current in pulses as a means of detaching the welding droplet in a controlled, periodic manner. In pulsed transfer mode the welding current cycles between two different currents, a low base current that is high enough to maintain the welding arc, to a much higher pulse current. When the system is in the high current phase, the strong electromagnetic forces cause the detachment of a welding droplet similar to spray transfer mode. This cyclic pulse is timed in such a way that each pulse will detach only a single droplet making it a controlled spray transfer mode [14]. Pulsed transfer is used in a wide variety of applications and can be used to weld all thicknesses of metals. It also has the advantage of being able to be used in all welding positions [13].

2.2.2.2. Controlled Short Arc

Controlled short arc or controlled contact transfer mode is a controlled transfer mode that aims to improve the performance in short circuit transfer mode. Controlled short arc transfer was first implemented by [6]. Controlled short arc transfer works by controlling the current in the short circuit phase which leads to a smoother droplet detachment by relying on the surface tension to detach the droplet in a similar fashion to bridging short circuit transfer mode. Controlled short arc is generally used to weld very thin sheets of metal that require low heat input as well as joining aluminum alloys. Controlled short arc also has the advantage of being able to be used in vertical and overhead positions [13].

2.2.3. Interchangeable transfer modes

When welding with natural welding transfer modes, depending on the welding parameters it may be difficult to maintain one single transfer mode for the duration of the weld. When the welding parameters fit within the transition zone between two transfer modes, what is known as an interchangeable transfer mode can occur. An interchangeable transfer mode is when two or more transfer modes periodically change throughout the duration of the weld. Research done by [15] shows the presence of a number of interchangeable transfer modes and created a classification system to document them. These transfer modes can be seen in **Figure 2.7**, which shows in its third box the different types of interchangeable transfer modes.

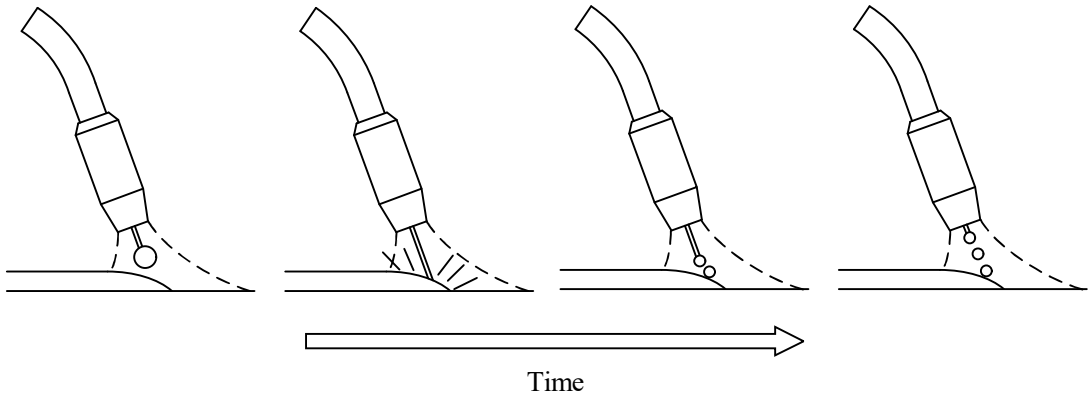

Figure 2.11 - Interchangeable Transfer Mode

2.3. Welding Defects

In a GMAW weld, there are numerous different irregularities and defects that can occur which can compromise the quality of a weld in numerous different ways. In general a good quality GMAW weld is defined as having uniform width distribution along the length of the bead as well as containing little or no artefacts on the weld bead surface [6]. However these conditions are not always easy to achieve due to a number of factors that could occur throughout the welding process such as excess heat, lack of heat, extended periods of arc extinguishment, lack of shielding gas and contamination of the materials. In addition to these factors, incorrect selection of transfer modes for the specific task can also lead to many defects and imperfections occurring. All of these factors can lead to a number of defects occurring in the weld bead such as porosity, burn through, and lack of penetration/fusion. These common defects and their appearances can be seen in **Figure 2.12** and will be outlined further in the following sections.

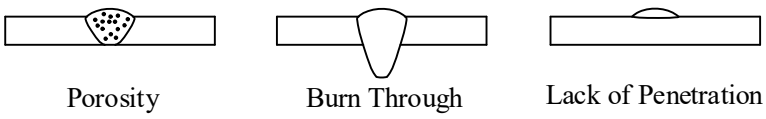

Figure 2.12 – Common Defects

2.3.1. Porosity

Porosity is the presence of air pockets inside the solidified weld bead which can greatly reduce its mechanical strength. Porosity is caused by the trapping of gasses inside the molten weld pool, generally as a result of a combination of gasses, in particular oxygen, hydrogen and nitrogen released from imperfections and contaminants along the weld path. Similarly, several atmospheric gases also have a chance of being trapped within the molten weld pool. As the weld pool begins to cool, these gases become permanently trapped within the solidified weld bead.

Typically, many electrode wire compositions contain a strong deoxidising component to help extract a large portion of these trapped gasses from the weld pool, however depending on the severity and source of the contamination, there still remains a significant risk of porosity forming. In particular, if an inadequate amount of shielding gas is present to effectively cover the weld pool, the deoxidising agent in the electrode wire is not robust enough on its own to successful prevent the formation of porosity.

Depending on the cause and severity of the conditions, several different forms of porosity can occur. These forms include surface porosity, subsurface porosity, wormholes and craters which can all be seen with their descriptions and causes in **Figure 2.13**.

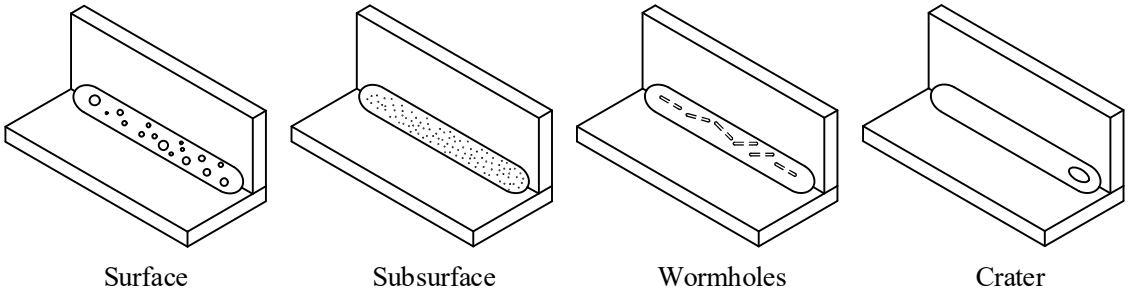

Figure 2.13 – Porosity in weld bead

Surface porosity: Surface porosity occurs when large amounts of oxygen and nitrogen gas are trapped within the weld pool, only releasing at the point of solidification. This leads to the gas pockets breaking the surface of the weld bead, severely compromising the integrity of the weld bead. This type of porosity is generally caused by an inadequate cover of shielding gas, either as a result of low gas flow rate or crosswind blowing the shielding gas away. In addition welding over excessive coatings, particularly thick layers of primer paints or zinc coatings can generate an excessive amount of fumes which cannot be successfully extracted from the weld pool with a combination of shielding gas and deoxidiser [16].

Subsurface porosity: Subsurface porosity, similar to surface porosity, occurs when large amounts of oxygen and nitrogen gas are trapped within the weld pool. However unlike surface porosity, these gas pockets are not large enough to break the surface of the weld bead upon solidification. Much like surface porosity, it can be caused by inadequate shielding gas coverage, however it is much more likely to occur as a result of contamination, trapping small pockets of gas within the solidifying weld bead [17].

Wormholes: Wormholes are the elongated pores that run down the length of the weld bead. In most circumstances, wormholes are formed in areas where a pocket of gas can form beneath the weld bead, essentially becoming trapped underneath as the weld bead solidifies. This is normally a direct result of poor joint design, particularly in tee type welds where both sides are being welded [18]. If an air gap is present beneath the 2 welded plates, gases produced from contaminants can be easily trapped underneath as shown in **Figure 2.14**.

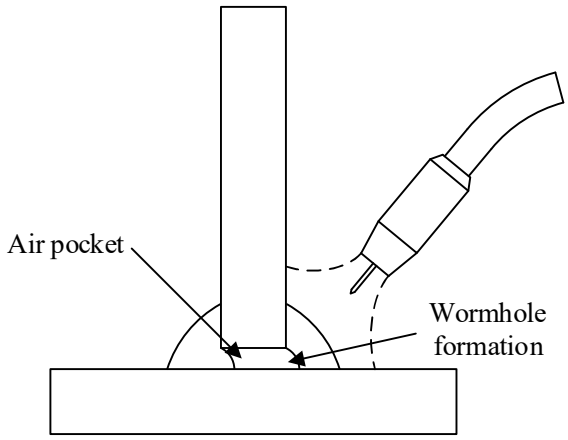

Figure 2.14 - Wormhole generation

Craters: Craters are pores that form on the weld bead as a direct result of shrinkage that forms during weld bead solidification. This can occur if the weld bead cools too rapidly, leading to the weld pool shrinking as it solidifies. Generally this type of porosity is most common towards the end of the weld bead when the arc is extinguished, leading to much faster cooling than the rest of the bead, however it can also occur at any point where there is a prolonged period of arc extinguishment.

2.3.2. Burn Through

Another common defect that can occur during the GMAW process is burn through. Burn through occurs when the molten weld pool fully penetrates through the base metal and melts a hole completely through it. The occurrence of burn through is normally a result of the localised heat input being far too large for the thickness of the base material. Typically, the risk of burning through the base material is greatest when working with thinner materials, in particular sheet metal applications, however it is still possible to burn through thicker materials depending on the variables being used. Burning through the material,

other than the obvious aesthetic damage, also severely compromises the structural integrity of the weld bead. **Figure 2.15** shows the appearance of a defective weld due to burn through.

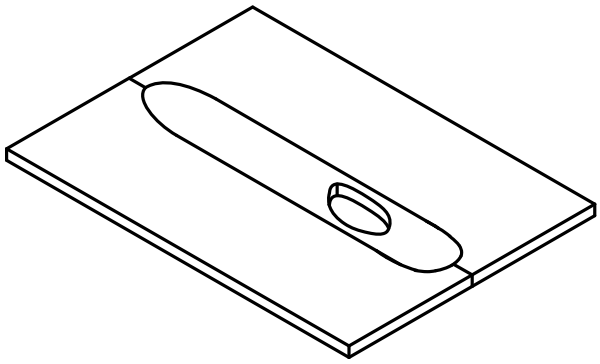

Figure 2.15 – Burn through appearance

Burn through can be caused by a number of different factors, normally a direct result of several welding parameters. In particular the heat input being too intense as a result of the voltage being too high, or the wire feed speed being too fast are the most common causes for burn through. Similarly if the welding travel speed is too slow in combination with the metal deposition rate, the welding arc can quite easily burn through thinner materials.

Despite burn through normally occurring as a result of incorrect input parameter settings, determining the correct settings is a complex process especially with thinner materials. Typically, thinner materials and smaller parts do not have as large a thermal capacity as large thick metal plates, heating up significantly faster, requiring a smaller heat input to fuse them together [19].

2.3.3. Lack of penetration

In contrast to burn through, lack of penetration occurs when the molten weld pool does not successfully penetrate deep enough into base material to adequately mix and fuse with it. Successful fusion with adequate penetration is one of the most crucial components to the structural integrity of the weld bead. Inadequate penetration can lead to mechanically weak joints, susceptible to failure particularly in situations where the joint is subject to sizeable structural and cyclic loads.

In many scenarios penetration depth can be difficult to determine by simply observing the produced weld bead. Many weld beads may appear structurally sound from external inspection, however below the surface they have not adequately penetrated into the base materials.

Typically, lack of penetration occurs when there is an insignificant amount of heat being transferred into the weld pool. This can be a direct result of several different factors including the travel speed being too slow, both the travel and work angles being too steep, the heat transfer being too low, and the mass transfer rate being too fast [20]. In contrast to the causes of burn through, lack of penetration is more likely to occur in thicker base materials and larger workpieces where the base material can absorb

a sizeable amount of the heat from the welding process as opposed to thinner materials. **Figure 2.16** shows a weld which lacks penetration in comparison to an adequately fused weld.

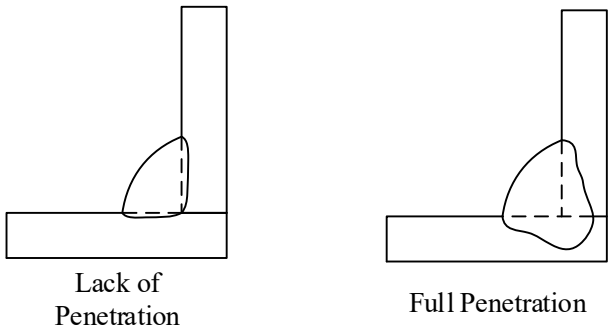

Figure 2.16 – Comparison of penetration states

2.4. Welding Automation

As mentioned in **CHAPTER 1**, automated robotic welding systems have become popular, widespread solutions across several different industries. However, due to the lack of an experienced human welder, they lack the quality control and process monitoring abilities that come with one. Typically, these systems rely purely on the welding input parameters and preparation of the welding joint, leaving quality control checks to be performed post production. These checks can range from simple observations to expensive non-destructive testing procedures such as using x-rays and ultrasonics to confirm the integrity of the weld.

Previously, researchers have investigated the effectiveness of using several different methods to monitor the GMAW process. These methods include monitoring the dynamic changes in the input and intermediate variables in real time as well as monitoring both the acoustic and visual signals similar to manual welders [21]. These different methods for monitoring the GMAW process will be briefly introduced in the following subsections below. More in depth coverage of these modes will be presented later in this thesis in the introduction sections of each chapter in which they are relevant to.

2.4.1. Process Monitoring

The first major area of GMAW automation is process monitoring. In GMAW process monitoring, several different characteristics of the welding process can be monitored. These include the droplet formation and transfer process, arc plasma and properties of the electric arc, and weld pool growth and formation. Each of these different welding characteristics can be monitored in one of two ways, either through passive monitoring, or through active monitoring.

In GMAW, passive monitoring involves monitoring one or more signals throughout the GMAW process to analyse after the weld bead has been performed. Typically, this type of monitoring is used to detect the presence of welding defects or to estimate the mechanical properties of the weld bead in post production.

In contrast to passive monitoring, active monitoring analyses the welding process in real time by monitoring a variety of different signals. This method of monitoring allows for real time analysis, allowing several different properties to be monitored in real time. Common areas in which this type of monitoring is used include transfer mode detection, defect detection, weld seam tracking and weld pool growth monitoring.

As outlined, GMAW is a dynamic process with several uncontrollable factors affecting the welding process. Simply selecting the desired input variables and blindly performing the weld is unsatisfactory for producing a high quality weld bead. Therefore active monitoring of the welding process is needed to effectively control the formation of the weld bead, in turn ensuring the overall quality of the weld.

Traditionally, in most welding scenarios, the GMAW process is performed by highly trained and skilled professional welders. Through experience, these welders are able to monitor the welding process through a combination of audible and visual cues. How these manual welders observe these cues will be described in the following sections below.

2.4.1.1. Acoustic Signals

The acoustic signal in GMAW is typically a good indicator of the current behaviour of the welding arc. While performing a GMAW weld, depending on the behaviour of the welding arc, a distinctive "crackling" or "sizzling" sound is produced. This sound is a direct result of the current behaviour of the welding arc, producing distinctive pulses at the points of arc extinguishment and reignition [22]. Under standard operating conditions, these points of arc extinguishment and reignition occur whenever a droplet detaches from the end of the electrode wire. However as stated above, this droplet detachment process is dependent on the welding transfer mode. Because of this, each transfer mode has its own distinct sound signal that it produces, in turn acting as a good indicator of the welding process.

Of the three major natural transfer mode groups, short circuit transfer generally produces the loudest, most distinctive sound signal. When reaching the short circuiting stage where the wire dips into the weld pool, the welding arc is extinguished as the current flows purely through the electrode into the weld pool. This sudden extinguishment of the arc generates a small sound pulse followed by a period of silence while the material is being transferred into the weld pool. After the transfer process has occurred, and the wire "snaps" off the droplet, the welding arc is then violently re-established. This violent arc reignition creates a sharp, loud sound pulse resulting in the stereotypical "crackling" sound associated with GMAW.

Unlike short circuit transfer, both globular and spray transfer modes do not have a distinctive periods of complete arc extinguishment and reignition. Therefore, the sound profile produced by these methods is significantly quieter than that in short circuit transfer mode. In both globular and spray transfer mode, pulses in the sound signal are still produced, however this occurs at the point in which a droplet detaches from the end of the welding electrode [23]. At this point, a small air gap is produced between the molten droplet and the end of the electrode, resulting in a small arc being ignited between the two. This ignition

results in a small pulse in the sound signal, resulting in a “sizzling” sound with increasing frequency as the transfer mode transitions from globular to spray.

The sound generation mechanics of the 3 main transfer mode categories can be seen in **Figure 2.17**.

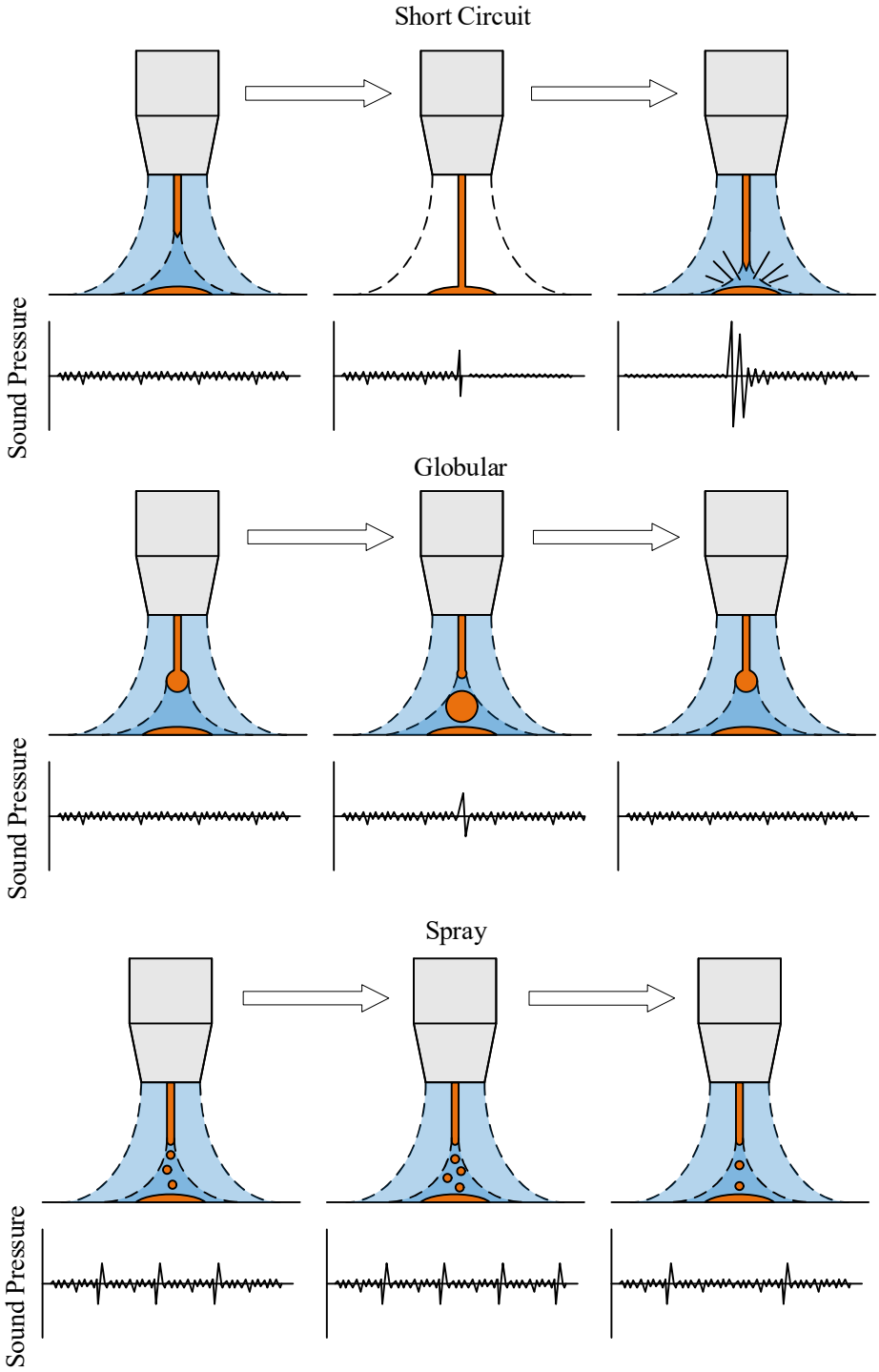

Figure 2.17 – GMAW sound generation

2.4.1.2. Visual Signals

The other side of manual process monitoring in GMAW is the visual observation of the welding process. In the GMAW process there are normally 2 main sources of light emissions. These two sources are the light generated by the ignition of the welding arc and the glow from the weld pool and molten electrode. The first source of light, the light generated from the welding arc can be broken down into two main components [24]. The first of these is the plasma generated from the argon based shielding gas, while the other is the plasma formed by the vaporised iron from the electrode. Both of these two gasses emit different peak light emissions around different wavelengths.

The second source of light that is generated from the welding process is the light generated from the weld pool and molten wire electrode. The light emitted from weld pool, wire electrode and molten droplet are all treated as blackbody radiation [25] which causes the light that is emitted to follow a continuous radiation spectrum.

Research performed by [26] aimed to show the relative intensity of light at different wavelengths between the two main sources of light radiation. The light intensity of the welding arc is higher than that of the weld pool in the ultraviolet range while the peak intensity of the weld pool is higher in the near infrared range.

While predominantly using the acoustic signal to monitor the welding arc behaviour, welders use visual observations to monitor the formation and behaviour of the molten weld pool. As the base material starts to melt and form the weld pool, manual welders are able to observe its position, flow and growth throughout the welding process. Using this information, welders can actively manipulate the weld pool by increasing the travel speed or CTWD as well as actively correcting the welding path.

2.4.2. Active Feedback Control

In addition to simply monitoring the welding process, active feedback control systems are another critical area in welding automation. As previously mentioned, the GMAW process can be quite unstable, requiring more than simply setting up the correct input parameters to produce a high quality weld. Typically, these types of systems fall into one of two categories, the first involving controlling the welding process itself, with the second involving controlling the robotic path planning along the weld joint. These two categories will be further outlined below.

2.4.2.1. Welding Process Controls

As mentioned, actively controlling the welding process is critical in maintaining high quality and uniformity across the entire length of the weld bead. This can be done by using several active monitoring methods to monitor specific characteristics of the welding process, allowing information about the welding process to be extracted in real time. This information can then be used to predict the necessary changes to the input parameters and modify them in real time, improving the overall quality of the produced weld bead. To predict these necessary changes to the welding input parameters, several

different methods can be used. These include a wide range of machine learning techniques, numerical models, as well as digital twin systems.

2.4.2.2. Path Planning Controls

Similar to controlling the physical welding process, adjusting the welding speed and robotic pathing is crucial in producing high quality welded joints. In majority of robotic welding applications, the welding path is manually programmed prior to beginning the GMAW process. Typically, this is done by teaching the robot the correct path based on either the physical weld piece or using a 3D CAD model of the weld piece. However, depending on the dimensional accuracy of the weldment and the jig used to hold it in place, this pre-determined weld path may not be perfectly aligned to the desired weld seam locations. Therefore, to accurately follow the correct weld path, several active monitoring techniques can be used to allow the original weld path to be updated in real time. Traditionally this form of path planning can be performed using laser or visual feedback systems as outlined above by monitoring the location of the weld pool with respect to the weld seam ahead of the current position.

2.5. Summary

When reviewing the literature it can be seen that there is great potential in using the acoustic signals generated by the GMAW process as a means to understand and control the system. However it can be seen that there is still much research to be done in some areas. There is no comprehensive method for detecting weld faults across all the different transfer methods. Most literature normally only focusses on a system for one transfer method such as only for short circuit transfer. This can cause many issues as what may work for one transfer mode does not necessarily work for all of them. On top of this there does not seem to be a reliable method of accurately detecting weld transfer modes across both continuous and pulsed GMAW transfer modes.

CHAPTER 3 – EXPERIMENTAL DESIGN

3.1. Chapter Introduction

To achieve the aims outlined above in **CHAPTER 1**, an experimental test rig was developed to perform the necessary tests. This chapter outlines the design and features of this test rig.

3.2. Test Rig

To effectively gather data and undertake the tests outlined in **CHAPTER 1**, a comprehensive GMAW data collection system needed to be developed. This system needed to be able to effectively monitor several welding input and output parameters in real time, while holding several input parameters constant. To do this, a robotic welding system was designed as shown in **Figure 3.1**.

Figure 3.1 – Experimental Test Rig

This robotic welding system consists of a Unimig Razorweld 350 MIG welder, with the welding gun mounted onto the end effector of a 6 axis ABB IRB 140 robot manipulator. By using the robot

manipulator, constant welding speed, CTWD, torch angle and the weld path could all be effectively controlled and maintained as necessary. All welds were performed on top of a levelled, fixed welding table which was mapped and allocated a coordinate system using the ABB's teach pendant and robot controller.

To monitor the welding process, several parameters were monitored using a variety of sensors. The welding current was measured using a LEM HTA 300-S current sensor installed around the welding cable and the welding voltage was measured directly from the positive welding torch cable to the negative workbench clamp. The gas flow rate was monitored using a Miller ArcAgent gas flow sensor installed inline on the welding cable to measure the gas flow rate to the welding gun and the wire feed speed was measured using a miller wire feed speed unit also installed inline on the welding cable.

In addition to these input parameters, the output parameters were measured using both the acoustic signal and high speed video footage. The acoustic signal was measured by mounting a GRAS 40 PH free field microphone directly to the end of the robot end effector 300mm away from the welding torch. Similarly the high speed video footage was recorded using a Basler ace 640-750 um USB camera also mounted to the robot end effector.

3.3. Signal Acquisition

To acquire the signals in real time, a custom National Instruments labview program was designed to record and synchronise the various signals. A national instruments cDAQ 9185 chassis was used in combination with 3 different modules. A 9234 Sound and Vibration module was used to record the acoustic signal from the microphone, a NI 9215 Analogue Voltage Input module was used to capture the current and gas flow rate signals and a NI9221 Voltage Input module was used to capture the voltage. The high speed video footage was captured and processed directly by the PC using the custom labview program.

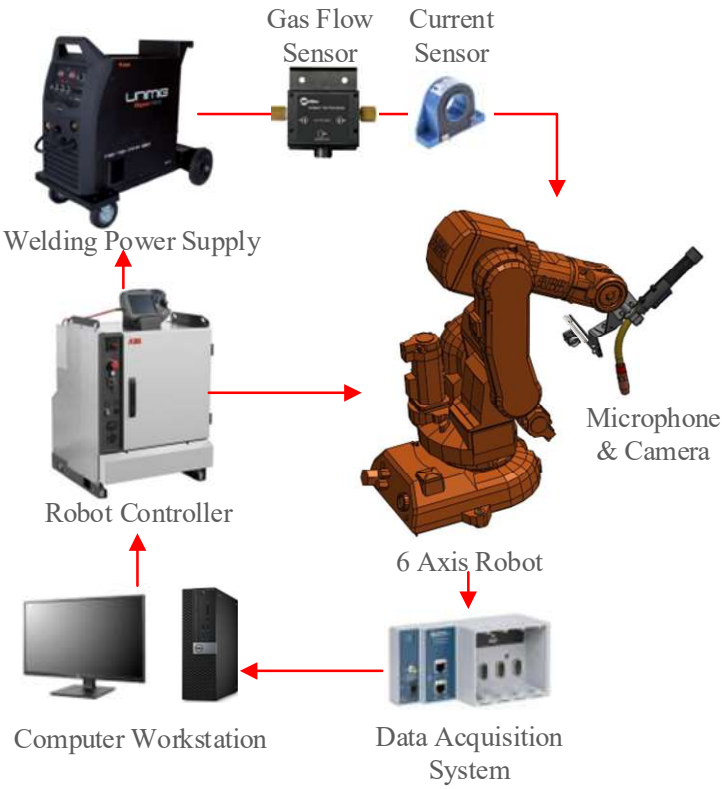

Figure 3.2 - Data acquisition system

To effectively capture the dynamically changing welding process, the current, voltage and gas flow rates were captured at a sampling rate of 3000 Hz, the high speed footage at 2000 fps, and the acoustic signal was captured at 51.2 kHz to effectively capture the human hearing range [27]. The signals were all synchronised using the labview program with the camera being synchronised using the trigger output from the cDAQ 9185 chassis. The camera was set to a resolution of 640x480 pixels.

3.4. Camera Design

While the high speed footage will not be used directly in any of the methods outlined in this work, it is still a crucial component in manual classification and understanding the physical processes that are occurring. However due to the intensity of the light produced by the welding arc, it is difficult to record the footage directly without additional filtering. As explained in **CHAPTER 2**, there are two main sources of light emitted during the welding process, the much brighter light generated by the welding arc, and the light emitted by the molten weld pool and wire electrode. For the purpose of the tests undertaken, the molten weld pool and droplet formation on the end of the electrode were chosen as the point of focus as they would give greater insight into the weld bead formation and droplet transfer process.

To effectively capture the weld pool and molten droplet, several filters were used to remove as much of the arc light as possible. As outlined by [28], the greatest contrast in the image can be achieved when a band-pass filter is selected at a wavelength where the largest difference between the relative intensity

of light between the welding arc and the molten weld pool occurs. This occurs roughly in two positions, 600 – 680 nm and anywhere from 850 nm to 950 nm [29]. Based on the experimental results shown in [26, 30] as well as the spectral response of the selected camera shown in **Figure 3.3**, a band-pass filter with a wavelength of 660 nm was selected to most effectively highlight the contrast between the molten metal and the welding arc. In addition to this bandpass filter, an additional 1.5 neutral density filter was used to further reduce the intensity of the arc. **Figure 3.4** shows an example image recorded using this filter set up.

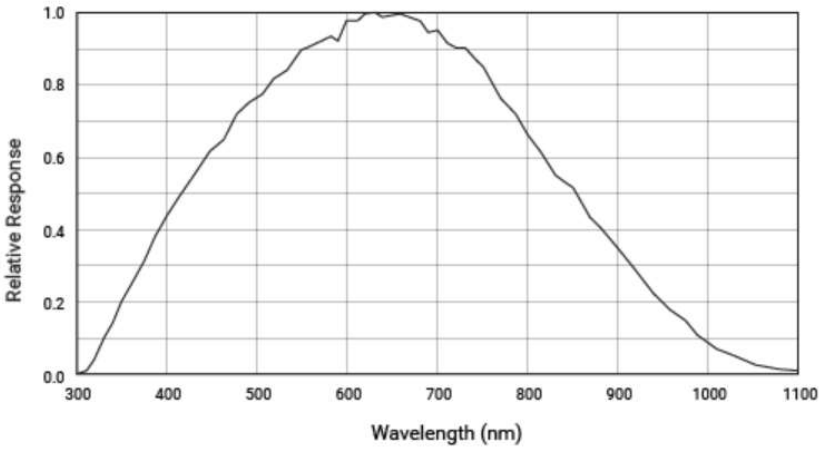

Figure 3.3 - Spectral response of Basler Aca640-750um Camera

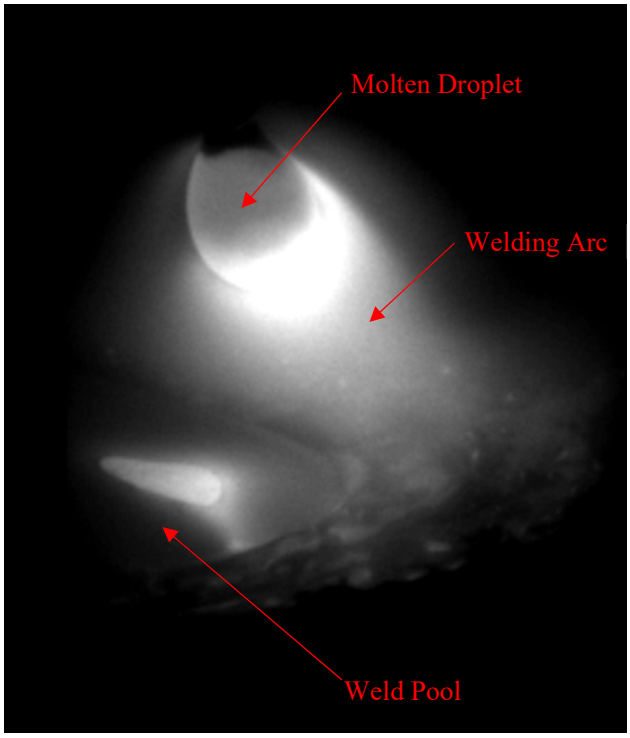

Figure 3.4 – Example recorded images

Due to the relatively high frequency of the molten droplet transfer process, in addition to the brightness of the welding arc, the exposure time of the camera needed to be set to the shortest feasible timespan. For this test rig, the exposure time was set to the camera's minimum possible value of 59 µs, which also allowed the camera to successfully operate at the required 2000 fps. Similarly the aperture of the camera was fine-tuned experimentally with its optimal setting being f/22.

3.5. Example Data

All data recorded using this test rig were further processed and analysed using Matlab. Some examples of the recoded datasets for the voltage, current, gas flow rate, and acoustic signals are shown in **Figure 3.5** to **Figure 3.8**.

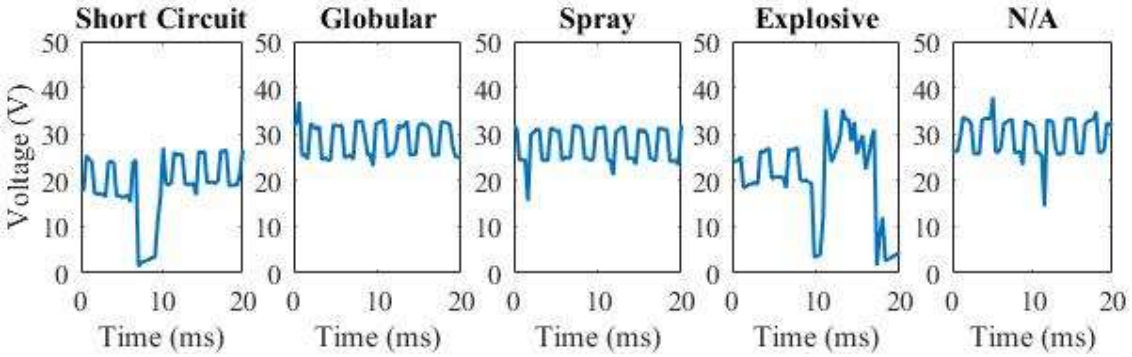

Figure 3.5 - example voltage signals

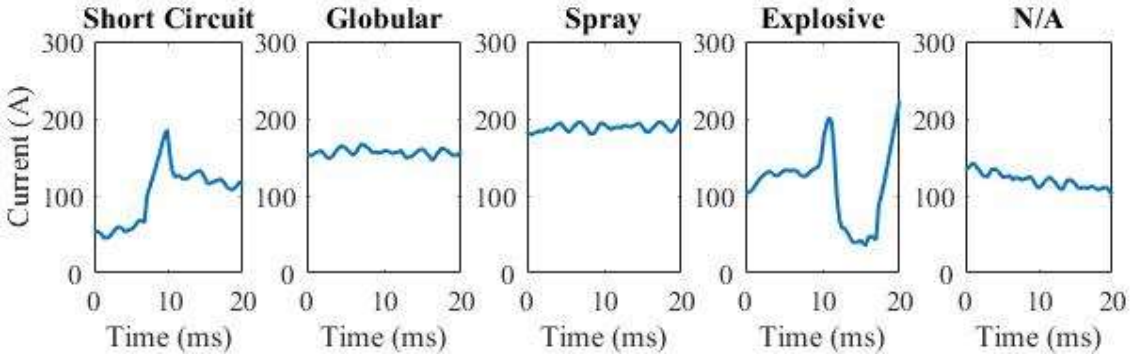

Figure 3.6 - example current signals

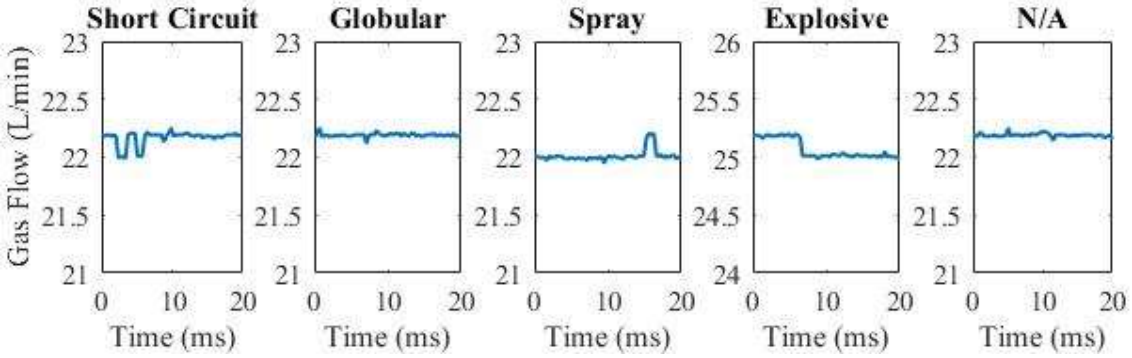

Figure 3.7 - example gas flow signals

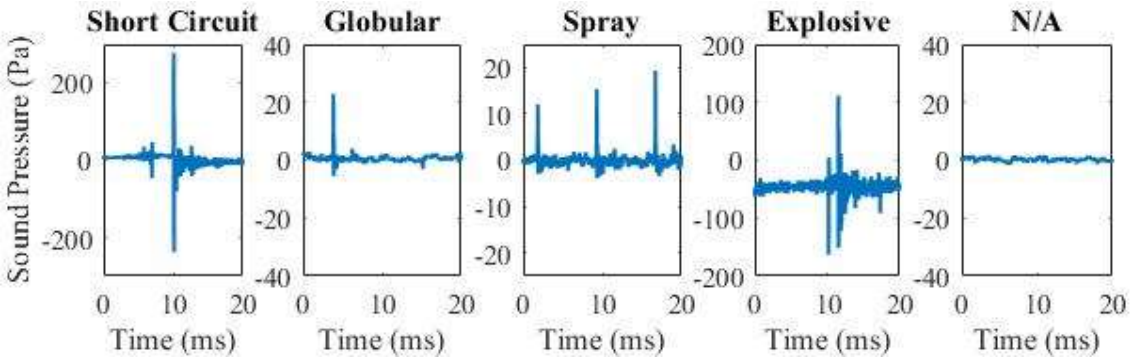

Figure 3.8 - Example Acoustic signals

Similarly, some example images of different transfer modes captured using the high speed camera can be seen in **Figure 3.9**.

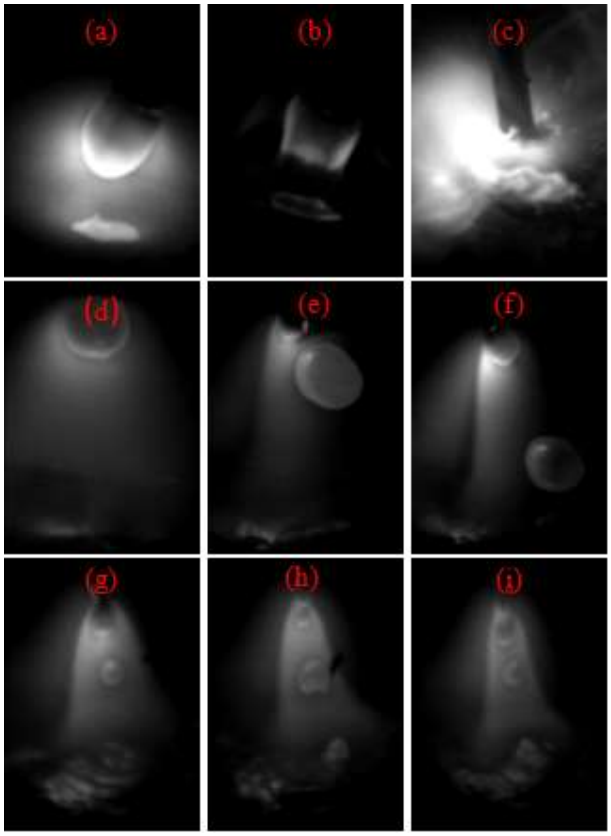

Figure 3.9 - (a-c) Short Circuit, (d-f) Globular, and (g-i) Spray Transfer modes

3.6. Chapter Conclusion

In this chapter, a new robotic welding test rig was presented to perform and record audio, current, voltage, gas flow and high speed video signals. This test rig was be used to perform and record datasets for the following 4 chapters.

CHAPTER 4 – TRANSFER MODE DETECTION

4.1. Introduction

As outlined in **CHAPTER 2**, in GMAW, the molten droplets are transferred from the electrode tip into the molten weld pool along the electric welding arc in a number of different modes, depending on factors such as the droplet size, growth time and detachment frequency [8]. These droplet transfer modes are a critical factor in determining the final quality of the weld, by affecting the weld bead penetration, heat transfer and material deposition rate of the welding process. The transfer modes are influenced by a number of different welding parameters including the welding current, voltage, stick out distance, electrode material, shielding gas composition, wire feed speed, welding speed and material composition [13]. A timely identification of transfer modes can provide vital information to analyze weld quality and to develop smart welding technology, enabling the development of an adaptive feedback system to achieve full automation of the welding process.

In the welding industry it has been well documented that expert welders are able to distinguish the metal transfer modes by listening to the sound generated by the welding arc and use this to control the welding process accordingly [23]. Experiments by [1] showed further evidence to this by performing psychoacoustic experiments on welders to determine how the welding sound affects their ability to control the welding arc. It was found that when the acoustic signal was delayed by 400 ms, the welders no longer had the ability to control the welding process effectively. These results inspired the current work to investigate the feasibility of droplet transfer mode identification based on acoustic signals in the GMAW processes.

To understand the sound generation mechanism in GMAW processes and explore its applications in welding process monitoring and quality control, various theoretical and experimental studies have been conducted in the past decades [31]. One of the earliest sound based monitoring studies was undertaken by [32], who investigated the GMAW sound signal using piezoelectric sensors, in addition to the current and voltage signals, as a means to investigate the relationship between the three signals and the welding droplet detachments. Similarly [4] also utilized the sound signals to investigate GMAW parameters and transfer modes, where both time and frequency domain features of the sound signal were found to be potential indicators of GMAW transfer modes. Recently, [33] investigated the peaks of the sound signal in GMAW and found that the peak sound pressure, impulse interval and event duration are good indicators of GMAW transfer modes. Later, [34] looked at classifying pulsed transfer modes using a statistical model and [35] investigated the weld deposition efficiency using the sound signal and found that the signal kurtosis was highly correlated to arc stability.

In addition to investigating the relationship between the features of the sound signal and the GMAW process, machine learning algorithms have also been used to predict welding features in GMAW. [36] used artificial neural networks to predict the welding parameters from the acoustic signal. [37] used artificial neural networks with a naïve Bayesian classifier to classify the transfer modes using the

acoustic signal. Similarly, [38] developed both a grey and black box model using neural networks to predict the transfer modes and found that it was difficult to classify the transfer modes between the transition from globular to spray mode due to the instability of the welding arc. [5] developed an online weld penetration detection system using neural networks based around the acoustic signal. Despite the previous research which has shown the significance of the acoustic signal in defect detection and process monitoring in GMAW, there is still limited research in automatic and effective detection system that can differentiate between the numerous transfer modes [39].

To further understand the physical processes that drive these transfer modes, several researchers have also developed accompanying numerical models to simulate the welding process. [40] developed a dynamic mass-spring mathematical model to simulate short circuit transfer mode. [41] developed a numerical model combining the methods of enthalpy, effective-viscosity and volume-of-fluid for globular and spray transfer mode. [42] constructed a numerical model based on the solution of the magnetohydrodynamic equations within the framework of phase field algorithm to model the transition between globular and spray transfer modes.

In addition to monitoring the transfer mode process using the acoustic signal, several other researchers have tried a variety of different monitoring methods. [43] used high speed video footage to monitor the droplet transfer process in hybrid plasma GMAW.[44] Developed a vision system that is able to detect the size of the molten droplet and determine optimal time for droplet detachment in laser enhanced GMAW.[45] developed an edge detection algorithm for computing the size and growth of the welding droplet in underwater GMAW applications. [46] developed a mathematical model for short circuit transfer using a dynamic electrical model. [47] used a high-speed vision system to monitor the droplet transfer process in pulsed ultrasonic GMAW. [48] developed an image processing system that is able to monitor the transfer modes in real time using a laser backed lighting system. [49] developed a spectroscopic system to monitor the stability of globular transfer mode by measuring the deviation between argon and iron ratios in the welding arc. [50] performed calorimetric measurements of the droplet temperature for both globular and spray transfer modes. [51] monitored the voltage and current alongside the high-speed imaging using a xenon lamp to detect the transfer modes in real time for robotic welding. [52] developed a vision system to further clarify the boundaries between different transfer modes. [53] investigated the effects of gas composition on the transition between globular and spray transfer mode.

As mentioned above, the metal transfer mode is a key factor that determines the weld quality, thus an automatic transfer mode classification system is desired for quality control in GMAW processes. Furthermore, identifying the transfer modes automatically with acoustic sensing and analysis can be beneficial in developing a real-time adaptive feedback control system for automated robotic welding, which will lay a solid foundation for further development of a smart welding facility, such as a portable

device either individually or to be integrated into other real-time monitoring systems in the manufacturing industry, in particular in hazardous environments.

This chapter investigates the application of acoustic sensing on automatic real-time metal transfer mode identification. A multi-sensor measurement system is developed to simultaneously measure the welding current, arc voltage, gas flow rate and acoustic signals, from which various time and frequency domain features are extracted and selected to train a Support Vector Machine (SVM) classifier for droplet transfer mode identification. The SVM classifiers for the 4 different signals are compared to evaluate their performance. A feature selection algorithm is developed to reduce the feature dimensionality and improve accuracy. The results demonstrate the feasibility of automatic droplet transfer mode identification based on various signals, among which the acoustic sensing based approach has a distinct advantage over the others due to its non-intrusiveness and ease of installation, making it a promising plug-and-play solution for GMAW processes.

4.2. Experimental apparatus and procedure

To explore the differences between the GMAW transfer modes, 32 individual welds were performed using a range of pre-set input values for the Contact Tip to Workpiece Distance (CTWD), travel speed, wire feed rate, average voltage, gas flow rate, gas composition, and inductance. The values were chosen in order to reproduce the 4 desired transfer modes, namely, Short Circuit (SC), Globular (G), Spray (SP), Explosive (E) and an additional mode where no droplets have transferred (N/A), with 32 individual welds allowing for several of each mode to be recorded. Each of these 32 welds were later confirmed to have produced the expected transfer mode by analysing the corresponding high speed camera images. This was done by analysing the accompanying videos of each of the 32 welds every 20 ms and classifying them as either SC, G, SP, E or N/A. Each of these tests were undertaken in a factory environment using the test rig outline above in **CHAPTER 3** in order to capture the background noises that would be present in a real world situation. This method was chosen as a means to test the robustness of the algorithm in an unideal environment. The parameters for these welding tests are shown in **Table 4.1** alongside their corresponding transfer modes.

Table 4.1 - Welding Parameters

Test Number	Transfer Mode	Gas Composition	Voltage (V)	Inductance (%)	Gas Flow Rate (L/min)	CTWD (mm)	Travel Speed (mm/s)	Wire Feed Rate (m/min)	Gun Angle
1	SC	Argon	20	0	20	16	3.5	4.85	Push
2	SC	Argon	18	0	20	16	3.5	4.36	Push
3	SC	Argon	22	50	20	15	3.5	5.29	Pull
4	SC	Argon	20	30	20	15	3.5	6.33	Pull
5	SP	Argon	30	0	20	18	7	9.31	Push
6	SP	Argon	28	0	20	18	7	8.01	Push
7	SP	Argon	34	0	20	18	7	11.35	Pull
8	SP	Argon	30	0	20	18	7	9.31	Pull
9	E	Argon	20	0	0	16	3.5	4.85	Push
10	E	Argon	30	0	0	18	7	9.31	Push
11	SP	Argon	28	0	20	18	7	8.74	Pull
12	G	Argon	28	0	20	28	7	8.74	Pull
13	G	Argon	27	0	20	28	7	8.01	Pull
14	I	Argon	31.5	30	20	23	7	6.81	Push
15	I	Argon	27	0	20	16	7	7.32	Push
16	I	Argon	26	50	20	16	7	8.01	Push
17	SC	Mix	20	30	20	16	3.5	4.85	Push
18	SC	Mix	18	0	20	16	3.5	4.36	Push
19	SC	Mix	22	50	20	15	3.5	5.54	Pull
20	SC	Mix	20	30	20	15	3.5	6.33	Pull
21	SP	Mix	30	0	20	18	7	9.31	Push
22	SP	Mix	28	0	20	18	7	8.74	Push
23	SP	Mix	34	0	20	18	7	11.35	Pull
24	SP	Mix	30	0	20	18	7	9.31	Pull
25	G	Mix	30	0	20	20	5.5	5.54	Pull
26	G	Mix	30	50	20	19	5.5	6.06	Push
27	G	Mix	29	0	20	18	7	8.01	Push
28	G	Mix	29	0	20	18	5.5	5.54	Push

29	E	Mix	25	0	0	18	5.5	6.06	Push
30	I	Mix	30	0	20	18	7	7.32	Push
31	I	Mix	27	0	20	16	7	7.32	Push
32	I	Mix	26	50	20	16	7	8.01	Push

Figure 4.1 shows the examples of 100 ms segments of the acoustic, voltage, current, and gas flow rate signals for each of the 5 transfer modes. These signals were recorded with the apparatus given in **CHAPTER 3** using the parameters outlined in **Table 4.1**.

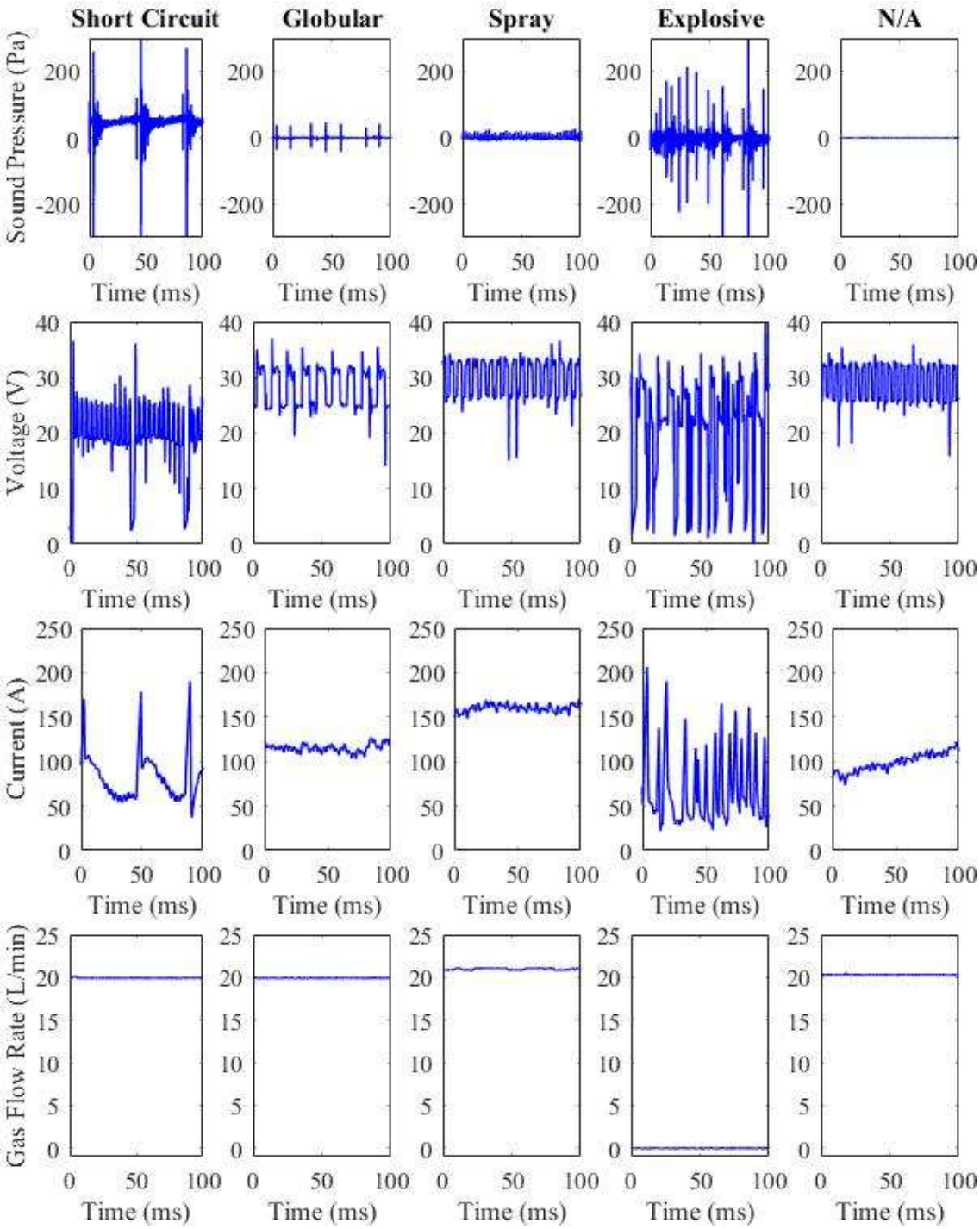

Figure 4.1 - Comparison of the Sound, Voltage, Current and Gas Flow Rate signals for the 5 GMAW Transfer Mode Classifications

From the signals across the different transfer modes above, it can be seen that there are several differences between the 4 signals. When comparing the acoustic signals it can be observed that there is a distinct difference in the shape and frequency of the signal peaks. In particular, short circuit transfer mode has distinct, well defined peaks in the signal, whereas the globular, spray and explosive transfer

modes are significantly flatter with peaks that are difficult to distinguish from the time domain waveforms. It can also be observed that short circuit and explosive transfer modes display louder sound pulses when compared to the other three transfer modes. This larger sound pulse can be attributed to the high energy arc ignition that occurs when the molten electrode bridge is broken during short circuiting.

When examining the current signal, several differences in the shape of the signal can also be observed. Short circuit transfer mode displays very distinct current peaks, when compared to both globular and spray transfer modes. In particular, short circuit transfer mode shows large, wider peak while dropping down to a lower base current. This occurs due to the short circuiting of the welding electrode that occurs in short circuit transfer [40]. In contrast, globular and spray transfer modes demonstrates a flatter signal with less obvious peaks while being at a significantly higher current value when compared to the other signals. Despite their much smaller peaks, it can be seen that the frequency of the peaks in spray transfer is significantly higher than that in globular transfer mode, with a higher base current value. In addition, explosive transfer mode demonstrates a much more erratic signal with many pulses varying across several different current values.

In comparison to the acoustic and current signals, the voltage and gas flow rate signals display a less obvious distinction between the 5 transfer modes. For the voltage signals, valleys can be seen demonstrating drops in voltage in the short circuit and explosive transfer modes corresponding to the short circuiting of the system. Similar to the current signal, the globular and spray transfer modes display less obvious peaks and are flatter than the other signals. Explosive transfer mode however, is much more distinguishable with the voltage and gas signals when compared to the other transfer modes, with the voltage signal being substantially more unstable as well as having zero gas flow rate. This is due to the gas flow being absent in this transfer mode which is evidenced by the zero flow rate shown in **Figure 4.1**.

Finally, when looking at the 4 signals corresponding to no droplet transfer, it can be seen that the acoustic signal is significantly quieter than the other modes. Similarly, no distinctive peaks can be seen in the current and voltage signals.

4.3. Analysis of Transfer Mode Features

4.3.1. Feature extraction

In order to analyse the acoustic, current, voltage and gas flow rate signals, several time and frequency domain features are extracted, which are listed in **Equations** 4.1 to 4.17. Several of these features have been used previously to analyse the acoustic signal of the welding process. [39, 54] used the acoustic features in **Equations** 4.1 **to** 4.11 and **Equations** 4.12 to 4.17 to detect the welding transfer modes and the peak detection analysis seen in **Section 4.3.1.2**. The Number of Peaks and Average Peak Height features are based on the investigation into the shape and frequency of the acoustic signal peaks between different transfer modes conducted by [33]. In addition to these, Mel Frequency Cepstral Coefficients

(MFCC) are also being used as a feature and have been previously used by [55] to detect defects in GTAW.

Time Domain Features	
Zero Crossing Rate	$X_{zcr} = \frac{f_s}{s_l}\sum_{k=1}^{s_l}\left\lvert sgn\big(s(k)\big) - sgn\big(s(k-1)\big)\right\rvert$ (4.1)
Root mean square	$X_{rms} = \left(\frac{1}{s_l}\sum_{k=1}^{s_l} s^2(k)\right)^{\frac{1}{2}}$ (4.2)
Square root of the amplitude	$X_{sra} = \left(\frac{1}{s_l}\sum_{k=1}^{s_l}\sqrt{\lvert s(k)\rvert}\right)^2$ (4.3)
Kurtosis value	$X_{kv} = \frac{1}{s_l}\sum_{k=1}^{s_l}\left(\frac{s(k)-s_{avg}}{\sigma_s}\right)^4$ (4.4)
Skewness value	$X_{sv} = \frac{1}{s_l}\sum_{k=1}^{s_l}\left(\frac{s(k)-s_{avg}}{\sigma_s}\right)^3$ (4.5)
Peak-peak value	$X_{p2p} = \max(s) - \min(s)$ (4.6)
Crest factor	$X_{cf} = \max(\lvert s\rvert)\Big/\left(\frac{1}{s_l}\sum_{k=1}^{s_l} s^2(k)\right)^{\frac{1}{2}}$ (4.7)
Impulse factor	$X_{if} = \max(\lvert s\rvert)\Big/\frac{1}{s_l}\sum_{k=1}^{s_l}\lvert s(k)\rvert$ (4.8)
Margin factor	$X_{mf} = \max(\lvert s(k)\rvert)\Big/\left(\frac{1}{s_l}\sum_{k=1}^{s_l}\sqrt{\lvert s(k)\rvert}\right)^2$ (4.9)
Shape factor	$X_{sf} = \left(\frac{1}{s_l}\sum_{k=1}^{s_l} s^2(k)\right)^{\frac{1}{2}}\Big/\frac{1}{s_l}\sum_{k=1}^{s_l}\lvert s(k)\rvert$ (4.10)
Number of Peaks	(See section 4.3.2)

Average Peak Height	(See section 4.3.2)
Signal Average	$X_{avg} = \frac{1}{s_l}\sum_{k=1}^{s_l}\lvert s(k)\rvert$ (4.11)
Peak frequency	$X_{pf} = maxarg(f_{sp})$ (4.12)
Frequency centre	$X_{fc} = \int_0^{+\infty} s f_{sp} df \Big/ \int_0^{+\infty} f_{sp} df$ (4.13)
RMS frequency	$X_{rmsf} = \left(\int_0^{+\infty} s^2 f_{sp} df \Big/ \int_0^{+\infty} f_{sp} df\right)^{\frac{1}{2}}$ (4.14)
Root variance frequency	$X_{rvf} = \left(\int_0^{+\infty} (s - X_{fc})^2 f_{sp} df \Big/ \int_0^{+\infty} f_{sp} df\right)^{\frac{1}{2}}$ (4.15)
Max Frequency	$X_{maxf} = \max(f_{sp})$ (4.16)
Average Frequency	$X_{avgf} = \frac{1}{s_l}\sum_{k=1}^{s_l} f_{sp}(k)$ (4.17)
MFCC	(see section 3.3)

where f_s is the sampling frequency, s_l is the segment length, $s(k)$ is the signal segment amplitude at position k, σ_s is the standard deviation of the signal segment, s_{avg}, is the average segment amplitude, and f_{sp} is the frequency spectrum of the signal segment.

4.3.1.1. Mel Frequency Cepstral Coefficients

MFCC's are a common feature used in speech recognition algorithms and are used to distinguish phonemes in speech. MFCC's aim to calculate the energy present between two frequency bands in an audio signal. However due to the human ear's limited ability to detect small frequency changes at higher frequencies, a non-linear Mel scale is used in order to better represent the frequency bands for which the features are calculated. **Equation** 4.18 to transform this regular frequency into Mel frequencies can be seen [56].

$$M_f(f_{sp}) = 1125 \ln\left(1 + \frac{f_{sp}}{700}\right) \quad (4.18)$$

As it is well known that professional welders can tell the difference between transfer modes using only the sound signal [36], the use of MFCC's as a feature is both reasonable and appropriate in replicating the ability that professional welders possess.

4.3.1.2. Peak Detection

In order to calculate the number of peaks and average peak height features listed above, the peaks of the recorded signals need to first be obtained. As documented by [33], the frequency and amplitude of the signal peaks varies between the different transfer modes, hence the two features mentioned above are supposed to act as a decent indicator of the current transfer mode of the system.

To analyse the appearance, frequency and shape of the signal peaks, a peak detection algorithm is used to automatically detect the peaks in the signal that correspond to the welding droplet transfers. To detect and calculate the peaks of the signal, the signal envelope of the absolute value of the signal is estimated first then the peaks are calculated by finding $s(k)$ points where.

$$s(k-1) < s(k) \text{ and } s(k) > s(k+1) \quad (4.19)$$

After finding all the peaks in the envelope signal, the next step is to analyse the peaks and determine which of the peaks correspond to a single droplet transfer. In order to do this, thresholds need to be set to properly filter out the false peaks in the signal. However, these thresholds need to be relative to each individual signal as an absolute value cannot be determined due to the amplitude differences between different transfer modes. To overcome this difficulty, a two-threshold strategy is used to remove these false peaks, where a threshold is set for both the peak prominence (M_{PP}) and the peak amplitude (M_{PA}). Trial and error shows that the thresholds of $0.5\times M_{PA}$ and $0.2\times M_{PP}$ are optimal to filter out the false peaks. As an example, **Figure 4.2** shows the absolute value of the acoustic signal (upper panels) and the signal envelope (lower panels) with the detected peaks (red circles) of a 20 ms period for the short circuit and free flight transfer modes, respectively. It can be seen that only one distinct pulse is detected in the short circuit transfer mode in comparison to the Spray mode which registers several peaks within the same time period.

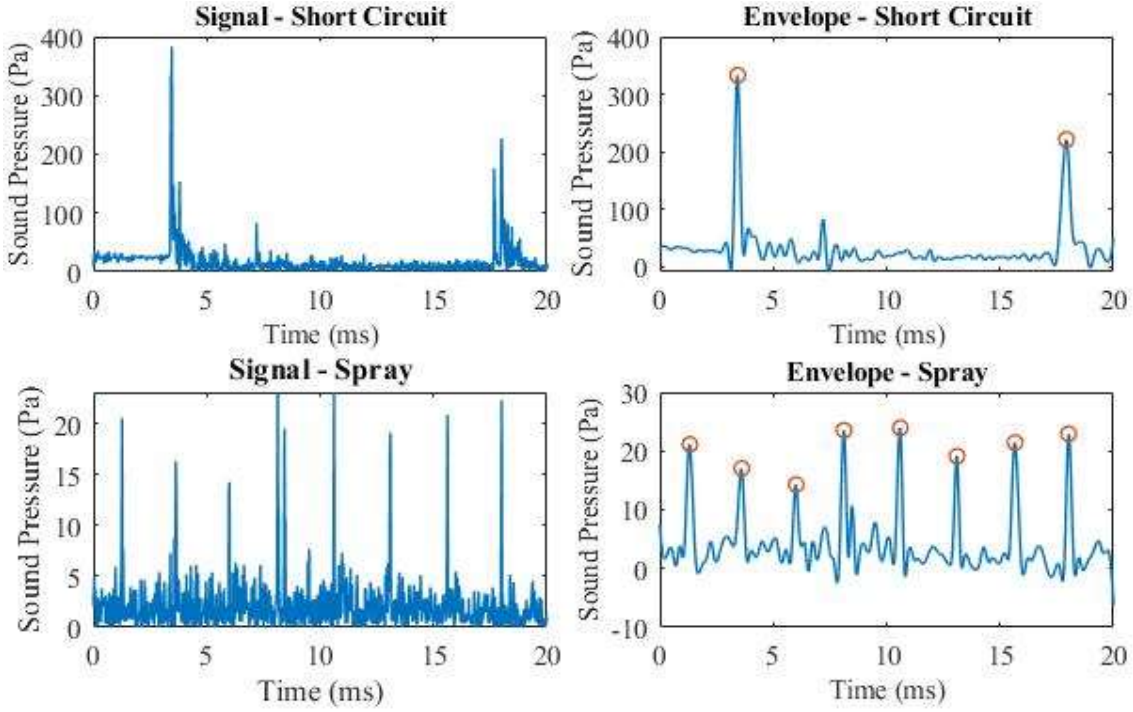

Figure 4.2 - Peak Detection of Short Circuit and Spray transfer

4.3.2. Feature Selection

To reduce the redundant information in the feature set and choose the most appropriate features, a feature selection method is introduced to maximise the distance between each classes' multivariate probability distribution. This distance between each class can be calculated using the Bhattacharyya distance formula [57] in **Equations** 4.20 & 4.21.

$$D_{\mathrm{B}} = \frac{1}{8}\left(\mu_f(k_1) - \mu_f(k_2)\right)^T \Sigma_{\mathrm{f}}^{-1}\left(\mu_f(k_1) - \mu_f(k_2)\right) + \frac{1}{2}\ln\left(\frac{det\Sigma_{favg}}{\sqrt{det\Sigma_f(k_1) + det\Sigma_f(k_2)}}\right) \quad (4.20)$$

$$\Sigma_{favg} = \frac{\Sigma_f(k_1) + \Sigma_f(k_2)}{2} \quad (4.21)$$

where D_{B} is the Bhattacharya distance, and μ_f and Σ_f are the mean and covariance matrices for multivariate probability distributions k_1 and k_2, respectively.

As the Bhattacharya distance can only calculate the distance between two classes, all possible combinations between are calculated to achieve a distance that is representative of all the classes. Using all combinations of D_{B}, a new weighted, unitless distance classifier, T_h is calculated to represent the overall viability that the feature set has at maximising the distance between all of the classes. This T_h value is calculated using **Equations** 4.22 to 4.24.

$$D_{\min} = \min\left(D_{\mathrm{B}}(k_1, k_2) \,|k_1 \in \{1, \dots, C_T\}, k_2 \in \{k_1 + 1, \dots, C_T\}\right) \quad (4.22)$$

$$D_{\mathrm{avg}} = \frac{2!\,(C_T - 2)!}{C_T!} \sum_{k_1=1}^{C_T} \sum_{k_2=k_1+1}^{C_T} D_{\mathrm{B}}(k_1, k_2) \quad (4.23)$$

$$T_h = \frac{\left(D_{\min} + D_{\text{avg}}\right)}{L_f}\sqrt{1 + c_0^2} \tag{4.24}$$

where $D_{\min}$ and D_{avg} are the minimum and average values of D_{B} for all class combinations respectively, C_T is the number of classes, L_f is the current number of features selected, and c_0 is the threshold constant.

The T_h value calculated above takes into account both $D_{\min}$ and D_{avg} in order to make sure that the average value of D_{B} can be maximised while still making sure that each class combination maintains a maximum distance between each other. As the distance D_{B} will always grow as the number of features increase, the threshold value T_h needs to be normalised as the number of features increases. This is done by dividing L_f and multiplying by the square root of the threshold value plus one [58].

To obtain the optimal set of features F_f from the initial feature set F_i, a modified version of the Sequential Forward Floating Selection (SFFS) algorithm [57, 59] is developed. This algorithm selects one feature from the initial feature set first, and then adds additional features to the set that maximises the value of T_h. Whenever the algorithm adds a feature to the feature set, it also tests to see if removing any of the features from the feature set can further maximise the value of T_h. This process is repeated until such a point where both adding or removing features no longer increases the value of T_h. This algorithm is schematically illustrated in **Figure 4.3** which shows the process to select the optimal feature set, where f is a feature of the original feature set F_i, f_{add} is the feature that is added to the current feature set F_t that maximises the value of T_h, and f_{sub} is the feature that is subtracted from F_t that maximises the value of T_h.

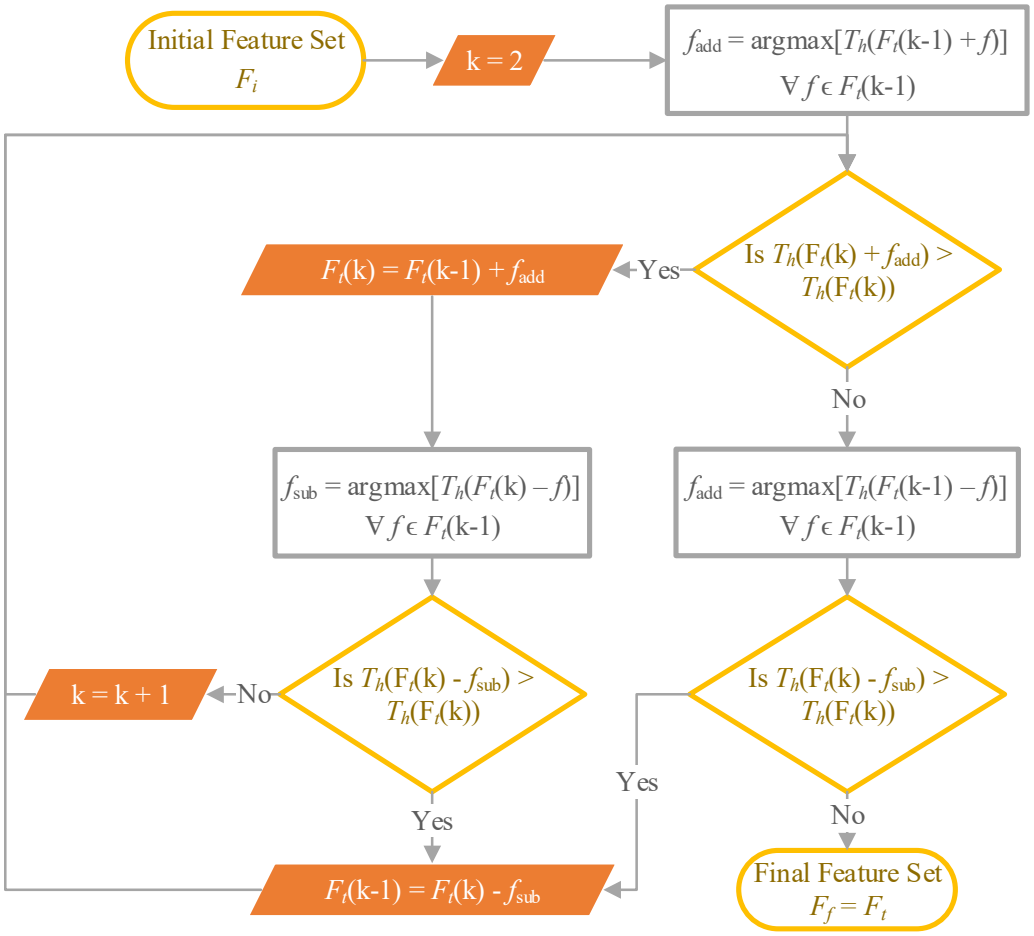

Figure 4.3 - Diagram of the Feature Selection Algorithm

4.3.3. SVM classifier training and testing

The SVM is used as the classifier for the automatic metal transfer mode classification system because it is simple and easy to implement in a portable system. The SVM classifiers use a Radial Basis Function (RBF) kernel and are trained with the features selected by the feature selection algorithm which are then normalised.

To create a large enough database of signals to train the SVM classifiers, each of the 32 recorded signals shown in **Table 4.1** are divided into subsets containing smaller segment lengths. Ideally, the optimum length of these smaller segments would be as short as possible without sacrificing the prediction accuracy of the SVM classifiers because it would allow for less individual droplet transfers being analysed in each segment. Therefore 5 different segment lengths are chosen to train the SVM classifier in order to investigate the prediction accuracy as the segment lengths become shorter. These segment lengths are 100 ms, 50 ms, 40 ms, 30 ms, and 20 ms, respectively. Each of these segment's corresponding video footage was manually analysed and classified as one of each of the 4 target transfer modes or as "N/A" if no droplet was transferred.

Using the database of smaller signal segments, the optimal features are extracted for each segment and are then used to train the SVM classifiers. A total of 5 tests are performed in the experiments. The SVM classifier is first trained using the features obtained from the individual acoustic, current, voltage, and gas flow rate signal segments, respectively. Then the combined features obtained from all the four base signals are used to train the SVM classifier. This process is then repeated 5 times using each of the 5 different segment lengths.

In order to test the prediction accuracy, each SVM classifier is subjected to 10-fold cross validation. The training data set is randomly divided into 10 equal sets, 9 of which are used to train the SVM classifier while the 10^{th} set is used to test the accuracy. This is repeated again until all 10 sets have been used to train and test the model, and the accuracy for each set are averaged to produce a prediction rate.

4.4. Results and Discussions

4.4.1. Feature selection results

The feature selection algorithm is able to effectively reduce the dimensionality of the original feature set while only retaining the optimal features for class separability. In the experiment, the desired features, which maximise the value of T_h, are selected from the original feature set F_i. As an example, **Table 4.2** shows the features selected by the feature selection algorithm using only the acoustic signals across the 5 different segment lengths.

Table 4.2 - Common Acoustic only Method Features

Features	Signal segment length				
	100 ms	50 ms	40 ms	30 ms	20 ms
Zero Crossing Rate	Y	Y	Y	Y	Y
Root Mean Square	Y	Y	Y	Y	Y
Square root of amplitude	Y	Y	Y	Y	Y
Kurtosis Value	Y	Y	Y	Y	Y
Skewness value	Y	Y	Y	Y	Y
Peak to Peak Value	Y	Y	Y	Y	Y
Crest Factor	Y	Y	Y	Y	Y
Impulse Factor	Y	Y	Y	Y	Y
Margin Factor	Y	Y	Y	Y	Y
Shape Factor	Y	Y	Y	Y	Y
Peak Frequency	Y	Y	N	N	N
Frequency centre	N	N	N	N	N
Root Mean Square Frequency	N	N	N	N	N
Root Variance Frequency	N	N	N	N	N
Number of Peaks	Y	Y	Y	N	N
Average Peak Height	Y	Y	Y	Y	Y
Signal Average	Y	Y	Y	Y	Y
Max Frequency	Y	Y	Y	Y	Y
Average Frequency	Y	Y	Y	Y	Y
MFCC log energy	Y	Y	Y	Y	Y
MFCC band 0-500hz	Y	Y	Y	Y	Y
MFCC band 200-850hz	Y	Y	Y	Y	Y
MFCC band 500-1300hz	Y	Y	Y	Y	Y
MFCC band 850-1900hz	Y	Y	Y	Y	Y
MFCC band 1300-2650hz	Y	Y	Y	Y	Y
MFCC band 1900-3650hz	N	N	N	N	N
MFCC band 2650-4900hz	N	N	N	N	N
MFCC band 3650-6550hz	N	N	N	N	N
MFCC band 4900-8700hz	N	N	N	N	N

MFCC band 6550-11450hz	N	N	N	N	N
MFCC band 8700-15000hz	N	N	N	N	N
MFCC band 11450-19650hz	N	N	N	N	N
MFCC band 15000-25600hz	N	N	N	N	N

From **Table 4.2** it can be observed that approximately a third of the features (on average 13 out of 33) from the original feature set are excluded by the feature selection algorithm. It can also be seen that while majority of the features selected by the algorithm are identical among the 5 segment length tests, both the Number of Peaks and Peak Frequency features were selected in only the longer segment lengths tests. This leads to some of the selected features being situationally useful, where they only show a large amount of class separability at either short or long segment lengths. The features selected by the algorithm in the 20 ms test can be seen in **Figure 4.4**, which shows the mean values of each feature for each of the 5 transfer mode. The results for other segment lengths (30 ms, 40 ms, 50 ms and 100 ms) and other signals (current, voltage and gas flow rate) are similar and not shown here for the sake of brevity.

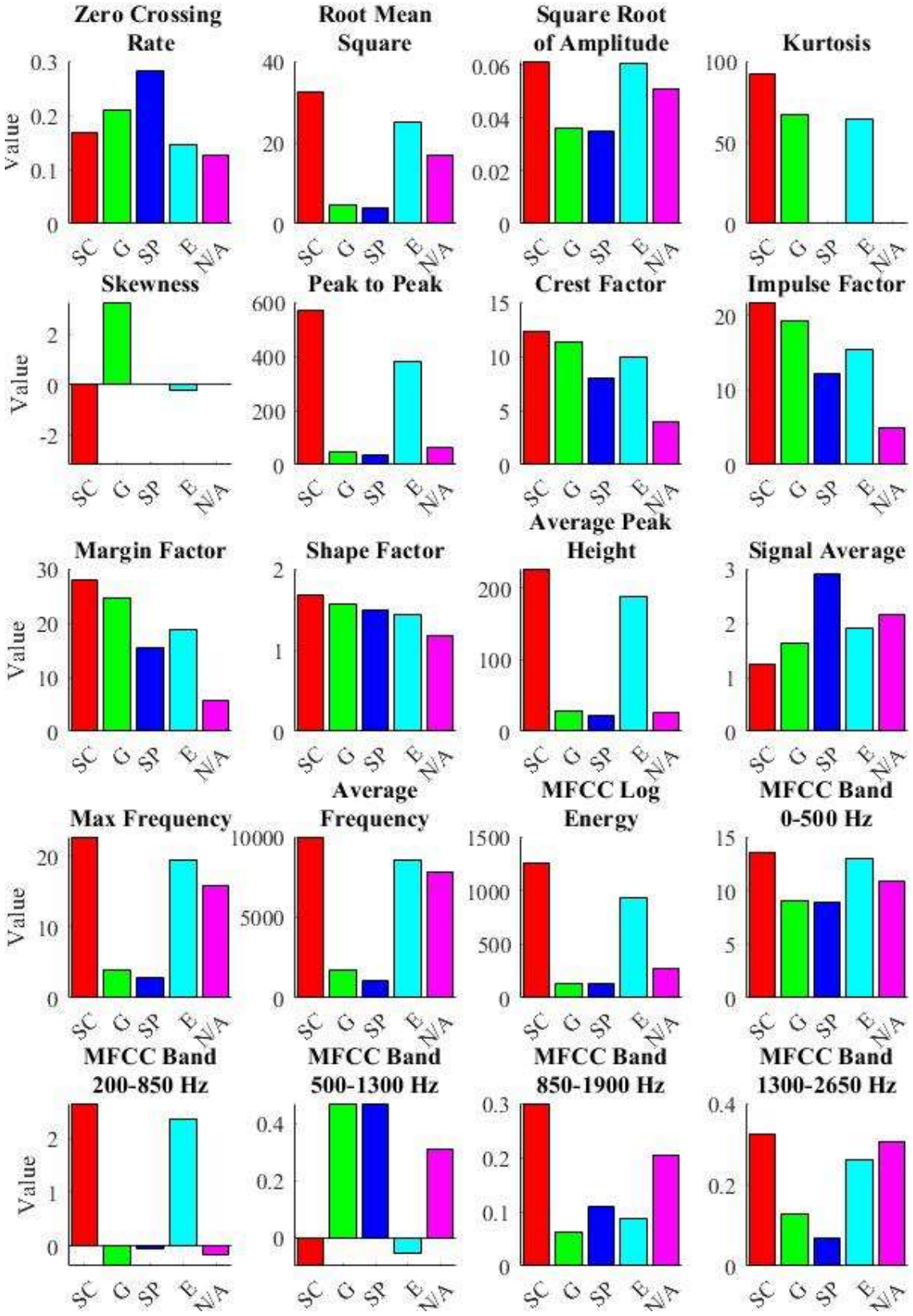

Figure 4.4 - Mean values of Acoustic Features selected by the feature selection algorithm for 20 ms segments

Figure 4.4 shows that each individual feature selected by the algorithm cannot effectively separate all 5 classes on its own. However, the feature selection algorithm successfully chooses a combination of features that are able to maximise the distance between each of the individual classes. For example, when looking at the short circuit transfer (Red Bar) and explosive transfer (Cyan Bar) values in majority of the common features shown in **Figure 4.4**, it can be seen that the mean values are shown to be very similar. However, due to the class separability value, T_h shown in **Equation** 4.24, the feature selection algorithm selects features to address this issue such as MFCC Band 850-1900 Hz, which shows a large degree of separability between short circuit and explosive modes. This can be better understood when observing the values of the class separability value, T_h at each iteration of the feature selection algorithm as shown in **Figure 4.5**.

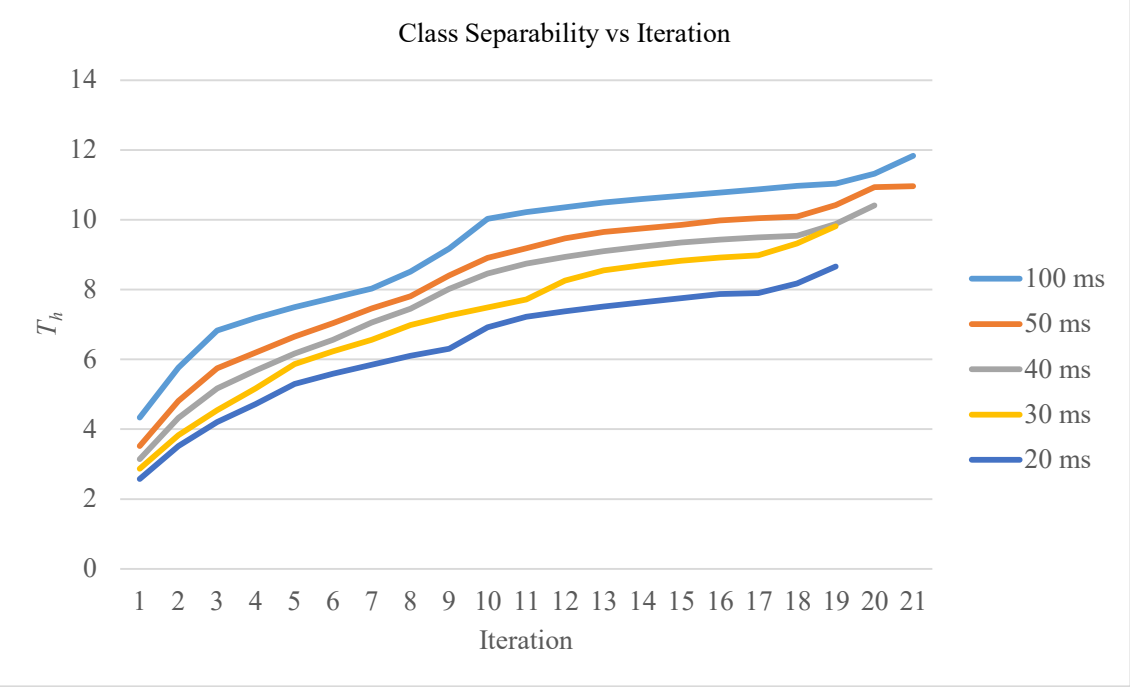

Figure 4.5 - Class separability value T_h at each iteration of the feature selection algorithm for the acoustic only method

The class separability values in **Figure 4.5** show that as additional features are added and removed at each iteration of the feature selection process, the overall value of the class separability is increased. At iteration 1 of the feature selection algorithm, the 2 features with the highest class separability value are selected. The results displayed in **Figure 4.5** however show that the value of T_h for the feature set selected at iteration 1 can be improved by upwards of 300% when more features are added, reaching a maximum class separation value at its final iteration. For comparison, the values of T_h for the original feature set alongside the final T_h values when using the feature selection algorithm as well as the values for the excluded features are summarised in **Table 4.3**.

Table 4.3 - Class Separability value T_h for the feature selection and original feature sets

Feature Set	Segment Length				
	100 ms	50 ms	40 ms	30 ms	20 ms
Unselected Features	2.33	1.97	1.67	1.49	1.15
Original	11.37	10.18	9.54	8.92	7.72
Feature Selection	11.83	10.96	10.41	9.82	8.66

Observing the results in **Table 4.3** it can be seen that the feature selection algorithm is able to effectively increase the value of T_h when compared to the value obtained using the original feature set. As stated above in the feature selection algorithm section, a higher class separability value T_h corresponds to a larger average separation distance between the 5 different classes. This increase in value is also shown to be much larger in the shorter segment length tests than it is in the longer segment length tests, suggesting that many of the features that the feature reduction algorithm excludes have a larger negative impact on the class separability at shorter segment lengths.

4.4.2. Classification results

As outlined in Section 3, five tests were performed and repeated across 5 different segment lengths. The first 4 tests used feature sets from either the acoustic, current, voltage or gas flow rate signals individually while the final test used a combined feature set consisting of the features from all the 4 signals. When the original feature set is used (without the feature selection algorithm), the 10-fold cross validation results are shown in **Table 4.4**. It can be seen that the SVM classifier was able to achieve a level of accuracy greater than 80% across the five tests. Both the gas flow rate and current only methods show the highest accuracies being approximately 85% accurate with the acoustic, voltage and combined methods being slightly less accurate with prediction accuracies of approximately 80%.

Table 4.4 - SVM accuracy results (Original Feature Set)

Segment Length	Accuracy (%)				
	Acoustic features only	Current features only	Voltage features only	Gas features only	Combined features
100 ms	81.1	86.6	81.7	87.2	80.0
50 ms	81.2	86.5	81.6	85.6	80.0
40 ms	81.3	85.8	81.6	85.2	80.0
30 ms	81.2	85.8	81.4	84.9	80.0
20 ms	81.2	86.1	81.4	83.5	79.9

Similarly, the 10-fold cross validation of the SVM classifiers trained using the feature sets selected by the feature selection algorithm are summarised in **Table 4.5**. By comparing **Tables 4.4** and **4.5**, it can be observed that the application of the feature selection algorithm leads to significantly higher prediction accuracies across the acoustic, current, voltage, and combined methods. On average the inclusion of the feature selection algorithm improved the classification accuracies by approximately 15% when compared to the results shown in **Table 4.4**.

Table 4.5 - SVM Classifier Accuracy Results (Feature Selection)

Segment Length	Accuracy (%)				
	Acoustic features only	Current features only	Voltage features only	Gas features only	Combined features
100 ms	94.5	96.3	96.9	82.6	97.7
50 ms	94.3	96.1	96.6	84.3	97.7
40 ms	94.7	96.9	96.5	85.5	97.8
30 ms	94.9	96.8	96.4	85.2	97.7
20 ms	94.1	95.5	95.5	85.2	97.8

When comparing the classification accuracies among the 5 methods in **Table 4.5** it can be seen that the combined signal method produced the highest level of accuracy with an average prediction accuracy of greater than 99.7% across the 5 different segment length trials. This was expected as the feature reduction algorithm uses all features calculated from the 4 signals and chooses the best feature set accordingly. In addition to the combined signal method, the accuracies of the Acoustic, Current and Voltage only methods all were able to achieve a prediction accuracy of 96%, 98%, 99% respectively. When comparing these methods to the combined method it can be seen that there is only a minor drop in accuracy. This is especially the case for the current and voltage methods which have an average accuracy of only 2% lower than the combined mode. Despite the presence of loud background noise in the factory, the achieved prediction accuracy is as high as 96.8% when the SVM classifier is trained with the acoustic signal only, which is promising for practical applications with the advantage of non-intrusiveness and portability. The accuracy of acoustic signal only prediction can be further improved in the future, by utilizing various beamforming algorithms based on a microphone array to enhance the welding sound signal from other noises and increase the robustness of the acoustic sensing based approach.

It should be noted that when the gas flow rate is used as the individual signals for the SVM classifier, it is significantly less accurate than the other methods once the feature selection algorithm is applied. This is reasonable as the gas flow rate is incredibly similar between 4 of the 5 transfer mode classes with only the explosive transfer mode with no shielding gas. The higher accuracy of this method when

the feature selection algorithm is not used compared to the other tests in **Table 4.4** may be the result of overfitting due to the gas flow rate having an almost constant value throughout each of the 12 original signals.

Both **Tables 4.4** and **4.5** show that the accuracies remained relatively similar across the 5 different segment lengths in both the acoustic only and combined signal trials, demonstrating the feasibility of real-time process monitoring within a time window as short as 20 ms. This can also provide instant feedback information on welding quality, enabling adaptive real-time control of weld parameters for fully automated welding robots.

4.4.3. Discussions

4.4.3.1. Transfer Mode Comparison

A further breakdown of the 20 ms acoustic model can be seen in the confusion matrix in **Figure 4.6**

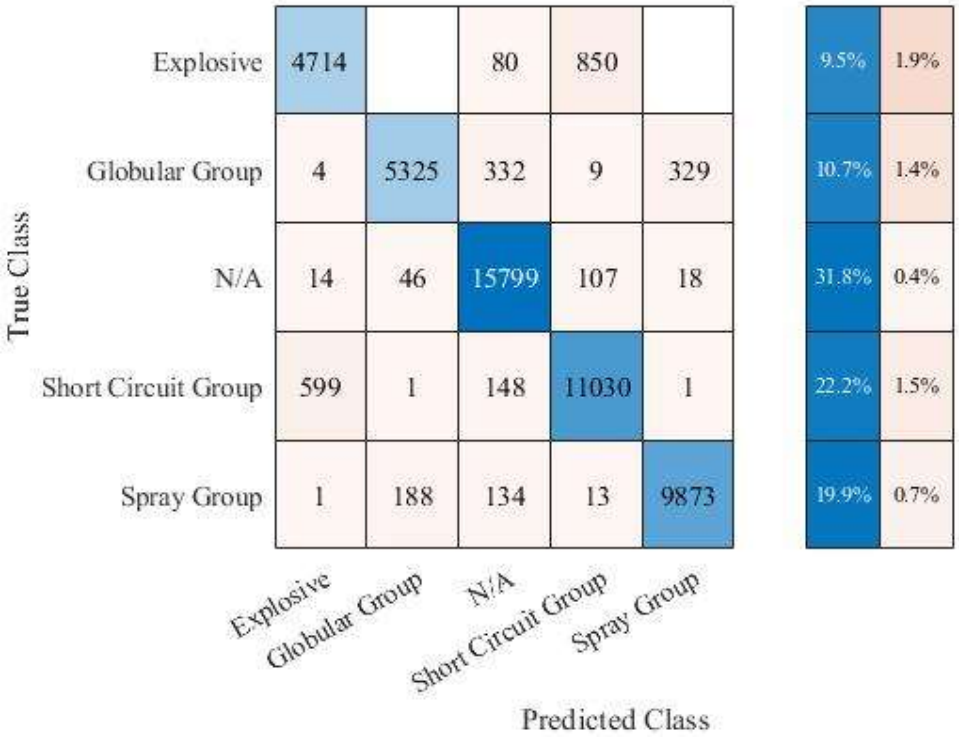

Figure 4.6 - SVM Confusion Matrix

When further analysing the results found in **Figure 4.6**, it can be seen that there are a few key areas in which the model tends to have a higher misclassification rate. In particular, the model has a high misclassification rate between globular and spray transfer modes as well as short circuit and explosive transfer modes. To understand why these areas contained the largest percentages of misclassification, each of the misclassified segments were re-examined.

When looking at the misclassification results of the globular and spray transfer groups, it was found that majority of the misclassifications existed in a grey area between the 2 different transfer modes.

This is illustrated in **Figure 4.7** which shows a standard spray transfer, a standard globular transfer, and one of the misclassified segments in between. From the current literature definition of spray and globular transfer [15], a droplet is considered to be in spray transfer when the diameter of the droplet is less than or equal to the diameter of the welding electrode. When the diameter is larger it is considered to be in globular transfer. Using this classification system, it can be seen that the misclassified segment is technically a globular transfer, however it is right on the border of being a spray transfer.

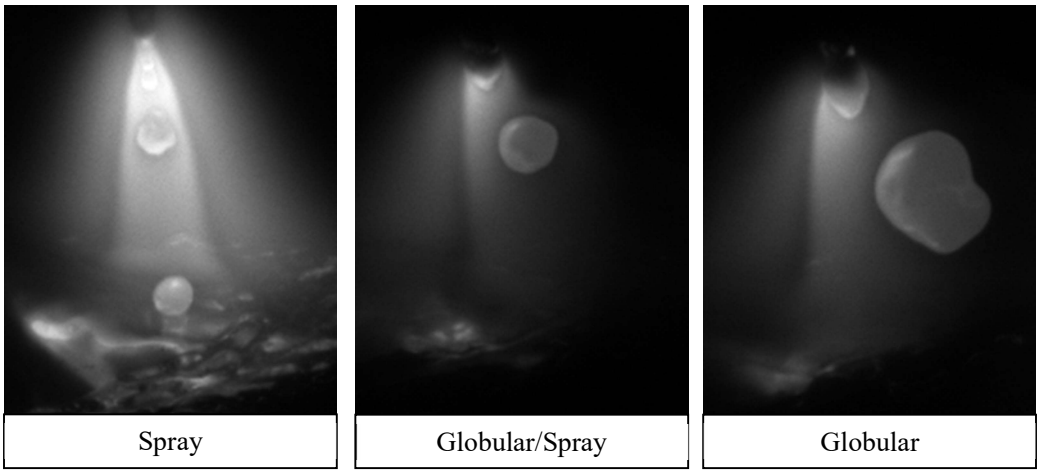

Figure 4.7 - Globular/Spray Comparison

Similar to the misclassification between globular and spray transfer, a similar phenomenon can be observed with short circuit and explosive transfer modes. **Figure 4.8** shows both a standard short circuit and explosive transfer mode. In both modes, the electrode makes contact with the weld pool creating a short circuit before transferring material into the weld pool. However, due to the lack of shielding gas, the explosive transfer process is not as smooth as in short circuit transfer, leading to a more violent explosion and turbulent weld pool. When analysing the misclassified segments between these two modes, it can be seen that majority of the misclassified segments occur when there is either a particularly turbulent transfer of material in a short circuit transfer, or more commonly, a particularly smooth transfer of material in an explosive transfer. Technically, despite the lack of gas, if the material smoothly transfers from the end of the electrode to the weld pool while short circuiting, it should be classified as a short circuit transfer mode. Because of this, many of the misclassifications between explosive and short circuit transfer are technically correct and should not be counted as misclassifications.

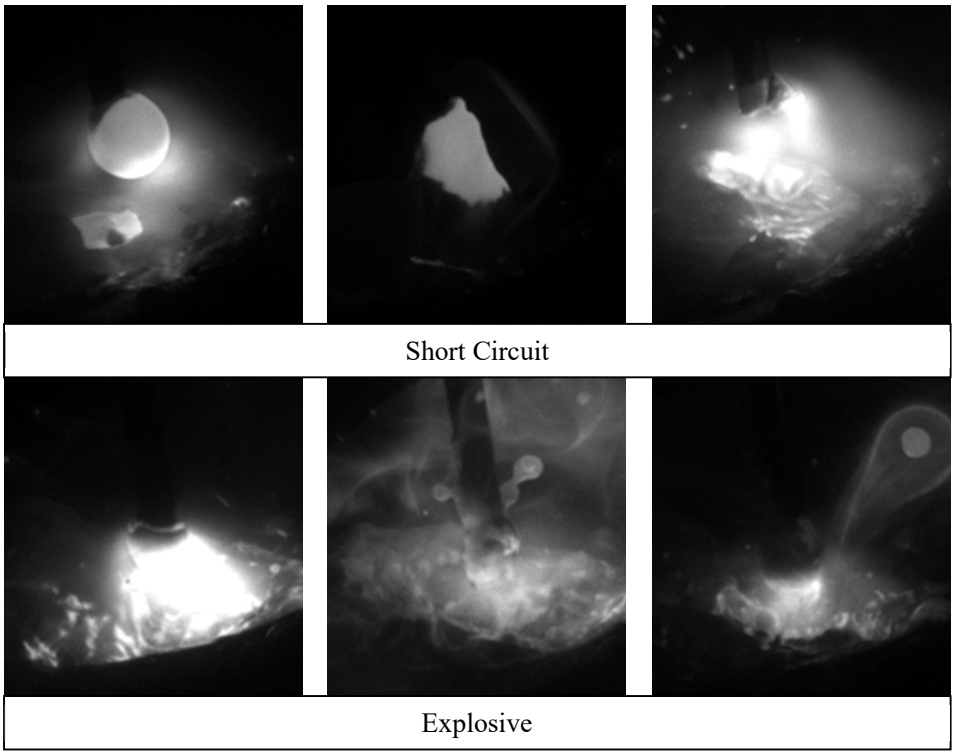

Figure 4.8 - Short Circuit/Explosive Comparison

Taking both of the above cases into account, it can be concluded that the overall accuracy of the SVM classifier may actually exceed 94% due to the ambiguity of some of the manual classifications.

4.4.3.2. Segment Length Comparison

When further analysing the results for both the acoustic and combined tests, it was found that the accuracy results of the longer segment lengths may not be as accurate as they are initially presented. As previously stated in **CHAPTER 2**, droplets can transfer from the end of the electrode at frequencies as high as once every 2 ms. This high frequency allows multiple droplets to transfer within the timespan of a single segment, with the possibility for several changes in transfer mode to occur. The likelihood of these transfer mode changes occurring within a single segment increases significantly with segment length, leading to a high chance of multiple modes being captured within a single segment. To further analyse this problem, a breakdown of individual transfer mode classifications can be seen in **Table 4.6** for the acoustic only tests.

Table 4.6 - Acoustic only SVM classification accuracies by transfer modes

Signal Length	Short-circuit	Globular	Spray	Explosive	N/A
100 ms	93.4	89.1	89.9	85.1	99.1
50 ms	93.0	88.4	89.5	84.4	98.4
40 ms	93.1	88.5	90.7	84.5	98.5
30 ms	93.1	88.8	91.3	84.8	98.8
20 ms	93.6	88.8	96.7	83.5	98.8

Looking at these results, it can be seen that despite the overall accuracy going up as the segment length increases, the accuracy of spray transfer mode starts to decrease. This is a result of several of the segments being manually classified as spray transfer mode due to them being predominantly under spray transfer, being classified differently by the SVM as short circuit transfer mode due to the presence of a short circuit occurring at some stage during the segment. Technically, if these transfer modes are being analysed at longer segment lengths, then they would be classified as interchangeable transfer modes due to several different forms of droplet transfer being present at once. However, since the purpose of the transfer mode detection algorithm is to dynamically measure the transfer mode in real time, there is a greater benefit in attempting to classify the natural transfer modes and not classify them as interchangeable.

Below are two examples that can further help explain the difficulties in detecting spray or globular transfer if the system is in an interchangeable transfer mode. **Figures 4.9** and **4.10** show the acoustic, voltage, and current signals of an interchangeable and short circuit transfer mode over a 100 ms time span respectively.

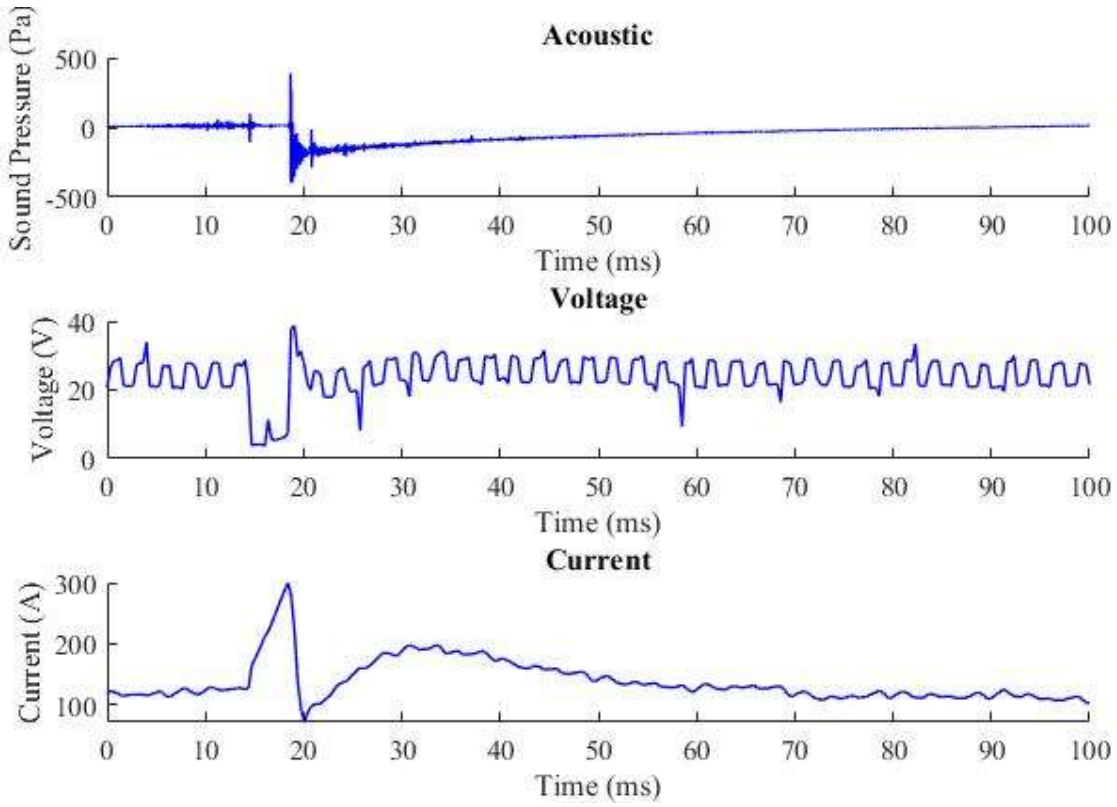

Figure 4.9 - Interchangeable Transfer Mode Signal

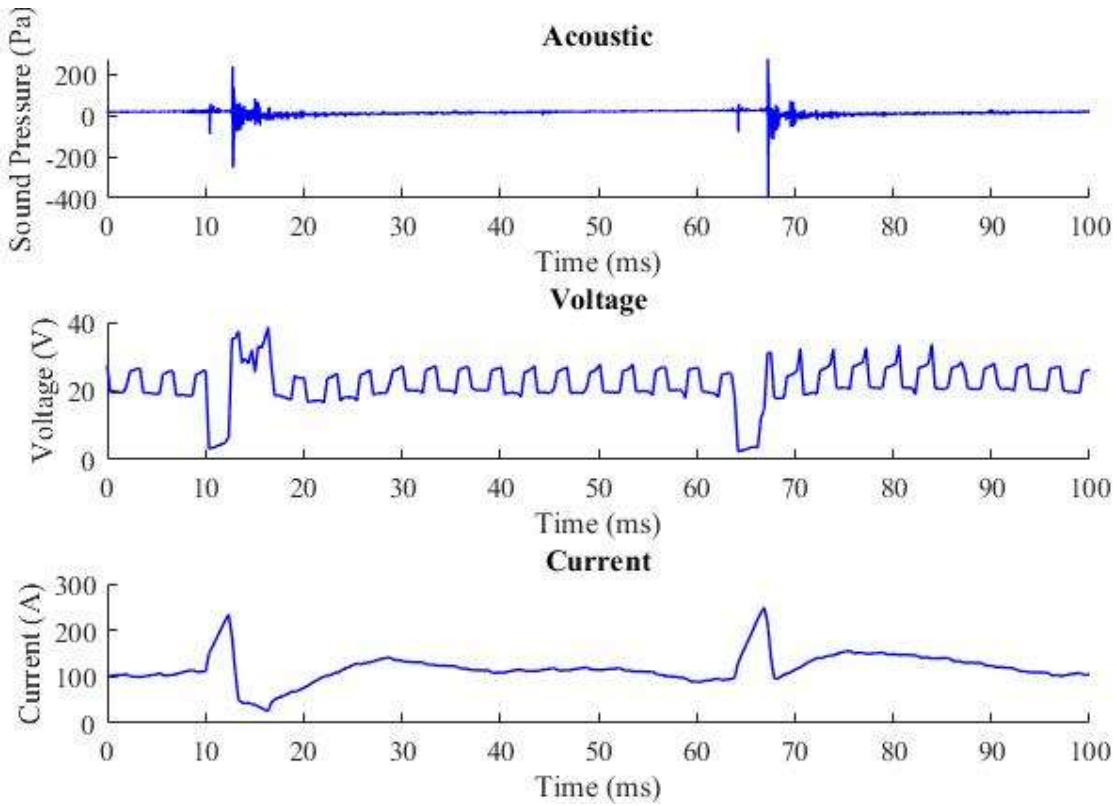

Figure 4.10 - Short Circuit Transfer Mode Signal

The acoustic signals in the figures above both look very similar with distinct peaks heavily representing short circuit transfer mode. The corresponding video footage of the two different signals illustrate that they both were in fact short circuit transfer modes confirming this observation in the acoustic signal. However, immediately after the short circuit transfer occurs in **Figure 4.9**, several spray droplets are produced followed by a globular droplet which are not easily seen using only the acoustic signal. However when analysing the current signals, it can be seen that the base level of the current in **Figure 4.9** is higher than that in **Figure 4.10** directly after the first short circuit transfer. This higher current fits the conditions for Globular-Short Circuit- Streaming Spray Interchangeable Mode [15] which is the literature classification of the interchangeable seen in this test.

Taking the observations above into consideration, it is extremely beneficial to use 20 ms segments over longer 100 ms segments as shown in **Figure 4.9** & **Figure 4.10** in order to minimise the chance of capturing 2 different transfer modes in a single segment. While there is still a possibility of capturing more than one transfer mode within a 20 ms segment, a large majority of the cases will be similar to those above in **Figure 4.9** & **Figure 4.10** where a globular or spray transfer is captured directly after a short circuit transfer. In this scenario, there is not much benefit in classifying the transfer mode as spray, globular, or even as a new interchangeable category, as there is a strong likelihood that the following segment will still be in this mode and will be captured regardless. Similarly the mixed model using current and voltage signals could also be incorporated to detect the presence of the additional spray and globular droplets, however the cons of the additional system complexity and possible SVM overfitting to input parameters far out way the benefits of the marginal detection accuracy increase. From this perspective, it is more beneficial to use only the acoustic signal to classify the transfer modes, because it is more accurately able to achieve the correct classification based on the actual droplet transfer instead of the shape of the welding parameter signals that cause the process to occur.

4.5. Conclusion

In this chapter, a new GMAW transfer mode classification method has been introduced based on acoustic signal analysis. Five models were created using a combination of time and frequency domain features extracted from the acoustic, current, voltage and gas flow signals. The time and frequency features are used to train a SVM classifier for automatic transfer mode detection. A feature selection algorithm is proposed to find the optimal features with minimum redundant information to further improve the prediction accuracy. It was found that, when using only the acoustic signal, the proposed feature selection algorithm improves the prediction accuracy from around 81% to approximate 94%. This is comparable to the prediction accuracy with all the acoustic, current, voltage and gas flow rate signals, which are approximate 97% and 80% with and without using the developed feature selection algorithm, respectively. The high accuracy of the acoustic signal only model shows the most promise due to its non-intrusiveness and the simplicity of the measurement system, which allows it to be easily implemented into a smart welding system. The robustness of the acoustic signal analysis can also be

improved via the use of multiple microphone arrays and the incorporation of beam forming algorithms. In addition to this, a real time adaptive feedback control system will be developed based off of the transfer mode detection algorithm introduced in this chapter.

This work has been published in both a conference paper [60] and a journal article [61].

CHAPTER 5 – DEFECT DETECTION

5.1. Introduction

In this chapter, a new real time GMAW defect detection algorithm is introduced. Using the transfer mode detection algorithm outlined in **CHAPTER 4**, the rapidly changing droplet transfer process is monitored to detect the presence of both burn through and porosity in real time. This algorithm is able to accurately detect the presence of both burn through and porosity across a wide range of GMAW transfer modes.

5.2 Background

As industrial manufacturing lines adopt an increasing amount of automated welding systems, there is a growing need for online quality control [62]. In particular automated GMAW robots are becoming more common, particularly in sheet metal fabrication lines due to their advantages of lower costs, faster welds, greater reliability and higher productivity when compared to traditional manual methods [13]. However despite these advantages, there is still a lack of an online inspection and quality control system available to detect critical welding faults that can occur throughout the welding process.

As covered in **CHAPTER 2**, two of the most common faults that occur in GMAW are both porosity and burn through. Traditionally, these faults are normally detected in post-production after the weld bead has already been formed. However, several researchers have attempted to develop methods to accurately detect these faults in real time using a variety of different methods.

Due to the acoustic signal generated by the welding process being heavily correlated with the droplet transfer mode and arc stability, several researchers have investigated using the sound signal for defect detection. One of the earliest studies in this area was carried out by [63], who used the acoustic signal to locate defects in Gas Tungsten Arc Welding (GTAW). Similarly [4] investigated online quality control using the sound signal for GMAW. [6] also used time and frequency domain features of the sound signal to detect possible defects in GMAW welds and found that time domain features were particularly useful in defect detection. A more comprehensive study was performed by [22] who used acoustic signal analyses to investigate the feasibility of detect welding faults in short circuit GMAW. Similarly [64] used the sound signal to detect defects in short circuit welding. A similar investigation was also undertaken by [65] who also investigated the feasibility of the using sound analyses to detect faults in GMAW. [66] developed a model for defect detection using acoustics in GMAW. [67] also developed a model for defect detection using acoustics in GMAW. [68] developed a welding defect detection system based on the acoustic signal using a sequence tagging and logistic regression algorithm. [69] developed a porosity detection system based on the acoustic signal using a convolutional neural network. [70] developed a data fusion model using spectroscopy and acoustic signals for real time welding defect detection in GTAW. [71] used a time delayed microphone array to analyse to detect defects in the weld seam in laser welding. [3] found that porosity in GMAW welds could be detected

by analysing the sound signal using the Hilbert Huang Transform. [72] also analysed the sound signal in GMAW and found that the sound kurtosis was an excellent indicator for weld bead porosity. [73] used the acoustic emissions alongside air coupled ultrasonics to classify the degree of burn through in GTAW in real time. [74] used the arc sound signal to develop a penetration estimation monitoring system for pulsed GMAW.

Similarly, researchers have also tried a variety of other methods to monitor and detect GMAW defects. An early attempt was by [75] who designed a parametric model for detecting burn through based on the current signal in pulsed GMAW. [76] developed a defect detection system using optical spectroscopy to detect the presence of contaminants in the weld pool in real time. [77] developed a real time burn through monitoring system using non contact ultrasonics. [78] developed a porosity detection system using a statistical model base on the current and voltage signals in short circuit transfer. [79] Developed an SVM model to classify porosity, burn through, and lack of penetration in butt welded pipe joints. [80] developed a monitoring system for laser mag welding, using a vision system to monitor how the input parameters effect pore growth. More recently [62] developed a defect detection system for GMAW base on the voltage and current signals while [81] was able to develop a model for detecting burn through and penetration depth based on ultrasonics.

All of these methods outlined above however fit in to one of two categories. The first involving pure observations and not methods of detection. The second category involving detection methods, however with the shortcoming of only being applicable to one specific GMAW transfer mode.

The issue with the current existing methods is that they are designed to only work for one specific transfer mode, which in most cases is short circuit transfer mode. The issue with this is that the recorded acoustic signal varies greatly between the different modes, with the existing peak analysis methods not working for other modes such as globular and spray. This is a quite a large shortcoming as a lot of modern robotic applications tend to use spray transfer due to its high heat input, in turn allowing for faster welding speeds to be used. However other modes are still required for other applications depending on factors such as thickness and weld geometry. Therefore, the method introduced in this chapter aims to solve this problem by being able to detect both burn through and external porosity independent of the transfer mode.

5.2. Methodology

As both burn through and porosity are caused by different factors that occur during the welding process, several different features of the acoustic signal need to be analysed. For burn through, it is shown in the literature [22] that the presence of burn through normally coincides with prolonged periods of arc extinguishment. When the welding arc is extinguished, no droplets are transferred from the end of the electrode into the weld pool and the welding process effectively stops. In some transfer modes it is relatively easy to detect this extended length of arc extinguishment from the sound signal. For example,

short circuit transfer mode, has very defined sound peaks when a droplet is transferred to the weld pool and a period of low intensity in between transfers. On the other hand, transfer modes such as spray transfer do not show such defined periods of droplet transfer making it significantly harder to detect when there is an extended period of arc extinguishment. This can be seen in **Figure 5.1** where the burn through locations are displayed in red.

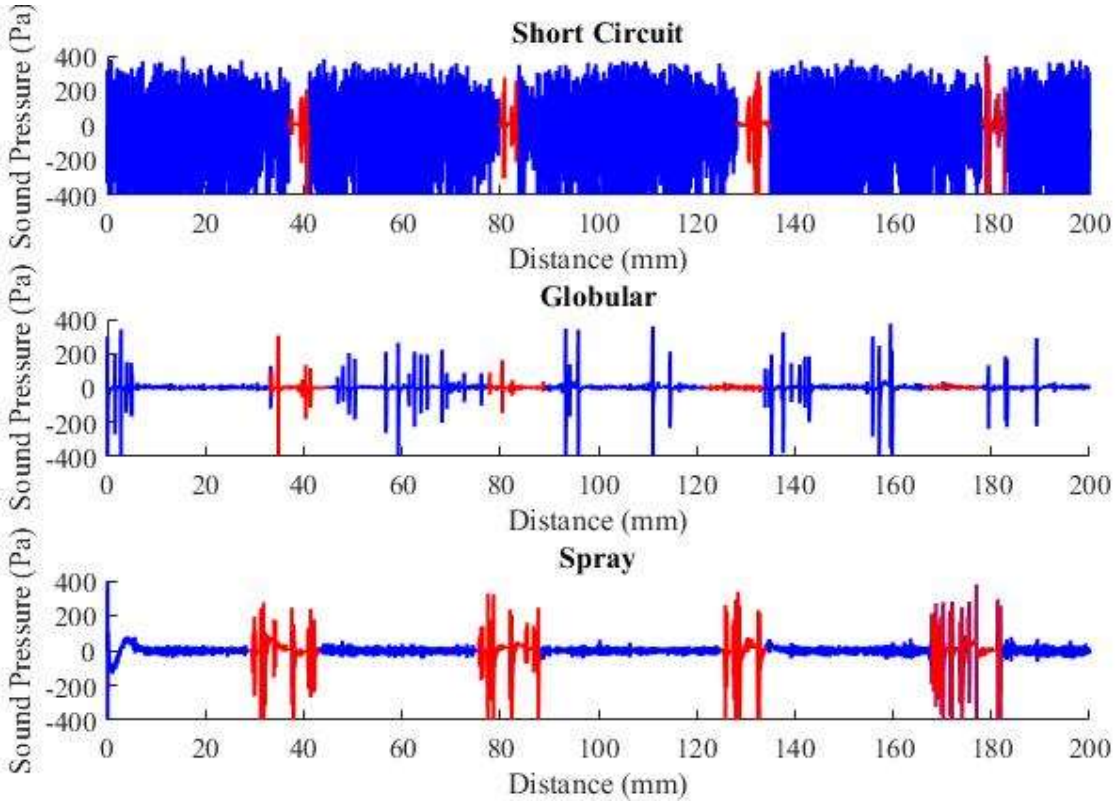

Figure 5.1 - Burn through occurrences under different transfer mode conditions

Similar to burn through, porosity generally coincides with a prolonged period of explosive, or erratic droplet transfer. Explosive transfer mode normally occurs as a symptom of additional active gasses being present within the weld pool and welding arc. This may be caused by contaminants present in the weld pool or insignificant shielding gas coverage, caused by either insignificant flow rate or external air flow blowing away the covering gas. While these disturbances may be visible under certain transfer modes such as spray and globular, they are much harder to detect in interchangeable and short circuit transfer modes as shown in **Figure 5.2** where the porosity event locations are displayed in red.

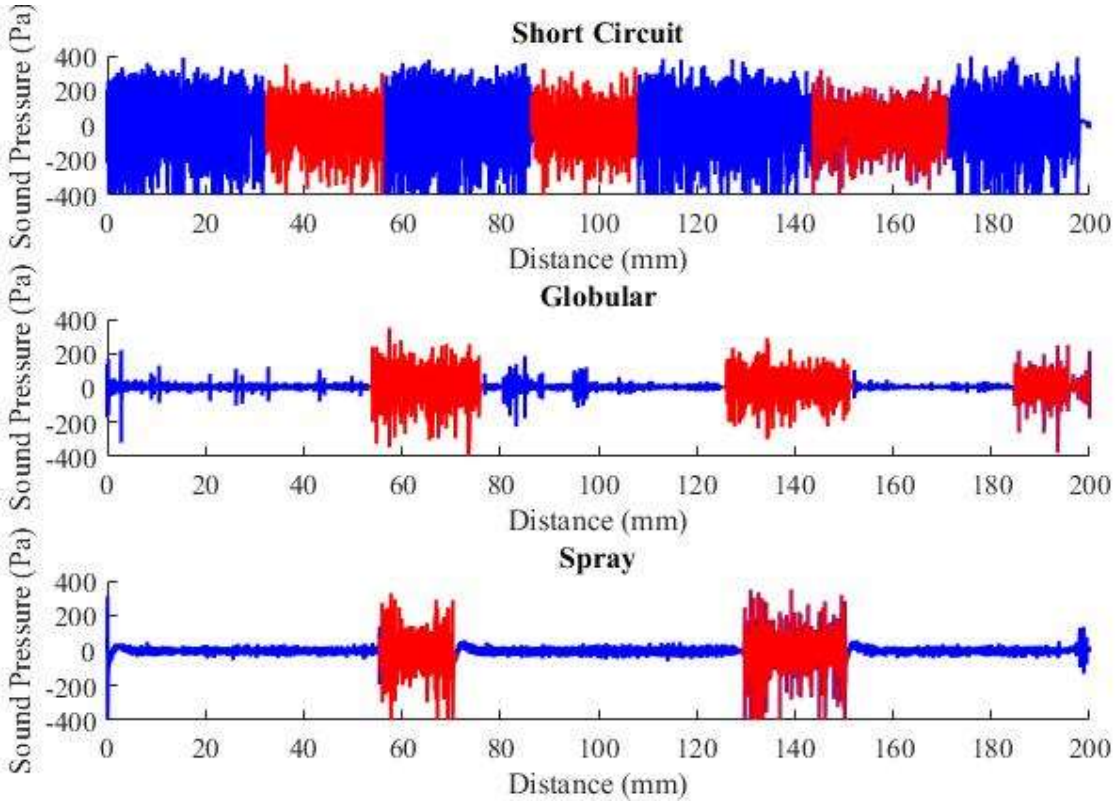

Figure 5.2 – Porosity occurrences under different transfer mode conditions

Due to this variance between different transfer mode signals, it becomes increasingly difficult to determine the locations of porosity and burn through universally for all transfer modes. For this reason, this chapter introduces a new method which uses prolonged periods in which no droplet is transferred as an indicator for detecting burn through and prolonged periods of explosive transfer for detecting porosity. To do this, the acoustic signal is first recorded alongside the welding process. As the signal is being captured, segments of the signal every 20 ms are analysed to determine the current transfer mode using the method introduced in **CHAPTER 4**. From here, the transfer mode of the segment is compared to previous segments and the average amount of time in which the signal spends not transferring droplets for burn through or transferring droplets explosively for porosity is calculated. This is achieved by calculating the moving average pulse width of a set window of previous segments. This moving average is then compared with a moving median threshold to determine if any defects are currently occurring in the forming weld bead. This process can be seen in **Figure 5.3**.

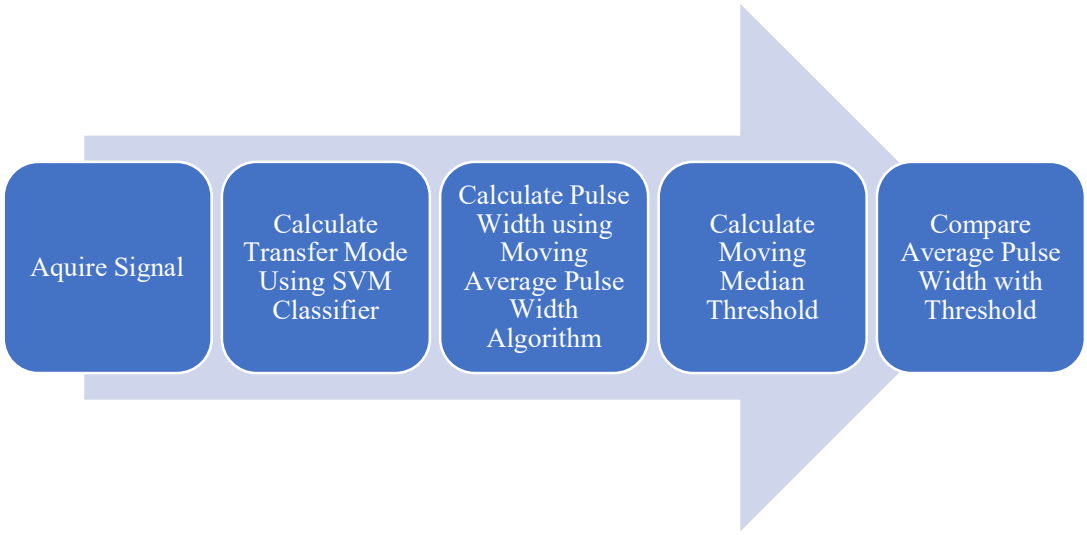

Figure 5.3 – Defect Detection Process Flow Chart

5.2.1. Signal Acquisition

To record the signals, experiments were performed using the test rig outlined in **CHAPTER 3**. Two different sets of tests were performed to accurately reproduce both burn through and porosity in pre-determined locations along the produced weld beads.

The first set of tests performed were designed to produce burn through in 4 pre-determined locations along a single weld bead. To do this, 8 individual welds were performed on 10 mm mild steel plates with 4 25mm x 8mm slots milled on the underside. Each of these slots effectively change the thickness of the material in predetermined locations along the weld path to deliberately cause the welding arc to burn through. This weld plate design was originally developed by [71] to be used for laser welding defect detection.

The second set of tests were performed to deliberately produce porosity along the weld bead profile in pre-determined locations. To do replicate porosity in the weld bead, another set of 8 welds were performed on 10mm mild steel plates. These performed welds however would have the gas flow rate stopped periodically throughout the welding process to emulate a scenario in which an inadequate amount of shielding gas is present around the welding arc. The settings used to record both sets of welds are outlined in **Table 5.1**.

Table 5.1 - Welding Parameters

Test Number	Defect	Transfer Mode	Gas Composition	Voltage (V)	Inductance (%)	Gas Flow Rate (L/min)	CTWD (mm)	Travel Speed (mm/s)	Wire Feed Rate (m/min)	Gun Angle
B1	Burn Through	SC	Mix	22	30	20	16	3.5	6.4	Push
B2	Burn Through	SC	Mix	24	30	20	16	3.5	6.4	Push
B3	Burn Through	SP	Mix	30	30	20	18	5.5	10.6	Push
B4	Burn Through	G	Mix	29	50	20	19	5.5	6.4	Push
B5	Burn Through	SC	Mix	22	30	20	15	5.5	7.1	Push
B6	Burn Through	SP	Mix	34	50	20	15	7	12.7	Push
B7	Burn Through	G	Mix	29	30	20	18	5.5	9.2	Push
B8	Burn Through	I	Mix	27	30	20	16	5.5	8.5	Push
P1	Porosity	SC	Mix	22	50	20	16	3.5	6.4	Push
P2	Porosity	G	Mix	30	50	20	19	3.5	7.1	Push
P3	Porosity	SP	Mix	34	0	20	18	7	12.7	Push
P4	Porosity	I	Mix	30	0	20	18	7	8.5	Push
P5	Porosity	SC	Mix	20	30	20	16	3.5	5	Push
P6	Porosity	G	Mix	29	0	20	18	5	6.4	Push
P7	Porosity	SP	Mix	30	0	20	18	7	10.6	Push
P8	Porosity	I	Mix	26	50	20	16	7	9.2	Push

All the tests were performed using 0.9 mm ER70S-6 welding wire and a mixed gas consisting of 93% argon, 5% carbon dioxide and 2% oxygen. Each test was performed under a different combination of parameters outlined in **Table 5.1** with the intention of replicating a range of different transfer modes with each weld bead being approximately 200 mm in length.

5.2.2. Segment Breakdown and Transfer Mode Classification

After recording the 16 different signals, each signal is broken down into smaller 20 ms segments. From here the transfer mode detection algorithm introduced in **CHAPTER 4** is used to classify each segment as one of either 5 categories: Short Circuit, Globular, Spray, Explosive, or No Transfer. After classification, the segments are then analysed using the Moving Average Pulse Width (MAPW).

5.2.3. Moving Average Pulse Width Algorithm

The MAPW algorithm operates by finding the average amount of time in which the welding process is currently in a state which may lead to the formation of a defect. For burn through this state is when no droplets are being actively transferred into the weld pool, while for porosity this state is when the welding process is currently in explosive transfer mode. To find the average length of time in which the process is in a defect state, the transfer mode of each segment can be checked. If the segment is found to be in a defect state, then it can be determined that a pulse is currently occurring and the pulse width vector, $P_{width} = 1$ and if found to not be in a defect state, $P_{width} = 0$.

If a pulse is found to be currently occurring, the MAPW algorithm then determines the width of the pulse by comparing the current value $P_{width}(k)$ to the previous values$P_{width}(k-1, k-2, \dots)$. The algorithm looks back at the previous values up until the point z in which P_{width} is equal to 0, then retroactively amends the values $P_{width}(z+1, \dots, n)$ to be equal to the width of the current pulse which is equal to $k - z + 1$.

The final part of the algorithm is to take the average of the values of P_{width} over a window of previous values w_{pw}. This process is illustrated in **Figure 5.4**.

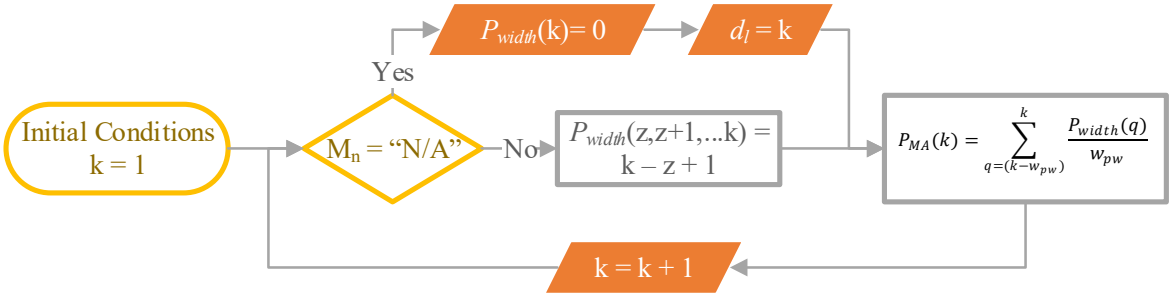

Figure 5.4 - Moving Average Pulse Width Algorithm using no droplet transfer as the defect criteria

where k is the current segment number, d_l is the location of the last droplet transfer, w_{pw} is the window width, M_n is the predicted transfer mode, P_{width} is the current pulse length, and P_{MA} is the moving average pulse width.

The results of the MAPW algorithm can be seen in **Figure 5.5** & **Figure 5.6** which show the comparison of the original signals, pulse widths, and their MAPW plots.

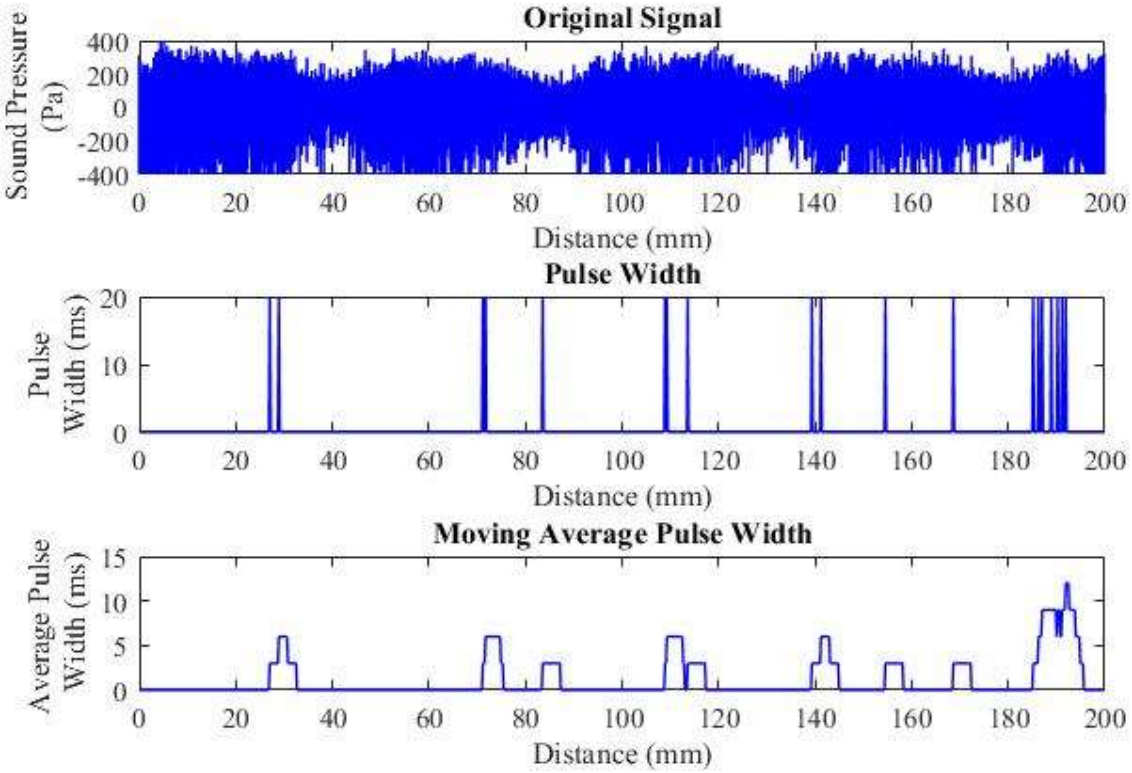

(a) Signal B1

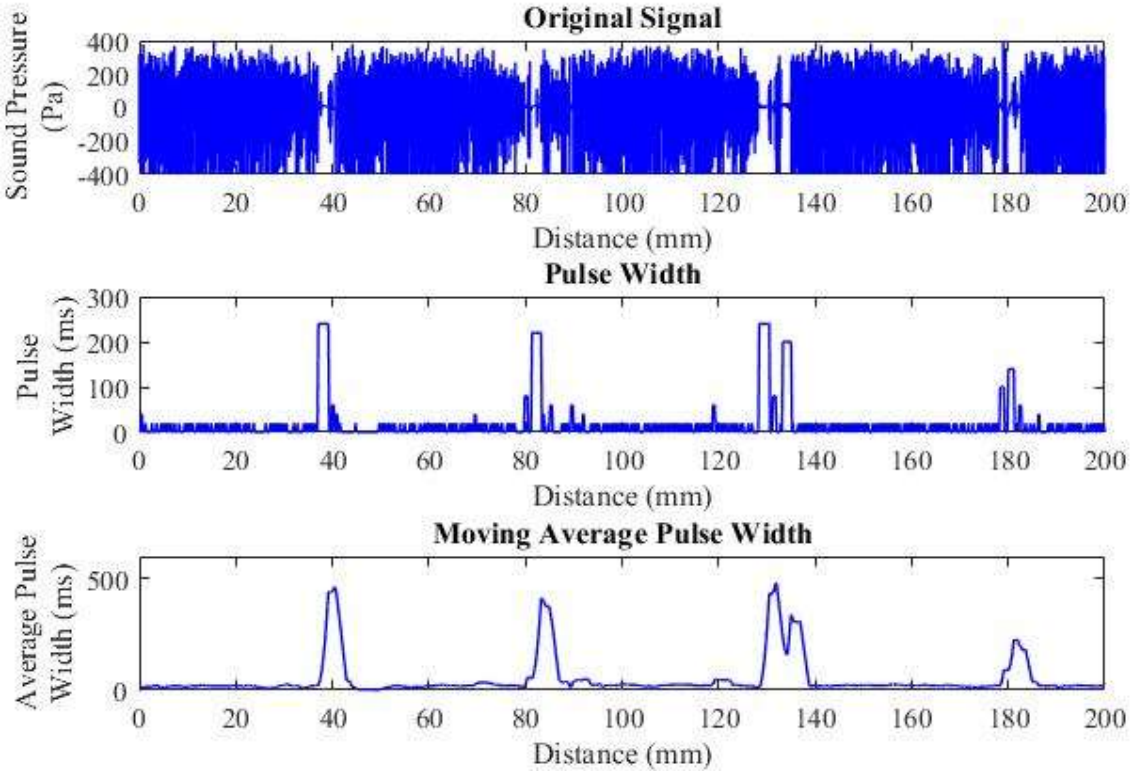

(b) Signal B2

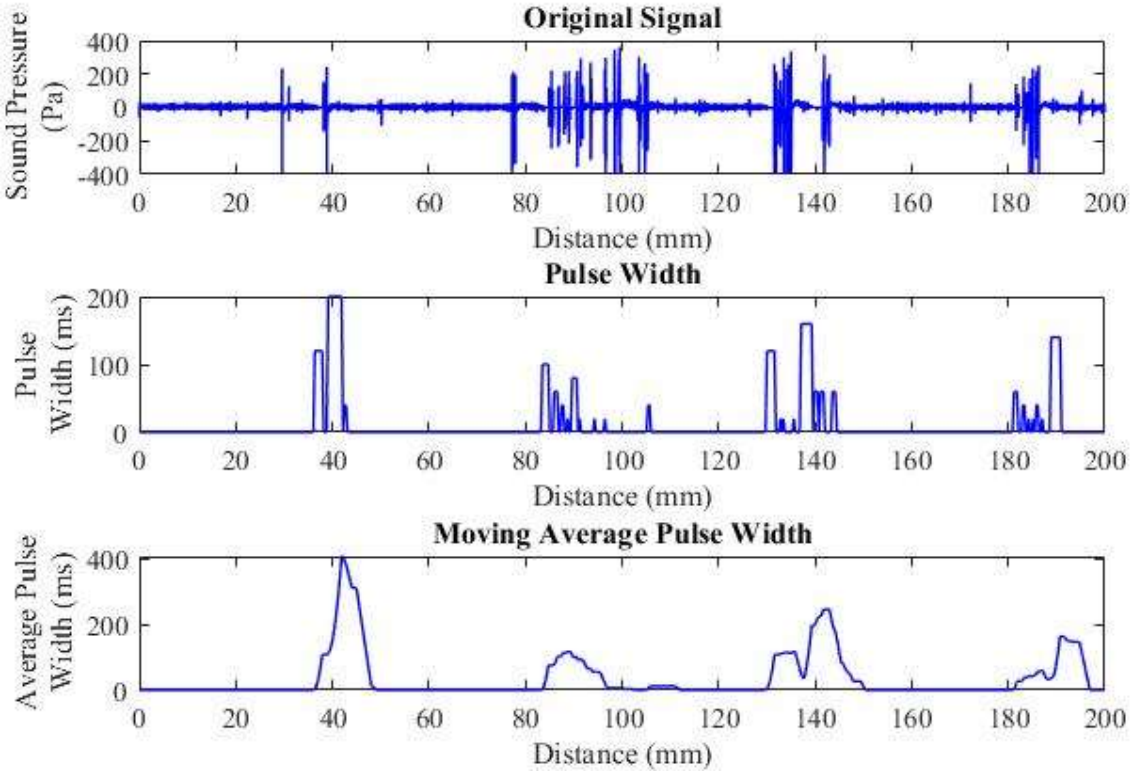

(c) Signal B3

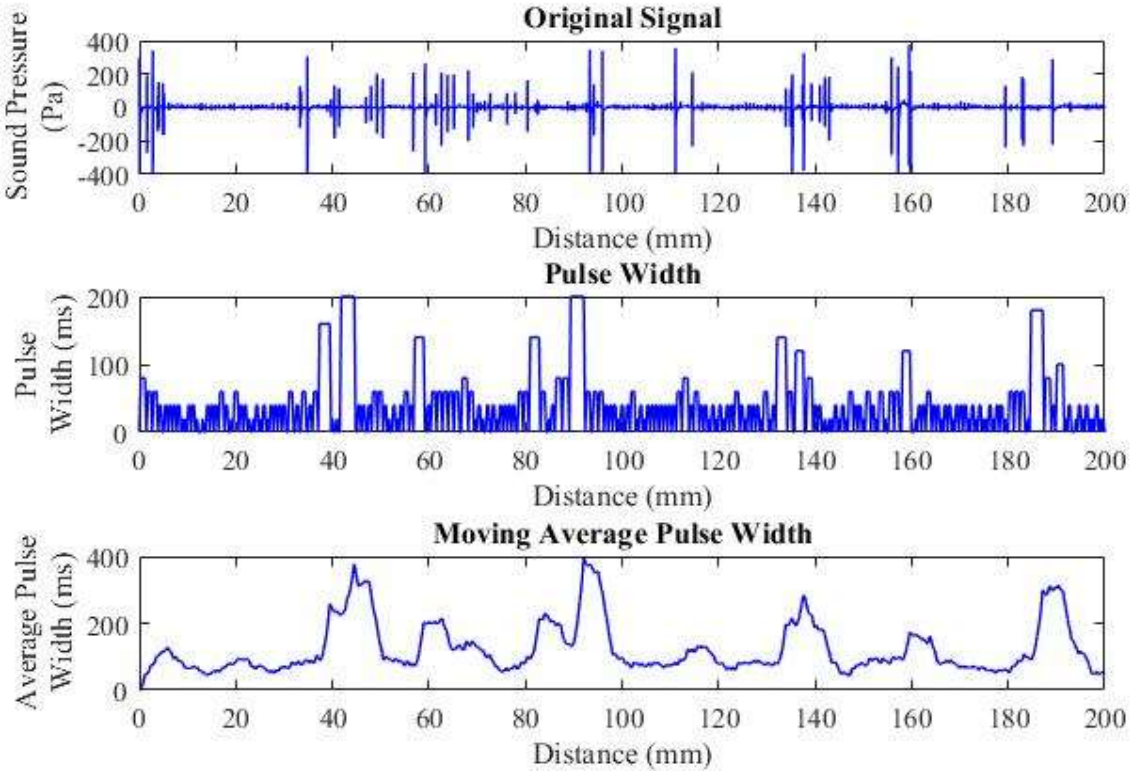

(d) Signal B4

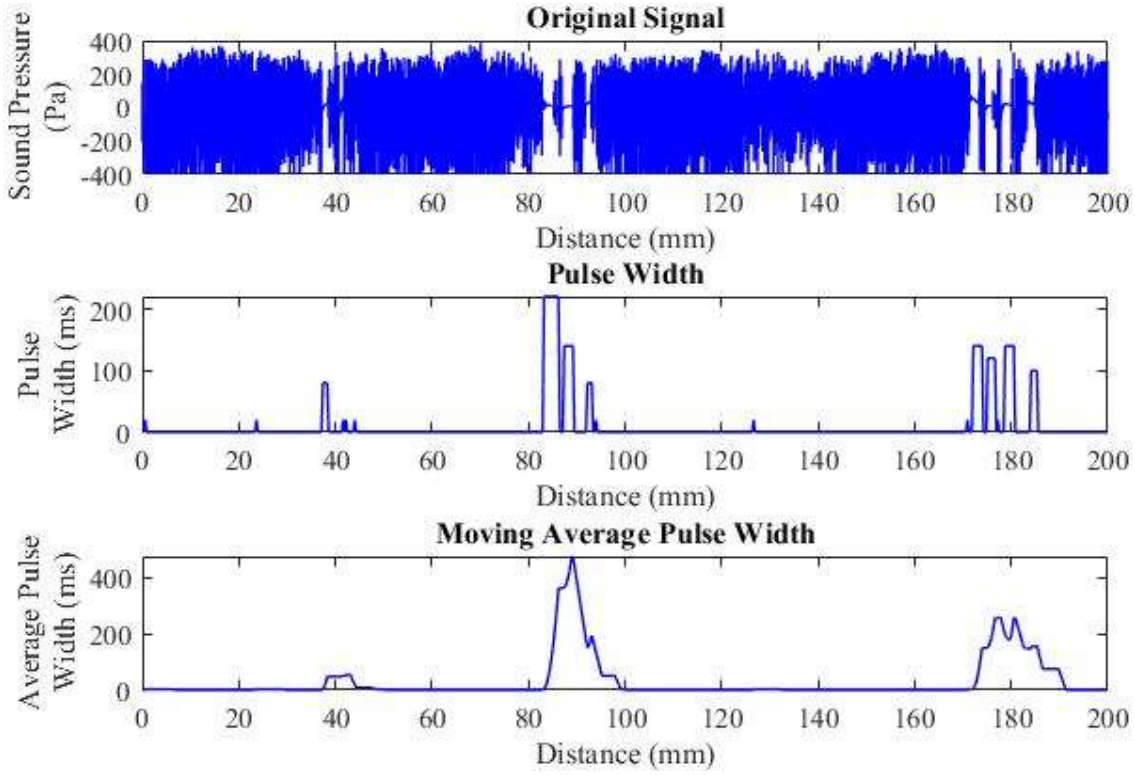

(e) Signal B5

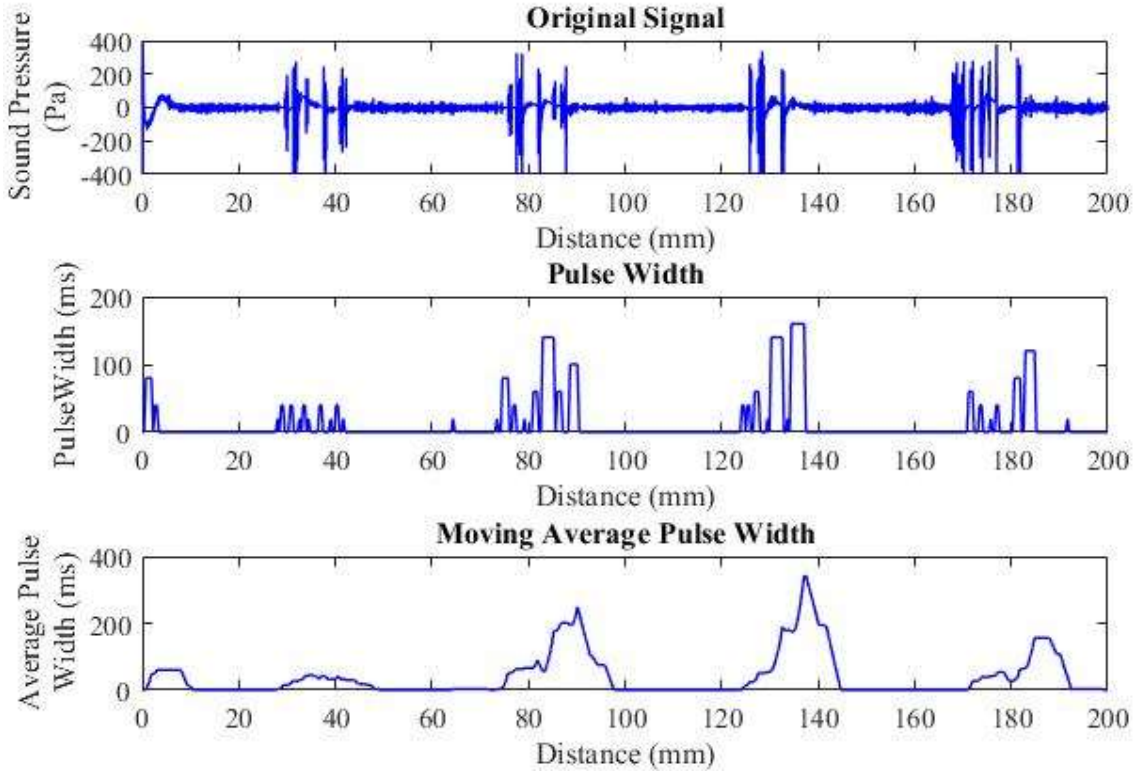

(f) Signal B6

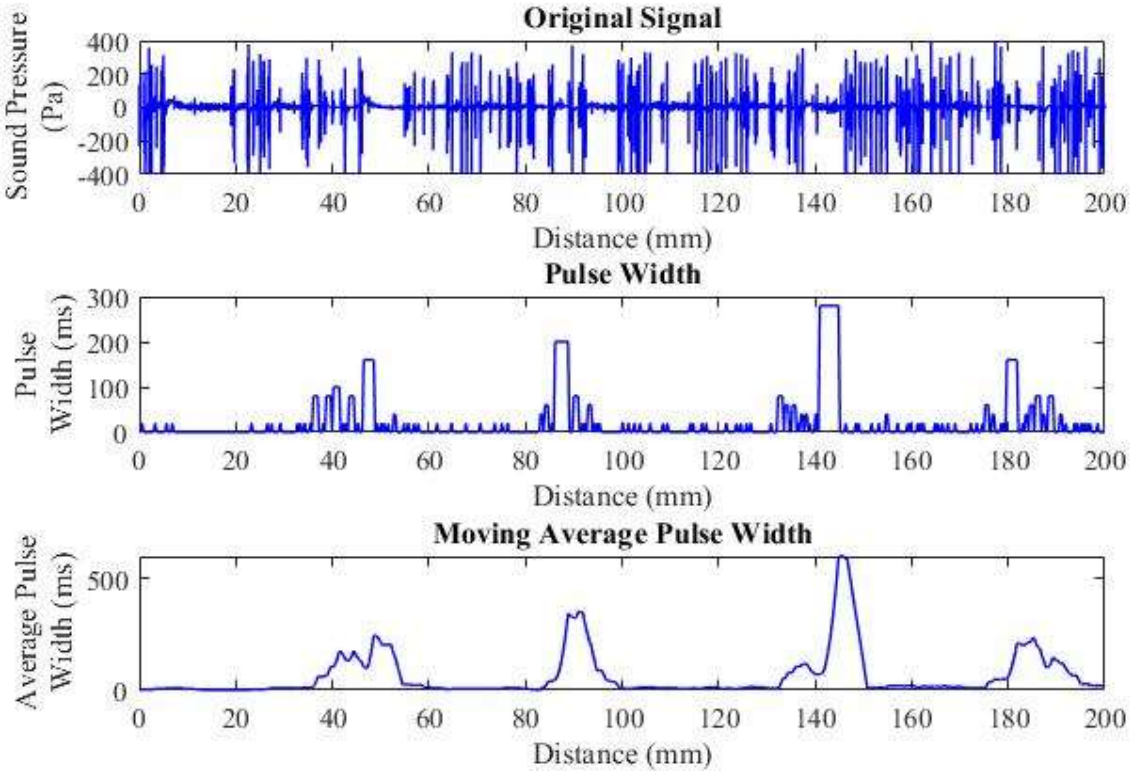

(g) Signal B7

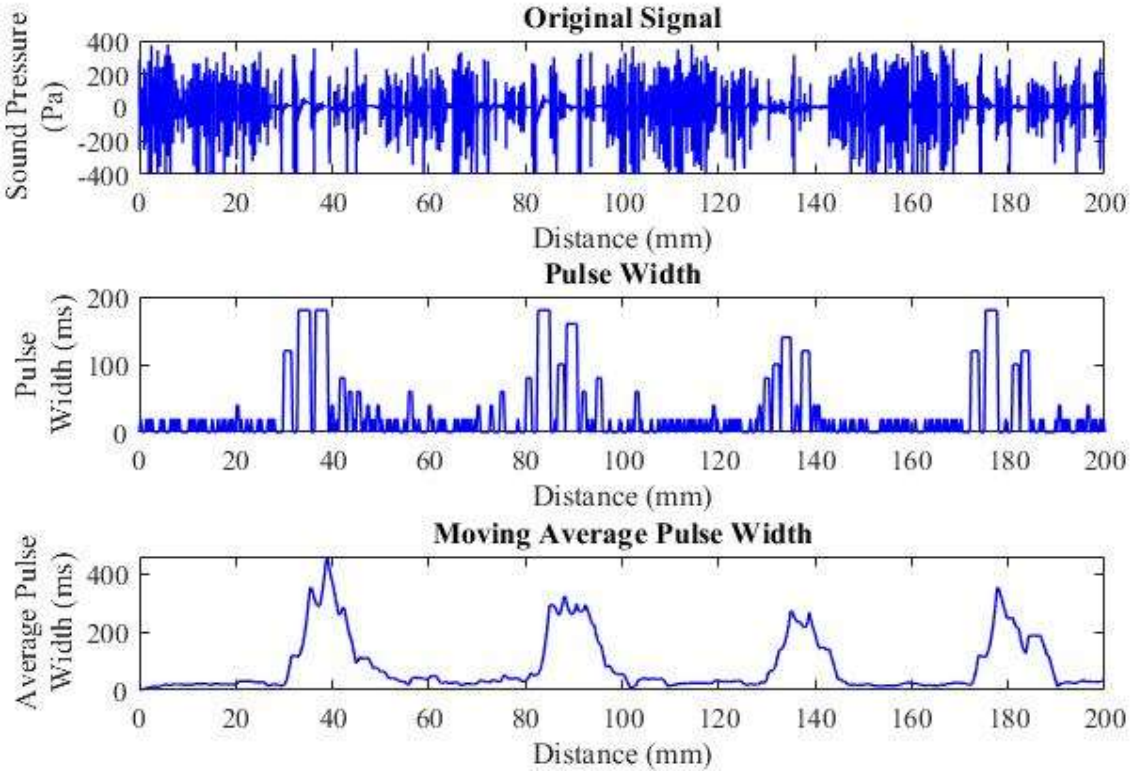

(h) Signal B8

Figure 5.5 (a-h) – Original vs Pulse Width vs MAPW Burn Through Signals

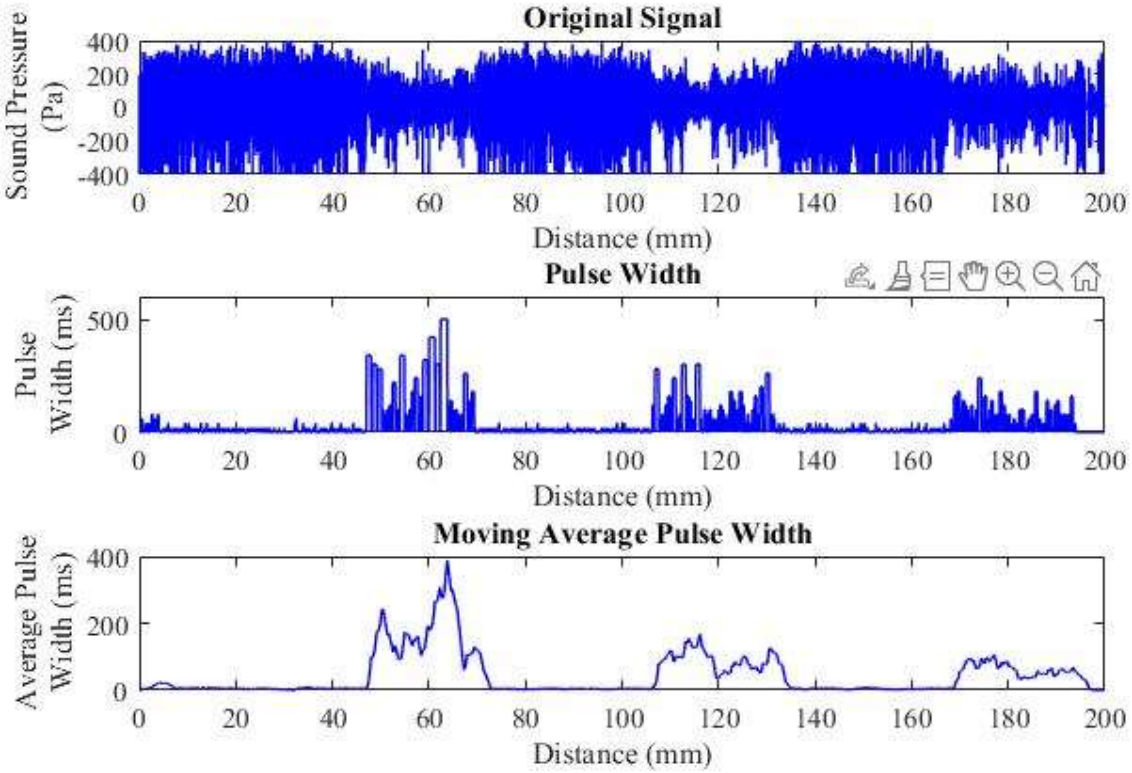

(a) Signal P1

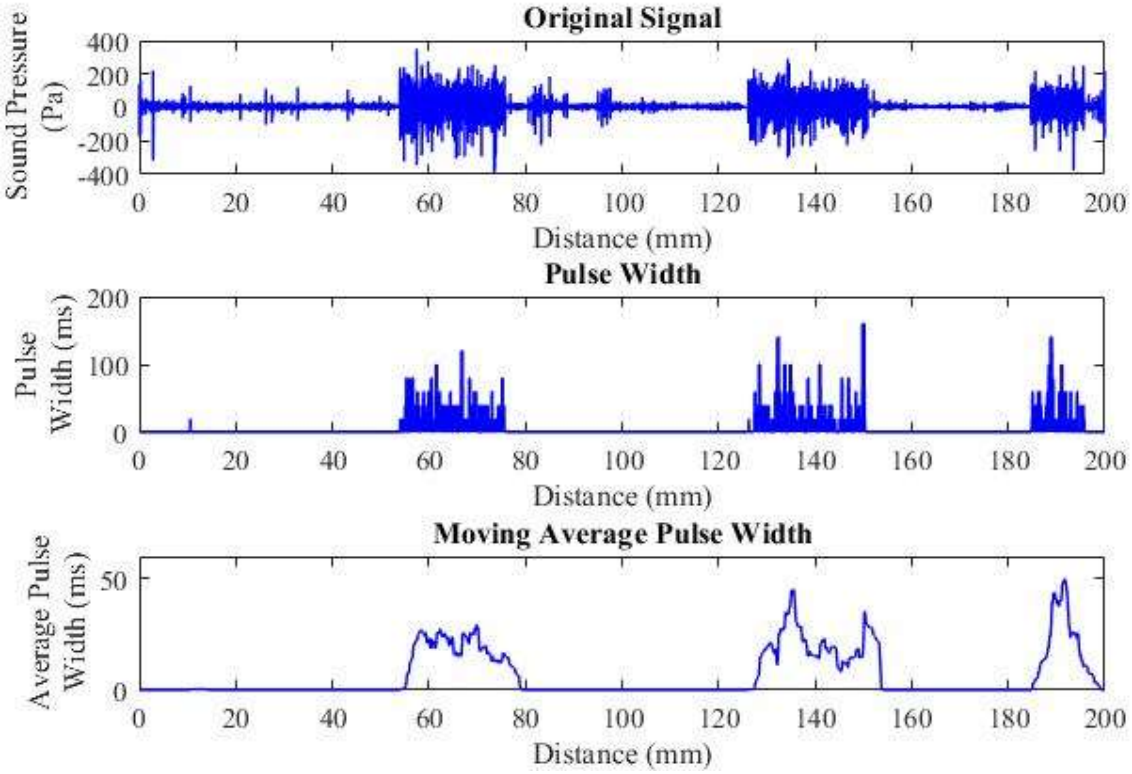

(b) Signal P2

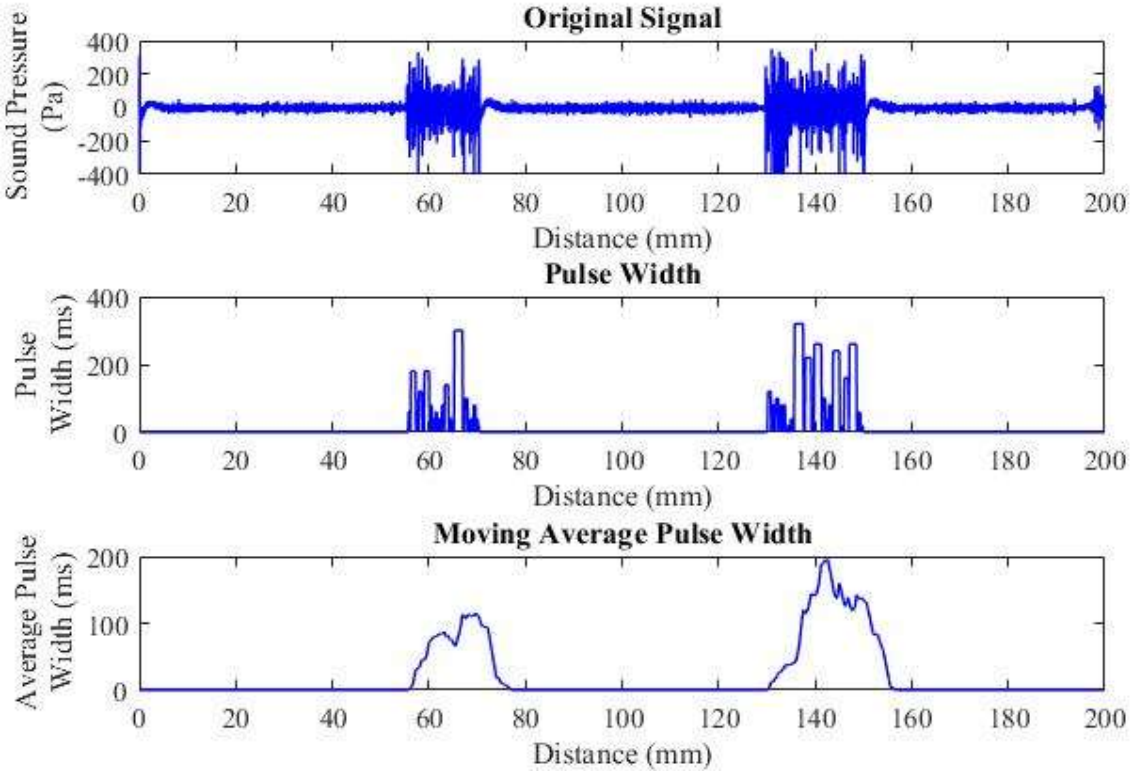

(c) Signal P3

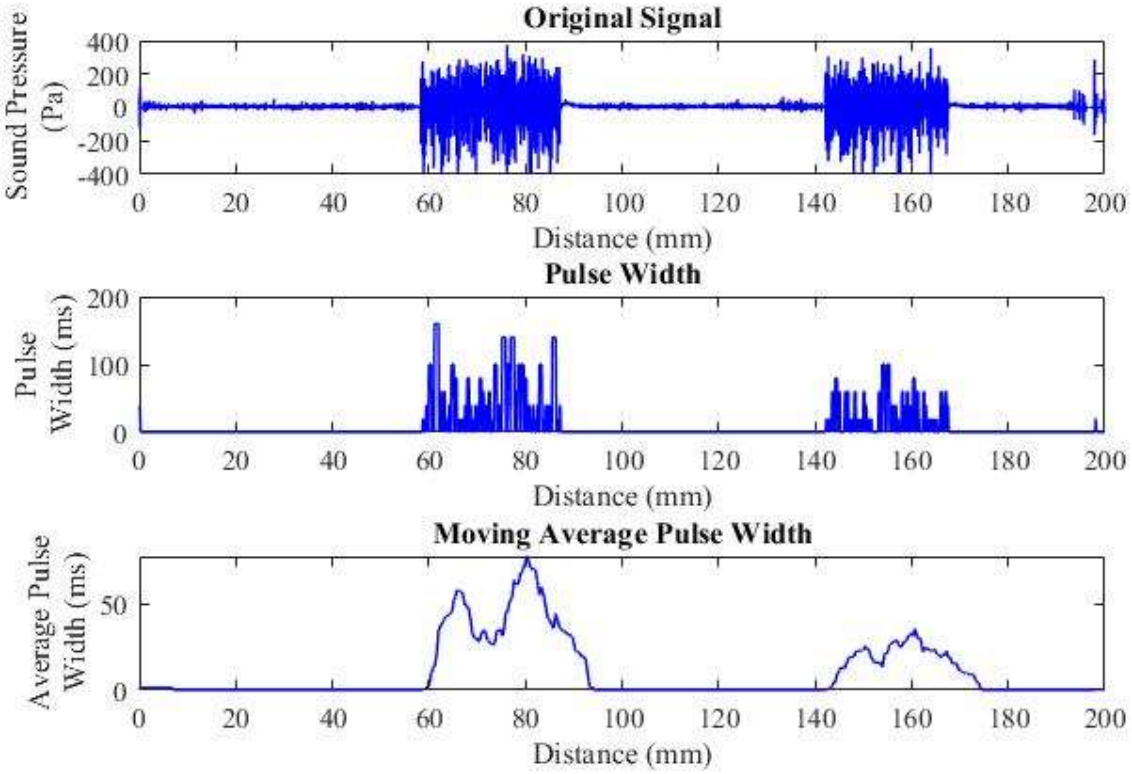

(d) Signal P4

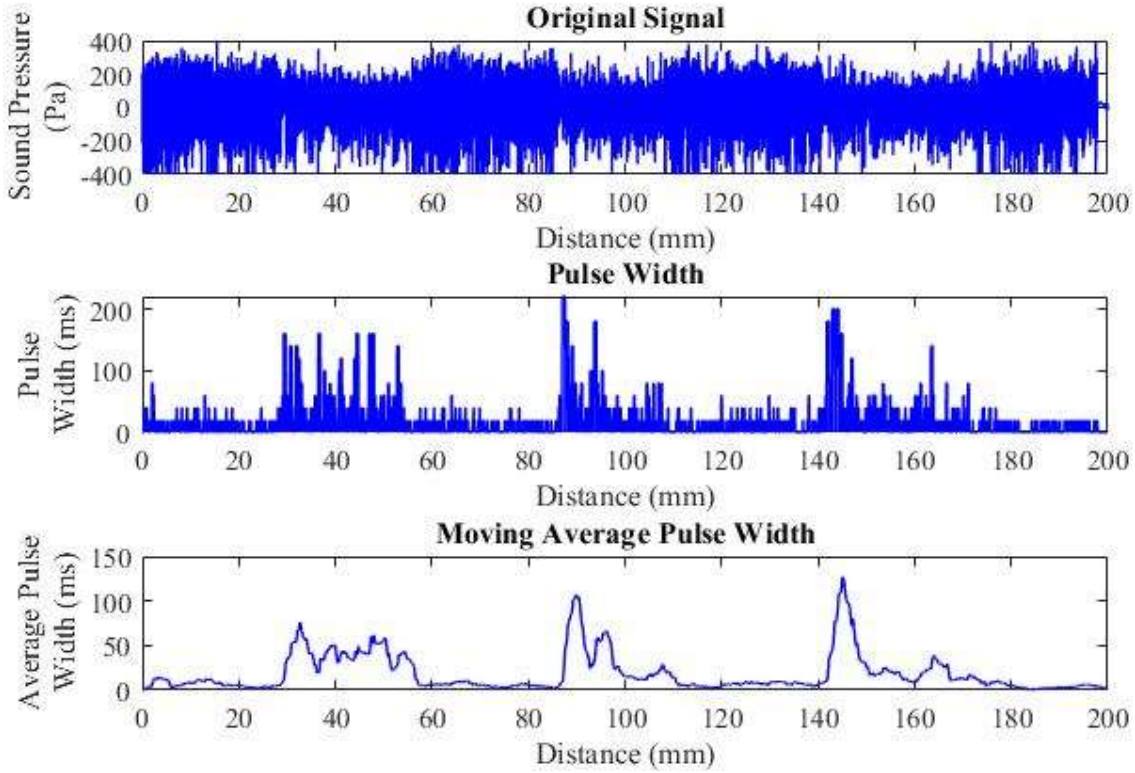

(e) Signal P5

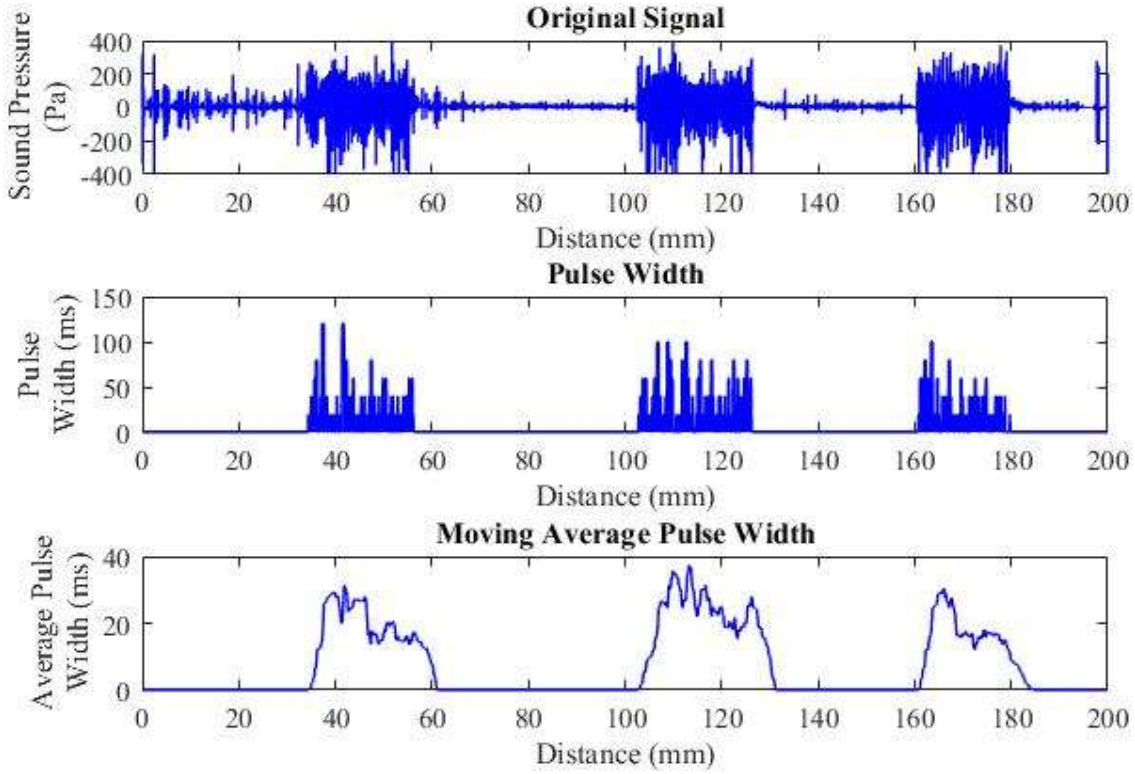

(f) Signal P6

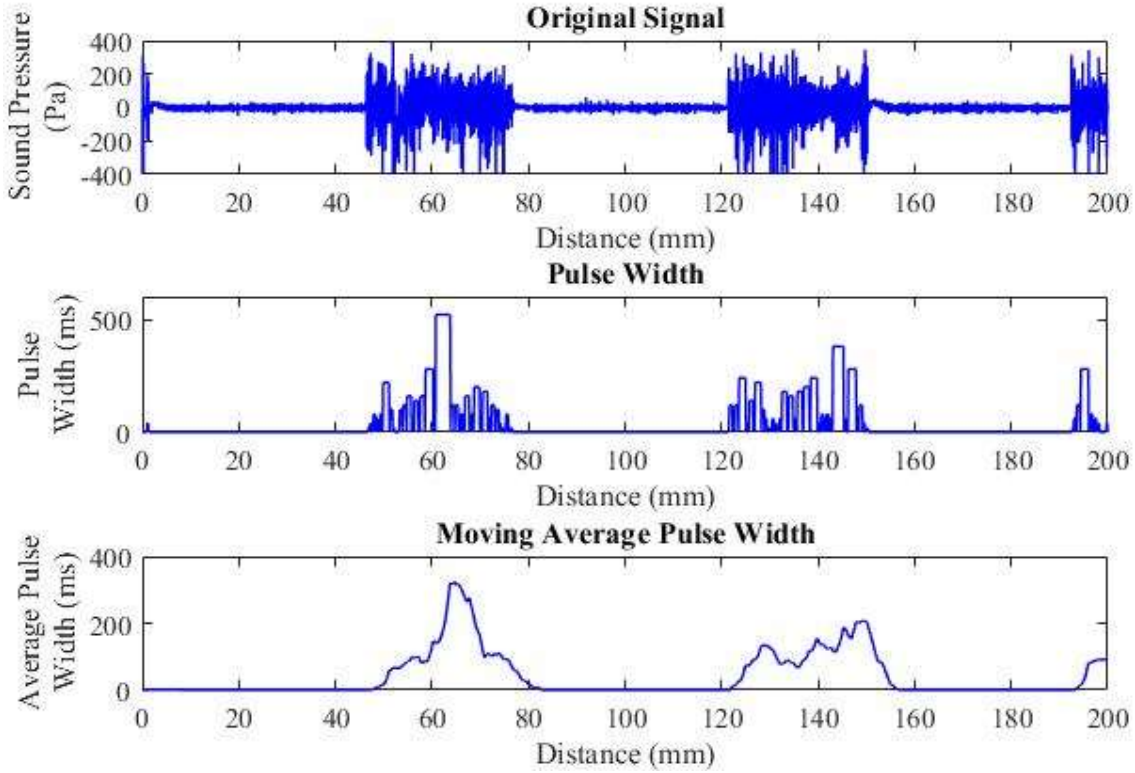

(g) Signal P7

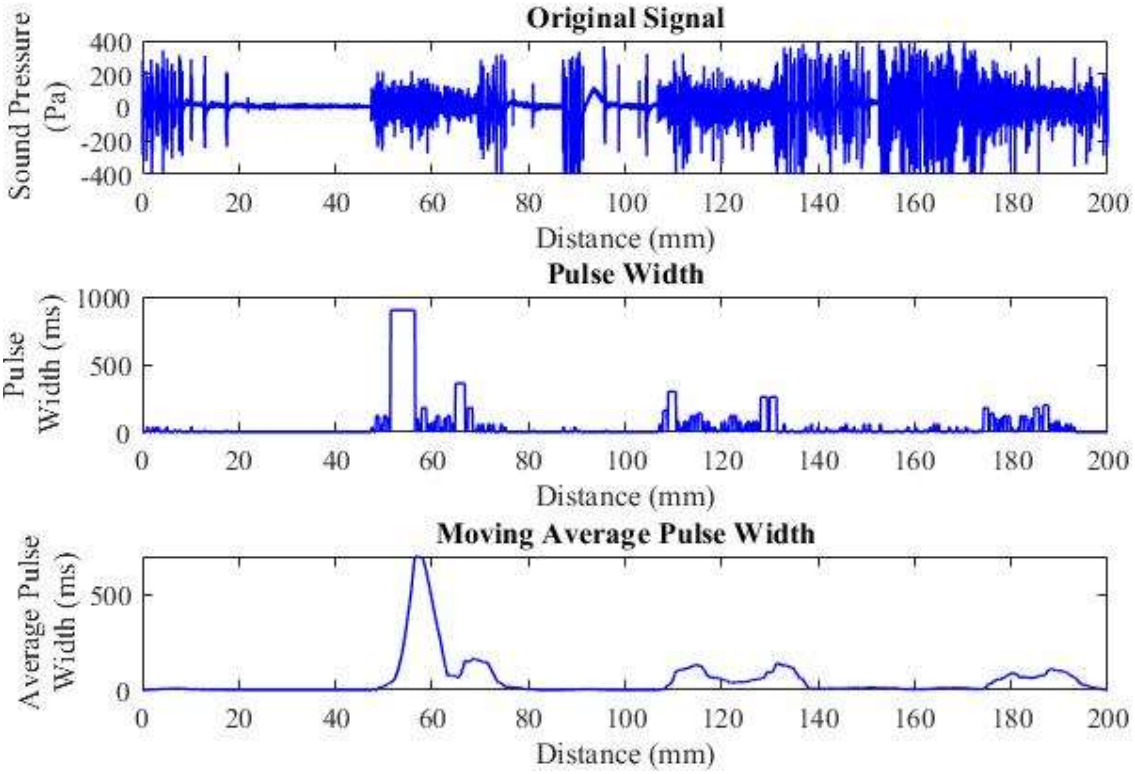

(h) Signal P8

Figure 5.6 (a-h)- Original vs Pulse Width vs MAPW Porosity Signals

5.2.4. Threshold Calculation

For the algorithm to be able to detect the presence of either burn through or porosity from the average pulse width calculation, a relative threshold needs to be implemented to filter out any false peaks from the data. As previously mentioned in **CHAPTER 2**, the frequency of droplet transfers is relative to the current transfer mode of the system. When analysing **Figures 5.5** and **5.6**, it can be seen that the base level of average pulse width varies between signals. Therefore a threshold relative to the current weld needs to be used. This can be done by using **Equation** 5.1.

$$T_{pw} = \begin{cases} median(2.5P_{\mathrm{MA}} + 20), & \text{Burn Through} \\ median(P_{\mathrm{MA}} + 12), & \text{Porosity} \end{cases} \quad (5.1)$$

where T_{pw} is the moving median threshold value.

The median value is taken in favour of the mean in order to minimise the impact that peaks have on the value of the threshold. The +20 and +12 values are also added to give the threshold a base value for cases such as B5 and B6 in **Figure 5.5** which has a base average pulse width value of 0.

While this threshold works well for the welds analysed in this chapter, it does have one major flaw. If the welding arc was to immediately start burning through the material or start transferring material explosively at the start of the welding process, the median pulse width value would immediately rise too high and would not be able to accurately detect the defect. Therefore a second static absolute threshold is also used to circumnavigate this issue. This value can be seen in **Equation** 5.2.

$$T_{Spw} = \begin{cases} 300, & \text{Burn Through} \\ 125, & \text{Porosity} \end{cases} \quad (5.2)$$

where T_{Spw} is the static pulse width threshold value.

The true threshold value is taken to be the minimum value of both T_{pw} and T_{Spw} as shown in **Equation** 5.3.

$$T_{Apw} = \begin{cases} T_{pw}, & T_{pw} < T_{Spw} \\ T_{Spw}, & T_{pw} > T_{Spw} \end{cases} \quad (5.3)$$

where T_{Apw} is the absolute moving median threshold value.

5.3. Results

Figures 5.7 to **5.9** show the resulting physical welds for both the burn through and porosity tests respectively. For the burn through plates in **Figures 5.7** & **5.8** the locations of each of the 4 burn through locations are marked as L1 to L4 respectively. It should also be noted that the welding arc did not successfully burn through the plate in locations L1 & L2 in weld B1.

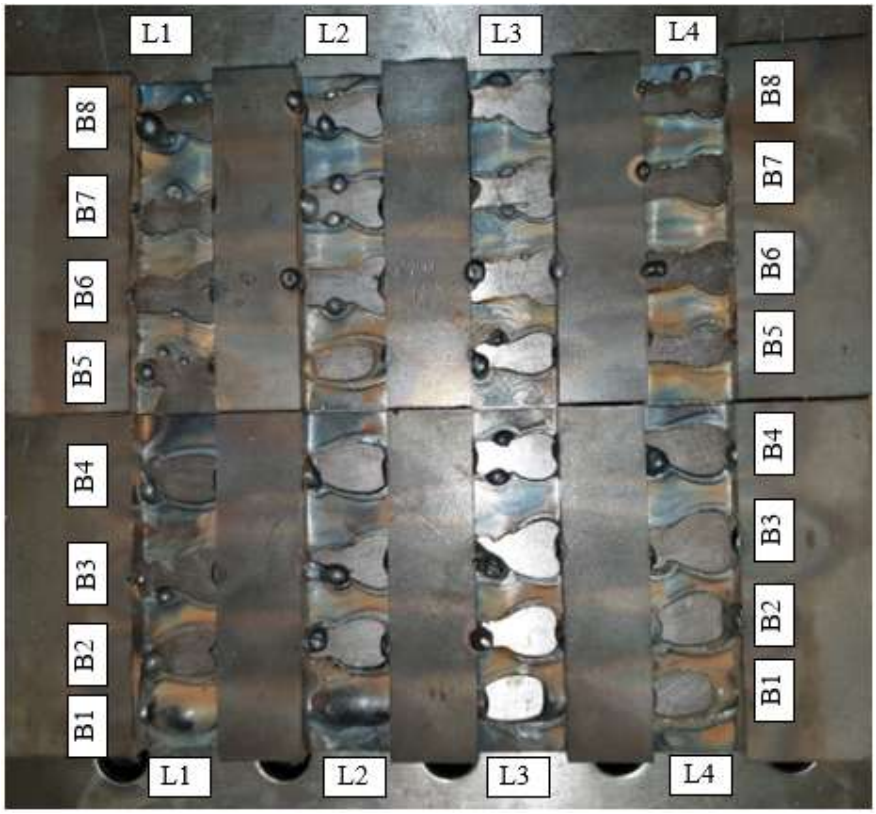

Figure 5.7 – Burn Through Plates Top Face

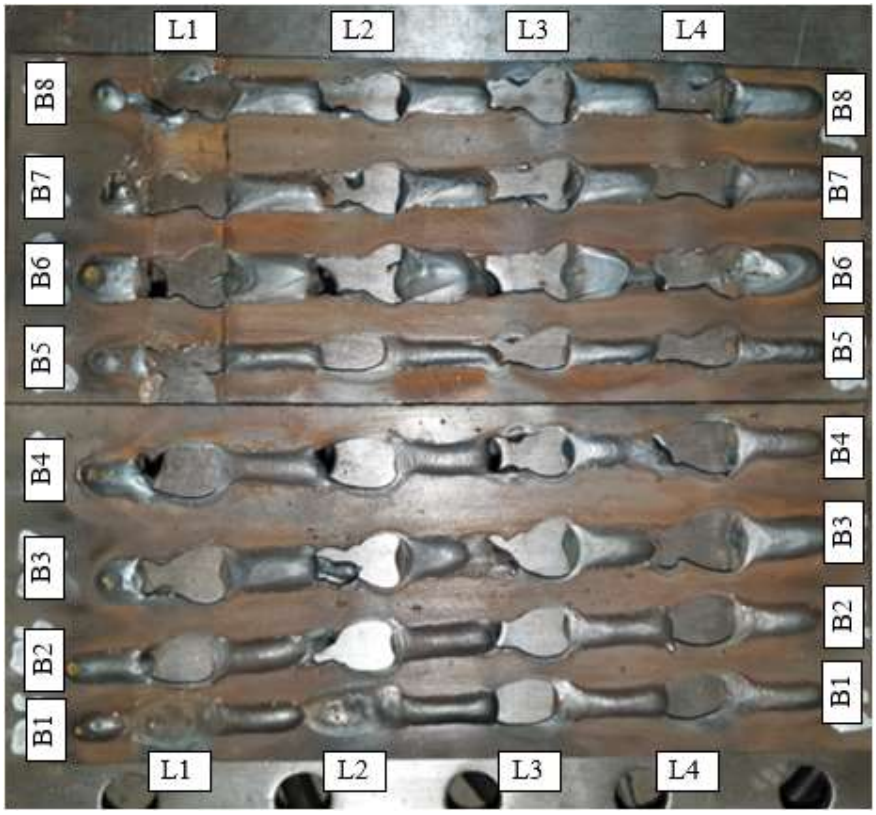

Figure 5.8 – Burn Through Plates Bottom Face

Figure 5.9 - Porosity Test Plates

Similarly, **Figures 5.10** and **5.11** show the final results of the defect detection algorithm for both the burn through and porosity tests respectively. In these figures, the blue line is used to represent the average pulse width value when the welding process is determined to be in a normal state, the green line represents the absolute moving average threshold value T_{Apw}, and the red line represents the locations in which the algorithm has detected the presence of either burn through or porosity.

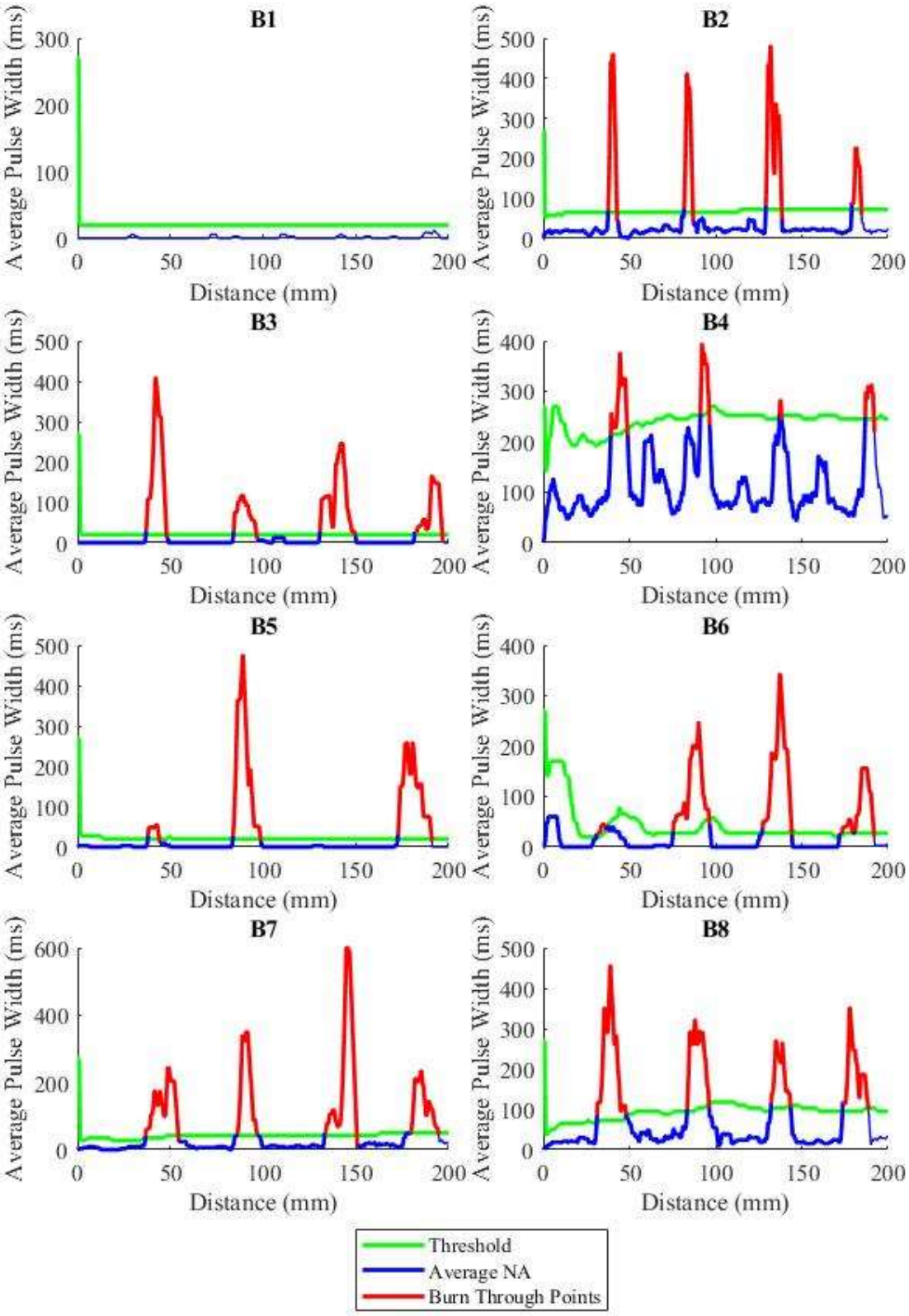

Figure 5.10 - Detected Burn Through Events using Median Threshold Value

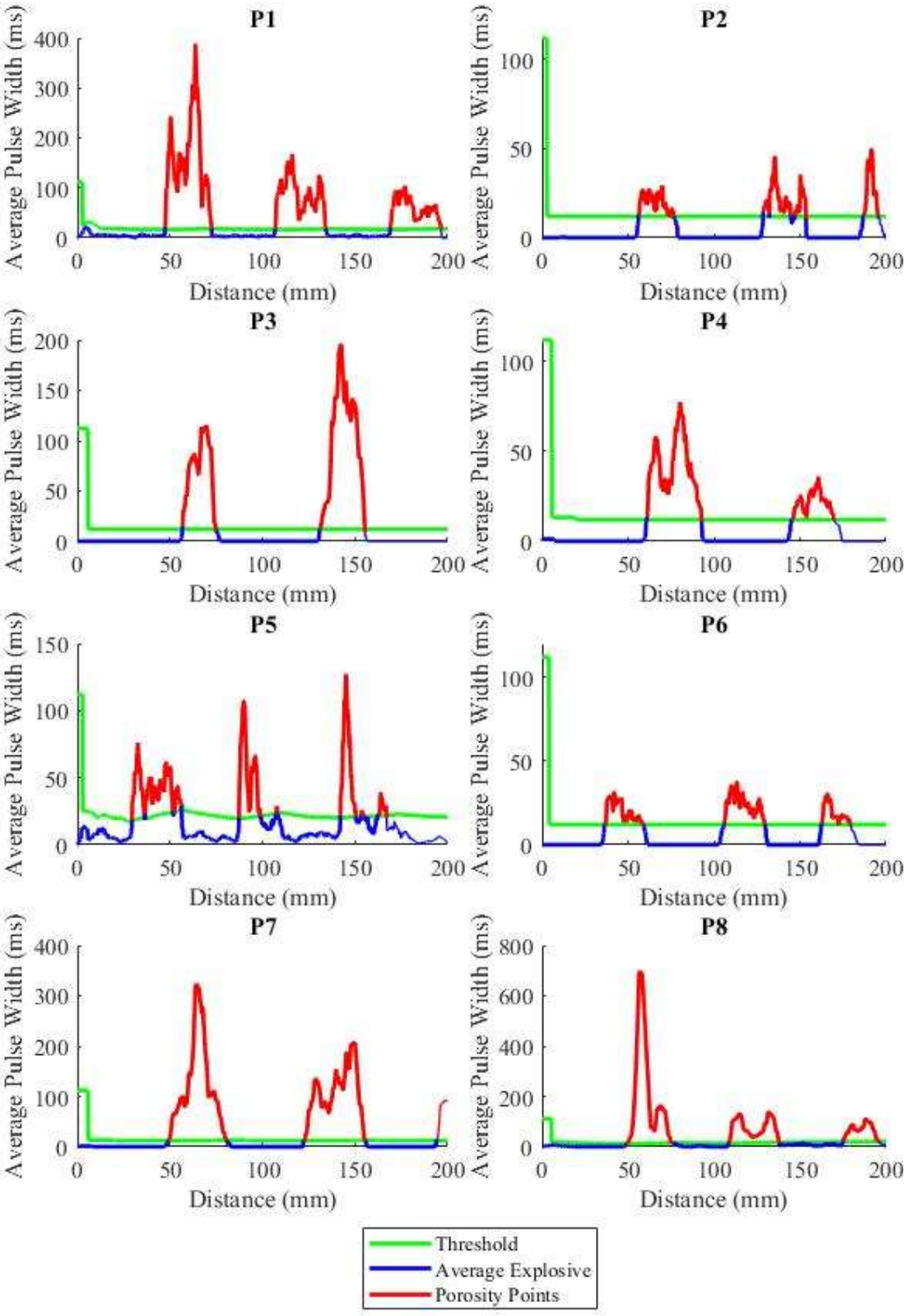

Figure 5.11 – Detected Porosity Events using Median Threshold Value

The locations detected by the defect detection algorithm shown in **Figures 5.10** and **5.11** can be compared to the locations on the test plates as seen in **Figures 5.7** and **5.9** respectively. From here it can be seen that the algorithm is able to accurately detect the location of 27 out of the 30 burn through events that occurred and all 22 porosity locations.

To understand why the algorithm missed 3 of the 30 burn through locations, the accompanying high speed videos for welds B1 and B5 where the 3 undetected burn throughs occurred (B1 L3 & L4, B5 L3) were analysed. When observing this footage however, it was found that the welding arc did not actually burn through the base material in these locations. While in **Figure 5.7** it can be seen that there is clearly a hole left in the material at these locations, it appears that these did not occur directly below the welding arc. It is theorised that the weld pool melted through the base material and collapsed after the welding arc had already advanced past the location. This was caused by both welds B1 and B5 being relatively low powered short circuit signals which did not have quite enough heat input to outright burn a hole straight through the base material. They did however have enough power to penetrate deep enough into the base material to create a sizeable molten weld pool. This weld pool with the addition of the added filler material, is theorised to be heavy enough to collapse the thin section of the base material and drip down after the welding arc had advanced. This theory is based on the presence of the failed burn through occurrences in weld B1 at locations L1 and L2 as shown in **Figure 5.8**. In both of these positions, it can be seen that the weld pool had started to drip down through the base material, however it resolidified before it could completely drip through.

It can also be seen when analysing the results in **Figure 5.10**, the algorithm is able to detect the presence of burn through regardless of the transfer mode. For example, take weld B4, which is a globular transfer mode. When observing its original time domain signal in **Figure 5.5**, it can be seen that there is no obvious disturbance such as increased peak amplitude or decreased peak frequency which are normally used as indicators in established detection methods. These results show a clear improvement over currently existing methods, allowing burn through to be detected under a wider range of conditions.

Figure 5.12 shows a breakdown of the first burn through occurrence L1 in weld B3 consisting of images of the electrode throughout the process.

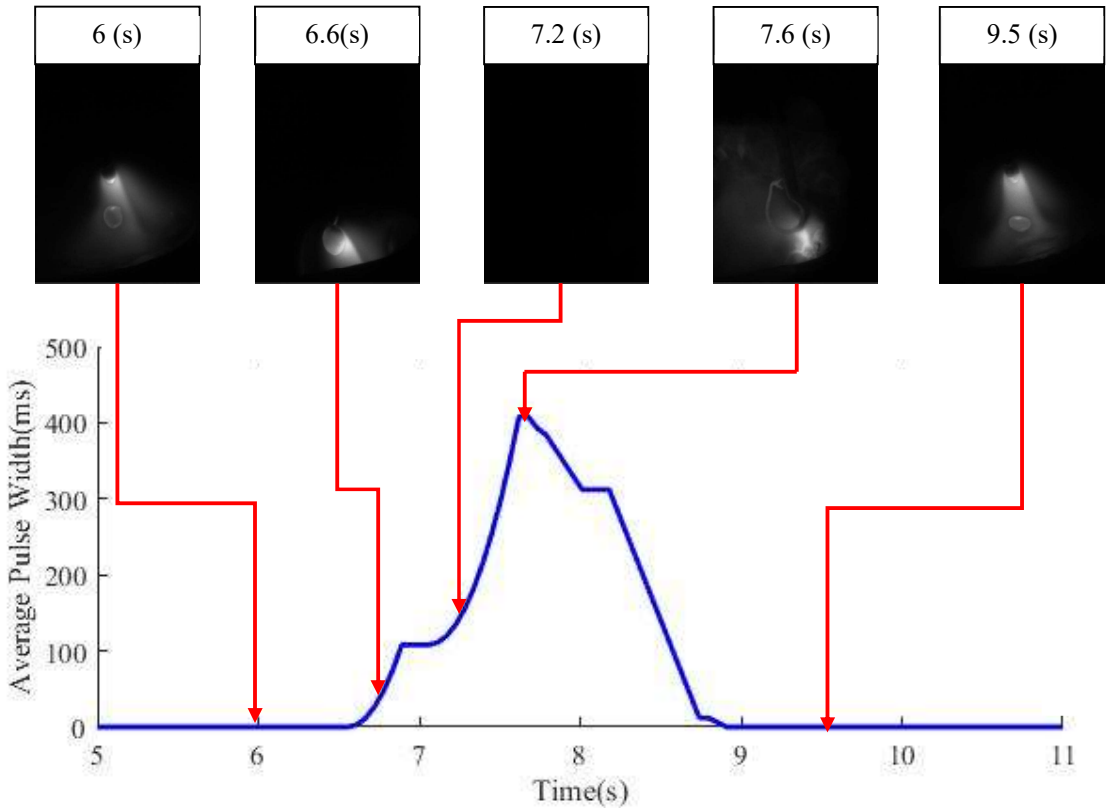

Figure 5.12 - B3 (Spray Transfer) 1st Burn Through Event

In **Figure 5.12**, it can be seen that prior to the burn through event, the welding process is currently in a low power projected spray mode, with several small droplets detaching from the end of the electrode. As there is a constant transfer of droplets, it can be seen that the average pulse width at this point is zero. At approximately 7 seconds the arc burns through the base material, and at 7.4 seconds it can be seen that there is no longer any material directly beneath the electrode. This leads to a change in the resistance of the arc column, effectively slowing down the transfer of the welding droplets. As no droplets are currently transferring at this point, the average pulse width value starts rising. At 7.8 seconds the electrode passes through the base material and the arc is completely extinguished, causing the average value to continue to rise. After a period of arc extinguishment, the electrode makes contact with the leading edge of the hole, re-establishing the welding arc. At this point the droplet transfer begins to restabilize and the weld can continue effectively.

It should be noted however that depending on the welding settings, the electrode may not fully pass through the burn through hole and reignite by touching the leading edge. In some cases, such as the slow globular transfer in B4, the end of the electrode does not move fast enough to fully travel through the hole and instead just slows down the droplet transfer while it is currently burning through.

One point of interest from this breakdown however is that the burn through process occurs along the leading edge of the peak, stating at around 7 seconds and finishing at the actual peak at approximately 8.2 seconds. However, using the detection algorithm, it detects the burn through occurrence about both sides of the peak. While not being a major issue, it should be noted however that there is a delay between the burn through event occurring and the algorithm being able to detect its presence.

5.4. Conclusion

In this chapter, a new real time GMAW defect detection algorithm based on the transfer mode monitoring was introduced. This algorithm is able to detect both burn through and porosity by analysing the average timespan in which the welding process is in no droplet, and explosive transfer modes respectively. 27 out of 30 burn through occurrences and 22 out of 22 porosity defects were successfully detected using the defect detection algorithm with no false positives occurring. The high accuracy and simplicity of the algorithm and measurement system excellent potential for the system to be implemented into real world automated welding systems.

This work has been published in a conference paper for the Australasian Congress of Applied Mechanics [82].

CHAPTER 6 – PENETRATION DETECTION

6.1. Introduction

In this chapter, a new GMAW penetration estimation system is introduced. Similar to the defect detection system in **CHAPTER 5**, this system is designed using the transfer mode detection algorithm introduced in **CHAPTER 4**. This penetration estimation system uses the aforementioned transfer modes to estimate the heat input into the weld pool. Using this, an average penetration depth for the weld bead can be accurately determined.

6.2. Background

As outlined above in **CHAPTER 2**, weld pool penetration is a critical feature in GMAW, being one of the principle components in determining the structural integrity of a weld. Currently to confirm that the penetration depth of the weld bead is satisfactory, specialised post production quality control checks are required. These tests such as ultrasonic and x-ray scanning are generally very expensive and time consuming [83], resulting in reworks of the welded part if the weld is deemed to have inadequately penetrated deep enough into the base material. This chapter aims to address this issue by introducing an online weld bead penetration estimation system similar to the defect detection system outlined above in **CHAPTER 5**. By using such a system, the weld bead penetration depth can be monitored in real time, allowing for parameters to be adjusted accordingly to guarantee the weld bead has adequately penetrated deep enough into the base materials.

In addition to these methods, there has been much research into measuring the penetration depth in similar automated welding procedures. One of the earliest attempts at monitoring weld quality using acoustic sensing was performed by [84] who used the variance of a segmented sound signal to monitor the weld bead penetration in GTAW. Another investigation performed by [85], where they used the power spectral density extracted from the acoustic signal to monitor the weld pool and in turn the penetration of the weld seam. [86] extracted the sound pressure deviation and band power to develop an artificial neural network to determine the penetration state of the weld bead. [87] also used the sound signal generated in pulsed GTAW to detect the penetration level of the weld bead using a dynamic long short-term memory (DLSTM) network model. [5] developed an online weld penetration detection system using neural networks based around the acoustic signal. [88] developed an algorithm based on the difference in sound pressures between partial and full weld bead penetration that was able to monitor penetration state of the weld seam in real time. [89] used a combination of sound, voltage and current to detect the penetration states in GTAW. [90] developed a penetration state detection system using a central auditory perception model based on the acoustic signal.

[91] looked into how transfer modes affect the penetration of the weld bead and was able to predict the penetration states for different transfer modes in GMAW using the welding current.

Other researchers have used Finite Element Analysis (FEA) and Computational Fluid Dynamics (CFD) calculations to estimate the penetration profile based on the welding input parameters.[92] developed a numerical model for mapping the weld pool growth and heat distribution in GMAW. [93] produced a CFD model for laser welding that was able to predict the penetration profile in laser welding. [94] used a FEA model to predict the heat distribution and penetration in thin welded plates. All these methods however require significantly longer processing times and are not ideal for use in a real time monitoring system.

Similarly, researchers have also looked into other methods of monitoring the penetration state in GMAW. [81] used ultrasonics and [95] used a combination of thermographic data, welding current and welding voltage to classify different penetration states in GMAW. Similarly, [96] developed a GMAW penetration detection system using dimensional and thermal sensor fusion. [97] developed an ANN to monitor the penetration state in multi-pass GMAW using the voltage, current and wire feed rate as input parameters. [89] developed a real time feature level data fusion model in order to predict the penetration states of weld seams in GTAW.

As GMAW arc heat input is critical in determining the penetration state, several researchers have investigated methods of measuring both the arc and droplet temperatures. [98] used optical emission spectroscopy to monitor the temperature of the welding arc under different transfer modes. [30] developed an image processing system to derive measurements of the surface tension, viscosity, density, and temperature of the molten droplet. [99] developed a two colour spectroscopy method using a high speed camera to monitor the temperature underneath the welding arc in globular transfer mode. [100] developed a vision system to measure the temperature and surface tension of the droplets in pulsed transfer mode. [101] developed a temperature measurement system using two colour pyrometry to measure the temperature of the welding droplet in globular transfer mode. [102] measured the weld pool temperature distribution in short circuit transfer using both a spectrometer and high speed video footage.

When analysing the existing literature, it can be seen that previous research tends to give a qualitative analysis of the penetration state instead of a quantitative measurement. In addition to this, most current methods only focus on one specific transfer mode, in particular short circuit transfer mode. Therefore, in the sections outlined below, a new method for estimating the penetration depth is developed. This new method aims to circumnavigate these problems by using the transfer modes themselves to estimate the penetration depth of the weld pool.

6.3. Methodology

As stated above, GMAW transfer modes are a good indicator of the intensity of the heat input in the system. Using this knowledge, an estimation for the penetration depth can be achieved using a combination of the welding travel speed, wire feed rate, and the Contact Tip to Workpiece Distance (CTWD), alongside information regarding the transfer mode. While the speed, feed rate and CTWD

can all be easily obtained from the input parameters in an automated system, the transfer mode cannot be directly determined from these parameters and is instead a dynamic process that can be affected by several uncontrollable factors. To detect the transfer modes in real time, the transfer mode detection algorithm introduced in **CHAPTER 4** is used.

To estimate the penetration depth of the weld bead, first the average cross sectional area is calculated using the wire diameter, wire feed rate and the welding travel speed. Using this, an average heat input can be calculated using the predicted transfer mode and the CTWD can be used to estimate how much of that heat penetrates into the base material. This is represented in **Equation** 6.1;

$$d_p = \frac{T_{avg} A_w C_s v_f}{{D_C}^2 v_s} \tag{6.1}$$

where d_p is the penetration depth, T_{avg}, is the average transfer mode coefficient in meters, A_w is the cross sectional area of the welding wire in meters squared, C_s is the scaling coefficient, D_c is the Contact Tip to Workpiece Distance (CTWD) in meters, v_f is the wire feed rate in meters/second and v_s is the wire feed rate in meters/second.

For this model, taking into account the segment time of 20 ms, the value for C_s is 1.43×10^5.

To determine the transfer mode coefficient above, T_{avg}, the transfer mode of the welding process needs to be analysed at 20 ms intervals for the duration of the welding process. From here a different value for T_{mc} can be calculated at each 20 ms interval depending on the detected transfer mode as seen in **Equation** 6.2.

$$T_{mc}(t) = \begin{cases} C_{sc}(t), & M_n(t) = "Short\ Circuit" \\ C_G(t), & M_n(t) = "Globular" \\ 2.2 + 1.2p, & M_n(t) = "Spray" \\ 1, & M_n(t) = "Explosive" \\ 0.2, & M_n(t) = "No\ Transfer" \end{cases} \tag{6.2}$$

where T_{mc} is the transfer mode coefficient in seconds, C_{sc} is the weighted short circuit transfer mode coefficient, C_G is the weighted globular transfer mode coefficient, C_{sp} is the weighted spray transfer mode coefficient, and p is the previous number of "No Transfer" Segments directly before segment number k.

These 5 possible conditions are explained in the subsections below.

6.3.1. Short Circuit Transfer

As outlined in **CHAPTER 2**, short circuit transfer mode involves the wire electrode melting at a rate slower than the wire feed speed, resulting in the wire electrode contacting the weld pool. This process creates a short circuit, in turn leading to a significant increase in current causing the wire to neck and snap due to the pinch effect. However as the welding heat input is increased, the electrode will start to melt at a much faster rate causing a large droplet to form at its tip. If the electrode wire feed speed is taken as a constant rate, the time interval between short circuit transfers should increase relative to the

heat input into the weld. This can be seen in **Figure 6.1** which shows the effects of increased heat input on short circuit transfer mode.

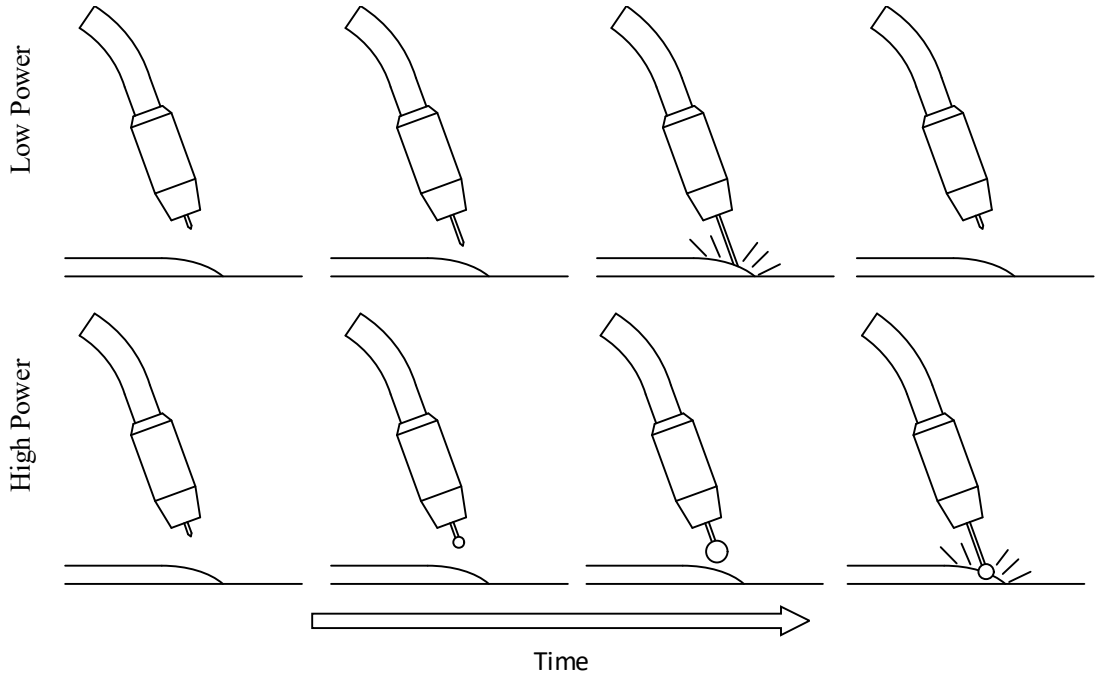

Figure 6.1 - Short Circuit Power Comparison

Using this observation, it can be assumed that T_{mc} for the short circuit mode should increase as the period between short circuits increases, corresponding to a larger heat input. This can be calculated in **Equation** 6.3.

$$C_{sc}(t) = \begin{cases} 1, & p = 1 \\ (C_{sc}(t-1) + 0.15)^2, & 1 < p \leq 3 \\ 5.4743, & p > 3 \end{cases} \quad (6.3)$$

6.3.2. Globular

With globular transfer mode, the welding wire melts fast enough relative to the feed speed as to not touch the weld pool and short circuit, causing a large globular droplet to form on the end of the electrode. When this droplet becomes large enough, gravity will detach it from the end of the electrode and it will fall towards the weld pool. In this mode, as the welding current and heat input increases, the frequency of the droplet detachment also increases due to the increased electromagnetic force helping detach the droplet. Therefore unlike short circuit mode, T_{mc} for globular transfer mode increases linearly as the period between droplet transfers increases as seen in **Figure 6.2**.

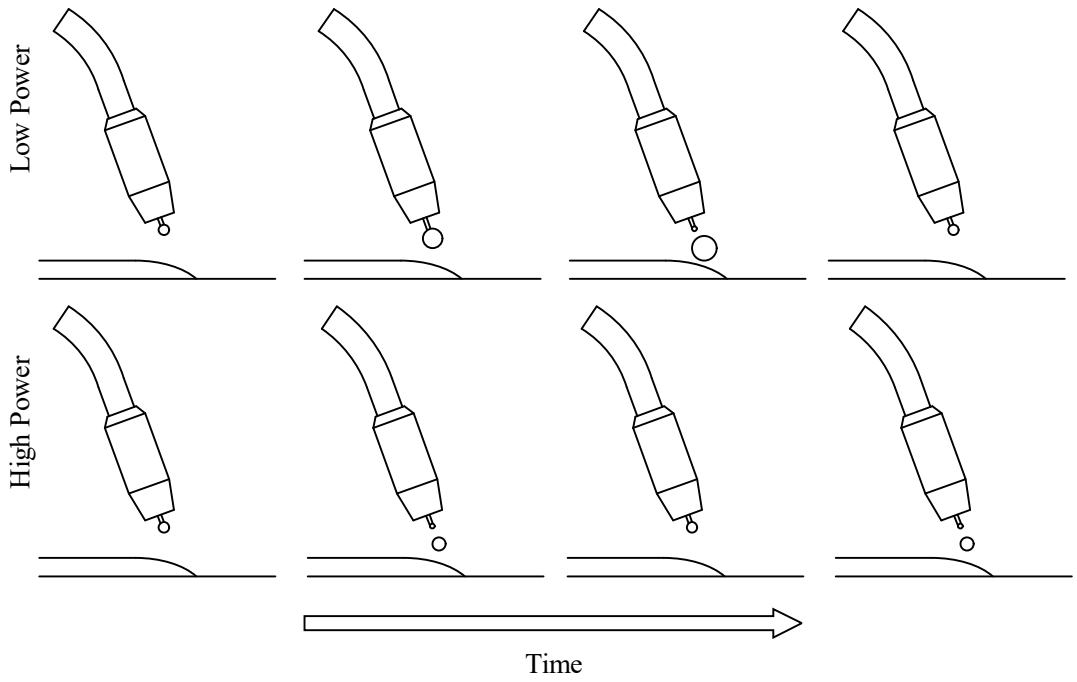

Figure 6.2 – Globular Power Comparison

As outlined in **CHAPTER 4**, it can be difficult to clearly differentiate globular and spray transfer modes when they are close to the transition zone between the two. Because of this, the current 20 ms segment can be compared with a set of previous segments to more accurately predict the heat input when the system is predicted to be in globular transfer mode. If previous segments are determined to be spray transfer mode, then it is determined that the system is currently in a very low power spray transfer mode. If previous segments are found to be all globular transfer modes, then it is determined that the system is in a high power, high frequency globular transfer mode. These additional criteria can be seen in **Equation** 6.4.

$$C_G(t) = \begin{cases} 2, & \left(\sum_{k=p-5}^{p} M_n(k) == "Spray"\right) > 2 \\ 1.8, & \left(\sum_{k=p-5}^{p} M_n(k) == "Globular"\right) == 5 \\ 1.4 + 0.9p, & p \geq 0 \end{cases} \tag{6.4}$$

6.3.3. Spray

Similar to globular transfer mode, spray transfer mode occurs when the electromagnetic force is high enough to rapidly spray small droplets from the end of the wire electrode. In this mode, a high constant base value for T_{mc} is used due to the high base heat input associated with spray transfer mode. However, since several droplets are expected to be transferred per every 20 ms segment, a small linear increase is used similar to globular transfer for when there is a period of no droplet transfer. This is due to a period of no droplet transfer occurring while the process is currently in spray transfer normally corresponding

to a change in transfer mode, as a period of no droplet transfer is not to be expected during spray transfer. This value for spray transfer can be seen in **Equation** 6.5.

$$C_{Sp}(t) = \begin{cases} 2.2, & p \geq 0 \\ 2.2 + 1.2p, & p \geq 0 \end{cases} \quad (6.5)$$

6.3.4. Explosive and No Transfer

Explosive or gasless explosive transfer is normally a result of some form of contamination in the base material or the welding gas. For the purpose of this model, T_{mc} for explosive transfer mode is given a flat value of 1. Similarly if no droplet transfer has been detected, T_{mc} is given a value of 0.2.

6.4. Experimental Set up

To test the methods introduced in this chapter, 16 bead on plate welds were performed to replicate 5 different transfer modes which can be seen in **Figure 6.3**. Each of these weld beads were approximately 200 mm in length with the welding parameters of each bead being outlined in **Table 6.1**. For all the performed welds, 0.9 mm diameter er70s-6 type welding wire was used in combination with a welding gas consisting of 93% argon, 5% carbon dioxide and 2% oxygen. All of the welds were also performed on 10 mm mild steel plates.

Figure 6.3 - Weld Bead Profiles

Table 6.1 - Welding Parameters

Test Number	Transfer Mode	Gas Composition	Voltage (V)	Inductance (%)	Gas Flow Rate (L/min)	CTWD (mm)	Travel Speed (mm/s)	Wire Feed Rate (m/min)	Gun Angle
1	SC	Mix	20	30	20	16	3.5	4.85	Push
2	SC	Mix	18	0	20	16	3.5	4.36	Push
3	SC	Mix	22	50	20	15	3.5	5.54	Pull
4	SC	Mix	20	30	20	15	3.5	6.33	Pull
5	SP	Mix	30	0	20	18	7	9.31	Push
6	SP	Mix	28	0	20	18	7	8.74	Push
7	SP	Mix	34	0	20	18	7	11.4	Pull
8	SP	Mix	30	0	20	18	7	9.31	Pull
9	G	Mix	30	0	20	16	5.5	5.54	Push
10	G	Mix	30	50	20	18	5.5	6.06	Push
11	G	Mix	29	0	20	18	7	8.01	Pull
12	G	Mix	29	0	20	28	5.5	5.54	Pull
13	E	Mix	25	0	0	28	5.5	6.06	Pull
14	I	Mix	30	0	20	23	7	7.32	Push
15	I	Mix	27	0	20	16	7	7.32	Push
16	I	Mix	26	50	20	16	7	8.01	Push

To confirm the robustness of the purposed penetration detection system, the experiments were performed in a noisy factory environment in order to replicate the real-world conditions that it would be expected to handle.

Each of the 16 welds recorded in this experiment were cut every 50 mm along their cross sections, sanded and polished to mirror finish, and etched using a ferric chloride solution to reveal the penetration profile of the weld beads. These cross sections can be seen in **Figure 6.4**.

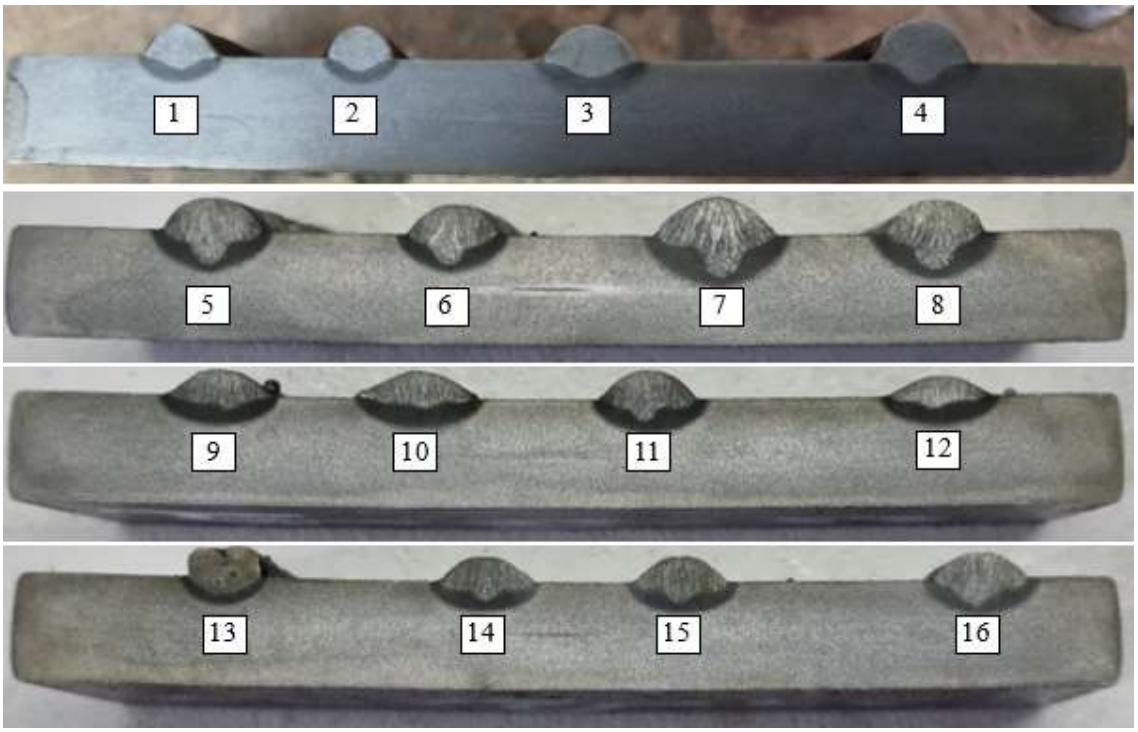

Figure 6.4 - Weld Bead Cross Sections

To determine the penetration depth of the weld beads, the root penetration depth is measured as shown in **Figure 6.5**. From here an average penetration depth can be calculated by averaging all of the measured penetration depths belonging to the same weld bead.

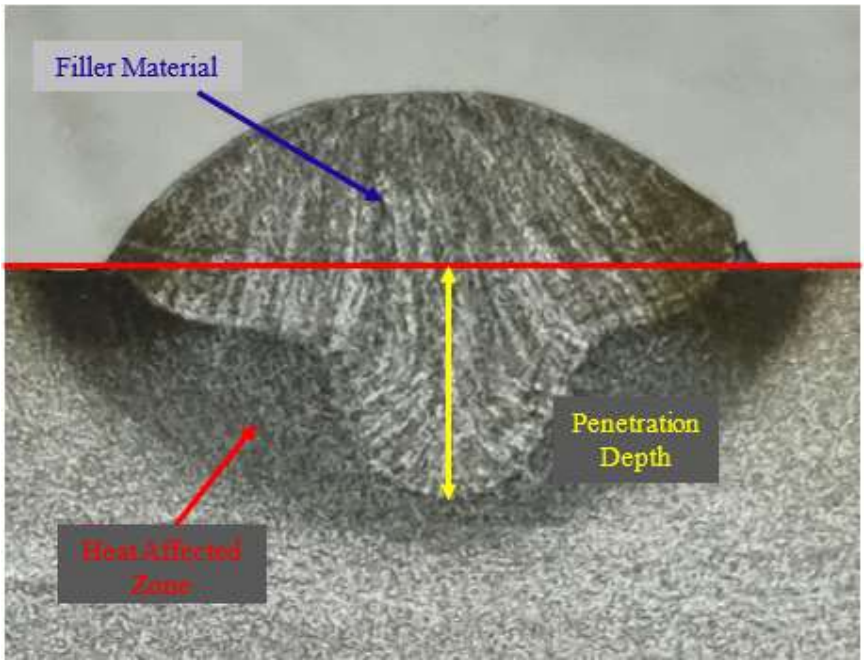

Figure 6.5 - Detailed cross section with penetration measurement

6.5. Results

Figure 6.6 shows the estimated penetration depth using the proposed method in comparison with the actual penetration depth measured using the cross sectional etches.

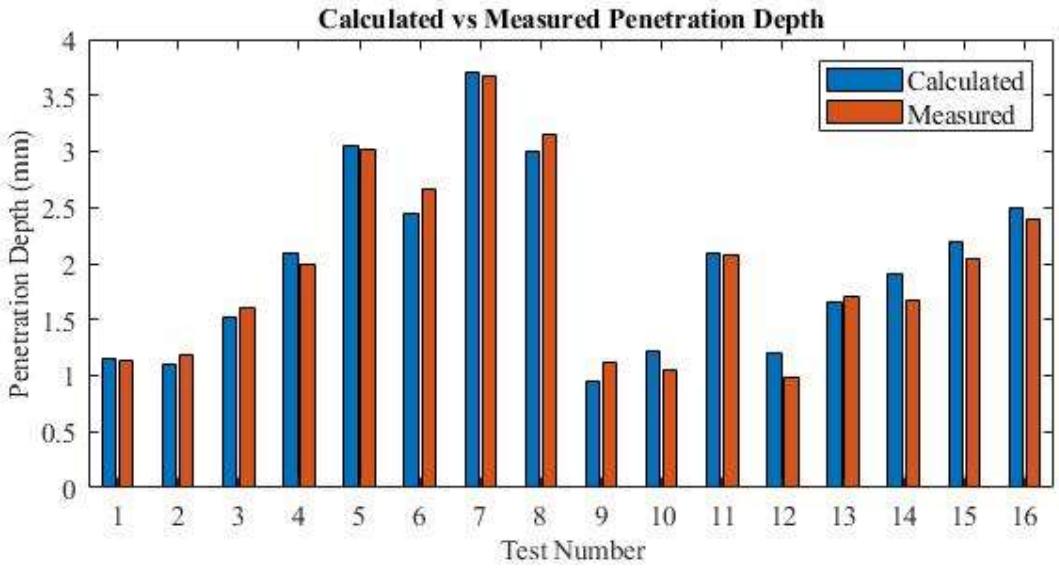

Figure 6.6 - Calculated vs measured penetration depth

From the results it can be seen that the proposed model is able to accurately predict the penetration depth, producing similar results to the measurements taken from the etched cross section. In particular, the model is very good at estimating the penetration depths in the primarily short circuit (1-4) and spray (5-8) signals, with a maximum error of approximately 10% due to the high stability of the welding arc, and uniformity of the material deposition. The lowest prediction accuracy is among the globular signals (9-12) and the interchangeable signals (14-16) with a maximum error of approximately 15%. In particular, this inaccuracy with the globular tests may be due to the very shallow and wide cross section profiles which are common with low power globular transfers, resulting in an inconsistent penetration profile due to the extensive periods of time between droplet transfers. Similarly, the inaccuracy that occurs in the interchangeable modes may be a result of the inconsistent material transfer rates due to the instability of the welding arc in these modes.

6.6. Conclusion

This chapter introduced a new GMAW penetration measurement method using the acoustic signal to monitor the droplet transfer process. Several bead on plate welds were produced under different transfer modes while recording their sound signal, and their penetration depths were measured from their etched cross sections. Using a combination of welding travel speed, wire feed rate, CTWD and the changes in transfer mode across the duration of the weld, an average value for weld bead penetration was calculated. When compared to the measured results, the penetration detection method was able to

predict the average weld bead penetration with a minimum of 80% accuracy. This work has been published in a conference paper for CASE 2022 [103].

CHAPTER 7 – Weld Bead Profile Growth Digital Twin

7.1. Chapter Introduction

In this chapter, a new weld bead profile monitoring algorithm is developed. In the previous chapter, a detection system for the average penetration depth of GMAW welds was introduced as a low cost passive detection method. However, this model can be further extended to plot the weld bead formation alongside the penetration profile in a localised area. Using the transfer mode detection algorithm outlined in **CHAPTER 4**, an estimation of the heat input of the GMAW system can be determined and used to plot the penetration profile and material transfer as the weld bead forms. Using this, a theoretical model with real time feedback can be developed to predict the bead formation and present the data as a digital twin of the system.

To outline the steps taken in the development of this model, the chapter is set out into several sub sections. To begin with, the methodology of the theoretical model is presented alongside the algorithms and additional assumptions that have been made. After this the experiments used to validate the theoretical model are outlined followed by the results and analysis of the data.

7.2. Methodology

As mentioned previously in **CHAPTER 4**, monitoring the penetration profile of GMAW is critical in determining the overall quality and structural integrity of the final weld bead. However due to the instability and complexity of the GMAW process, it can be difficult to build a heat transfer and weld bead formation model that works effectively in real time.

Previously researchers have investigated the melting process and weld bead formation in GMAW using a variety of methods. [104] investigated the effects of different input parameters on the penetration depth in GMAW and the viability of monitoring their changes to develop an online penetration estimation system. [127] investigated the effects of the welding arc on the formation of the weld pool. [105] measured the effects of several input parameters on the dilution of the weld pool in pulsed GMAW. [106] undertook an analytical study of the thermal behaviour and geometry of the weld pool are effected by the input parameters in pulsed GMAW. [107] developed an analytical model to determine the weld bead shape under different gas compositions and found that the heating efficiency of the welding arc differed in the perpendicular direction as compared to the welding direction. [108] studied the arc characteristics and how they affect the weld bead shape.

Similarly several researchers have also investigated several different methods of estimating the weld bead and penetration profiles in GMAW. [109] developed one of the earliest dilution estimation methods based on the melting efficiency of the GMAW process. [110] developed a penetration and bead geometry estimation system using an ANN with several welding parameters as the inputs. [111] developed a back propagation neural network to predict the weld bead geometry using several welding parameters as its input. [112] analysed the fusion zone in GMAW and used a neural network to estimate

the penetration profile. [113] developed an ANN model for predicting the weld bead geometry for laser micro welding of thin metal sheets. [114] developed a temperature measurement system to monitor the strain in situ using a finite element model. [115] used a neural network to predict the width and height of the final weld bead using the wire feed speed, travel speed, voltage and CTWD as inputs.

In addition to monitoring the penetration and weld bead profiles, several researchers have also developed numerous models to estimate the melting and bead formation process. [116] developed a method to determine the dilution in multi pass GTAW welding using an FEA method. [117] developed a weld pool and weld microstructure monitoring and measurements system using a custom high speed vision system. [118] developed a computational model to simulate the penetration profile by combining a heat transfer and fluid flow model with a genetic algorithm. [119] developed a FEA model to predict the welding penetration profile, residual stress and deformation in GTAW. [120] developed new variable heat source models to be used in conjunction with FEA to determine the penetration and weld bead profile in GMAW. [121] developed a 3-dimensional FEA model to simulate the GTAW welding process in butt welded pipes. [122] developed a numerical FEA simulation of the temperature and residual stress of the weld pool in friction stir welding. [123] developed a CFD model for analyse the formation of the weld bead on curved surfaces for additive manufacturing GMAW processes. [124] developed a penetration profile plotting approximation system for multi pass GMAW based additive manufacturing. [125] developed a statistical model using several input parameters to estimate the penetration depth of the weld bead. [126] used a FEM model to simulate the melting process in aluminium plates.

Currently all of these methods outlined in the literature fall into two different categories. The first category focuses on estimating the penetration depth and weld bead profile as an average across the complete weld bead while the second category focuses on plotting the penetration profile using FEA or CFD analysis in post-production. The method introduced in this chapter aims to bypass these limitations by introducing a new model that is able to estimate the localised weld bead and penetration profiles in real time. As CFD and FEA analysis are both too computationally intensive to work on the time scales required by the transfer mode detection algorithm outlined in **CHAPTER 4**, a simplified analytical estimation model was developed in this study.

This model is based on geometric assumptions made about the weld bead profile and builds upon previous melting efficiency and heat transfer estimations in GMAW and weld pool formation in the literature. The following sub sections will outline how this model functions, the overall algorithm and the governing equations on which it is built.

7.3. Algorithm Design

As the GMAW process is a rapidly changing process, cycling between transfer modes at high frequency, the weld bead and penetration parameters need to be consistently calculated at small time intervals to accurately capture the dynamic nature of the weld pool formation. To capture the dynamic changes in

the metal transfer from the electrode to the weld pool, the GMAW plotting algorithm uses the transfer mode detection algorithm introduced in **CHAPTER 4** as a feedback system. Because of this, the penetration profile needs to be calculated every 20 ms to match the same sampling frequency as the transfer mode detection algorithm.

An overview of the GMAW plotting algorithm can be seen in **Figure 7.1**.

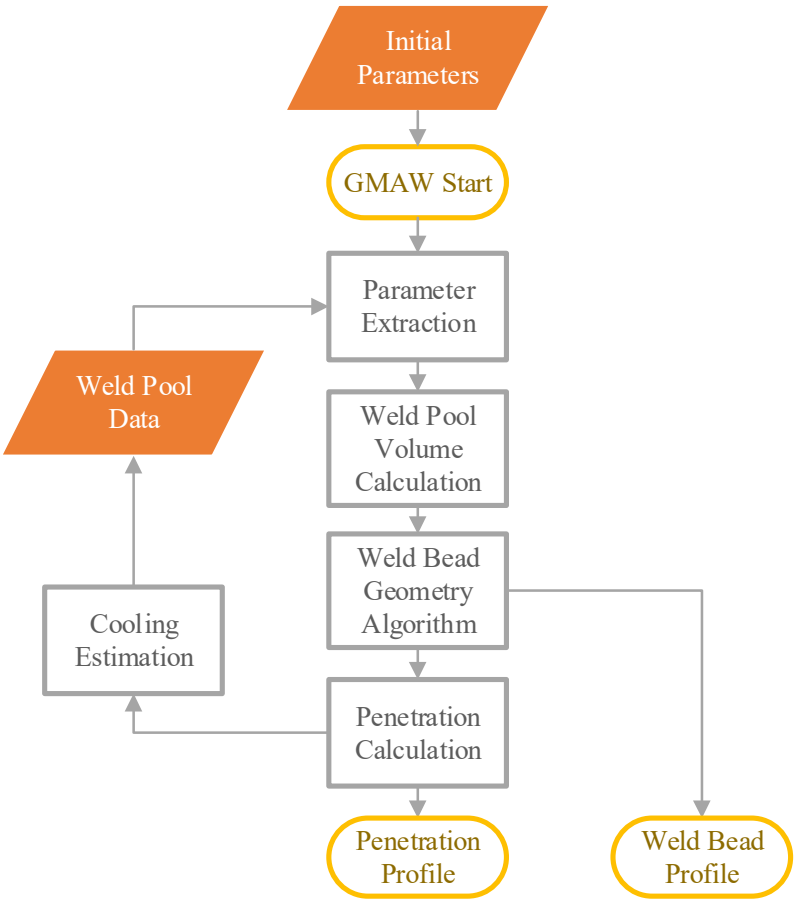

Figure 7.1 – GMAW Plotting Algorithm

As seen in **Figure 7.1** above, some initial parameters need to be set before the GMAW process begins. After setting these initial parameters, several additional parameters can be extracted based on the transfer mode detection system and the current weld pool data extracted from the previous time segment. After extracting these parameters, the current weld pool volume can be calculated followed by an estimation for the weld bead geometry formation. Using this weld bead geometry information, the penetration depth can be calculated as well as an estimate for the final weld bead. From the penetration calculation, the final penetration profile can be plotted, and the new weld pool area can be calculated after cooling has been considered.

The following sections will outline each of the steps in the GMAW plotting algorithm in greater detail.

7.4. Initial Parameters

7.4.1. Grid Formation

To begin with, a grid system is used to calculate the penetration depth and weld bead height in a localised area. To do this, the following grid system is used as shown in **Figure 7.2**.

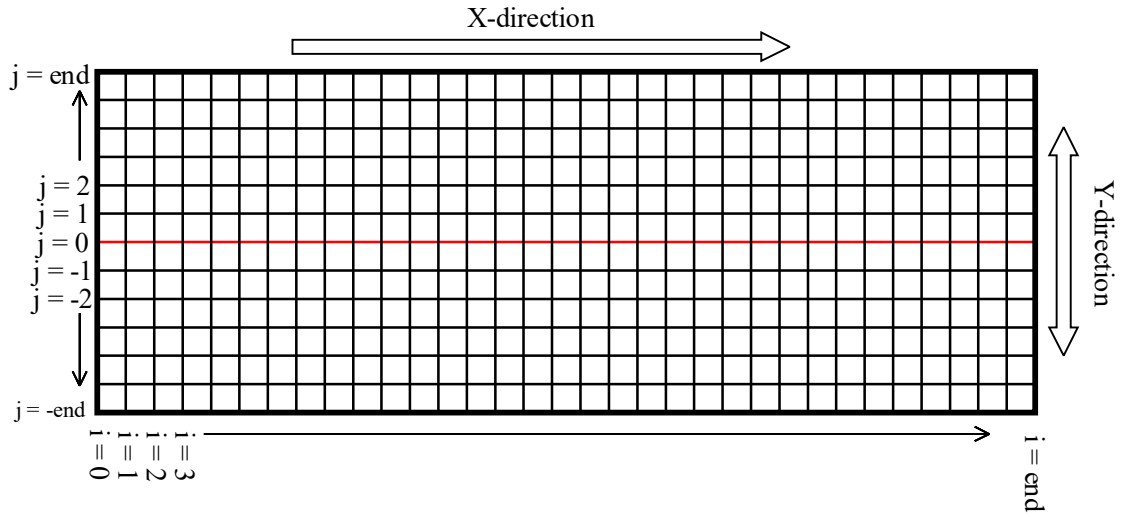

Figure 7.2 - Example Grid System

The x and y directions in **Figure 7.2** indicate the distance in the parallel and perpendicular to the welding direction respectively. Each individual element in the grid system is denoted using i and j in the x and y directions respectively. The distance between each element in the x direction, w_x is dependent on the welding speed v_s as shown in **Equation** 7.1.

$$w_x(i) = v_s(i)t_s \tag{7.1}$$

where w_x is the distance in mm, v_s is the welding speed in mm/s, and t_s is the segment duration in seconds.

Similarly the distance in the y direction, w_y can be set as a constant value and will stay consistent regardless of the welding speed. Using the values w_x and w_y, the distance in the x and y directions at each element can be denoted using **Equations** 7.2 and 7.3.

$$x_d(i) = \sum_{k=1}^{i} w_x(k) \tag{7.2}$$

$$y_d(j) = j \cdot w_y \tag{7.3}$$

where x_d and y_d are the distances in the x and y directions respectively in mm.

To further simplify this grid system and increase the computation speed, the assumption is made that the produced weld bead will be symmetrical about the welding path, therefore allowing only one half of the weld bead profile to be calculated.

7.4.2. Weld Bead Height

To effectively calculate the growth of the molten weld pool and its subsequent solidification into the weld bead profile, the weld pool was modelled in a similar manner to a standard liquid pool or droplet. Using **Equation** 7.4 [128], it can be assumed that there will be a theoretical maximum height that the weld pool can reach in its molten state based on two main parameters; the surface tension σ and the wetting angle θ_w.

$$h_m = 10\sqrt{\frac{2\sigma(1-\cos\theta_w)}{\rho g}} \tag{7.4}$$

where h_m is the maximum weld pool height in mm, σ is the surface tension of the weld pool in dyne/cm, θ_w is the maximum wetting angle of the weld pool, ρ is the density at melting point in g/ml^3 and g is the acceleration due to gravity in cm/s^2.

In GMAW, the surface tension of the weld pool is influenced by several different factors. As the weld pool is generally a mixture of both the molten filler wire and the base weld material, the chemical properties of the pool will change depending on the current admixing rate, causing the surface tension to change dynamically. In addition to this, the composition of the welding gas and temperature of the weld pool also have an effect on the surface tension. For the purpose of this model, the assumption is made that the temperature of the weld pool remains constant at the melting point of the base material and the welding wire composition is similar enough to the base material so that the admixing rate has a negligible effect on the weld pool surface tension.

The wetting angle is defined as the maximum angle a liquid surface and a solid surface at the point in which they meet. The wetting angle can be influenced by several factors including the weld pool chemical composition, the base material composition and the geometry of the area in which it rests. For the purpose of this method, the wetting angle is determined experimentally and considered to be constant throughout the weld.

7.5. Parameter Extraction

After defining the initial conditions of the model, the first stage of the GMAW plotting algorithm is to extract several parameters from the molten weld pool and previously solidified weld bead. To begin with, each element in the grid is checked to determine if it is currently in its molten state by determining if its current molten penetration volume. This can be done using **Equation** 7.5.

$$A_m(i,j,t) = \begin{cases} 0, & V_p(i,j,t) = 0 \\ 1, & V_p(i,j,t) > 0 \end{cases} \tag{7.5}$$

From here an assumption is made that if the molten area is plotted, it will form the shape of a double ellipse. Taking this assumption into account, several key locations for determining this shape can be extracted from the current molten weld pool. These points are the centre of the weld pool, x_c, and the furthermost points at the leading and trailing edges of the weld pool, x_f and x_0. Both x_f and x_0 can be

obtained directly from the molten penetration volume profile, V_p, whereas x_c can be taken at the point where the distance away from the centreline in the y direction, R_y is the maximum. Using these three points, the distance from the centre of the weld pool to the leading and trailing edges, R_x and R_0 can be calculated. **Figure 7.3** shows these 3 points and radii in the context of the weld pool where all distances are in mm.

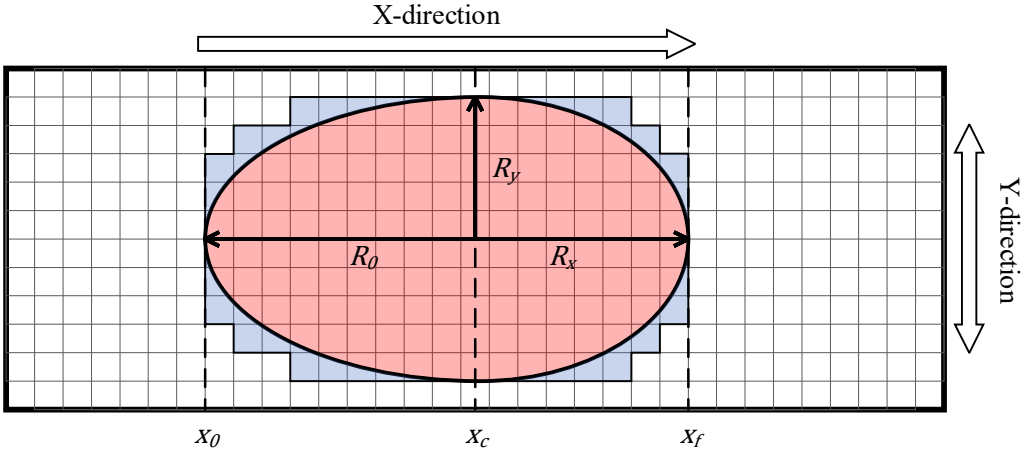

Figure 7.3 - Parameters R_x, R_y & R_0 in context of the weld pool

7.6. Weld Pool Volume Calculation

Despite the assumptions that the molten weld pool area will perfectly fit the shape of a double ellipse, this will obviously not be completely true due to the limitations of using a square element mesh system. This can be seen in **Figure 7.3**, where the molten weld pool area as calculated from the molten penetration volume, V_p is shown in blue. However, this molten weld pool area can be reshaped to fit the idealised double ellipse shape as shown in red by using the new co-ordinate system and extracted parameters R_0, R_x and R_y. Using **Equation** 7.6, this new ellipsoid shape can be determined.

$$y_p(x,t,n) = \begin{cases} R_y(t)\sqrt{1-\dfrac{(x-x_c(t,n))^2}{R_0(t,n)^2}}, & x < x_c(t,n) \\ R_y(t)\sqrt{1-\dfrac{\left(x-x_c(t,n)\right)^2}{R_x(t,n)^2}}, & x \geq x_c(t,n) \end{cases} \tag{7.6}$$

where y_p is the ellipse distance in the y direction in mm, x is the distance in the x direction, t denotes the current time segment and n is the weld bead growth iteration.

From here the total area of the elliptical weld pool can be determined using **Equation** 7.7.

$$A_T(t,n) = \int_{x_0(t)}^{x_f(t,n)} y_p(x,t,n)\,dx \tag{7.7}$$

where A_T is the total area of the weld pool in mm^2.

However, since the grid elements are still square, the percentage of each element that fits within the bounds of the ellipse needs to be calculated in order to effectively determine the correct volume of molten material within the weld pool. To determine this, the area of each individual element that fits within the bounds of the ellipsoid equation must be calculated. This can be done using **Equations** 7.8 to 7.10 with the lower and upper bounds of the integral being dependant on the individual element as shown in **Figure 7.4**.

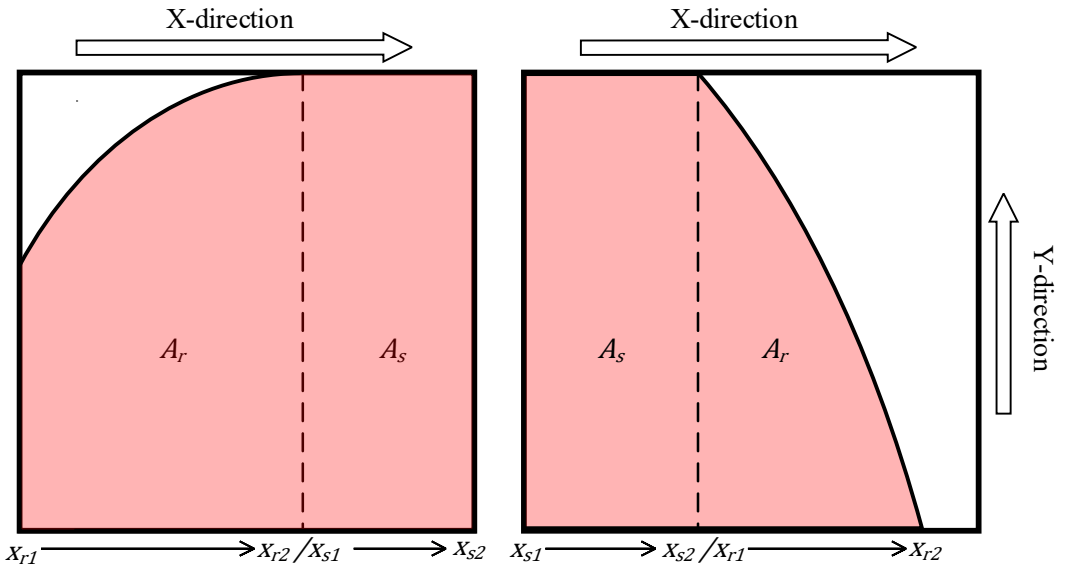

Figure 7.4 - Element bounds for A_r and A_s

$$A_r(i,j,t,n) = \int_{x_{r1}(i,j,t,n)}^{x_{r2}(i,j,t,n)} y_p(x,t,n)\,dx \tag{7.8}$$

$$A_s(i,j,t,n) = \int_{x_{s1}(i,j,t,n)}^{x_{s2}(i,j,t,n)} y_p(x,t,n)\,dx \tag{7.9}$$

$$A_{wp}(i,j,t,n) = A_s(i,j,t,n) + A_r(i,j,t,n) \tag{7.10}$$

where A_{wp} is the total element area within the bounds of the weld pool in mm^2, A_s and A_r are the rectangular and radial areas of each element in mm^2, and x_{s1}, x_{s2}, x_{r1} and x_{r2}, are the rectangular and radial limits in mm respectively.

Each element in the grid will fall into one of seven categories depending on how many corners of the element fit within the bounds of the ellipse produced by **Equation** 7.6. For example, the left element shown above in **Figure 7.4** has the top right, bottom left and bottom right corners within the bounds of **Equation** 7.6, whereas the right element has the top and bottom left corners. To classify each of these elements, a binary system can be used as shown in **Equations** 7.11 and 7.12.

$$M_c(i,j,t,n) = \begin{cases} 1, & y_d(j) < y_p(x_d(i),t,n) \\ 0, & y_d(j) \geq y_p(x_d(i),t,n) \end{cases} \tag{7.11}$$

$$T(i,j,t,n) = M_c(i,j,t) + 2M_c(i+1,j,t,n) + 4M_c(i,j+1,t,n) + 8M_c(i+1,j+1,t,n) \tag{7.12}$$

Using this new classification value T, the bounds of **Equations** 7.8 and 7.9 can now be determined using **Equations** 7.13 and 7.14.

$$A_r(i,j,t) = \begin{cases} \begin{cases} x_{r1}(i,j,t,n) = x_d(i) \\ x_{r2}(i,j,t,n) = x_p(i,j,t,n) \end{cases}, & T(i,j,t,n) = 1 \\ \begin{cases} x_{r1}(i,j,t,n) = x_p(i,j,t,n) \\ x_{r2}(i,j,t,n) = x_d(i+1) \end{cases}, & T(i,j,t,n) = 2 \\ \begin{cases} x_{r1}(i,j,t,n) = x_d(i) \\ x_{r2}(i,j,t,n) = x_d(i+1) \end{cases}, & T(i,j,t,n) = 3 \\ \begin{cases} x_{r1}(i,j,t,n) = x_p(i,j+1,t,n) \\ x_{r2}(i,j,t,n) = x_p(i,j,t,n) \end{cases}, & T(i,j,t,n) = 5 \\ \begin{cases} x_{r1}(i,j,t,n) = x_p(i,j+1,t,n) \\ x_{r2}(i,j,t,n) = x_d(i+1) \end{cases}, & T(i,j,t,n) = 7 \\ \begin{cases} x_{r1}(i,j,t,n) = x_p(i,j,t,n) \\ x_{r2}(i,j,t,n) = x_p(i,j+1,t,n) \end{cases}, & T(i,j,t,n) = 10 \\ \begin{cases} x_{r1}(i,j,t,n) = x_d(i) \\ x_{r2}(i,j,t,n) = x_p(i,j+1,t,n) \end{cases}, & T(i,j,t,n) = 11 \\ \begin{cases} x_{r1}(i,j,t,n) = 0 \\ x_{r2}(i,j,t,n) = 0 \end{cases}, & T(i,j,t,n) = 15 \\ \begin{cases} x_{r1}(i,j,t,n) = 0 \\ x_{r2}(i,j,t,n) = 0 \end{cases}, & T(i,j,t,n) = 0 \end{cases} \tag{7.13}$$

$$A_s(i,j,t) = \begin{cases} \begin{cases} x_{s1}(i,j,t,n) = 0 \\ x_{s2}(i,j,t,n) = 0 \end{cases}, & T(i,j,t,n) = 1 \\ \begin{cases} x_{s1}(i,j,t,n) = 0 \\ x_{s2}(i,j,t,n) = 0 \end{cases}, & T(i,j,t,n) = 2 \\ \begin{cases} x_{s1}(i,j,t,n) = 0 \\ x_{s2}(i,j,t,n) = 0 \end{cases}, & T(i,j,t,n) = 3 \\ \begin{cases} x_{s1}(i,j,t,n) = x_d(i) \\ x_{s2}(i,j,t,n) = x_p(i,j+1,t,n) \end{cases}, & T(i,j,t,n) = 5 \\ \begin{cases} x_{s1}(i,j,t,n) = x_d(i) \\ x_{s2}(i,j,t,n) = x_p(i,j+1,t,n) \end{cases}, & T(i,j,t,n) = 7 \\ \begin{cases} x_{s2}(i,j,t,n) = x_p(i,j+1,t,n) \\ x_{s2}(i,j,t,n) = x_d(i+1) \end{cases}, & T(i,j,t,n) = 10 \\ \begin{cases} x_{s1}(i,j,t,n) = x_p(i,j+1,t,n) \\ x_{s2}(i,j,t,n) = x_d(i+1) \end{cases}, & T(i,j,t,n) = 11 \\ \begin{cases} x_{s1}(i,j,t,n) = x_d(i) \\ x_{s2}(i,j,t,n) = x_d(i+1) \end{cases}, & T(i,j,t,n) = 15 \\ \begin{cases} x_{s1}(i,j,t,n) = 0 \\ x_{s2}(i,j,t,n) = 0 \end{cases}, & T(i,j,t,n) = 0 \end{cases} \tag{7.14}$$

where x_p is the maximum bounds of the double ellipse equation in the x direction in mm and can be calculated using **Equation** 7.15.

$$x_p(i,j,t,n) = \begin{cases} x_c(t,n) + R_0(t,n)\sqrt{1 - \dfrac{y_d(j)^2}{R_y(t,n)^2}}, & x_d(i) < x_c(t,n) \\ x_c(t,n) + R_x(t,n)\sqrt{1 - \dfrac{y_d(j)^2}{R_y(t,n)^2}}, & x_d(i) \geq x_c(t,n) \end{cases} \quad (7.15)$$

After calculating the total area of each element, the elements need to be normalised using **Equations** 7.16 and 7.17.

$$A_e(i,j) = w_x(i) \cdot w_y \quad (7.16)$$

$$A_n(i,j,t,n) = \frac{A_w(i,j,t,n)}{A_e(i,j)} \quad (7.17)$$

where A_e and A_n are the total area and normalised area of each element in mm^2.

7.7. Volume Input

After calculating the area of the weld pool, the total molten volume can be calculated by using the normalised area A_n. This can be done using **Equation** 7.18.

$$V_{wp}(t,n) = \sum_{i=i_0}^{i_f} \sum_{j=j_0}^{j_f} V_B(i,j,t,n) \cdot A_n(i,j,t,n) \quad (7.18)$$

where V_{wp} is the current volume of the weld pool, V_B is the weld bead volume above the base material per element in mm^3, and i_0, i_f, j_0 and j_f are the element locations at the trailing and leading edges of the weld bead respectively.

In addition to the volume currently in the weld pool $V_{wp}(t)$, the volume of the filler wire that has melted and transferred to the weld pool needs to be calculated. To do this, the transfer mode co-efficient introduced in section **CHAPTER 6** needs to be used to determine if any material has transferred into the weld pool for the current time segment t. From here the wire feed speed and cross-sectional area can be used to determine the amount of material transferred as shown in **Equations** 7.19 to 7.21.

$$W_c(t) = \begin{cases} W_c(t-1) + 1, & M_n(t) = \text{"No Transfer"} \\ W_c(t-1) + 1, & M_n(t) \neq \text{"No Transfer" and } M_n(t-1) = \text{"No Transfer"} \\ 1, & M_n(t) \neq \text{"No Transfer" and } M_n(t-1) \neq \text{"No Transfer"} \end{cases} \quad (7.19)$$

$$V_F = v_f A_w t_s \quad (7.20)$$

$$V_T(t,n) = V_F W_c(t) S_L(t) + V_{wp}(t,n) \quad (7.21)$$

where V_F, is the volume of the filler wire in in mm^3, v_f is the wire feed speed in mm/s, A_w is the cross sectional area of the electrode wire in mm^2, M_n is the current transfer mode, S_L is the spatter loss coefficient, W_c is the number of time steps since last droplet transfer and V_T is the current volume of the weld pool after droplet transfer in mm^3.

7.7.1. Spatter Loss

To more accurately determine the total volume of the molten weld pool, the spatter loss, or the amount of material ejected from the weld pool during the droplet transfer process needs to be accounted for. To do this an estimation for spatter loss can be achieved using **Equation** 7.22 based on the current transfer mode and an estimate of the molten droplet size.

$$S_L(t) = \begin{cases} 0.9, & M_n(t) = "Short\ Circuit" \\ 0.95, & M_n(t) = "Globular" \\ 1, & M_n(t) = "Spray" \\ 0.8, & M_n(t) = "Explosive" \\ 1, & M_n(t) = "No\ Transfer" \end{cases} \quad (7.22)$$

As shown above, the spatter loss is much greater in explosive and short circuit transfer modes due to the more violent nature of the droplet detachment ejecting more material away from the weld pool.

7.8. Weld bead Geometry Algorithm

7.8.1. Governing Equations

Since the geometry of both the weld pool and the solidified weld bead are crucial in determining the melting efficiency of the welding arc, a specialised geometric distribution system needs to be used to accurately calculate the volume in each individual element. In order to calculate this penetration profile a few additional assumptions will need to be made. In this work it is assumed that the total volume of the weld bead above the base material is equal to the volume of filler wire deposited, with the molten weld pool taking the form of the cap of a double ellipsoid as it solidifies as shown in **Figure 7.5**.

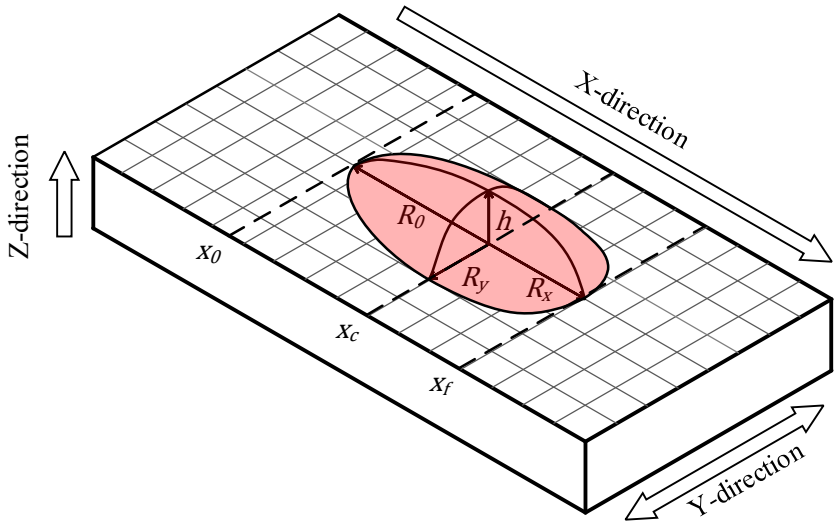

Figure 7.5 - Example Weld Pool Shape

To maintain continuity of the weld bead with the previously solidified section, the previous height value h_p at x_0 is presumed to exist on the surface of the ellipsoid. The equation of this profile can be determined similarly to the weld pool area by using the governing ellipsoid **Equation** 7.23.

$$z(x,y,t,n) = h(t,n) - c + c\sqrt{1 - \frac{(x - x_c(t,n))^2}{a(t,n)^2} - \frac{y^2}{b(t,n)^2}} \tag{7.23}$$

where z is the height of the weld bead at location (x, y) in mm, h is the maximum height of the weld bead in mm, and a, b, & c are the radii of the ellipsoid in the x, y, & z directions respectively in mm.

Similar to the weld pool area calculation, the ellipsoid is presumed to consist of both a front and rear component, with different maximum values for their radii about the x direction. However unlike the case shown in **Figure 7.5**, it is presumed that $h_p > 0$ therefore not creating a perfect ellipsoidal cap, instead creating a shape similar to the one shown in **Figure 7.6**.

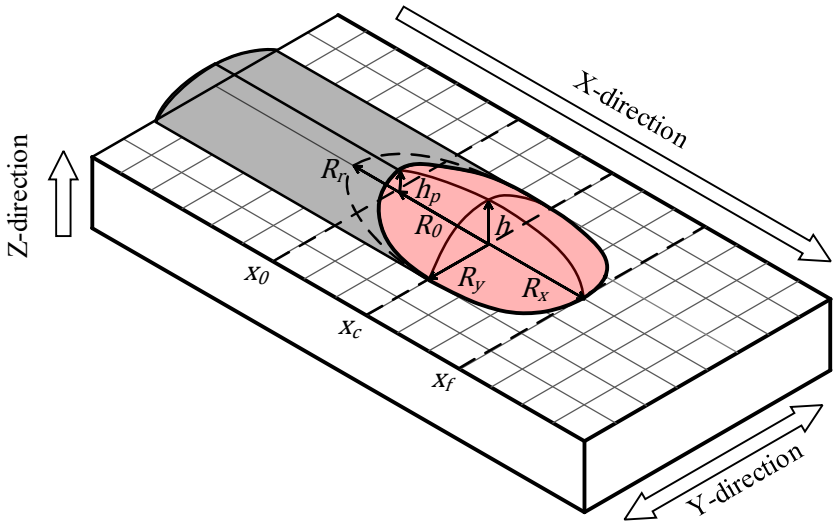

Figure 7.6 - Partial Double Ellipsoid Cap Shape

Therefore, to calculate the rear side radius R_r to the projected ellipse shown in **Figure 7.6**, can be calculated using **Equation** 7.24.

$$R_r(t,n) = x_c(t,n) - \frac{x_c(t,n)}{\sqrt{1 - \frac{\left(h_p(t) + c - h(t,n)\right)^2 + (c - h(t,n))^2}{c^2 - (c - h(t,n))^2}}} \tag{7.24}$$

where R_r is the projected radius in mm.

Using this projected radius, the geometric parameters a and b can be expressed in terms of c as shown in **Equations** 7.25 and 7.26.

$$a(t,n) = \begin{cases} \sqrt{\dfrac{c^2(R_r(t,n) - x_c(t,n))^2}{c^2 - (c - h(t,n))^2}}, & x < x_c(t,n) \\ \sqrt{\dfrac{c^2(R_x(t,n) - x_c)^2}{c^2 - (c - h(t,n))^2}}, & x \geq x_c(t,n) \end{cases} \tag{7.25}$$

$$b(t,n) = \sqrt{\frac{c^2 R_y(t,n)^2}{c^2 - (c - h(t,n))^2}} \tag{7.26}$$

After finding the geometric terms a and b the original ellipsoid **Equation** 7.23 can now be expressed purely in terms of known parameters and the geometric parameter c. To simplify **Equation** 7.23, an additional assumption can be made by assuming the ellipsoid will want to minimize its height with respect to the wetting angle θ_w, causing the true radius in the z direction, c to be infinite. Therefore the limit of z can be taken to derive the final ellipsoid equation in terms of the input parameters as shown in **Equation** 7.27.

$$\begin{aligned} z_l(x,y,t,n) &= \lim_{c\to\infty} z(x,y,t,n) \dots \\ &= \begin{cases} h(t,n) - \dfrac{\Big(h(t,n) - h_p(t)\Big)\,(x_c(t,n) - x)^2}{R_0(t,n)^2} - \dfrac{h(t,n)y^2}{R_y(t,n)^2}, & x < x_c(t,n) \\ h(t,n) - \dfrac{h(t,n)(x_c(t,n) - x)^2}{R_x(t,n)^2} - \dfrac{h(t,n)y^2}{R_y(t)^2}, & x \geq x_c(t,n) \end{cases} \end{aligned} \tag{7.27}$$

Similarly, the total volume of the molten weld pool can be found using **Equation** 7.28.

$$\begin{aligned} V_l(t,n) &= \int_{x_0(t,n)}^{x_f(t,n)} \int_0^{R_y(t,n)} z_l(x,y,t,n)\,dy\,dx \dots \\ &= \frac{\pi}{8}\Big(2h(t,n)R_y(t,n)R_x(t,n) + R_0(t,n)R_y(t,n)\big(2h(t,n) - h_p(t)\big)\Big) \end{aligned} \tag{7.28}$$

where h_p is the current height of the weld bead at position $(x_0, 0)$ in mm.

7.8.2. Shape Criteria

By assuming that the weld bead will have solidified outside of the molten weld pool area, additional assumptions can be made in order to calculate the distribution of the molten material across this volume. The first assumption is that the angle between the ellipsoid and the perpendicular direction must always be less than or equal to the wetting angle θ_w in 3 key positions. These points being the previous non molten point $(x_0, 0)$, the point at the front of the weld pool in the welding direction $(x_f, 0)$ and the point in the perpendicular direction (x_0, R_f). Using these points, 3 maximum values for the height of the weld bead under its current cross-sectional area can be calculated using **Equations** 7.29 to 7.31.

$$h_0(t,n) = \frac{R_0(t,n)\tan\theta_w}{2} + h_p(t) \tag{7.29}$$

$$h_x(t,n) = \frac{R_x(t,n)\tan\theta_w}{2} \tag{7.30}$$

$$h_y(t,n) = \frac{R_y(t,n)\tan\theta_w}{2} \tag{7.31}$$

where h_0, h_x, and h_y are the maximum heights of the weld bead when using R_0, R_x, and R_y respectively in mm.

As these 3 values all represent the respective maximum height under the current weld pool parameters, they also determine the maximum theoretical volume that would fit the ellipsoid (**Equation** 7.27**)** under those conditions. If the assumption is made that the molten area always aims to maintain the maximum wetting angle θ_w at the minimum radial direction of either R_x or R_y, then the minimum required dimensions of the molten weld bead can be determined. The assumption is also made that the deposited molten material will always try to fit within the bounds of the currently molten weld pool area. However if the volume of the deposited material exceeds the limits of the volume of the ellipsoid (**Equation** 7.27**)**, it is assumed that the material will essentially "spill over" onto the surrounding plate while still maintaining the wetting angle criteria. Taking these assumptions into account, several critical volumes can be determined that define the boundaries of the molten weld bead under different conditions. These critical volumes and their respective shapes and boundaries are outlined below.

7.8.2.1. Critical point 1 – when $h = 0$

At critical point 1, the molten weld bead volume is too small to develop into the double ellipsoid shape and only the rear half of the ellipsoid is considered to maintain continuity with the previous height h_p. This volume can be calculated using **Equation** 7.32 with its shape being shown in **Figure 7.7**.

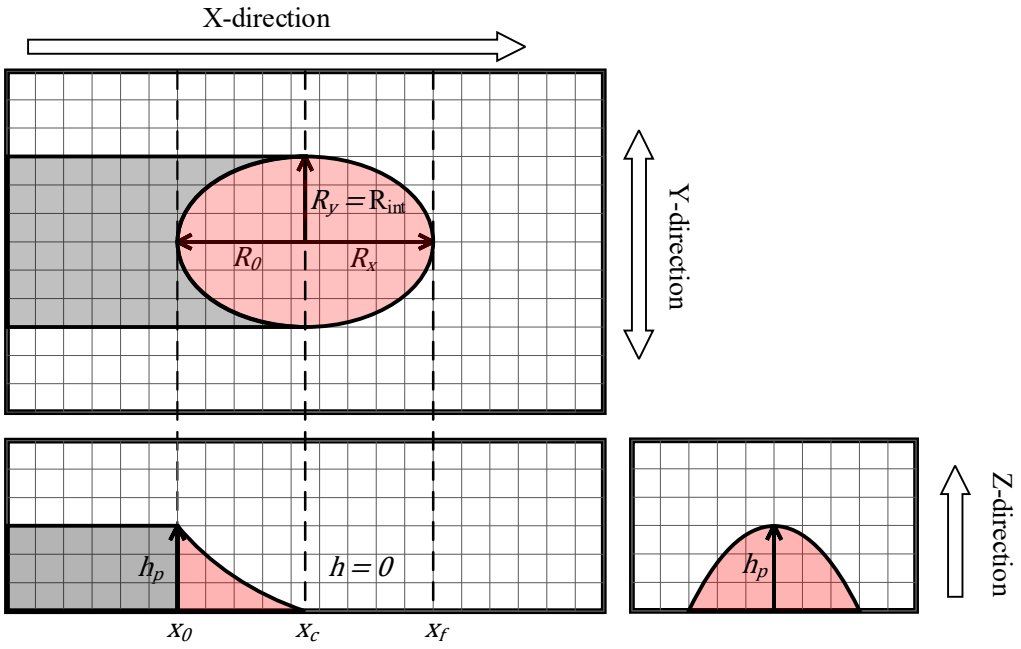

Figure 7.7 - Critical Point 1 Example

$$V_0(t,n) = \frac{\pi R_0(t,n) R_y(t,n) h_p(t)}{8} \tag{7.32}$$

where V_0 is the minimum volume in mm^3 required to maintain the double ellipsoid shape under current parameters.

7.8.2.2. Critical point 2 – maximised volume within current weld pool bounds

At critical point 2, the molten weld bead maximises its volume based on the initial bounds of the weld pool area, being R_0, R_x and R_y. To do this, the minimum height value from **Equations** 7.29**,** 7.30, and 7.31 is selected as to not exceed the maximum wetting angle θ_w as shown in **Equation** 7.33. After determining the maximum height value, the maximum volume of the weld bead under the current bounds can be determined as shown in **Equation** 7.34 with the shape being shown in **Figure 7.8**.

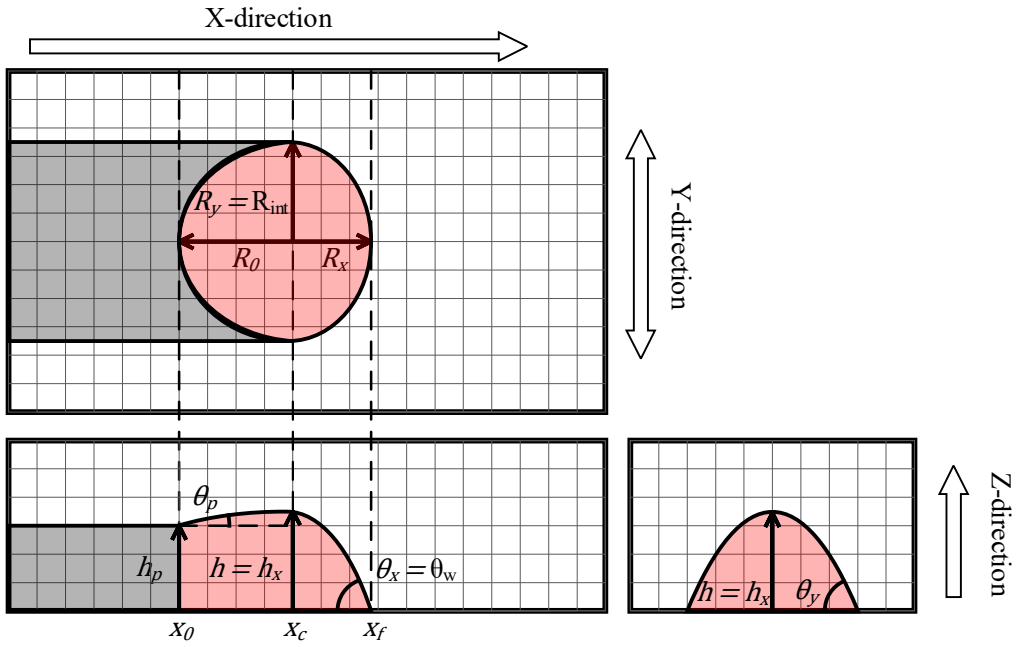

Figure 7.8 - Critical Point 2 Example

$$h_{min}(t,n) = \begin{cases} h_x(t,n), & h_x(t,n) < h_y(t,n) \text{ and } h_y(t,n) < h_m(t,n) \\ h_y(t,n), & h_x(t,n) \geq h_y(t,n) \text{ and } h_x(t,n) < h_m(t,n) \\ h_m(t,n), & h_m(t,n) < h_x(t,n) \text{ and } h_m(t,n) < h_y(t,n) \end{cases} \quad (7.33)$$

$$V_{min}(t,n) = \frac{\pi}{8}\Big(2h_{min}(t,n)R_y(t,n)R_x(t,n) + R_0(t,n)R_y(t,n)\big(2h_{min}(t,n) - h_p(t)\big)\Big) \quad (7.34)$$

where h_{min} and V_{min} are the maximum height and volume of the weld bead in mm and mm^3 respectively without exceeding the wetting angle or increasing the radial dimensions.

7.8.2.3. Critical point 3 – bead growth until $R_x = R_y$

At critical point 3, the volume of the molten weld bead exceeds the initial bounds of the weld pool area leading to it spilling out over the weld pool. It is assumed that the bead will try to form a uniform shape where $R_x = R_y$ with the maximum wetting angle occurring about both directions. In this case, the maximum height is taken to be the maximum value of either h_x or h_y which will correspond to the new maximum radius value R_{int}. To maintain continuity, the value of R_0 must also remain large enough so that the height value does not exceed the original condition, h_0. This volume and corresponding

parameters can be calculated using **Equations** 7.35 to 7.38 with the respective shape being shown in **Figure 7.9**.

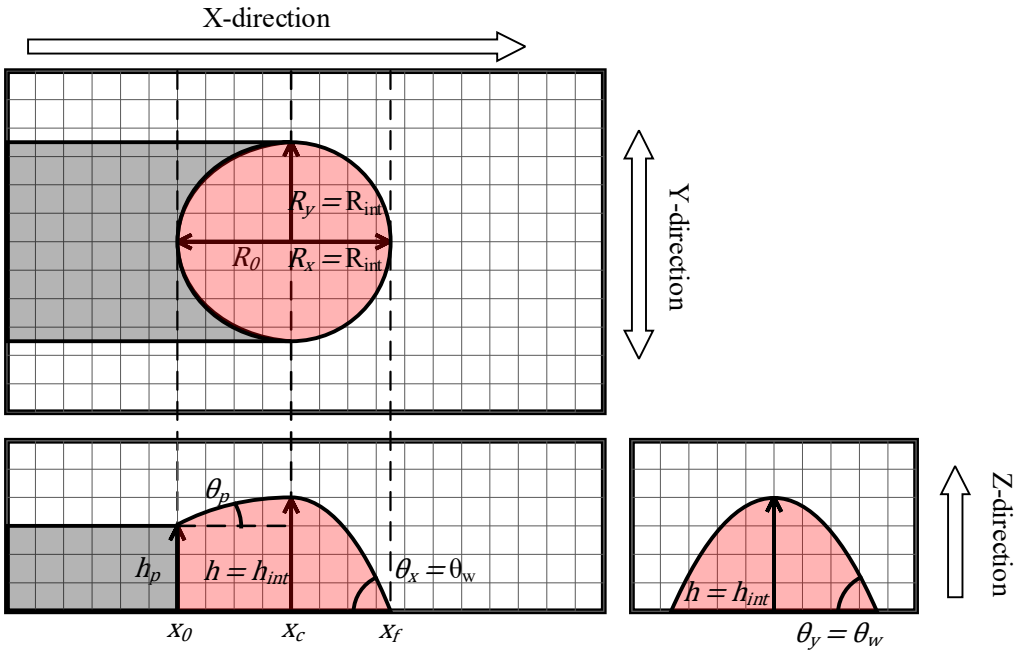

Figure 7.9 - Critical Point 3 Example

$$h_{int}(t,n) = \begin{cases} h_x(t,n), & h_y(t,n) < h_x(t,n) \; and \; h_y(t,n) < h_m(t,n) \\ h_y(t,n), & h_y(t,n) \geq h_x(t,n) \; and \; h_x(t,n) < h_m(t,n) \\ h_m(t,n), & h_m(t,n) < h_x(t,n) \; or \; h_m(t,n) < h_y(t,n) \end{cases} \quad (7.35)$$

$$R_{int}(t,n) = \begin{cases} R_x(t,n), & h_y(t,n) < h_x(t,n) \\ R_y(t,n), & h_y(t,n) \geq h_x(t,n) \end{cases} \quad (7.36)$$

$$R_{0_{int}}(t,n) = \begin{cases} \dfrac{R_{int}(t,n)\tan\theta_w - 2h_p(t)}{\tan\theta_w}, & h_0(t,n) < h_{int}(t,n) \\ R_0(t,n), & h_0(t,n) \geq h_{int}(t,n) \end{cases} \quad (7.37)$$

$$V_{int}(t,n) = \frac{\pi}{8}\Big(2h_{int}(t,n)R_{int}(t,n)^2 + R_{0_{int}}(t,n)R_{int}(t,n)\big(2h_{int}(t,n) - h_p(t)\big)\Big) \quad (7.38)$$

where h_{int}, R_{int}, $R_{0_{int}}$, and V_{int} are the height, leading edge radius, trailing edge radius, and volume in mm, and mm^3 respectively that maximise the volume of the weld bead when $R_x = R_y$.

7.8.2.4. Critical point 4 – maximum volume under conditions

Critical point 4 occurs when the maximum volume is achieved under the current conditions while maintaining the maximum wetting angle. In this scenario the molten weld bead has continued to spill over until the maximum height of h_m is finally achieved. This can be calculated using **Equations** 7.39 to 7.41 with **Figure 7.10** defining its shape.

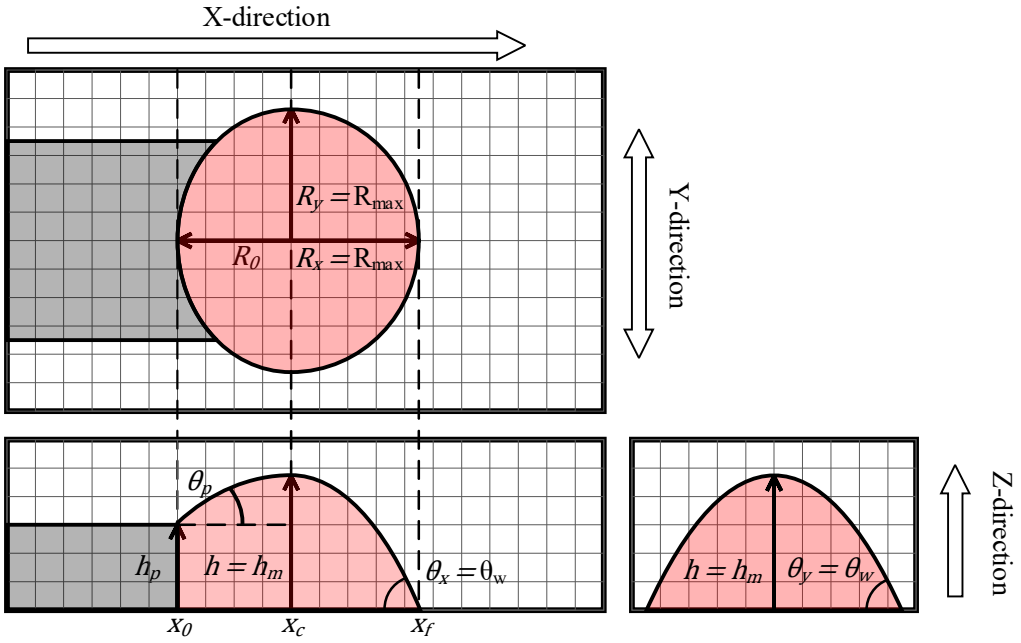

Figure 7.10 - Critical Point 4 Example

$$R_{max} = \frac{2h_m}{\tan\theta_w} \tag{7.39}$$

$$R_{0\_max}(t,n) = \begin{cases} \dfrac{R_{max}\tan\theta_w - 2h_p(t)}{\tan\theta_w}, & h_0(t,n) < h_m \\ R_0(t,n), & h_0(t,n) \geq h_m \end{cases} \tag{7.40}$$

$$V_{max}(t,n) = \frac{\pi}{8}\left(2h_m {R_{max}}^2 + R_{0\_max}(t,n)R_{max}\left(2h_m - h_p(t)\right)\right) \tag{7.41}$$

where R_{max}, R_{0_max}, and V_{max} are the leading edge radius, trailing edge radius, and volume in mm, and mm^3 respectively at the maximum height value h_m.

7.8.3. Case Selection

After calculating the theoretical weld pool volumes at the critical points outlined above, the real weld pool volumes under each of these situations can be calculated. Using the weld pool volume calculation in **Equation** 7.18, the maximum volume for each of these cases can be calculated using the inputs as shown in **Equation** 7.42.

$$V_{case}(t,n)\begin{cases}\begin{cases}R_x(t,n)=R_x(t,n)\\R_y(t,n)=R_y(t,n)\\R_0(t,n)=R_0(t,n)\end{cases}, & case\ 1\\ \begin{cases}R_x(t,n)=R_x(t,n)\\R_y(t,n)=R_y(t,n)\\R_0(t,n)=R_0(t,n)\end{cases}, & case\ 2\\ \begin{cases}R_x(t,n)=R_{int}(t,n)\\R_y(t,n)=R_{int}(t,n)\\R_0(t,n)=R_{0_{int}}(t,n)\end{cases}, & case\ 3\\ \begin{cases}R_x(t,n)=R_{max}(t,n)\\R_y(t,n)=R_{max}(t,n)\\R_0(t,n)=R_{0\_max}(t,n)\end{cases}, & case\ 4\end{cases} \tag{7.42}$$

In the cases where the radii exceeds the bounds of the current weld pool, it is assumed that the solidified weld bead volume V_b now encompassed by the new area will also become molten and add to the total volume of the weld pool. Because of this, the current weld pool volume V_T needs to be recalculated if its original value is found to be greater than the volume at critical point 2, V_{min}. To calculate the true weld pool volume and effectively plot the shape of the weld bead, the weld pool volume must be compared with the 4 critical volumes above, resulting in 5 different possible outcomes. Depending on these outcomes, 5 different algorithms can be used to calculate the final parameters and plot the true weld bead shape. These criteria are outlined in **Equation** 7.43.

$$Case\begin{cases}1, & V_T(t,n) < V_0(t,n)\\ 2, & V_{min}(t,n) > V_T(t,n) > V_0(t,n)\\ 3, & V_T(t,n) > V_{min}(t,n)\ and\ V_{int}(t,n) > V_{case3}(t,n)\\ 4, & V_{case3}(t,n) > V_{int}(t,n)\ and\ V_{max}(t,n) > V_{case4}(t,n)\\ 5, & V_{case2}(t,n) > V_{max}(t,n)\end{cases} \tag{7.43}$$

7.8.3.1. Case 1 – Volume less than minimum for weld pool bounds

In case 1, the current volume of the weld pool is less than the absolute minimum volume input to maintain the double ellipsoid shape. Therefore to maintain continuity, the distance to the centre of the ellipsoid needs to be decreased as shown in **Figure 7.11** and can be calculated using **Equation** 7.44.

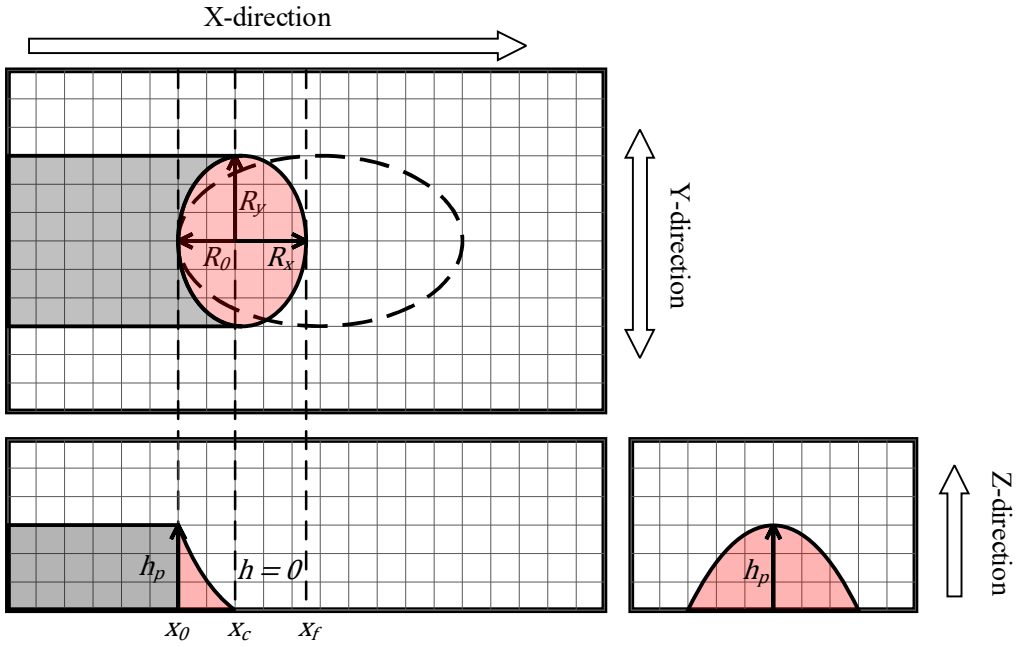

Figure 7.11 - Case 1 Example

$$R_0(t,n) = \frac{16V_0(t,n)}{\pi h_p(t) R_y(t,n)} \tag{7.44}$$

7.8.3.2. Case 2 – Volume fits within weld pool bounds

In case 2, the current volume of the weld pool is large enough to form the double ellipsoid shape while still being small enough to be within the constraints of the original weld pool parameters R_y, R_x and R_0. In this scenario the height of the weld pool can simply be calculated using **Equation** 7.45, with its shape being shown in **Figure 7.12**.

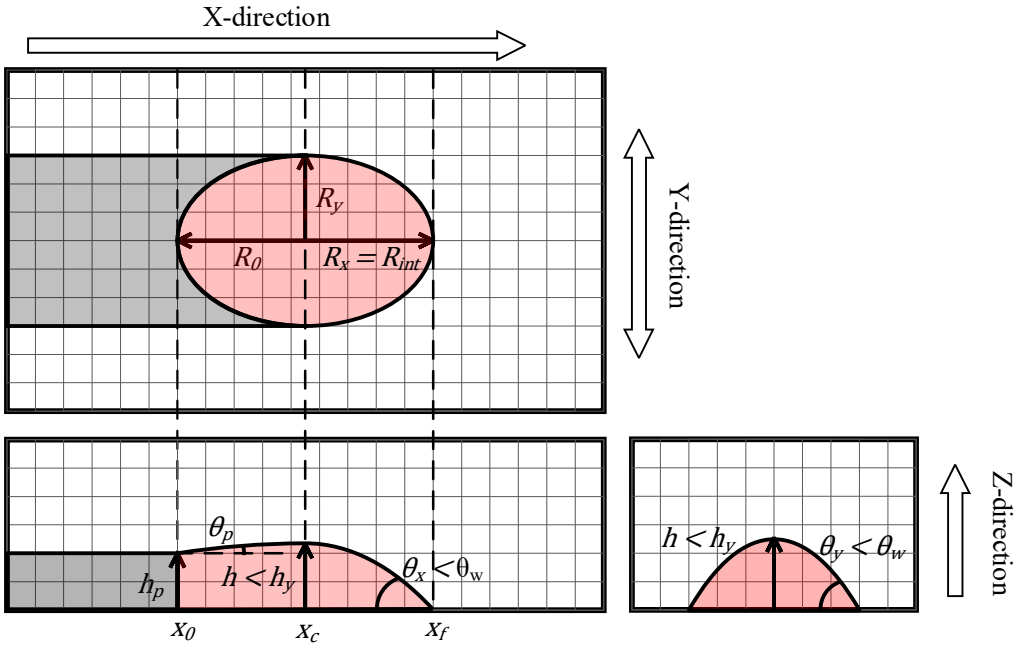

Figure 7.12 - Case 2 Example

$$h(t,n) = \frac{16V_T(t,n) - \pi R_0(t,n)R_y(t,n)h_p(t)}{2\pi R_y(t,n)(R_x(t,n) + R_0(t,n))} \quad (7.45)$$

7.8.3.3. Case 3 – Volume exceeds weld pool bounds in one direction

In case 3, the volume will have exceeded the maximum volume that the current weld pool parameters can contain while still being less than the volume if both R_y and R_x were equal, therefore leading the weld bead to spill over onto the surrounding plate. In this case scenario, the new values for R_y, R_x and R_0 need to be calculated for the weld pool volume, V_T. However as the values of R_y, R_x and R_0 increase, so too does the value of V_T. Therefore the values consistently need to be recalculated until an equilibrium between them is established. This can be done by using the algorithm shown in **Figure 7.13**.

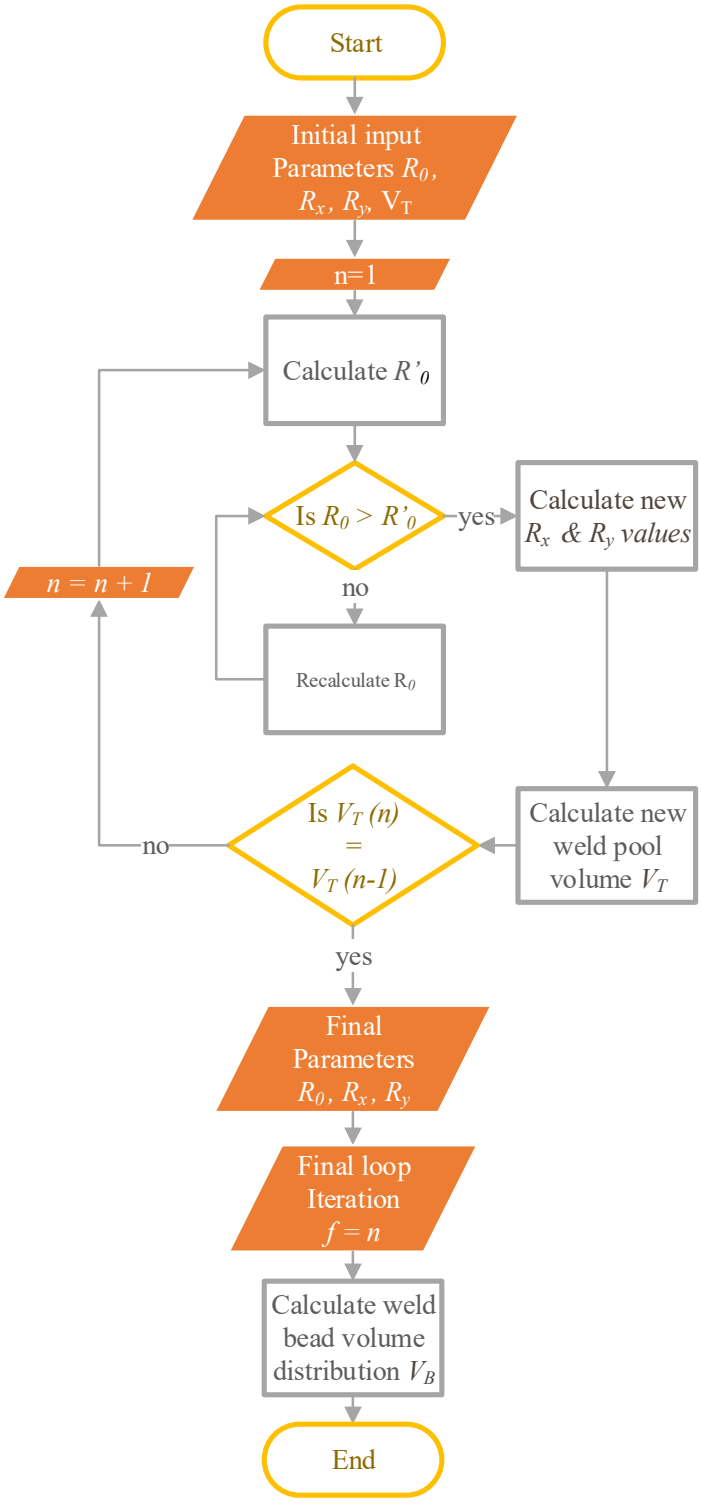

Figure 7.13 - Case 3-5 Algorithm

where R'_0 is calculated using **Equation** 7.46.

$$R'_0(t,n) = \begin{cases} R_{0int}(t,n), & case\ 3 \\ R_{0m}\ \ (t,n), & case\ 4\ and\ case\ 5 \end{cases} \tag{7.46}$$

To calculate the new values for R_y, R_x and R_0, the roots of **Equations** 7.47 to 7.49 can be used.

$$f\big(R_y(t,n)\big)\begin{cases} R_y(t,n-1), & R_x(t,n) < R_y(t,n) \\ \Big(\pi\tan\theta_w\left(R_x(t,n)+R_0(t,n)\right)\Big)R_y(t,n)^2 \ldots & \\ +\Big(\pi R_0(t,n)h_p(t)\Big)R_y(t,n) - 16V_T(t,n), & R_x(t,n) > R_y(t,n) \end{cases} \tag{7.47}$$

$$f\big(R_x(t,n)\big) \ldots$$
$$\begin{cases} \big(\pi R_y(t,n)\tan\theta_w\big)R_x(t,n)^2 + \big(\pi R_0(t,n)R_y(t,n)\tan\theta_w\big)R_x(t,n) \ldots & \\ \quad +\pi R_0(t,n)R_y(t,n)h_p(t) - 16V_T(t,n), & R_x(t,n) < R_y(t,n) \\ \quad R_x(t,n), & R_x(t,n) > R_y(t,n) \end{cases} \tag{7.48}$$

$$\big(\pi R_y(t,n)\tan\theta_w\big)R_0(t,n)^3 + \big(\pi R_y(t,n)R_x(t,n)\tan\theta_w\big)R_0(t,n)^2 \ldots$$
$$+\Big(3\pi R_y(t,n)h_p(t)\Big)R_0(t,n) + \big(2\pi R_y(t,n)R_x(t,n)h_p(t) - 16V_T(t,n)\big) = 0 \tag{7.49}$$

As **Equation** 7.49 is a third order polynomial, and **Equations** 7.47 and 7.48 are second order polynomials, only the maximum real root is taken as the solution to all three of these equations. After calculating the new values for R_y, R_x and R_0, the new height can be calculated using **Equation** 7.45, and the new weld pool area A_n and volume V_T can be recalculated using the method outlined in **Sections 7.6** and **7.7**. The final shape of the weld bead in this scenario can be shown in **Figure 7.14**.

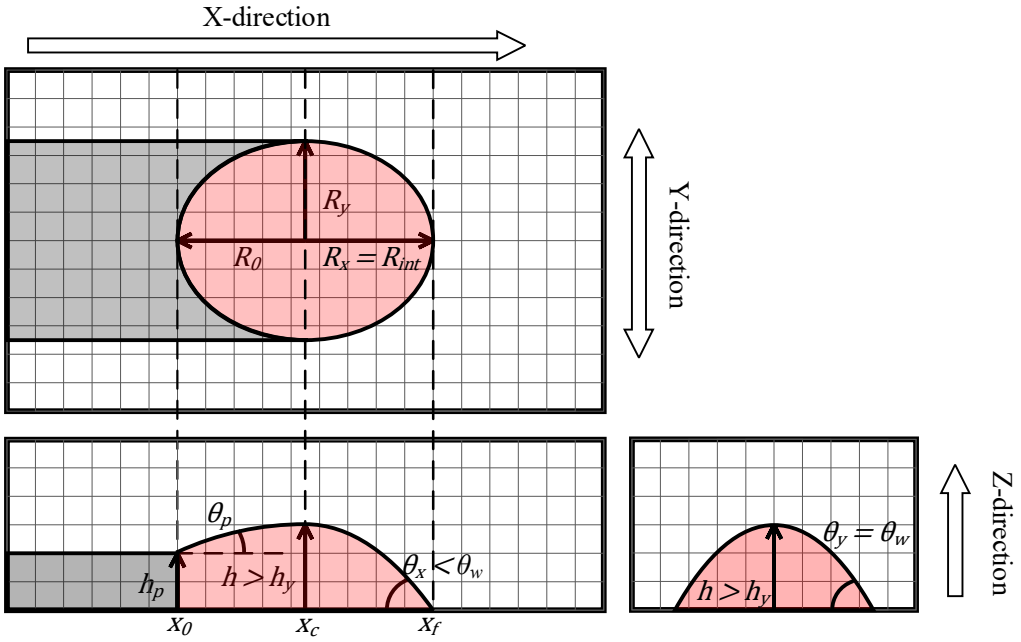

Figure 7.14 - Case 3 Example

7.8.3.4. Case 4 – Volume exceeds weld pool bounds in both directions

In the fourth case scenario, the input volume exceeds the bounds of the weld pool in both the R_x and R_y directions. Similar to case 3, the same algorithm can be used in **Figure 7.13** to find the equilibrium between the extracted parameters and the weld pool volume. However a simplified equation to calculate the weld pool radii can be used since $R_x = R_y$ as shown in **Equation** 7.50.

$$(\pi \tan\theta_w)R'(t,n)^3 + (\pi R_0(t,n)\tan\theta_w)R'(t,n)^2 \ldots + \left(\pi R_0(t,n)h_p(t)\right)R'(t,n) - 16V_T(t,n) = 0 \quad (7.50)$$

where $R' = R_x = R_y$.

The final shape of the weld bead in this scenario can be seen in **Figure 7.15**.

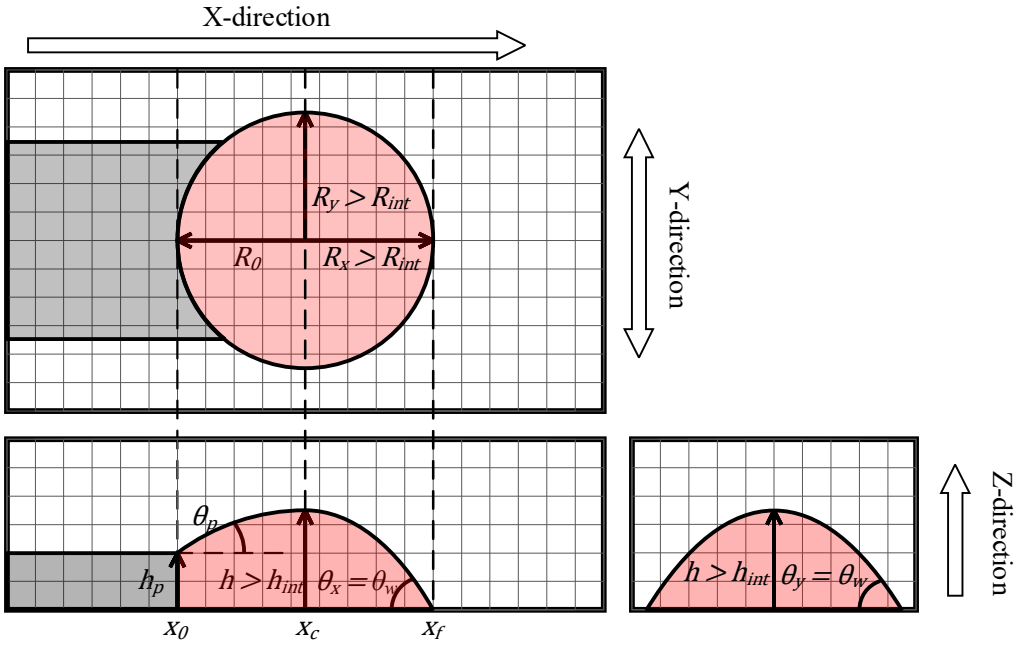

Figure 7.15 - Case 4 Example

7.8.3.5. Case 5 – Volume has reached maximum height

In the final case scenario, the volume of the molten weld bead is larger than the maximum bounds of the weld pool as defined by the maximum height value h_m. In this scenario, the weld bead parameters R_x and R_y continue to grow while maintaining the height h_m. Similar to cases 3 and 4, the algorithm in **Figure 7.13** can be used to find the equilibrium between the extracted parameters and the weld pool volume. **Equation** 7.51 can be used to calculate the value of R' in this situation, with **Figure 7.16** showing the final shape of the weld bead in this scenario.

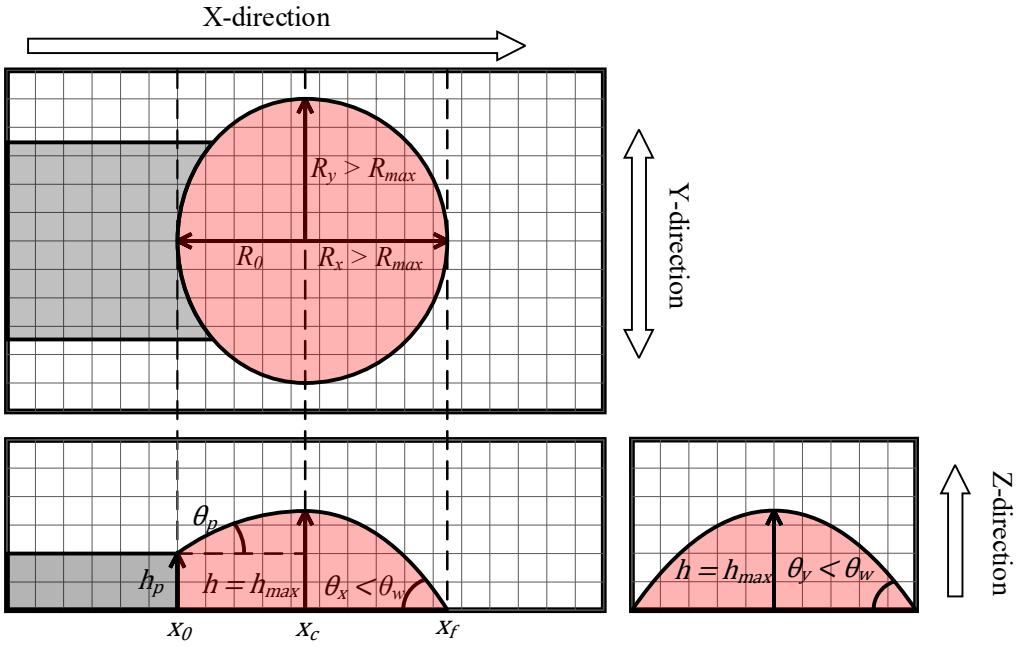

Figure 7.16 - Case 5 Example

$$(2\pi h_m)R'(t,n)^2 + \left(\pi R_0(t,n)\left(2h_m + h_p(t)\right)\right)R'(t,n) - 16V_T(t,n) = 0 \tag{7.51}$$

where $R' = R_x = R_y$.

7.8.4. Final Volume

After obtaining the final values for R_y, R_x and R_0, the volume distribution can be determined in a similar way to **Section 7.6**. Using the parameters R_y, R_x and R_0 the volume of each individual element can be calculated using **Equations** 7.52 to 7.54.

$$V_r(i,j,t) = \int_{x_{r1}(i,j,t,f)}^{x_{r2}(i,j,t,f)} \int_{y_d(j)}^{y_p(i,j,t,f)} z_l(x,y,t,f)dydx \tag{7.52}$$

$$V_s(i,j,t) = \int_{x_{s1}(i,j,t,f)}^{x_{s2}(i,j,t,f)} \int_{y_d(j)}^{y_p(i,j,t,f)} z_l(x,y,t,f)dydx \tag{7.53}$$

$$V_{mod}(i,j,t) = V_r(i,j,t) + V_s(i,j,t) \tag{7.54}$$

where V_r and V_s are the radial and rectangular volumes of each element respectively, x_{r1}, x_{r2}, x_{s1} and x_{s2} are the limits in **Equations** 7.13 to 7.14, z_l is calculated using **Equation** 7.27, V_{mod} is the final weld pool volume distribution and f is the final weld pool growth iteration.

After calculating the final volume per element for the molten weld pool, the total current volume for the entire weld bead profile including the already solidified component needs to be found. To do this, the molten weld pool volume V_{mod} as calculated above needs to be added to the total weld bead volume V_B. However since the total weld pool volume V_T in **Equation** 7.18 was calculated using a

percentage of the individual element areas as shown in **Equation** 7.17, the same percentage must first be subtracted before the new volume can be added as shown in **Equation** 7.55.

$$V_B(i,j,t) = V_B(i,j,t-1) + V_{mod}(i,j,t) - V_B(i,j,t-1) \cdot A_n(i,j,t) \quad (7.55)$$

In addition to this, the current weld bead height at each element can now be calculated by dividing by the total element area as shown in **Equation** 7.56.

$$z_b(i,j,t) = \frac{V_b(i,j,t)}{A_e(i)} \quad (7.56)$$

7.9. Melting Calculations

Once the current weld bead geometry has been determined, the heat transferred into the base material can be calculated.

7.9.1. Heat Model

To begin with, the heat model must be defined to effectively outline the distribution of the total heat energy amongst each element in the grid. For this model, a simplified 2-dimensional version of the double ellipsoid heat source was chosen [92, 94, 119, 129-131] which is defined by **Equation** 7.57 & 7.58.

$$W_n(i,j,t) = \frac{1}{\sqrt{|\Sigma_n|(2\pi)^2}} e^{\left(-\frac{1}{2}(L_m(i,j,t))\Sigma_n{}^{-1}(L_m(i,j,t))^T\right)} \quad (7.57)$$

$$L_m(i,j,t) = [x_d(i) - x_t(t) \quad y_d(j)] \quad (7.58)$$

Where Σ_n is the standard deviation matrix, L_m is the mean matrix and n corresponds to either the front or rear portion of the distribution as seen in **Figure 7.17**.

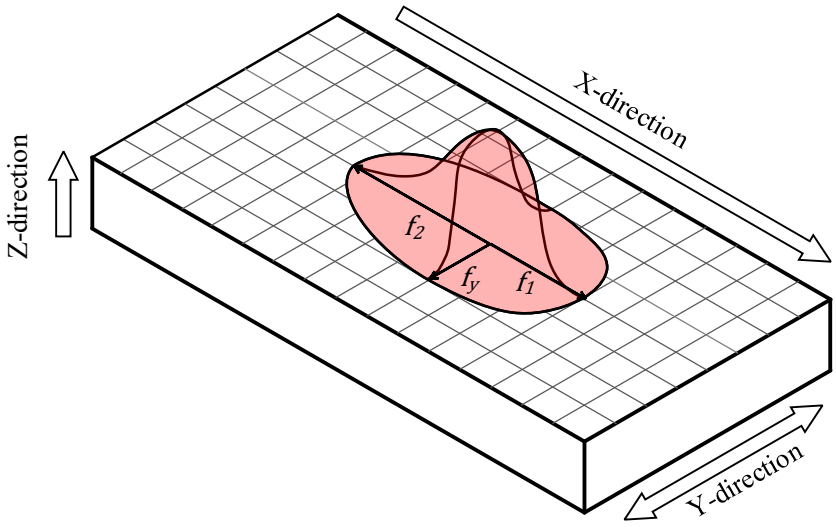

Figure 7.17 - Heat Source Model

This double ellipsoid distribution allows for different distribution parameters for both the leading and trailing edges. This allows the heat to have a larger distribution towards the trailing edge as a means to

simulate the additional heat that trailing edge is subjected to it being exposed to the heat flow for a longer period of time. In addition to this, to emulate the changes in heat distribution that is normally associated with the changes in transfer mode, the standard deviation matrix Σ_n is calculated differently depending on the current transfer mode as shown in **Equation** 7.59.

$$\Sigma_n(t) = \begin{bmatrix} M_x(t)f_n & 0 \\ 0 & M_y(t) \end{bmatrix} \tag{7.59}$$

where M_x and M_y are the scaling coefficients for the x and y directions respectively. These scaling factors can be determined using **Equation** 7.60 and 7.61.

$$M_x(t) = \begin{cases} 3, & M_n(t) = "Short\ Circuit" \\ 6, & M_n(t) = "Globular" \\ 3, & M_n(t) = "Spray" \\ 3, & M_n(t) = "Explosive" \\ 3, & M_n(t) = "No\ Transfer" \end{cases} \tag{7.60}$$

$$M_y(t) = \begin{cases} 2.5, & M_n(t) = "Short\ Circuit" \\ 6, & M_n(t) = "Globular" \\ 1.5, & M_n(t) = "Spray" \\ 1, & M_n(t) = "Explosive" \\ 3, & M_n(t) = "No\ Transfer" \end{cases} \tag{7.61}$$

To maintain continuity, the two values for f_n shown above in **Equation** 7.59 for the standard deviation of the heat distribution must be equal to 1 as shown in **Equation** 7.62.

$$f_1 + f_2 = 1 \tag{7.62}$$

Once the leading and trailing edges of the distribution have been calculated, they can then be added together and normalised as shown in **Equation** 7.63.

$$W(i,j,t) = \frac{W_1(i,j,t) + W_2(i,j,t)}{2(\sum W_1(t) + \sum W_2(t))} \tag{7.63}$$

where W is the normalised heat distribution.

Using this normalised distribution, the total heat transferred during each time segment can be calculated using the previously outlined transfer mode power transfer coefficient in **Equation** 6.2. The equation for this can be seen in **Equation** 7.64.

$$P(i,j,t) = 50 \cdot T_{mc}(t) \cdot W(i,j,t) \tag{7.64}$$

where P is the heat estimation per element in J.

7.9.2. Melting Calculation

Once the heat model has been established, the melting efficiency can then be calculated. Several different methods for calculating the melting efficiency exist in the literature [109, 132-141] however, they all have limitations and would not be able to adequately measure the melting efficiency correctly in the context of the method outlined in this chapter. The main issue with these methods are that they are all inversely proportional to the welding speed. However if the welding speed drops to 0, then the melting efficiency becomes zero, which is clearly not the case in such a situation. If the melting

efficiency is calculated over the length of a total weld and not just the localised area, then this is generally not an issue.

The purpose of using the travel speed in these melting efficiency calculations is to decrease the efficiency as the volume of the weld bead increases underneath the arc, in turn insulating the base material from the heat source. Using this knowledge, a new melting efficiency equation was developed as shown in **Equation** 7.65 which considers the current volume of melted material in each element underneath the welding arc.

$$\eta_m(i,j,t) = C \cdot \exp\left(\frac{-B_0 \cdot E \cdot \nu \cdot t_s^2}{\sum P(i,j,t) \cdot \eta_a \cdot w_y} \cdot \left(\frac{B_1 \cdot z_p(i,j,t) + B_2 \cdot z_b(i,j,t)}{w_x(i)}\right)^2\right) \tag{7.65}$$

where η_m is the melting efficiency, E is the average enthalpy between the filler wire and the base material in J/mm^3, ν is the kinematic viscosity in mm^2/s, η_a is the arc efficiency, z_p is the depth of the weld pool at each element in mm, and B_0, B_1, B_2 and C are scaling coefficients.

After calculating the melting efficiency, the weighted power estimate can be determined using **Equation** 7.66.

$$P_w(i,j,t) = \eta_m(i,j,t) \cdot \eta_a \cdot P(i,j,t) \tag{7.66}$$

where P_w is the weighted power estimate in J.

Using this weighted estimate, the penetration depth can be calculated using the energy balance **Equation** 7.67 [109].

$$V_p(i,j,t) = \frac{P_w(i,j,t) - A_h(i,j,t)V_F E_{fm} t_s}{E_s} \tag{7.67}$$

where V_p is the volume of the weld pool below the base material in mm^3, E_{fm} is the melting enthalpy of the filler wire in J/mm^3, E_s is the melting enthalpy of the base material in J/mm^3, and A_h is the normalised heat area which can be calculated using **Equations** 7.68 and 7.69.

$$A_{h0}(i,j,t) = \begin{cases} 0, & P_w(i,j,t) < 0 \\ 1, & P_w(i,j,t) \geq 0 \end{cases} \tag{7.68}$$

$$A_h(i,j,t) = \frac{A_e(i,j) \cdot A_{h0}(i,j,t)}{\sum A_e(i,j) \cdot A_{h0}(i,j,t)} \tag{7.69}$$

Once the volume V_p has been calculated, the penetration depth per element can be calculated similarly to **Equation** 7.56 for the weld bead height. This can be done using **Equation** 7.70.

$$z_p(i,j,t) = \frac{V_p(i,j,t)}{A_e(i,j)} \tag{7.70}$$

7.9.3. Cooling Estimate

After the penetration and weld bead profiles have been calculated, an estimate for the cooling needs to be established. As this method aims to avoid the high computational costs of using FEA or CFD analysis to accurately compute the heat transfer profile, a simplified estimation is used as a substitute. To do this

however, the assumption needs to be made that the base welded plate can be considered as a thick plate, therefore acting as a large heat sink in comparison to the welding parameters. This can be done using **Equation** 7.71 [117, 142].

$$t_p \sqrt{\frac{t_s c_s \rho \Delta T}{\sum P(t)}} > 0.75 \tag{7.71}$$

where t_p is the plate thickness in mm, ρ is the density of the weld bead in Kg·m^{-3}, c_s is the specific heat in J·Kg^{-1}·K^{-1}, ΔT is the melting point of the plate material.

Provided that the welded plate falls under this criteria, the following **Equation** 7.72 can be used to estimate the how much height is lost in each element per time step.

$$C_e(i,j,t) = \frac{C_c \cdot \left(z_b(i,j,t) + z_p(i,j,t)\right)}{P(i,j,t)} \tag{7.72}$$

where C_e is the bead height loss in mm, and C_c is the cooling constant in J.

7.10. Final Penetration Profile

After calculating the cooling estimate, the final penetration profile can be determined. To do this, two different values need to be taken, these being the current penetration profile V_b as well as the historical penetration profile V_h, which can be calculated using equation 7.73.

$$V_h(i,j,t) = \begin{cases} V_p(i,j,t), & V_h(i,j,t) < V_p(i,j,t) \\ V_h(i,j,t), & V_h(i,j,t) \geq V_p(i,j,t) \end{cases} \tag{7.73}$$

where V_h is the historical penetration profile in mm^3.

Using the historical penetration profile V_h, the total shape of the weld bead can be plotted alongside V_b at the current time step t to describe the complete profile of the weld. To feed back into the melting efficiency and weld pool area calculations however, the new value for the penetration depth can be calculated using **Equation** 7.74.

$$V_p(i,j,t+1) = V_p(i,j,t) - C_e(i,j,t) \tag{7.74}$$

7.11. Experimental Set up

To experimentally verify the model, several tests were performed using the test rig identified in **CHAPTER 3**. To do this, 8 welds were performed on 10 mm thick 1020 bright mild steel plates. Each of these weld beads were 210 mm long and performed under a variety of different welding conditions as shown in **Table 7.1**.

Table 7.1 - Experimental Parameters

Test Number	Transfer Mode	Gas Composition	Voltage (V)	Inductance (%)	Gas Flow Rate (L/min)	CTWD (mm)	Travel Speed	Wire Feed Rate (m/min)	Gun Angle
1	SC	Mix	20	30	20	16	Medium	5.54	Push
2	G	Mix	30	50	20	20	Medium	6.06	Push
3	SP	Mix	30	50	20	20	Fast	9.31	Push
4	I	Mix	27	50	20	18	Medium	7.32	Push
5	SC	Mix	20	50	20	16	Slow	4.36	Push
6	G	Mix	29	50	20	18	Medium	5.54	Push
7	SP	Mix	28	50	20	18	Medium	8.74	Push
8	I	Mix	24	50	20	16	Medium	5.54	Push

As shown in **Table 7.1**, all the tests were performed under different conditions in order to achieve different transfer modes. This allows for a more diverse range of weld beads to be produced, which would allow the constants in **Equation** 7.65 to be tuned more accurately, ensuring that they are not over fitted to one specific transfer mode. In addition to this, these tests were also performed using a variable travel speed which was changed every 42 mm along the weld. These travel speeds for each section can be seen in **Table 7.2**.

Table 7.2 - Welding Speed Parameters

Speed Category	Speed 20-62mm (mm/s)	Speed 62-104mm (mm/s)	Speed 104-146mm (mm/s)	Speed 146-188mm (mm/s)	Speed 188-230mm (mm/s)
Slow	2.5	5	7.5	5	2.5
Medium	3.5	7	10.5	7	3.5
Fast	5	10	15	10	5

These variable travel speeds were implemented in order to test the capabilities of the theoretical algorithm when the weld bead and penetration profiles are not consistent across the entire weld bead. This was also chosen to show the transition between bead and penetration profiles as the speed is decreased and increased, as well as to see how accurately the plotting algorithm can predict the profile through these transition zones.

Similar to the tests performed in **CHAPTER 6**, each of the 8 produced welds were cut and etched to bring out their cross sectional details. In these tests each weld was cut and etched at 5 different positions along the plate. Each of these cuts were made in the middle of each section corresponding to the welding speed changes. Each of these cross sections were then sequentially ground down using 40 to 120 grit sanding discs then brought up to a mirror finish using a buffing wheel. After buffing, the plate cross sections were then submerged in a 10% ferric chloride solution and washed down with distilled water.

Using these cross sectional etches, measurements were taken and compared with the values estimated by the plotting algorithm. To do this, images were taken of each cross sectional profile and measurements were taken using the pixel distance to several critical points. These include the bead height, bead width, penetration depth, bead area, penetration area and dilution. An example of these measurements is shown in **Figure 7.18** with the recorded values being shown in **Table 9.2**.

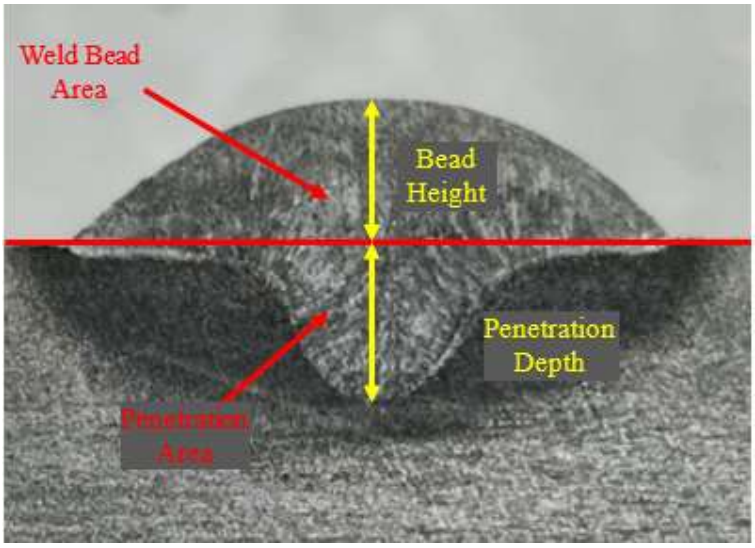

Figure 7.18 - Weld Bead Cross Section Example

7.12. Results

7.12.1. Initial parameters

Using the new set of signals shown in **Table 7.1**, the acoustic signal can be broken down into 20 ms segments and processed using the transfer mode detection system outlined in **CHAPTER 4**. Using this transfer mode data, alongside the wire feed speed and welding travel speed parameters, the weld bead could be theoretically plotted using the plotting algorithm outlined above in **Section 7.3**. For the performed test the following values were used for the constants in the algorithm.

The surface tension value σ, was determined to be 1230 dyne/cm at 1515°C as shown in both [143, 144]. The average density at melting point ρ for 1020 mild steel was taken as 7020 kg/m^3 [145]. The wetting angle θ_w in a typical GMAW application using 1020 mild steel and ER70S welding wire was determined to be approximately 50 degrees as shown in [146]. This wetting angle was further validated experimentally from the results of these tests as shown in **Figure 7.19**.

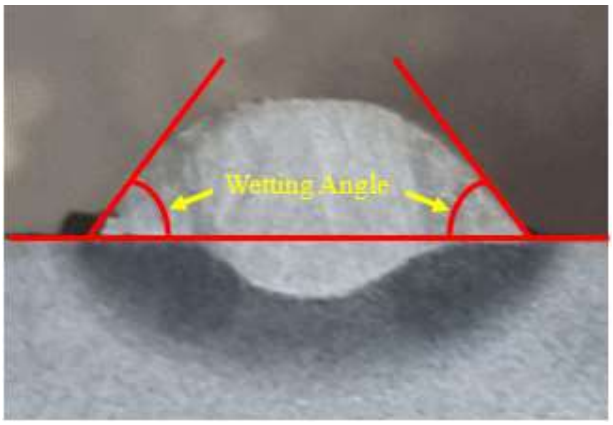

Figure 7.19 - Wetting angle example measurement

The enthalpy E used was 10.5 J/mm^3 [147], and kinematic viscosity ν was 0.79 mm^2/s [148, 149]. The arc efficiency for GMAW η_a used was 0.84 and was taken from [150].

The constant values B_0, B_1, B_2 and C in **Equation** 7.65 were found experimentally with their final values under the conditions of this experiment being 1, 12, 23, and 0.2 respectively. Similarly the cooling constant C_c in equation 7.72 was found to be 0.003.

The heat source standard deviation factors f_1 and f_2 in **Equation** 7.62 were taken from [129] and were found to be 0.8 and 1.2 respectively.

For the purpose of these tests, the element grid system was constructed using the smallest length step in the x direction when the welding speed is at its minimum as the width in the y direction, w_y. As outlined in **Equation** 7.1, the distance between elements in the x direction, w_x was determined by the current welding speed.

7.12.2. Area Calculation and Weld Bead Plotting

Using the recorded datasets, the GMAW plotting algorithm was checked at different stages throughout the process. To begin with, it was checked to confirm that the extracted parameters used to calculate the weld pool area as shown in **Section 7.6** were formed as expected. **Figure 7.20** shows the area profile before and after feature extraction for an average signal segment.

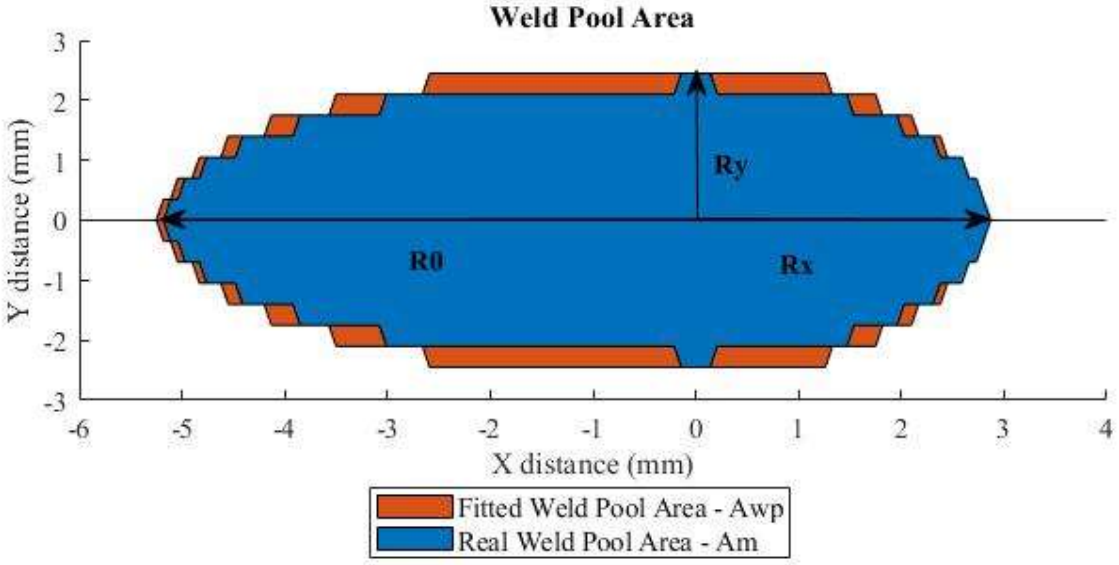

Figure 7.20 - Weld Bead Reshaping

As seen in the example in **Figure 7.20**, the real weld pool area A_{wp} did not perfectly fit within the bounds of the double ellipsoid shape y_p. Therefore, the modified weld pool area A_m was found to be slightly larger to fully contain the projected double ellipsoid shape as shown in **Figure 7.3**.

Similarly, the weld bead geometry algorithm under normal conditions also needed to be tested to confirm the shape fits the desired result. **Figure 7.21** shows examples of the weld bead geometry for each of the main cases outlined in **Section 7.8**.

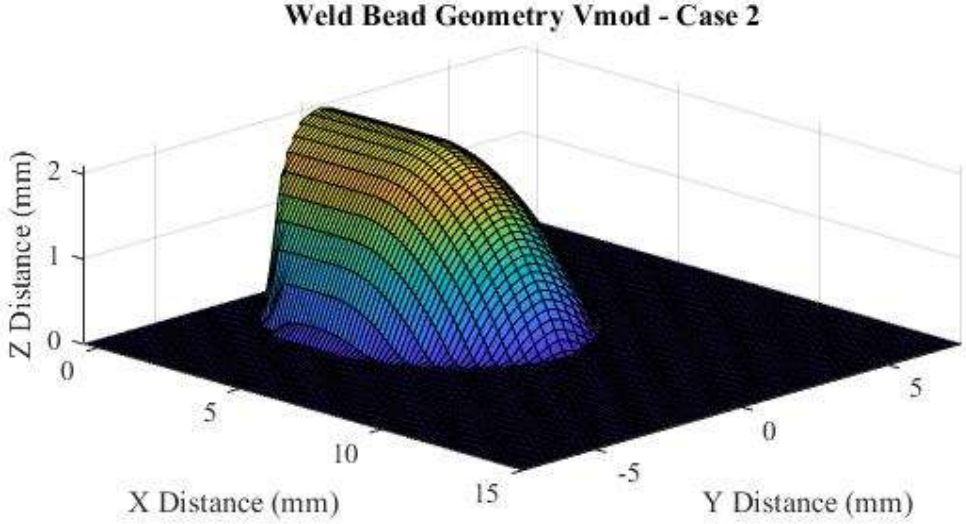

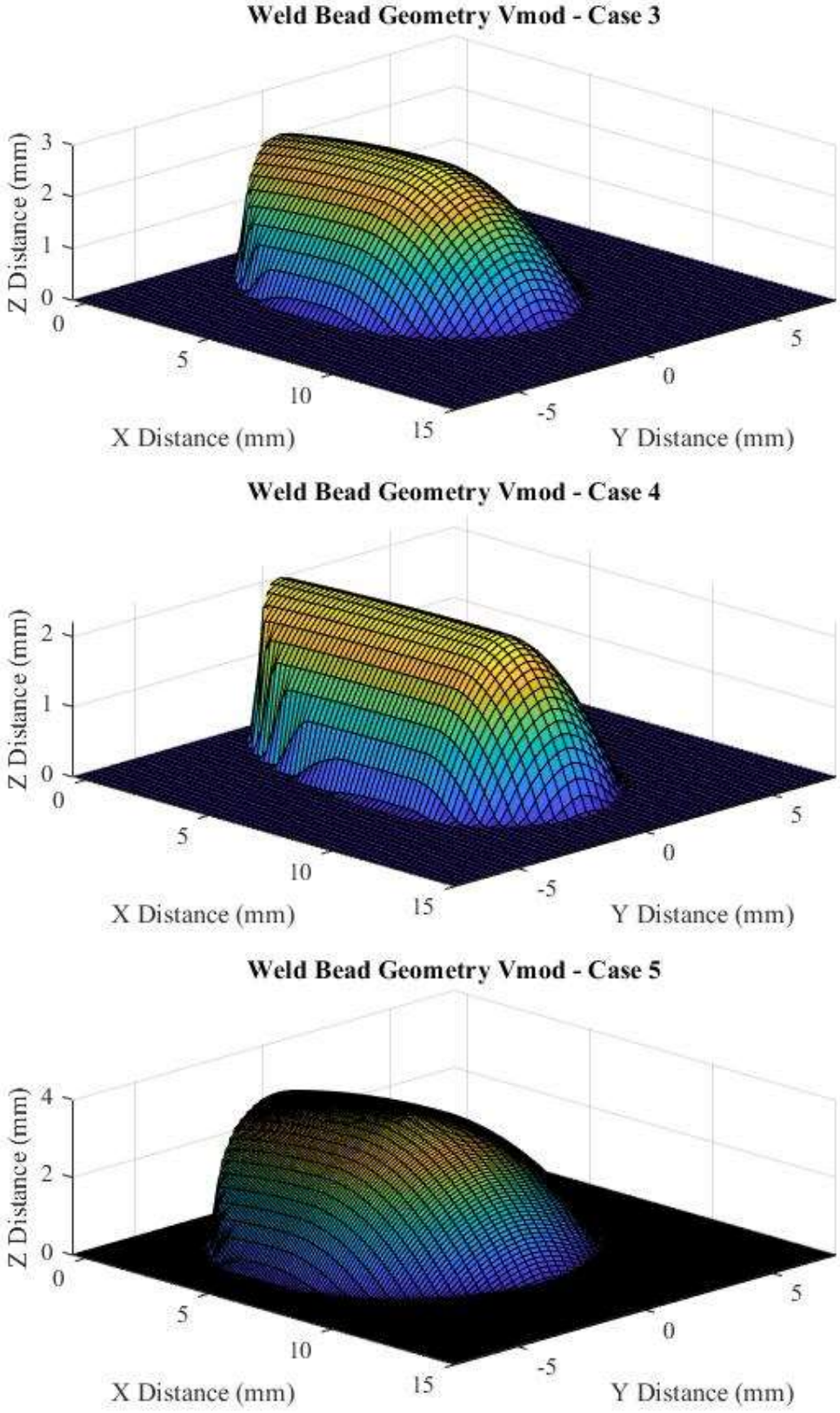

Figure 7.21 – Weld Bead Geometry V_{mod} for Cases 2-5

From the 8 performed tests, it was found that a situation never occurred in which case 1 in **Section 7.8.3.1** was triggered. Ideally this could only be triggered if there was a significant height difference of the weld bead between the current and previous weld bead segments in addition to a significant loss of molten weld pool volume.

When looking at the geometry in cases 2-4 it can be seen that the predicted shape was maintained as expected. For each case scenario however it can be noted that 2 possible shape outcomes can be achieved. These being for when $h > h_p$ or when $h < h_p$. In the situation for when $h < h_p$ and there is a large variation between the two, it can be seen that the volume no longer forms a realistic shape when compared to the realistic shape of the weld pool as shown in **Figure 7.22**.

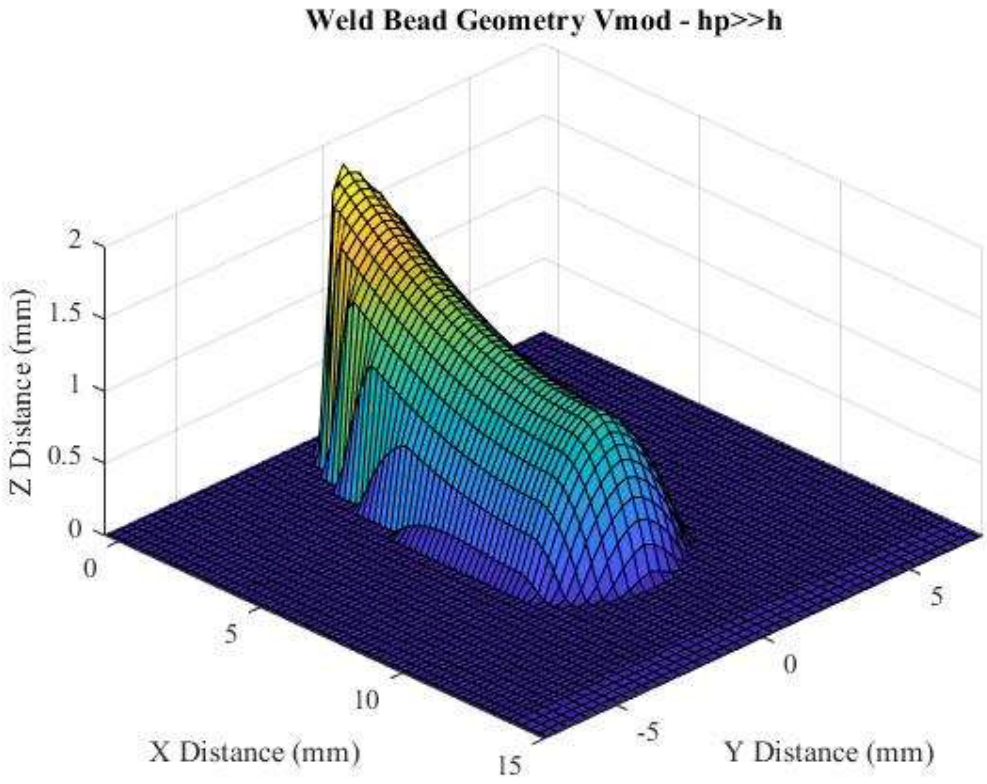

Figure 7.22 – Weld Bead Geometry V_{mod} when $h \ll h_p$

When analysing the data, it was found that this situation only occurred rarely as an outlier and was not a large hindrance on the overall accuracy of the plotting algorithm. However to get around this issue an extra criteria was added as shown in **Equation** 7.75 which helped maintain weld bead continuity in such situations.

$$h(t,n) = \begin{cases} h(t,n), & h(t,n) < h_p(t) - 0.2 \\ h_p(t) - 0.2, & h(t,n) \geq h_p(t) - 0.2 \end{cases} \quad (7.75)$$

7.12.3. Heat Distribution

Similar to the weld bead geometry algorithm, the heat distribution P, melting efficiency η_m and scaled heat distributions P_w were all checked to ensure that they performed as expected. **Figure 7.23** shows the heat distribution for standard short circuit, globular and spray transfer modes.

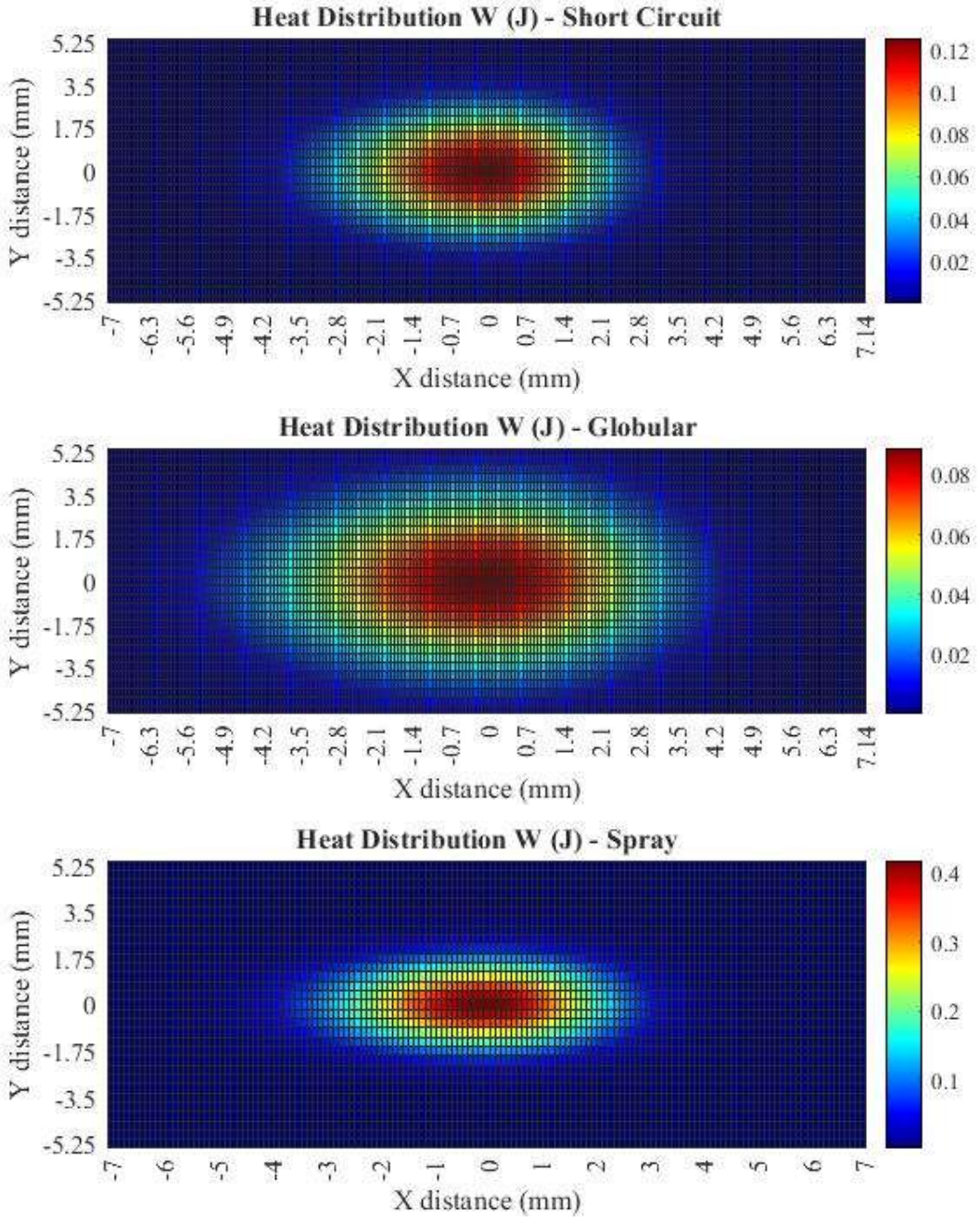

Figure 7.23 - Heat Distribution Plots

Looking at **Figure 7.23**, it can be seen that both short circuit and spray transfer have a much tighter heat distribution when compared to globular, with the overall heat input being largest when under spray transfer. Similarly the melting efficiency of the same 3 segments are shown in **Figure 7.24**.

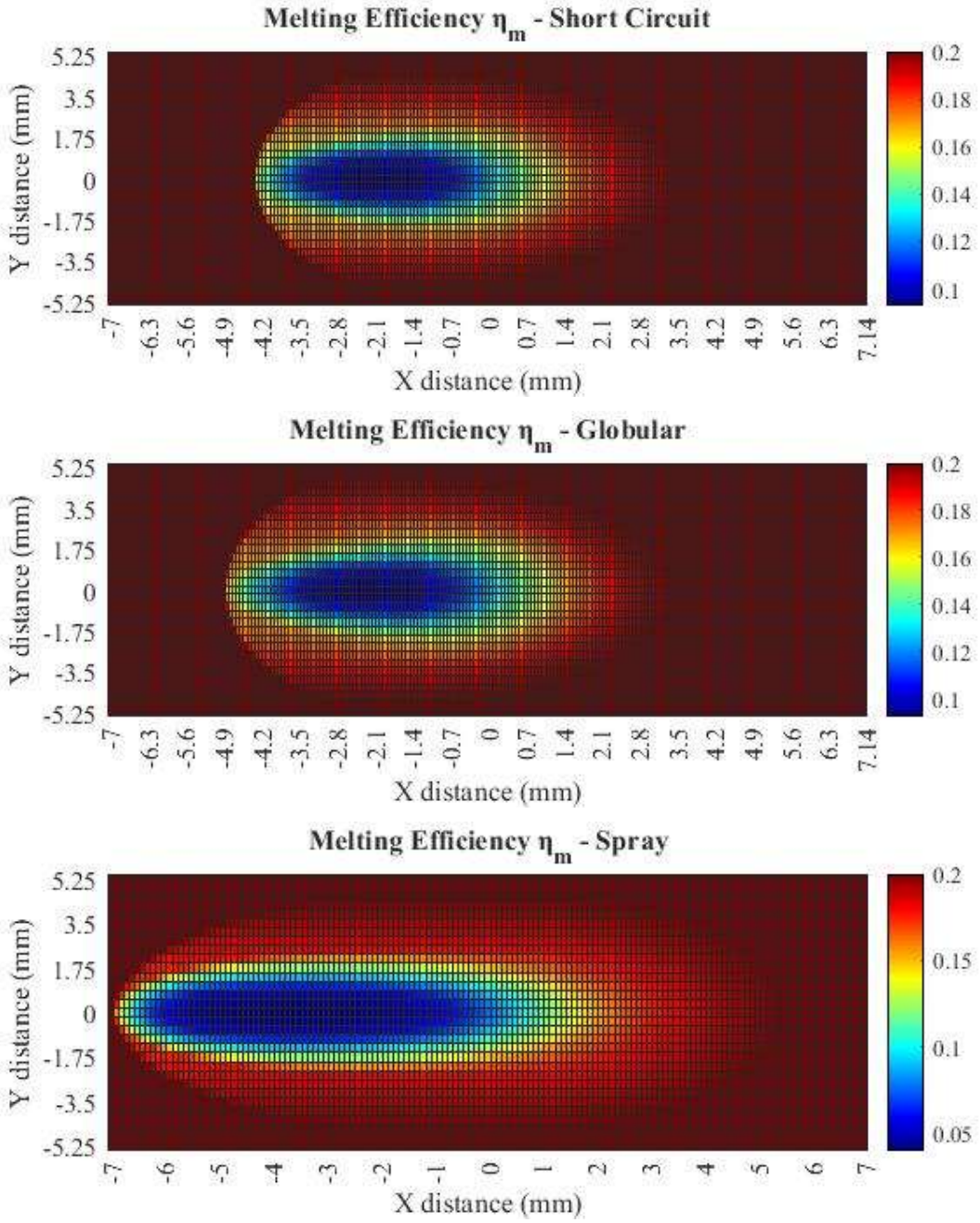

Figure 7.24 - Melting Efficiency Plots

When observing the melting efficiencies for the three different transfer modes it can be seen that the melting efficiencies in short circuit transfer and globular share significantly more similarities when compared to spray transfer. In spray transfer, it can be observed that the melting efficiency remains lower over a larger area when compared to the other 2 modes. This is due to the larger weld pool size and penetration depth that exists in higher powered spray transfer which effects the melting efficiency as shown in **Equation** 7.65. Similarly, as the weld pool and penetration depth is expected to be

significantly lower in short circuit and globular transfer, there is not as much molten material underneath the welding arc, in turn lowering the melting efficiency.

By multiplying the heat distribution and melting efficiency as shown in **Equation** 7.66, the scaled heat distribution can be obtained as shown in **Figure 7.25**

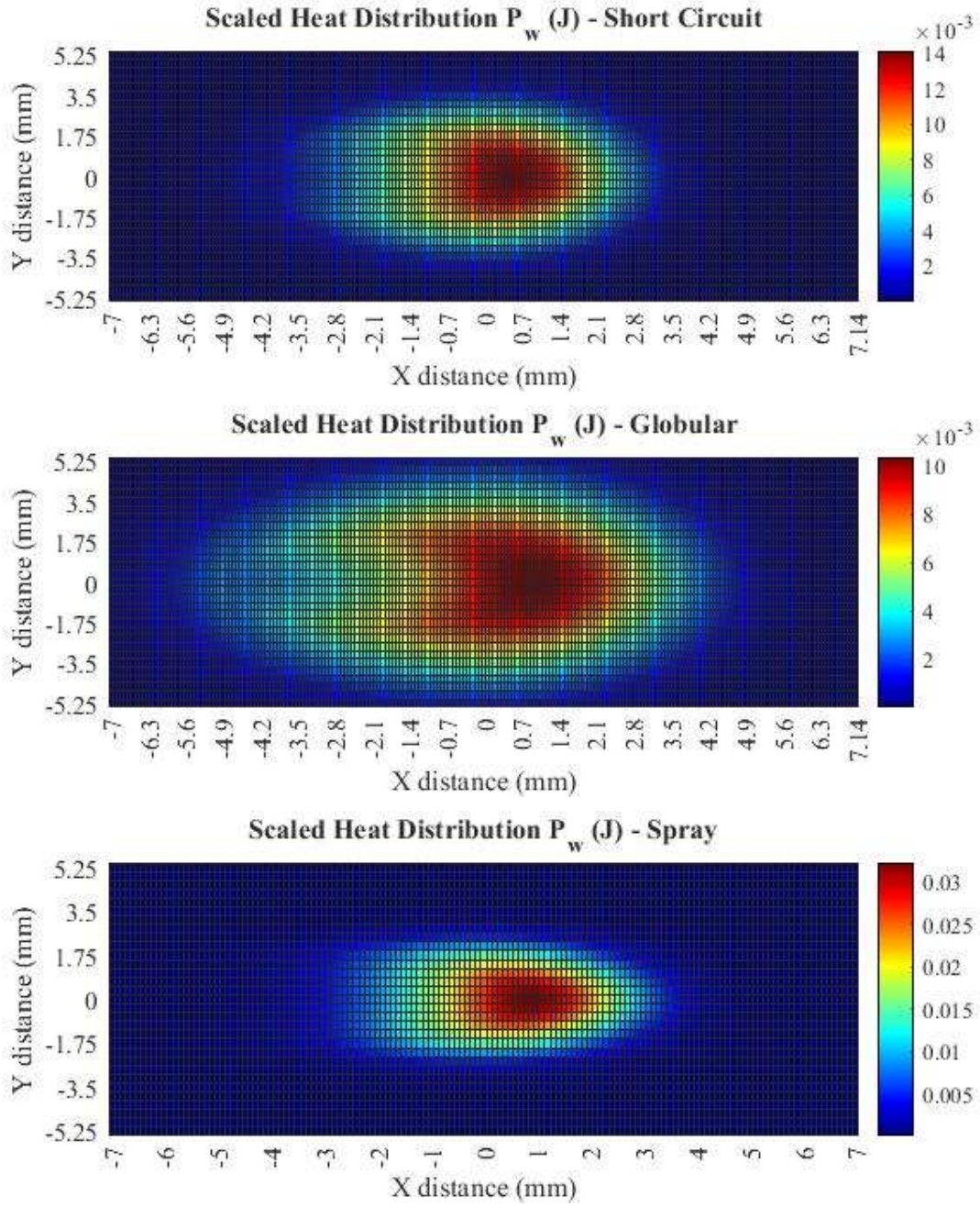

Figure 7.25 - Scaled Heat Distribution Plots

When observing the scaled heat distribution results, it can be seen that the trailing edge of the distribution of all three transfer modes is significantly lower when compared to the unscaled distribution as shown in **Figure 7.23**. It can also be seen that short circuit transfer has a similar total heat distribution,

while being more tightly distributed when compared to globular. Similarly, spray transfer is distributed similarly to short circuit transfer, however the total heat distribution is significantly higher.

7.12.4. Final results

The final weld bead and penetration profiles for the 8 welds outlined in **Table 7.1** can be seen in **Figure 7.26**.

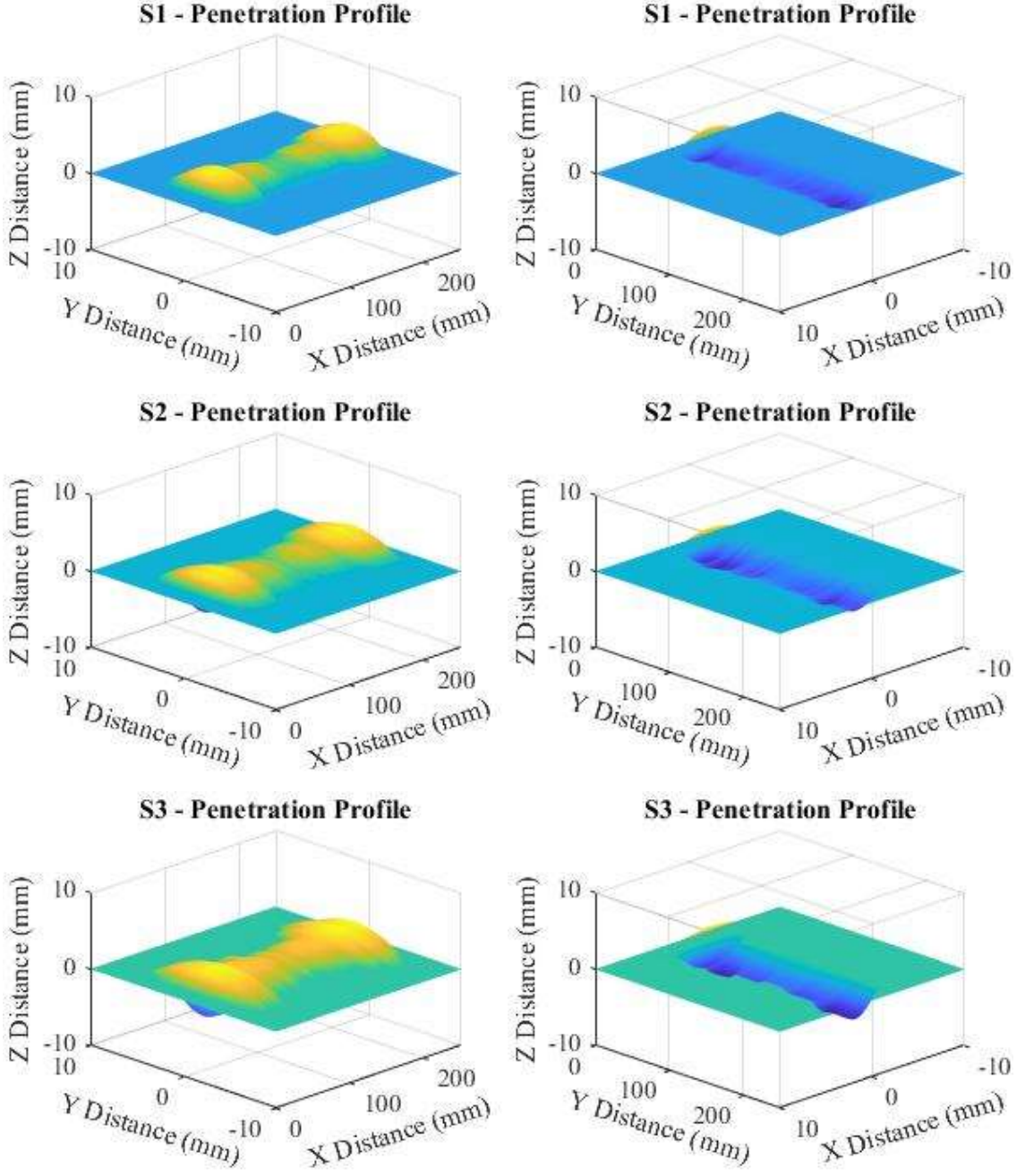

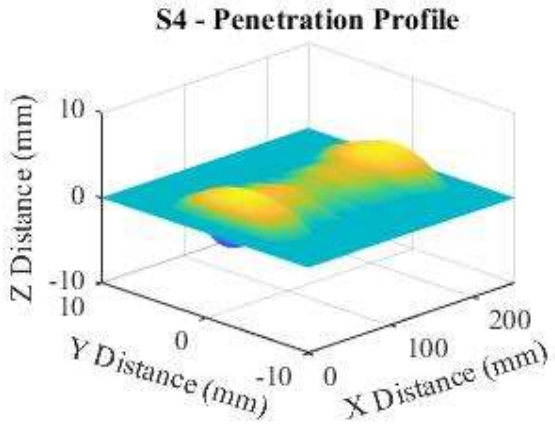
S4 - Penetration Profile
Z Distance (mm)
10
0
-10
10
0
-10
Y Distance (mm)
0
100
200
X Distance (mm)

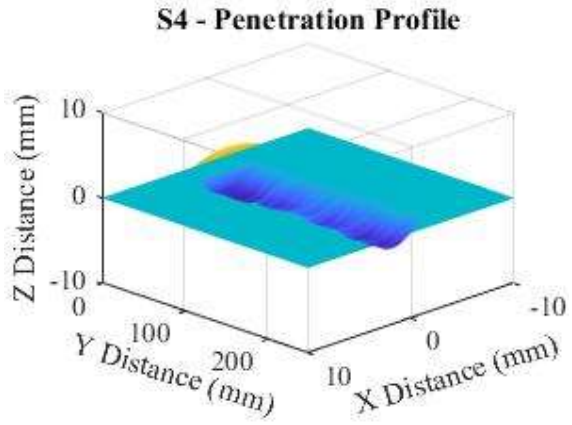
S4 - Penetration Profile
Z Distance (mm)
10
0
-10
0
100
200
Y Distance (mm)
10
0
-10
X Distance (mm)

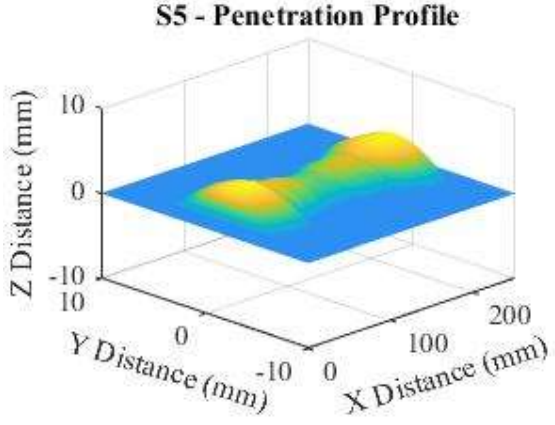
S5 - Penetration Profile
Z Distance (mm)
10
0
-10
10
0
-10
Y Distance (mm)
0
100
200
X Distance (mm)

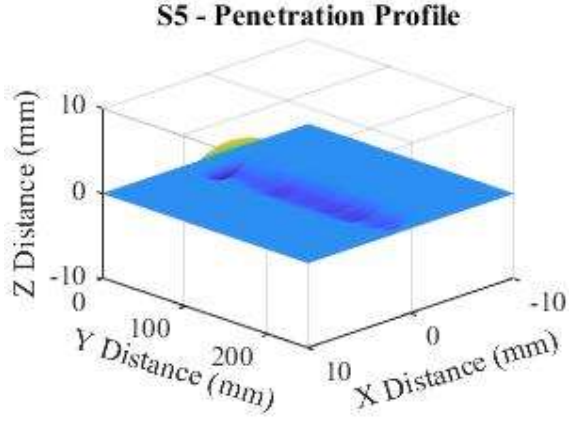
S5 - Penetration Profile
Z Distance (mm)
10
0
-10
0
100
200
Y Distance (mm)
10
0
-10
X Distance (mm)

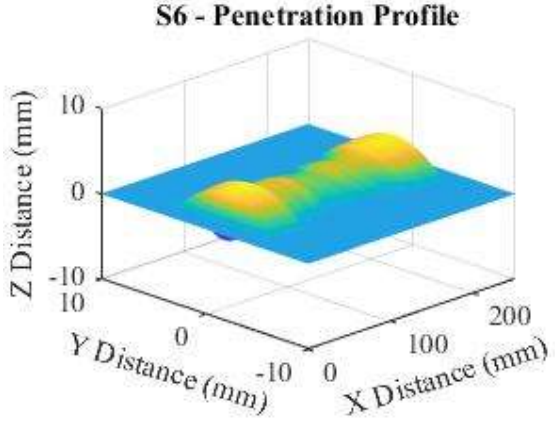
S6 - Penetration Profile
Z Distance (mm)
10
0
-10
10
0
-10
Y Distance (mm)
0
100
200
X Distance (mm)

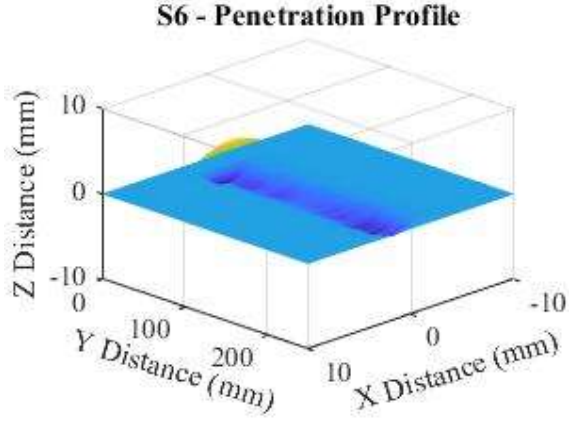
S6 - Penetration Profile
Z Distance (mm)
10
0
-10
0
100
200
Y Distance (mm)
10
0
-10
X Distance (mm)

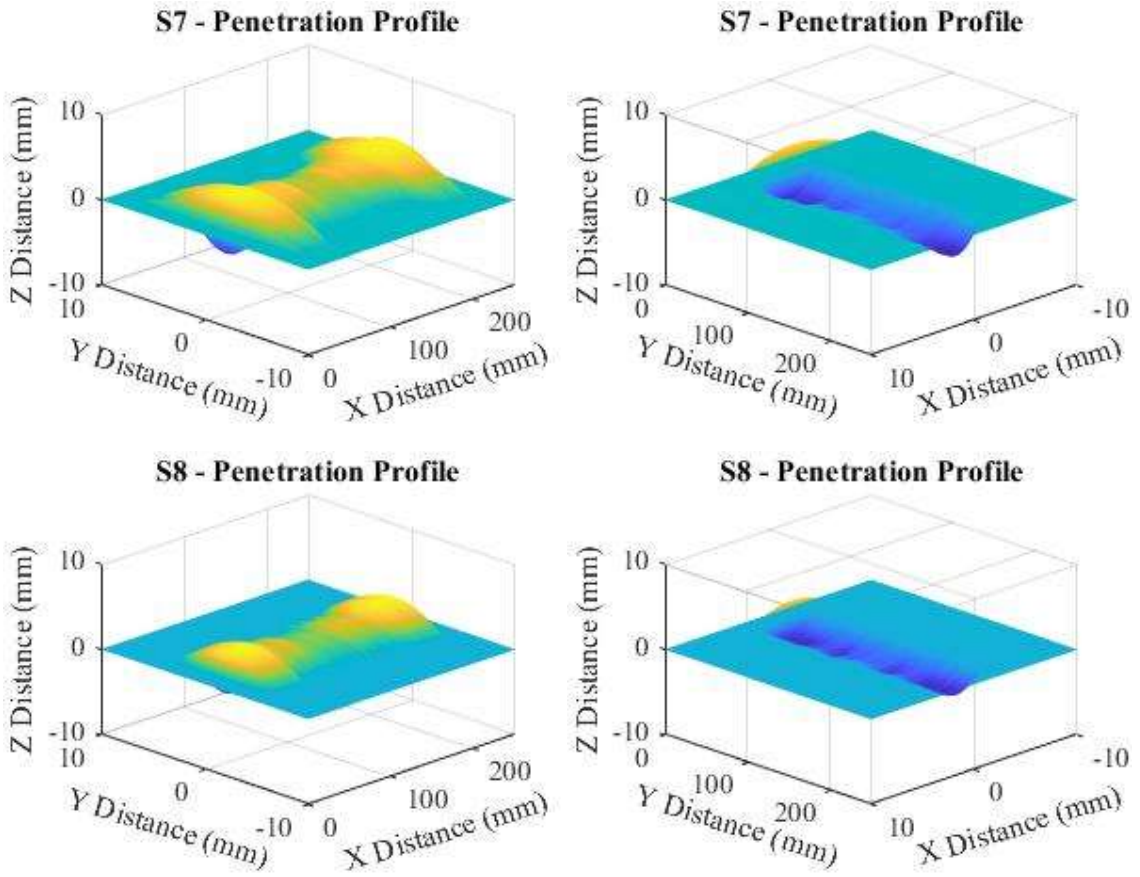

Figure 7.26 – Weld Bead Penetration Profiles

Similarly, the 2D penetration profiles about the centreline of the welds can be seen in **Figure 7.27**.

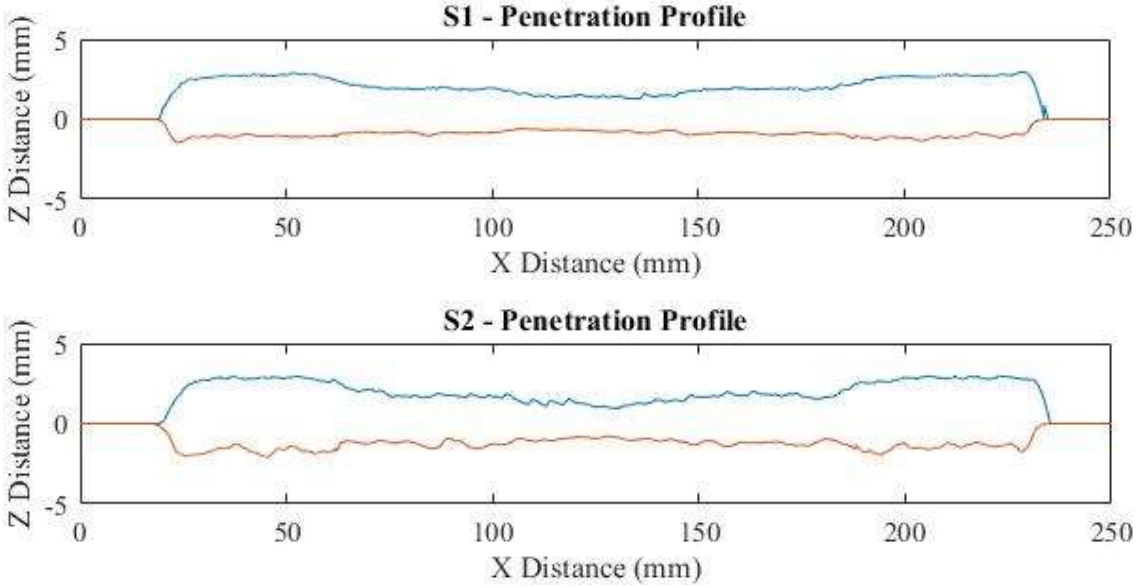

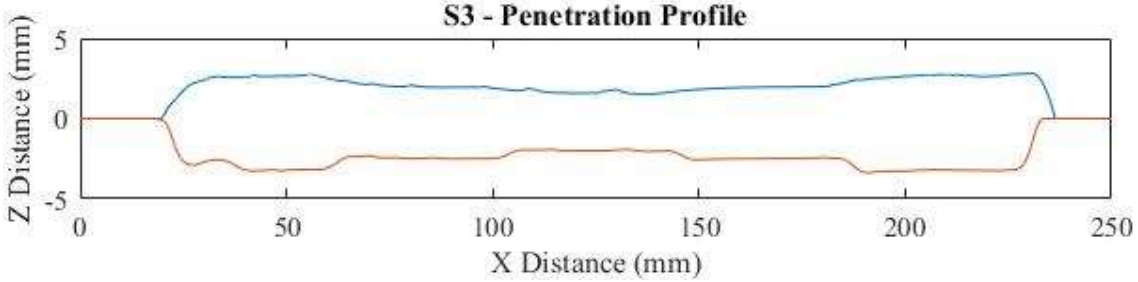
S3 - Penetration Profile
Z Distance (mm)
5
0
-5
0
50
100
150
200
250
X Distance (mm)

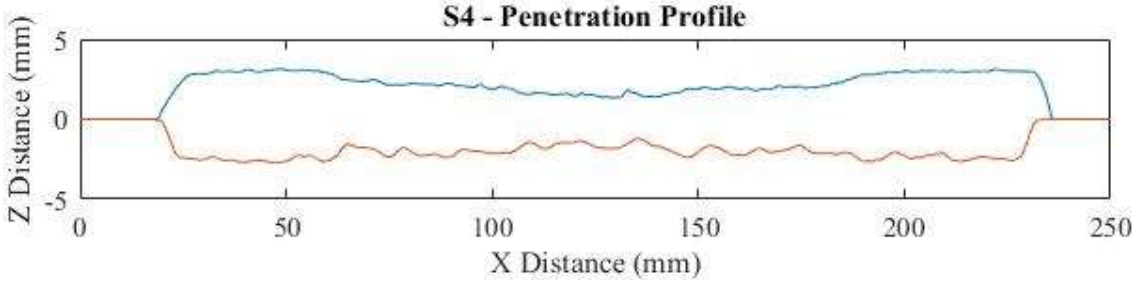
S4 - Penetration Profile
Z Distance (mm)
5
0
-5
0
50
100
150
200
250
X Distance (mm)

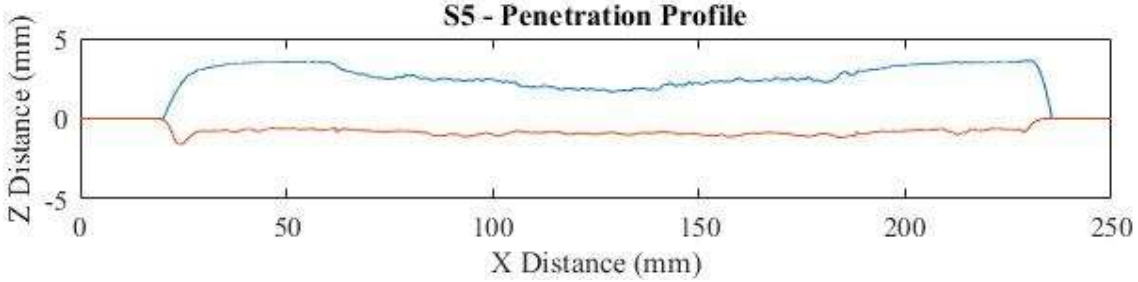
S5 - Penetration Profile
Z Distance (mm)
5
0
-5
0
50
100
150
200
250
X Distance (mm)

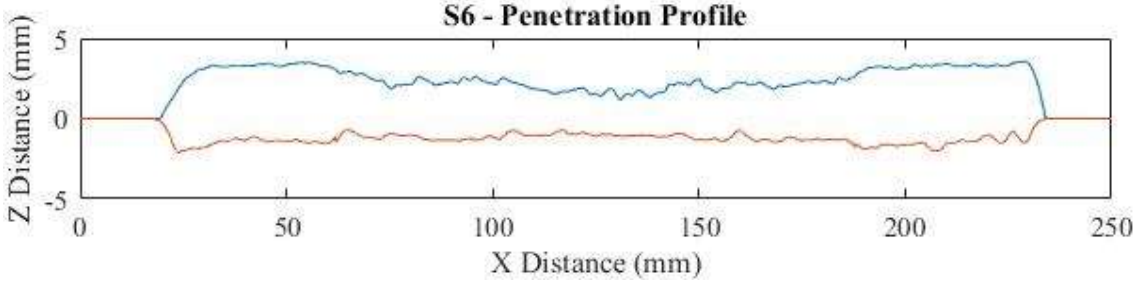
S6 - Penetration Profile
Z Distance (mm)
5
0
-5
0
50
100
150
200
250
X Distance (mm)

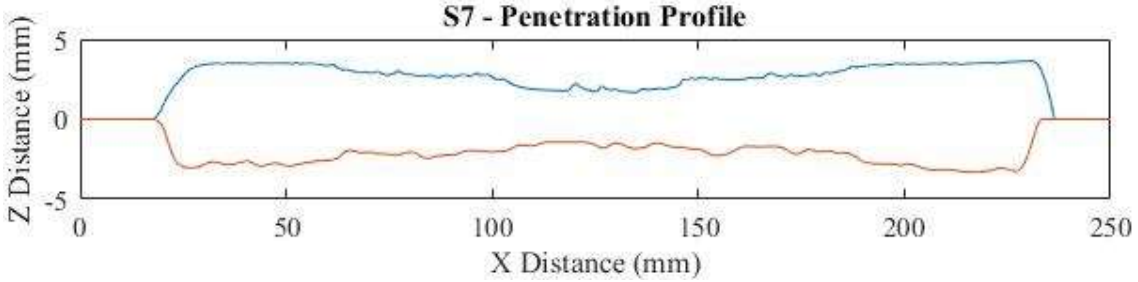
S7 - Penetration Profile
Z Distance (mm)
5
0
-5
0
50
100
150
200
250
X Distance (mm)

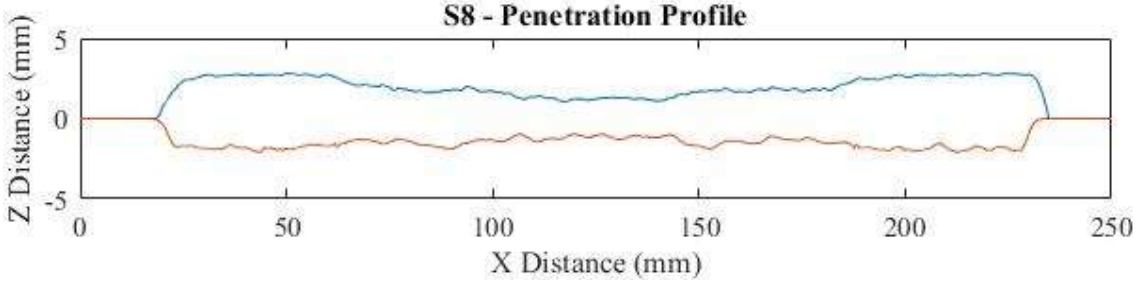

Figure 7.27 - Centreline Penetration Profiles

To compare the experimentally obtained cross sectional profiles with the calculated cross section profiles shown above in **Figure 7.26**, cross sectional slices were taken at the corresponding positions in which the weld beads were cut. **Figure 7.28** shows the calculated cross sections overlapping the measured cross sections at the 5 different cut locations for the 8 performed welds.

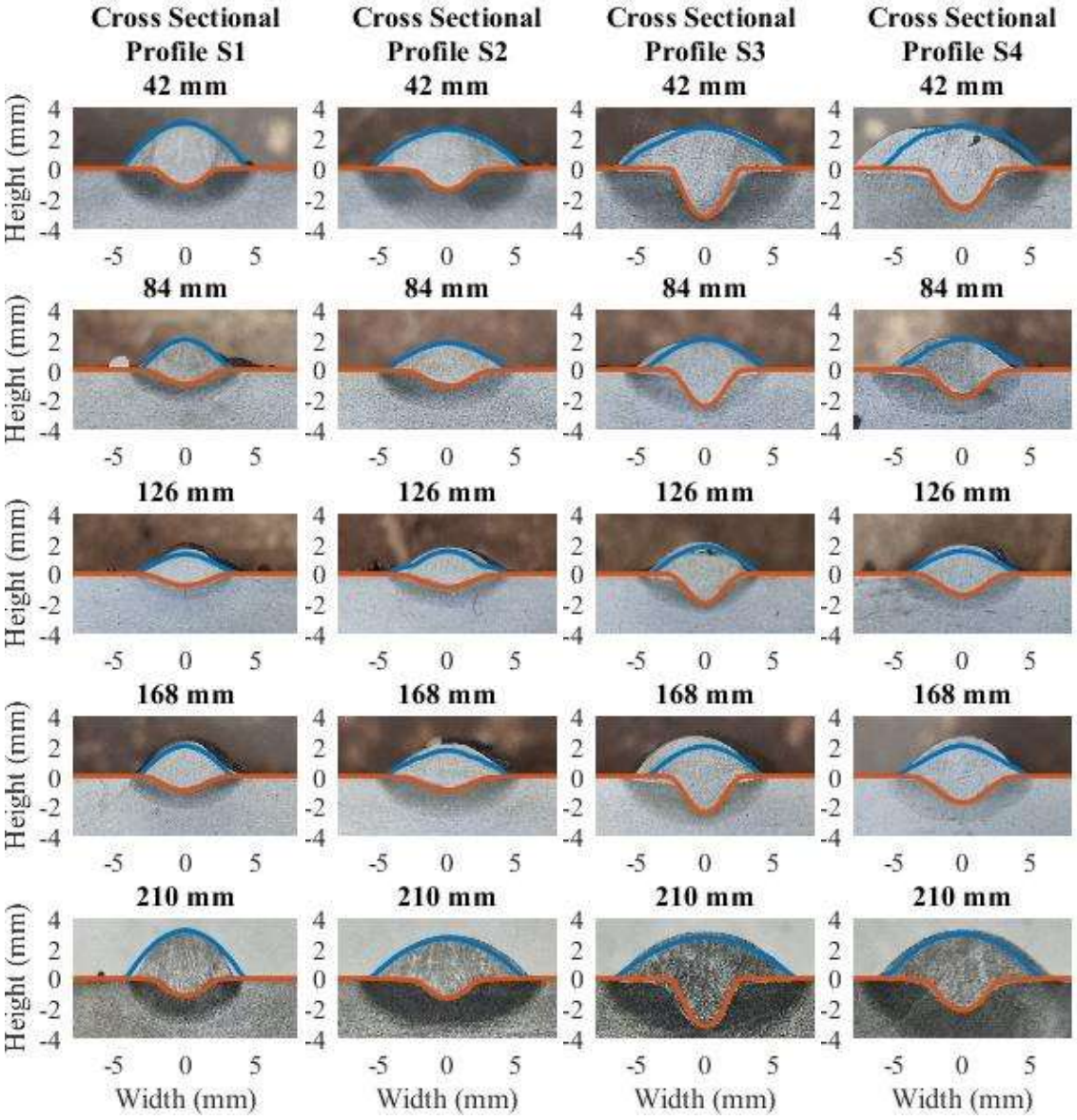

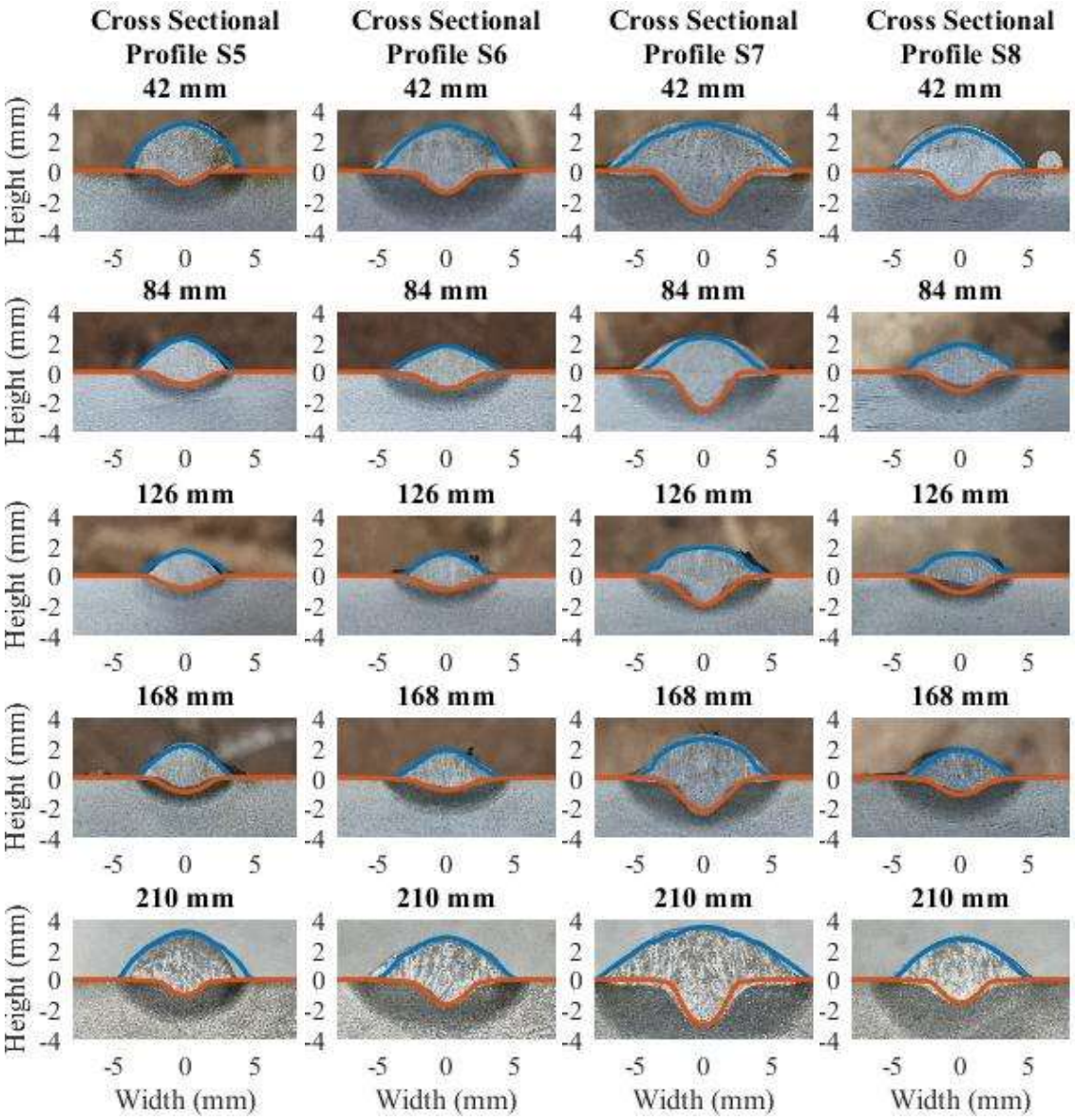

Figure 7.28 - Weld Bead Cross Sections

Looking at **Figure 7.28**, it can be seen that the algorithm is able to successfully plot the weld bead for all 40 analysed cross sections. In almost all of the above cross sections it is able to accurately plot the penetration profile within a margin of error of less than 10%. However, some of the weld bead shapes have a minor error as seen in tests S3 and S4, with the weld bead profile either being too small or being off centre. Due to the limitations of this system, the weld bead is always assumed to be symmetrical about the centreline of the weld path, however this is not always the case. Due to factors such as the instability of the welding arc, unevenness of the base geometry, fluctuations in the welding gas flow and contamination of the base material, the weld bead may form unevenly about the centreline as shown in the 42mm cross section for weld S4. Despite this, the penetration profile is still able to be accurately determined with only the bead profile being slightly off centre from the actual measured result.

7.13. Conclusion

This chapter introduced a new GMAW real time plotting system by monitoring the droplet transfer process. The model able to effectively plot the weld bead and penetration depth profiles of the weld in real time using an analytical geometric method in combination with the penetration depth estimation method introduced in **CHAPTER 6**. This innovative approach can generate cross-sectional profiles with a margin of error of under 10%, demonstrating its potential as an effective real-time penetration detection system.

CHAPTER 8 – CONCLUSION

In this thesis, a smart gas metal arc welding (GMAW) system was successfully developed based on acoustic signal monitoring. By monitoring the acoustic signal in real time throughout the welding process, a transfer mode detection algorithm was created to monitor changes in the droplet transfer process. The algorithm achieved a high accuracy of up to 96% in detecting and monitoring the droplet transfer mode every 20 ms. The system utilized time and frequency domain features extracted from the acoustic signal, which were then used to train a support vector machine (SVM) classifier. An innovative feature selection algorithm was also developed to determine the optimal feature set that maximizes the separability between different transfer modes.

Using the transfer mode detection system, a defect detection system was developed to identify the presence of porosity and burn-through in GMAW welds. A novel moving average pulse width algorithm was introduced to monitor real-time changes in the transfer mode during the welding process. It was observed that an unexpected increase in no droplet transfer indicated burn-through, while an unexpected increase in gasless explosive transfer suggested porosity in the weld bead.

Furthermore, the transfer mode detection system was employed to develop a penetration depth estimation system for GMAW welds. By combining the transfer mode detection with various input welding parameters, the system was capable of estimating the penetration depth of the weld bead. A dynamic energy estimation system based on the acoustic transfer mode detection was developed to estimate the root penetration depth.

By integrating the transfer mode detection, defect detection, penetration depth estimation, and weld bead plotting systems, a comprehensive smart GMAW system was established. This system effectively monitors the welding process, addressing quality control challenges often encountered in robotic welding applications. The acoustic monitoring system stands out due to its simplicity, ease of installation, and non-intrusiveness, making it an ideal plug-and-play solution for modern automated industrial GMAW welding applications. It minimizes costs and downtime associated with troubleshooting, non-destructive testing, and on-site reworks.

8.1. Future Work

Building upon the work presented in this thesis, future endeavors will focus on further improving and adapting the smart GMAW system. The following outlines the planned future work:

8.1.1. Development of a real time closed loop transfer mode control system

Currently, the system primarily focuses on monitoring transfer modes and detecting faults resulting from them. Future work will involve developing an active closed-loop feedback system capable of effectively adjusting welding input parameters to maintain arc stability. This will enhance weld uniformity and rectify potential defects before they occur.

8.1.2. Adapting the GMAW digital twin system for additional welding joint geometries

The current GMAW bead plotting and digital twin system is designed for standard bead-on-plate welds. However, it is important to consider other joint geometries. Future work will involve further developing the system to plot weld bead and penetration profiles for additional joint types, such as butt, tee, and lap joints.

8.1.3. Developing a AR welding assistance tool for manual welding

In addition to further developing the automated GMAW monitoring system, future work will include adapting the system as a training tool for manual welders. Utilizing the penetration and weld bead plotting system, an AR tool will be developed to allow manual welders to visualize the penetration profile of the GMAW process in real time. This system will be particularly beneficial for less-experienced welders, enabling them to assess the quality of their weld beads in real time without the need for costly post-production quality control checks.

CHAPTER 9 - Appendix

9.1. Nomenclature

a, coefficient in ellipsoid equation

A_e, element area

A_h, normalise heat distribution area

A_{h0}, element heat area indicator

A_m, currently melted area

A_n, normalised weld pool element area

A_r, radial area of an element

A_s, rectangular area of an element

A_T, total weld pool area

A_w, welding wire cross sectional area

A_{wp}, weld pool element area

b, coefficient in ellipsoid equation

B_0, melting efficiency constant

B_1, melting efficiency constant

B_2, melting efficiency constant

c, coefficient in ellipsoid equation

c_0, feature selection constant

c_s, specific heat

C, melting efficiency constant

C_c, cooling constant

C_e, cooling estimate

C_G, globular constant

C_s, penetration depth constant

C_{sc}, short circuit transfer constant

C_{Sp}, spray transfer constant

C_T, total number of classes

D_{avg}, average Bhattacharya distance

D_B, Bhattacharya distance

D_c, Contact tip to workpiece distance

D_{min}, minimum Bhattacharya distance

d_l, previous droplet location

d_p, penetration depth estimate

E, average melting enthalpy

E_{fm}, filler wire melting enthalpy

E_s, base material melting enthalpy

F_f, final feature set after feature selection

F_i, original complete feature set

F_t, temporary feature set

f, feature of feature set F_f

f_1, leading edge standard deviation constant

f_2, trailing edge standard deviation constant

f_{add}, feature selected for addition to feature set F_f

f_n, leading or trailing edge standard deviation constant

f_s, sampling frequency

f_{sp}, frequency spectrum

f_{sub}, feature selected for subtraction to feature set F_f

g, gravitational acceleration

h, weld pool height

h_0, maximum weld pool height when wetting angle is maximum at the trailing edge

h_{int}, weld pool height at critical point 3

h_m, maximum weld bead height

h_{min}, weld pool height at critical point 2

h_p, height of previous non molten point at trailing edge of the weld pool

h_x, maximum weld pool height when wetting angle is maximum at the leading edge

h_y, maximum weld pool height when wetting angle is maximum at the perpendicular edge

i, element co-ordinate in parallel welding direction

j, element co-ordinate in perpendicular welding direction

k, loop integer

k_1, 1st feature number

k_2, 2nd feature number

L_m, heat source location matrix

L_f, current number of features selected by the feature selection algorithm

M_c, element corner check

M_n, transfer mode classification

M_f, mel frequencies

M_{PP}, minimum peak prominence

M_{PA}, minimum peak amplitude

M_x, transfer mode standard deviation constant in the x direction

M_y, transfer mode standard deviation constant in the y direction

n, weld bead growth iteration

P, heat distribution

P_{MA}, moving average pulse width

P_w, weighted heat distribution

P_{width}, pulse width

p, number of segments since previous N/A transfer mode

R_0, radius of the trailing edge of the weld pool in the parallel direction

$R_{0_{int}}$, weld pool radius at trailing edge at critical point 3

R_{0_max}, weld pool radius at trailing edge at critical point 4

R_{int}, weld pool radius at critical point 3

R_{max}, weld pool radius at critical point 4

R_r, radius to projected trailing edge of the weld pool

R_x, radius of the leading edge of the weld pool in the parallel direction

R_y, radius of the weld pool in the perpendicular direction

R', modified weld pool radius

R'_0, modified weld pool radius at the trailing edge

s, signal segment

s_{avg}, signal average

s_l, segment length

S_L, Spatter loss coefficient

t, current time step

t_p, plate thickness

t_s, segment time step

T, weld pool element category

T_{avg}, average transfer mode coefficient

T_{Apw}, Absolute moving average pulse width algorithm threshold

T_{mc}, weighted transfer mode coefficient

T_h, feature selection algorithm threshold

T_{pw}, moving average pulse width algorithm threshold

T_{Spw}, Static moving average pulse width algorithm threshold

V_0, weld pool volume at critical point 1

V_B, weld bead volume above base material per element

V_{case}, current weld pool volume under each case's conditions

V_F, molten droplet volume

V_h, historical penetration volume

V_{int}, weld pool volume at critical point 3

V_l, total theoretical weld pool volume

V_{max}, weld pool volume at critical point 4

V_{min}, weld pool volume at critical point 2

V_{mod}, modified weld pool volume per element

V_p, penetration volume

V_r, radial volume of an element

V_s, rectangular volume of an element

V_T, total volume of weld pool and molten droplet

V_{wp}, molten weld pool volume

w_{pw}, moving average pulse width algorithm window width

w_x, element width in the parallel welding direction

w_y, element width in the parallel welding direction

W, normalised ellipsoid distribution

W_1, ellipsoid distribution for leading edge

W_2, ellipsoid distribution for trailing edge

W_c, number of time steps since last droplet transfer

W_n, ellipsoid distribution for leading or trailing edge

x, distance in parallel welding direction

x_0, distance co-ordinate at the trailing edge of the weld pool

x_c, distance co-ordinate at the centre of the weld pool

x_d, distance at coordinate i in parallel welding direction

x_f, distance co-ordinate at the leading edge of the weld pool

x_l, current welding position in the x direction

x_p, molten weld pool function in x direction

x_{r1}, trailing side radial coordinate

x_{r2}, leading side radial coordinate

x_{s1}, rectangular area coordinate

x_t, welding torch location

X_{avg}, signal average

X_{avgf}, average frequency

X_{cf}, crest factor

X_{fc}, frequency centre

X_{if}, impulse factor

X_{kv}, kurtosis value

X_{mf}, margin factor

X_{maxf}, max frequency

X_{p2p}, peak to peak value

X_{pf}, peak frequency

X_{rms}, root mean square

X_{rmsf}, root mean square frequency

X_{rvf}, root variance frequency

X_{sf}, shape factor

X_{sra}, square root of amplitude

X_{sv}, sharpness value

X_{zcr}, zero crossing rate

y, distance perpendicular to the welding direction

y_d, distance at coordinate j perpendicular to the welding direction

y_p, molten weld pool function in y direction

z, molten weld pool function in the z direction

z_b, weld bead height per element

z_l, molten weld pool function in the z direction at function limits

z_p, current penetration depth

ΔT, melting point of base material

η_a, arc efficiency

η_m, melting efficiency

θ_w, maximum wetting angle

μ_f, class separation mean

μ_n, ellipsoid distribution mean

ν, kinematic viscosity

v_f, wire feed speed

ρ, weld bead density

v_s, welding travel speed

σ, weld pool surface tension

σ_s, standard deviation of signal segment

Σ_f, class separation standard deviation

Σ_{favg}, average class separation standard deviation

Σ_n, ellipsoid distribution standard deviation

9.2. Cross Section Profile Data

Table 9.1 – Theoretically Calculated parameters

Test Number		Bead Height (mm)	Bead Width (mm)	Penetration Depth (mm)	Weld Bead Area (mm^2)	Penetration Area (mm^2)
1	42 mm	3.00	9.10	1.16	17.26	3.45
	84 mm	2.01	7.00	0.95	8.09	3.25
	126 mm	1.31	7.00	0.79	5.61	2.77
	168 mm	2.03	7.00	0.97	8.36	3.25
	210 mm	3.23	8.40	1.17	17.64	3.70
2	42 mm	2.56	10.20	1.43	18.48	4.73
	84 mm	1.77	9.10	1.14	9.92	4.26
	126 mm	1.51	9.10	0.90	7.01	3.71
	168 mm	1.70	9.10	0.94	9.43	3.80
	210 mm	2.70	10.20	1.33	19.58	4.31
3	42 mm	2.65	12.60	3.23	21.08	9.91
	84 mm	2.02	9.10	2.46	11.28	7.24
	126 mm	1.81	7.70	1.97	8.87	5.58
	168 mm	1.98	8.40	2.47	10.50	7.22
	210 mm	2.75	13.30	3.20	23.27	9.75
4	42 mm	2.78	11.90	2.62	21.87	8.91
	84 mm	2.02	9.80	1.91	11.84	6.49
	126 mm	1.52	8.40	1.44	7.50	5.05
	168 mm	2.03	9.80	1.76	11.40	6.99
	210 mm	2.99	11.90	2.14	22.37	7.52
5	42 mm	3.10	9.10	0.81	17.90	1.98
	84 mm	2.22	7.70	0.85	9.92	2.68
	126 mm	1.65	6.30	0.86	6.62	2.92
	168 mm	2.12	7.00	0.96	8.99	3.04
	210 mm	3.21	9.10	1.03	19.87	2.83
6	42 mm	2.60	10.50	1.43	19.02	4.50
	84 mm	1.73	9.10	1.10	8.50	4.20

	126 mm	1.48	7.00	0.94	5.86	3.71
	168 mm	1.87	7.70	0.85	7.90	3.52
	210 mm	2.81	10.50	1.67	17.62	5.45
7	42 mm	3.09	14.00	2.70	27.04	11.04
	84 mm	2.30	9.10	2.54	12.98	8.06
	126 mm	1.84	9.10	1.98	11.12	7.30
	168 mm	2.59	9.80	2.20	16.26	8.30
	210 mm	3.50	15.20	3.06	34.22	10.08
8	42 mm	2.72	10.50	1.75	17.11	5.56
	84 mm	1.83	8.40	1.29	9.63	4.37
	126 mm	1.46	7.70	1.14	7.31	4.20
	168 mm	1.86	7.00	1.15	8.61	4.22
	210 mm	2.75	9.80	1.55	17.21	4.75

Table 9.2 - Experimentally measured parameters

Test Number		Bead Height (mm)	Bead Width (mm)	Penetration Depth (mm)	Weld Bead Area (mm^2)	Penetration Area (mm^2)
1	42 mm	2.79	8.44	1.26	16.78	3.25
	84 mm	1.92	7.04	0.99	8.39	2.08
	126 mm	1.61	6.15	0.83	5.59	2.09
	168 mm	2.43	7.76	0.83	10.15	1.96
	210 mm	3.11	9.11	1.31	20.11	3.18
2	42 mm	2.46	10.94	1.39	18.37	3.95
	84 mm	1.86	8.78	1.03	9.19	2.94
	126 mm	1.71	7.45	0.93	6.12	2.20
	168 mm	2.10	8.72	0.88	10.87	2.51
	210 mm	2.78	11.55	1.51	20.21	4.60
3	42 mm	2.61	12.27	3.21	19.73	9.70
	84 mm	1.98	9.37	2.56	9.87	6.36
	126 mm	2.12	7.44	2.01	6.58	4.92
	168 mm	2.64	9.11	2.64	12.81	6.82
	210 mm	3.09	13.02	3.40	22.78	11.02
4	42 mm	2.83	13.45	2.43	22.16	7.61
	84 mm	2.14	9.26	1.58	11.08	4.94
	126 mm	1.34	7.97	1.34	7.39	3.80
	168 mm	2.66	9.21	1.89	12.87	4.93
	210 mm	3.21	13.02	2.14	23.93	7.61
5	42 mm	3.25	7.26	0.96	18.48	2.46
	84 mm	2.24	6.23	0.84	9.24	1.89
	126 mm	1.73	5.36	0.81	6.16	1.39
	168 mm	2.26	5.87	0.79	8.96	1.64
	210 mm	3.07	7.50	0.97	18.88	2.72
6	42 mm	2.84	10.17	1.58	16.78	4.73
	84 mm	1.66	8.23	1.13	8.24	2.96
	126 mm	1.43	6.78	0.80	5.61	2.27

	168 mm	1.71	7.90	0.83	7.97	2.72
	210 mm	2.60	10.60	1.70	15.99	5.10
7	42 mm	3.23	13.67	2.53	26.48	9.51
	84 mm	2.34	10.34	2.41	13.24	6.36
	126 mm	2.05	9.01	2.01	8.83	4.78
	168 mm	2.89	10.45	2.59	15.45	6.98
	210 mm	3.66	14.05	3.02	29.79	10.99
8	42 mm	3.01	9.83	1.77	16.23	5.44
	84 mm	1.87	7.76	0.98	8.51	3.02
	126 mm	1.46	6.81	0.80	5.72	1.92
	168 mm	1.88	8.33	1.01	8.69	3.18
	210 mm	2.67	10.81	1.56	15.31	5.36

REFERENCES

Uncategorized References

1. Tam, J. and J.P. Huissoon. *Developing psycho-acoustic experiments in gas metal arc welding*. in *International Conference on Mechatronics & Automation*. 2005. Niagara Falls, Canada.
2. Kah, P., *Chapter 1 - Gas metal arc welding*, in *Advancements in Intelligent Gas Metal Arc Welding Systems*, P. Kah, Editor. 2021, Elsevier. p. 1-103.
3. Yusof, M.F.M., et al., *Porosity detection by analyzing arc sound signal acquired during the welding process of gas pipeline steel.* 2017. **89**(9): p. 3661-3670.
4. Saini, D. and S. Floyd, *An investigation of gas metal arc welding sound signature for on-line quality control.* Welding Research Supplement, 1998: p. 172-179.
5. Lv, N., et al., *Automated control of welding penetration based on audio sensing technology.* Journal of Materials Processing Technology, 2017. **250**: p. 81-98.
6. Cayo, E.H. and S.C.A. Alfaro, *A Non-Intrusive GMA Welding Process Quality Monitoring System Using Acoustic Sensing.* Sensors (Basel, Switzerland), 2009. **9**(9): p. 7150-7166.
7. Sumesh, A., et al., *Use of Machine Learning Algorithms for Weld Quality Monitoring using Acoustic Signature.* Procedia Computer Science, 2015. **50**: p. 316-322.
8. Scotti, A., V. Ponomarev, and W. Lucas, *A scientific application oriented classification for metal transfer modes in GMA welding.* Journal of Materials Processing Technology, 2012. **212**(6): p. 1406-1413.
9. Lancaster, J.F., *Metal Transfer and Mass Flow in the Weld Pool*, in *The Physics of Welding (Second Edition)*, J.F. Lancaster, Editor. 1986, Pergamon Press: Oxford. p. 228-305.
10. Kim, Y.S. and T.W. Eager, *Analysis of metal transfer in gas metal arc welding.* Welding Journal, 1993. **72**: p. 269-278.
11. Iordachescu, D. and L. Quintino, *Steps toward a new classification of metal transfer in gas metal arc welding.* Journal of Materials Processing Technology, 2008. **202**(1): p. 391-397.
12. Weman, K., *19 - The weldability of steel*, in *Welding Processes Handbook (Second Edition)*, K. Weman, Editor. 2003, Woodhead Publishing. p. 191-206.
13. Kah, P., et al., *Usability of arc types in industrial welding.* International Journal of Mechanical and Materials Engineering, 2014. **9**: p. 1-12.
14. Kim, Y.S. and T.W. Eager, *Metal transfer in pulsed current gas metal arc welding.* Welding Journal (Miami); (United States), 1993. **72:7**.
15. Scotti, A., V. Ponomarev, and W. Lucas, *Interchangeable metal transfer phenomenon in GMA welding: Features, mechanisms, classification.* Journal of Materials Processing Technology, 2014. **214**(11): p. 2488-2496.
16. Kim, D.-Y., et al., *Effect of Porosity on the Fatigue Behavior of Gas Metal Arc Welding Lap Fillet Joint in GA 590 MPa Steel Sheets.* Metals, 2018. **8**(4): p. 241.

17. Sumesh, A., et al., *Establishing Correlation Between Current and Voltage Signatures of the Arc and Weld Defects in GMAW Process.* Arabian journal for science and engineering (2011), 2017. **42**(11): p. 4649-4665.
18. Mugrauer, C., *Modeling of Turbulent Particle/Gas Dispersion in the Mold Region and Particle Entrapment into the Solid Shell of a Steel Continuous Caster*. 2008.
19. Ueyama, T., et al., *AC pulsed GMAW improves sheet metal joining.* Welding Journal (Miami, Fla), 2005. **84**: p. 40-46.
20. Terner, M., et al., *Influence of Gas Metal Arc Welding Parameters on the Bead Properties in Automatic Cladding.* Journal of Welding and Joining, 2017. **35**: p. 16-25.
21. Cheng, Y., et al., *Real-time sensing of gas metal arc welding process – A literature review and analysis.* Journal of Manufacturing Processes, 2021. **70**: p. 452-469.
22. Grad, L., et al., *Feasibility study of acoustic signals for on-line monitoring in short circuit gas metal arc welding.* International Journal of Machine Tools and Manufacture, 2004. **44**(5): p. 555-561.
23. Matteson, A., R. Morris, and R. Tate. *Real-time GMAW quality classification using an artificial neural network with airborne acoustic signals as inputs*. in *OMAE `93: 12th international conference on offshore mechanics and arctic engineering*. 1993. Glasgow, United Kingdom.
24. Rouffet, M.E., et al., *Spectroscopic investigation of the high-current phase of a pulsed GMAW process.* Journal of Physics D: Applied Physics, 2010. **43**(43): p. 434003.
25. Zhiyong, L., et al., *On the Use of Arc Radiation to Detect the Quality of Gas Metal Arc Welds.* Materials and Manufacturing Processes, 2011. **26**(7): p. 933-941.
26. Zhao, Z., et al., *Optimal imaging band selection mechanism of weld pool vision based on spectrum analysis.* Optics & Laser Technology, 2019. **110**: p. 145-151.
27. Jacobsen, F. and P.M. Juhl, *Fundamentals of General Linear Acoustics*. 2013, New York, UNITED KINGDOM: John Wiley & Sons, Incorporated.
28. Dos Santos, E.B.F., et al., *On the Visualization of Gas Metal Arc Welding Plasma and the Relationship Between Arc Length and Voltage.* 2017. **7**(5): p. 503.
29. Zielińska, S., et al., *Investigations of GMAW plasma by optical emission spectroscopy.* Plasma Sources Science and Technology, 2007. **16**(4): p. 832-838.
30. Bachmann, B., E. Siewert, and J. Schein, *In situdroplet surface tension and viscosity measurements in gas metal arc welding.* Journal of Physics D: Applied Physics, 2012. **45**(17): p. 175202.
31. Zhao, S., et al., *A lumped-parameter model for sound generation in gas metal arc welding.* Mechanical systems and signal processing, 2021. **147**: p. 107085.
32. Carlson, N.M., J.A. Johnson, and H.B. Smartt, *Sensing of Metal-Transfer Mode for Process Control of GMAW.* Review of Progress in Quantitative Nondestructive Evaluation, 1990. **9**: p. 1965-1972.

33. Zhao, S., et al. *Statistical characteristics of Gas Metal Arc Welding (GMAW) sound*. in *23rd International Congress on Acoustics*. 2020. Aachen, Germany.
34. Praveen, P., M.J. Kang, and P.K.D.V. Yarlagadda, *Drop transfer mode prediction in pulse GMAW of aluminum using statistical model.* Journal of materials processing technology, 2008. **201**(1): p. 502-506.
35. Pal, K., S. Bhattacharya, and S.K. Pal, *Prediction of metal deposition from arc sound and weld temperature signatures in pulsed MIG welding.* International journal of advanced manufacturing technology, 2009. **45**(11-12): p. 1113-1130.
36. Tam, J., *Methods of Characterizing Gas-Metal Arc Welding Acoustics for Process Automation*. 2005, University of Waterloo. p. 120.
37. Wang, J. and J.P. Huissoon. *Classifying Arc Acoustic Data in GMA Welding Using Artificial Neural Network and Naïve Bayesian Classifiers*. in *Trends in Welding Research*. 2008. Georgia, USA.
38. Rudas, J.S., J.S. Restrepo, and L.M. Gómez. *Prediction of metal transfer modes in the GMAW process*. in *2015 IEEE 2nd Colombian Conference on Automatic Control (CCAC)*. 2015.
39. Zhao, S., et al. *GMAW metal transfer mode identification from welding sound*. in *Proceedings of ACOUSTICS 2018*. 2018. Adelaide, Australia.
40. Wang, Y., X. Lü, and H. Jing, *Dynamic simulation of short-circuiting transfer in GMAW based on the "mass-spring" model.* The International Journal of Advanced Manufacturing Technology, 2016. **87**(1): p. 897-907.
41. Wang, F., et al., *Modelling and analysis of metal transfer in gas metal arc welding.* Journal of Physics D: Applied Physics, 2003. **36**(9): p. 1143-1152.
42. Zhao, Y. and H. Chung, *Numerical simulation of the transition of metal transfer from globular to spray mode in gas metal arc welding using phase field method.* Journal of Materials Processing Technology, 2018. **251**: p. 251-261.
43. Kim, C.H., Y.N. Ahn, and K.B. Lee, *Droplet transfer during conventional gas metal arc and plasma-gas metal arc hybrid welding with Al 5183 filler metal.* Current Applied Physics, 2012. **12**: p. S178-S183.
44. Shao, Y., *Vision based real-time monitoring and control of metal transfer in laser enhanced gas metal arc welding*. 2013, University of Kentucky: ProQuest Dissertations Publishing. p. 140.
45. Jialei, Z., J. Xiangdong, and Q. Xi, *Application Study of Edge Detection for Droplet in Laser Enhanced GMAW Welding.* 2014. **6**: p. 952605.
46. Doodman Tipi, A.R., S.K.H. sani, and N.J.T.I.J.o.A.M.T. Pariz, *Improving the dynamic metal transfer model of gas metal arc welding (GMAW) process.* 2015. **76**(1): p. 657-668.

47. Chen, C., et al., *Analysis of droplet transfer, weld formation and microstructure in Al-Cu alloy bead welding joint with pulsed ultrasonic-GMAW method.* Journal of Materials Processing Technology, 2019. **271**: p. 144-151.
48. Wang, Z., *A laser back-lighting based metal transfer monitoring system for robotic gas metal arc welding.* Robotics and Computer-Integrated Manufacturing, 2016. **38**: p. 52-66.
49. Nomura, K., et al., *Tomographic spectroscopic observation of argon and metal vapor behavior in MIG arc welding.* 2016. **60**(1): p. 117-125.
50. Soderstrom, E.J., K.M. Scott, and P.F. Mendez, *Calorimetric Measurement of Droplet Temperature in GMAW.* Welding Journal, 2011. **90**(4): p. 77.S-84.S.
51. Chen, M., C. Wu, and Y. Lu, *Computer-based sensing and visualizing of metal transfer mode in gas metal arc welding.* China Welding, 2008. **17**(1): p. 71-74.
52. Teixeira, G.S., J.A.E.J.J.o.t.B.S.o.M.S. Mazzaferro, and Engineering, *GMA welding metal transfer mode study by high-speed imaging and electrical signal acquisition.* 2019. **41**(8): p. 315.
53. Valensi, F., et al., *Study of the spray to globular transition in gas metal arc welding: a spectroscopic investigation.* Journal of Physics D: Applied Physics, 2013. **46**(22): p. 224005.
54. Xia, Z., et al., *Spectral regression based fault feature extraction for bearing accelerometer sensor signals.* Sensors (Basel, Switzerland), 2012. **12**(10): p. 13694-13719.
55. Zhang, Z., G. Wen, and S. Chen, *Audible Sound-Based Intelligent Evaluation for Aluminum Alloy in Robotic Pulsed GTAW: Mechanism, Feature Selection, and Defect Detection.* IEEE Transactions on Industrial Informatics, 2018. **14**(7): p. 2973-2983.
56. Koolagudi, S.G., D. Rastogi, and K.S. Rao, *Identification of Language using Mel-Frequency Cepstral Coefficients (MFCC).* Procedia Engineering, 2012. **38**: p. 3391-3398.
57. García-Allende, P.B., et al., *Spectral processing technique based on feature selection and artificial neural networks for arc-welding quality monitoring.* NDT & E International, 2009. **42**(1): p. 56-63.
58. Tharwat, A., et al., *Linear discriminant analysis: A detailed tutorial.* 2017. **30**: p. 169-190.
59. Gómez-Chova, L., et al. *Feature Selection of Hyperspectral Data Through Local Correlation and SFFS for Crop Classification*. in *IEEE Int. Geosci. Remote Sens. Symp. Proc.* 2003. Toulouse, France.
60. Mitchell Cullen, S.Z., JC Ji, *Acoustic Based Classification of Transfer Modes in Gas Metal Arc Welding*, in *Acoustics 2021*. 2022: Wollongong, NSW, Australia.
61. Cullen, M., et al., *Classification of transfer modes in gas metal arc welding using acoustic signal analysis.* International journal of advanced manufacturing technology, 2021. **115**(9-10): p. 3089.
62. Adewole, A., *Learning and online prediction of weld quality in robotic GMAW*. 2019, Colorado School of Mines.

63. Jolly, W.D., *Acoustic Emission Exposes Cracks during Welding.* The Welding Journal, 1969. **48**: p. 21-27.
64. Čudina, M. and J. Prezelj, *Evaluation of the sound signal based on the welding current in the gas—metal arc welding process.* Proceedings of the Institution of Mechanical Engineers. Part C, Journal of mechanical engineering science, 2003. **217**(5): p. 483-494.
65. Čudina, M., J. Prezelj, and I. Polajnar, *Use of Audible Sound For On-Line Monitoring of Gas Metal Arc Welding Process.* Metalurgija, 2008. **47**.
66. Cayo, E. and S. Alfaro, *GMAW process stability evaluation through acoustic emission by time and frequency domain analysis.* Journal of Achievements in Materials and Manufacturing Engineering, 2009. **34**.
67. Luksa, K., *Correspondence between sound emissions generated in the GMA welding process and signals registered in the arc circuit.* Welding international, 2003. **17**(6): p. 438-441.
68. Asif, K., et al., *Machine learning model to predict welding quality using air-coupled acoustic emission and weld inputs.* Journal of intelligent manufacturing, 2020. **33**(3): p. 881-895.
69. Rohe, M., et al., *Detecting Process Anomalies in the GMAW Process by Acoustic Sensing with a Convolutional Neural Network (CNN) for Classification.* Journal of Manufacturing and Materials Processing, 2021. **5**(4): p. 135.
70. Zhang, Z., et al., *Multisensor-based real-time quality monitoring by means of feature extraction, selection and modeling for Al alloy in arc welding.* Mechanical Systems and Signal Processing, 2015. **60-61**: p. 151-165.
71. Luo, Z., et al., *Monitoring of laser welding using source localization and tracking processing by microphone array.* The International Journal of Advanced Manufacturing Technology, 2016. **86**(1): p. 21-28.
72. Pal, K., S. Bhattacharya, and S.K. Pal, *Investigation on arc sound and metal transfer modes for on-line monitoring in pulsed gas metal arc welding.* Journal of Materials Processing Technology, 2010. **210**(10): p. 1397-1410.
73. Zhang, L., et al., *Real-time monitoring of welding process using air-coupled ultrasonics and acoustic emission.* The International Journal of Advanced Manufacturing Technology, 2019. **101**(5): p. 1623-1634.
74. Pal, K. and S.K. Pal, *Monitoring of Weld Penetration Using Arc Acoustics.* Materials and manufacturing processes, 2011. **26**(5): p. 684-693.
75. Adolfsson, S., K. Ericson, and A. Grennberg, *AUTOMATIC DETECTION OF BURN-THROUGH IN GMA WELDING USING A PARAMETRIC MODEL.* Mechanical systems and signal processing, 1996. **10**(5): p. 633-657.
76. Alfaro, S.C.A., D. de S. Mendonça, and M.S. Matos, *Emission spectrometry evaluation in arc welding monitoring system.* Journal of Materials Processing Technology, 2006. **179**(1): p. 219-224.

77. Abbasi, Z., et al., *The Detection of Burn-Through Weld Defects Using Noncontact Ultrasonics.* Materials, 2018. **11**(1): p. 128.
78. Thekkuden, D.T., et al., *Instant detection of porosity in gas metal arc welding by using probability density distribution and control chart.* International journal of advanced manufacturing technology, 2018. **95**(9-12): p. 4583-4606.
79. Moinuddin, S.Q., et al. *A study on weld defects classification in gas metal arc welding process using machine learning techniques*. 2021. Elsevier Ltd.
80. Zhang, Y., et al., *Pores formation in laser–MAG welding of 42CrMo steel.* Journal of materials processing technology, 2017. **245**: p. 309-317.
81. Zhang, L., et al., *Characterization of GMAW (Gas Metal Arc Welding) Penetration Using Ultrasonics.* Materials, 2020. **13**(10): p. 2307.
82. Cullen, M., J.C. Ji, and S. Zhao, *Real time acoustic based burn through detection in gas metal arc welding*. 2021, Engineers Australia: BARTON, ACT.
83. Kah, P., et al., *Robotic arc welding sensors and programming in industrial applications.* International journal of mechanical and materials engineering, 2015. **10**(1): p. 1.
84. Wang, Y. and P. Zhao, *Noncontact acoustic analysis monitoring of plasma arc welding.* International Journal of Pressure Vessels and Piping, 2001. **78**(1): p. 43-47.
85. Saad, E., H. Wang, and R. Kovacevic, *Classification of molten pool modes in variable polarity plasma arc welding based on acoustic signature.* Journal of Materials Processing Technology, 2006. **174**(1): p. 127-136.
86. Huang, W. and R. Kovacevic, *A neural network and multiple regression method for the characterization of the depth of weld penetration in laser welding based on acoustic signatures.* Journal of Intelligent Manufacturing, 2011. **22**(2): p. 131-143.
87. Chen, C., et al., *Arc sound model for pulsed GTAW and recognition of different penetration states.* International journal of advanced manufacturing technology, 2020. **108**(9-10): p. 3175-3191.
88. Huang, W. and R. Kovacevic, *Feasibility study of using acoustic signals for online monitoring of the depth of weld in the laser welding of high-strength steels.* 2009. **223**(4): p. 343-361.
89. Zhang, Z. and S. Chen, *Real-time seam penetration identification in arc welding based on fusion of sound, voltage and spectrum signals.* Journal of Intelligent Manufacturing, 2017. **28**(1): p. 207-218.
90. Wang, Q., et al., *Weld bead penetration state recognition in GMAW process based on a central auditory perception model.* Measurement : journal of the International Measurement Confederation, 2019. **147**: p. 106901.
91. Mvola, B., P. Kah, and P. Layus, *Review of current waveform control effects on weld geometry in gas metal arc welding process.* International journal of advanced manufacturing technology, 2018. **96**(9-12): p. 4243-4265.

92. Zhang, H., C. Wang, and S. Lin, *Molten Pool Behaviors in Double-Sided Pulsed GMAW of T-Joint: A Numerical Study.* Metals, 2021. **11**(10): p. 1594.
93. Lee, Y., et al., *Effect of Fluid Convection on Dendrite Arm Spacing in Laser Deposition.* Metallurgical and Materials Transactions B, 2014.
94. Attarha, M.J. and I. Sattari-Far, *Study on welding temperature distribution in thin welded plates through experimental measurements and finite element simulation.* Journal of Materials Processing Technology, 2011. **211**(4): p. 688-694.
95. Bestard, G.A., et al., *Sensor Fusion to Estimate the Depth and Width of the Weld Bead in Real Time in GMAW Processes.* Sensors (Basel, Switzerland), 2018. **18**(4): p. 962.
96. Zalakain-Azpiroz, A., et al., *A calibration tool for weld penetration depth estimation based on dimensional and thermal sensor fusion.* International journal of advanced manufacturing technology, 2021. **119**(3-4): p. 2145-2158.
97. Penttilä, S., et al., *Artificial Neural Network Controlled GMAW System: Penetration and Quality Assurance in a Multi-Pass Butt Weld Application.* International journal of advanced manufacturing technology, 2019. **105**(7-8): p. 3369-3385.
98. Methong, T., et al., *Visualization of gas metal arc welding on globular to spray transition current.* Science and Technology of Welding and Joining, 2018. **23**(1): p. 87-94.
99. Mamat, S.B., et al., *Droplet Temperature Measurement in Metal Inert Gas Welding Process by Using Two Color Temperature Measurement Method.* Welding Society Proceedings, 2017. **35**(2): p. 160s-164s.
100. Monier, R., et al., *In situ experimental measurement of temperature field and surface tension during pulsed GMAW*. 2016. **60**(5): p. 1021-1028.
101. Yamazaki, K., et al., *The measurement of metal droplet temperature in GMA welding by infrared two-colour pyrometry.* Welding International, 2010. **24**(2): p. 81-87.
102. Kozakov, R., et al., *Weld pool temperatures of steel S235 while applying a controlled short-circuit gas metal arc welding process and various shielding gases.* Journal of Physics D: Applied Physics, 2013. **46**(47): p. 475501.
103. Mitchell Cullen, J.J., Sipei Zhao, *Acoustic based GMAW penetration depth identification using droplet transfer monitoring*, in *CASE 2022*. 2022: Mexico City, Mexico.
104. Karadeniz, E., U. Ozsarac, and C. Yildiz, *The effect of process parameters on penetration in gas metal arc welding processes.* Materials & Design, 2007. **28**(2): p. 649-656.
105. Nouri, M., A. Abdollah-Zadeh, and F. Malek, *Effect of welding parameters on dilution and weld bead geometry in cladding.* Journal of materials science & technology, 2007. **23**(6): p. 817-822.
106. Goyal, V.K., P.K. Ghosh, and J.S. Saini, *Analytical studies on thermal behaviour and geometry of weld pool in pulsed current gas metal arc welding.* Journal of materials processing technology, 2009. **209**(3): p. 1318-1336.

107. Azar, A.S., S.K. Ås, and O.M. Akselsen, *Analytical Modeling of Weld Bead Shape in Dry Hyperbaric GMAW Using Ar-He Chamber Gas Mixtures.* Journal of materials engineering and performance, 2012. **22**(3): p. 673-680.

108. Zhu, C., et al., *Study on arc characteristics and their influences on weld bead geometry in narrow gap GMAW of 5083 Al-alloy.* International journal of advanced manufacturing technology, 2016. **90**(9-12): p. 2513-2525.

109. Dupont, J.N. and A.R. Marder, *Dilution in single pass arc welds.* Metallurgical and materials transactions. B, Process metallurgy and materials processing science, 1996. **27**(3): p. 481-489.

110. Nagesh, D.S. and G.L. Datta, *Prediction of weld bead geometry and penetration in shielded metal-arc welding using artificial neural networks.* Journal of materials processing technology, 2002. **123**(2): p. 303-312.

111. Pal, S., S.K. Pal, and A.K. Samantaray, *Sensor based weld bead geometry prediction in pulsed metal inert gas welding process through artificial neural networks.* International journal of knowledge-based and intelligent engineering systems, 2008. **12**(2): p. 101-114.

112. Caio, L.B.A., *Analysis and estimation of extension of the fusion zone and sub-regions of the hear affected zone through neural networks in weld beads produced by GMAW process*. 2021, University of Brasilia.

113. Ismail, M.I.S., Y. Okamoto, and A. Okada, *Neural Network Modeling for Prediction of Weld Bead Geometry in Laser Microwelding.* Advances in optical technologies, 2013. **2013**: p. 1-7.

114. Chen, J., et al., *In situ strain and temperature measurement and modelling during arc welding.* Science & Technology of Welding & Joining, 2015. **20**(3): p. 181-188.

115. Xiong, J., et al., *Bead geometry prediction for robotic GMAW-based rapid manufacturing through a neural network and a second-order regression analysis.* Journal of intelligent manufacturing, 2012. **25**(1): p. 157-163.

116. Sun, Y.L., et al., *Effects of dilution on alloy content and microstructure in multi-pass steel welds.* Journal of Materials Processing Technology, 2019. **265**: p. 71-86.

117. Chen, T., et al., *Investigation on the Dynamic Behavior of Weld Pool and Weld Microstructure during DP-GMAW for Austenitic Stainless Steel.* Metals (Basel), 2020. **10**(6): p. 754.

118. Bag, S., A. De, and T. DebRoy, *A Genetic Algorithm-Assisted Inverse Convective Heat Transfer Model for Tailoring Weld Geometry.* Materials and manufacturing processes, 2009. **24**(3): p. 384-397.

119. Ahmad, A.S., et al., *Finite Element Prediction of Residual Stress and Deformation Induced by Double-Pass TIG Welding of Al 2219 Plate.* Materials, 2019. **12**: p. 2251.

120. Goldak, J.A., A.P. Chakravarti, and M. Bibby, *A new finite element model for welding heat sources.* Metallurgical Transactions B, 1984. **15**: p. 299-305.

121. Kermanpur, A., M. Shamanian, and V.E. Yeganeh, *Three-dimensional thermal simulation and experimental investigation of GTAW circumferentially butt-welded Incoloy 800 pipes.* Journal of materials processing technology, 2008. **199**(1): p. 295-303.

122. Zhu, X.K. and Y.J. Chao, *Numerical simulation of transient temperature and residual stresses in friction stir welding of 304L stainless steel.* Journal of materials processing technology, 2004. **146**(2): p. 263-272.

123. Ni, M., et al., *Forming characteristics and control method of weld bead for GMAW on curved surface.* International journal of advanced manufacturing technology, 2021. **119**(3-4): p. 1883-1908.

124. Hu, Z., et al., *Multi-bead overlapping model with varying cross-section profile for robotic GMAW-based additive manufacturing.* Journal of intelligent manufacturing, 2019. **31**(5): p. 1133-1147.

125. Chandrasekaran, R.R., et al., *Multi-variable statistical models for predicting bead geometry in gas metal arc welding.* International journal of advanced manufacturing technology, 2019. **105**(1-4): p. 1573-1584.

126. Vargas, J.A., et al. *Thermal analysis of GMAW process using Finite Element Method and experimental data*. in *2013 IEEE International Instrumentation and Measurement Technology Conference (I2MTC)*. 2013.

127. Craine, R.E., *On determining the shape of weld pools.* Applied Scientific Research, 1987. **44**(1-2): p. 261-275.

128. Keil, C. and G. Miller, *Modeling the size of small spills of pure volatile liquids for use in evaporation rate and air concentration modeling.* Journal of Occupational and Environmental Hygiene, 2020. **17**(7-8): p. 325-333.

129. Cai, X., et al., *Heat Source Characteristics of Ternary-Gas-Shielded Tandem Narrow-Gap GMAW.* Materials (Basel, Switzerland), 2019. **12**(9): p. 1397.

130. Fachinotti, V.D., A.A. Anca, and A. Cardona, *Analytical solutions of the thermal field induced by moving double-ellipsoidal and double-elliptical heat sources in a semi-infinite body.* International journal for numerical methods in biomedical engineering, 2011. **27**(4): p. 595-607.

131. Song Wu, C. and K.C. Tsao, *Modelling the three-dimensional fluid flow and heat transfer in a moving weld pool.* Engineering computations, 1990. **7**(3): p. 241-248.

132. Szymura, M., A. Czupryński, and M. Różański, *Research on the properties of high chromium cast iron overlay welds deposited by tubular electrodes.* Welding Technology Review, 2018. **90**.

133. Ryabtsev, I., A. Babinets, and I. Lentjugow, *The effect of the parameters of submerged arc surfacing with oscillating electrode on a padding weld forming, depth of fusion penetration and the content of parent metal in a weld.* Welding Technology Review, 2018. **90**.

134. Mas, F., et al., *Growth Morphologies and Primary Solidification Modes in a Dissimilar Weld between a Low-Alloy Steel and an Austenitic Stainless Steel.* Metals, 2018. **8**: p. 284.
135. Soudry, J., B.Z. Weiss, and I. *Weld Pool Segregation During the Welding of Low Alloy Steels with Austenitic Electrodes*. 2013.
136. Baeslack, W.A., J.C. Lippold, and W.F. Savage. *Unmixed zone formation in austenitic stainless steel weldments. [18 Cr-8 Ni weldments]*. 1979.
137. Tadamalle, A., et al., *Influence of welding speed on the melting efficiency of Nd:YAG laser welding.* Advances in Production Engineering & Management, 2014. **9**: p. 128-138.
138. Fuerschbach, P.W. and G.A. Knorovsky, *A study of melting efficiency in plasma arc and gas tungsten arc welding : a method for selecting optimal weld schedules to minimize net heat input is derived frm calorimetric measuremts.* Welding Journal, 1991. **70**: p. 287-297.
139. Lancaster, J.F., *CHAPTER 2 - The Physical Properties of Fluids at Elevated Temperatures*, in *The Physics of Welding (Second Edition)*, J.F. Lancaster, Editor. 1986, Pergamon. p. 9-46.
140. Zorc, M., et al., *Determining the Degree of Admixing Rate of the Base Material and the Melting Efficiency in Single-Bead Surface Welds Using Different Methods, Including New Approaches.* Materials, 2019. **12**(9): p. 1479.
141. Nguyen, N.T., et al., *Analytical approximate solution for double ellipsoidal heat source in finite thick plate.* Welding journal, 2004. **83**(3): p. 82s-93s.
142. Sen, M., et al., *Effect of double-pulsed gas metal arc welding (DP-GMAW) process variables on microstructural constituents and hardness of low carbon steel weld deposits.* Journal of Manufacturing Processes, 2018. **31**: p. 424-439.
143. Brooks, R.F. and P.N. Quested, *The surface tension of steels.* Journal of materials science, 2005. **40**(9-10): p. 2233-2238.
144. Fukuyama, H., H. Higashi, and H. Yamano, *Thermophysical Properties of Molten Stainless Steel Containing 5 mass % B4C.* Nuclear Technology, 2019. **205**(9): p. 1154-1163.
145. Rywotycki, M., et al., *Modelling Liquid Steel Motion Caused by Electromagnetic Stirring in Continuous Casting Steel Process.* Archives of Metallurgy and Materials, 2014. **59**: p. 487-492.
146. Chapuis, J., et al., *Dynamic behavior of the weld pool in stationary GMAW.* EPJ Web of Conferences, 2010. **6**.
147. Tajima, M. and Y. Umeyama, *Latent heats of phase transformations in iron and steels.* High Temperatures-high Pressures - HIGH TEMP-HIGH PRESS, 2002. **34**: p. 91-97.
148. Mustafa, M., A.F. Arif, and K. Masood, *Approximate Analytic Solutions of Transient Nonlinear Heat Conduction with Temperature-Dependent Thermal Diffusivity.* Abstract and Applied Analysis, 2014. **2014**.
149. Solek, K., *Identification of the steel viscosity and dynamic yield stress for the numerical modelling of casting simulations in the semi-solid state.* Archives of Metallurgy and Materials, 2017. **62**.

150. Dupont, J.N. and A.R. Marder, *Thermal efficiency of arc welding processes.* Welding Journal, 1995. **74**.